A novel quasi-Lagrangian perspective on the potential vorticity dynamics of blocked weather regime life cycles in the North Atlantic-European region

Zur Erlangung des akademischen Grades eines
DOKTORS DER NATURWISSENSCHAFTEN
von der KIT-Fakultät für Physik des
Karlsruher Instituts für Technologie (KIT)

genehmigte

DISSERTATION

von

M.Sc. Seraphine Hauser
aus Horb am Neckar

Tag der mündlichen Prüfung:	21.07.2023
Referent:	Jun.-Prof. Dr. Christian M. Grams
Korreferent:	Prof. Dr. Peter Knippertz
Ext. Korreferent (JGU Mainz):	PD Dr. habil. Michael Riemer

Abstract

Atmospheric blocking describes a midlatitude flow configuration, in which a quasi-stationary anticyclonic circulation anomaly – referred to as block – hinders the eastward propagation of synoptic-scale weather systems. This pattern often causes extreme weather in the vicinity of the block. The correct representation of blocking, and in particular the onset, is a major challenge in current numerical weather prediction models. One reason for this difficulty arises from the lack of the dynamical understanding of blocking. A multitude of theories on the complex blocking dynamics have been developed, each focusing on a specific aspect of blocking. Until today, the different theories could not be connected yet, and even revealed contradictionary results in the contribution of dry and moist processes, such that a consistent view on the relative role of dry and moist dynamics in blocking life cycles is still missing.

This thesis aims to shed light onto blocking dynamics, and, in particular, to disentangle the relative contributions of dry and moist processes. To this end, a novel quasi-Lagrangian potential vorticity (PV) framework is developed. Since the worst forecast busts linked to blocking occur over Europe, the focus is set on blocking in the North Atlantic-European region. Applied to state-of-the-art ERA5 reanalysis for the period 1979–2021, upper-tropospheric negative PV anomalies (PVAs$^-$) linked to blocking are tracked. Using piecewise PV tendencies, the contributions of dry and moist dynamics in the amplitude evolution of PVAs$^-$ are investigated. Blocking is examined using the concept of weather regimes, which are large-scale, persistent, and recurrent states of the extratropical circulation. With a unique year-round weather regime definition, the life cycles of four 'blocked' regime patterns are studied: European Blocking (EuBL), Scandinavian Blocking (ScBL), Atlantic Ridge (AR), and Greenland Blocking (GL).

A strong forecast bust linked to a EuBL regime life cycle in March 2016 was associated with an underestimation of moist processes over the eastern North Atlantic. The novel framework reveals that the PVA$^-$ linked to the block developed remotely near the East Coast of the United States and propagated into Europe. During the propagation, the PVA$^-$ experienced several episodes of amplification, mainly by moist processes associated with warm conveyor belt (WCB) activity. This finding confirms a previous hypothesis by Grams et al. (2018) that WCB activity upstream of the incipient block was key to the blocking onset in March 2016. Eulerian diagnostics would emphasize the dry-dynamical propagation of PVAs$^-$, and thereby miss the substantial moist contribution remote of the blocked region. Thus, by focusing on the physical processes relevant to blocking onset, the framework allows to disentangle dry and moist contributions, and their interconnection.

The systematic analysis of blocking dynamics for the four blocked regime types shows in this thesis, for the first time, that PVAs$^-$, triggering the onset of blocked regimes, develop remotely and propagate into the blocked region before the onset. Importantly, two pathways are identified that describe the propagation of PVAs$^-$ from the west (upstream pathway) and from the east (retrogression pathway) into the blocked region. PVAs$^-$ are amplified during the days before the onset when moist processes are the dominant contributions. However, the timing differs, such that retrograding PVAs$^-$ experience maximum amplification earlier than upstream PVAs$^-$. Consequently, the retrogression of PVAs$^-$ occurs not purely barotropically, but is an interplay with moist processes that amplify the PVA$^-$ on the western flank and thus shifts it westward. These pathways of PVAs$^-$ and the respective different dynamics were not known before and provide a novel perspective on blocking. The framework reveals a linkage of the regime and PVA$^-$ life cycle around the regime maximum stage. Moist processes dominate the maintenance of the PVAs$^-$ before, and quasi-barotropic dynamics lead to the degradation of the PVAs$^-$ after the maximum stage. The regime decay is associated with a strong decrease in PVA$^-$ amplitude, and, most importantly, with the propagation of PVAs$^-$ out of the regime region. Again, the framework unveils two pathways of PVAs$^-$ towards the west and east, which reveals that some PVAs$^-$ contribute to successor blocked regimes. The differences in dynamics between the blocked regime types are small, with clearer differences residing in the dynamics of the pathways. For the onset, two marginal differences are evident that make GL stand out. First, the retrogression pathway of PVAs$^-$ dominates for GL, but not for EuBL, ScBL, and AR. And second, moist processes play a similar role for PVAs$^-$ independent of the pathway for GL but exhibit a much higher contribution for upstream than retrograding PVAs$^-$ of EuBL, ScBL, and AR. This variation arises from the position of the block relative to the storm track and indicates the sensitivity of blocking dynamics to the exact blocking location.

Overall, this thesis, for the first time, reconciles different perspectives and theories on blocking in the North Atlantic-European region and provides a novel quasi-Lagrangian PV framework with potential for future work on blocking dynamics.

Zusammenfassung

In den mittleren Breiten kommt es gelegentlich zu einer Strömungskonfiguration, bei welcher eine quasistationäre antizyklonale Zirkulationsanomalie (oftmals als „Block" bezeichnet) eine Umkehrung der großräumigen westlichen Strömung hervorruft. Diese Situation wird im Englischen als „Blocking" bezeichnet und kann in angrenzenden Regionen zu Extremwetter führen. Die korrekte Darstellung von Blocking stellt eine große Herausforderung in aktuellen numerischen Wettervorhersagemodellen dar. Ein Grund dafür liegt im mangelnden dynamischen Verständnis von Blocking. In der Vergangenheit wurden zahlreiche Theorien zur Dynamik von Blocking entwickelt, von denen jede einen bestimmten Aspekt der Dynamik betrachtet. Bis heute konnten die verschiedenen feuchtdynamischen und trockendynamischen Theorien noch nicht miteinander verbunden werden und lieferten sogar widersprüchliche Ergebnisse. Noch immer fehlt eine konsistente Sicht auf die relative Rolle trockener und feuchter Dynamik in den Lebenszyklen von Blocking.

Diese Arbeit zielt darauf ab, die Dynamik von Blocking zu erfassen und insbesondere die relativen Beiträge trockener und feuchter Prozesse zu entflechten. Dazu wird eine neuartige quasi-Lagrangsche Methode auf Basis der potenziellen Vortizität (PV) entwickelt. Da Vorhersagefehler in Verbindung mit Blocking vor allem in Europa vorkommen, liegt der Fokus auf Blocking über dem Nordatlantik und über Europa. Anhand der hochmodernen ERA5-Reanalyse für den Zeitraum 1979–2021 werden negative PV-Anomalien in der oberen Troposphäre (PVAs^{-}) verfolgt, die mit Blocking in Verbindung stehen. Mithilfe stückweiser PV-Tendenzen werden die relativen Beiträge trockener und feuchter Dynamik zur Amplitudenentwicklung von PVAs^{-} quantifiziert. Blocking wird in dieser Arbeit aus Sicht von Wetterregimen betrachtet, die großräumige, anhaltende und wiederkehrende Zustände der außertropischen Zirkulation darstellen. Eine einzigartige Definition von Wetterregimen ermöglicht die Untersuchung der Lebenszyklen von vier verschiedenen „blockierten“ Regimen: Blocking über Europa (EuBL), über Skandinavien (ScBL), über dem Atlantik (AR) und über Grönland (GL).

Ein schwerwiegender Vorhersagefehler, der mit dem Lebenszyklus von Blocking im März 2016 über Europa zusammenhängt, war mit einer Unterschätzung feuchter Prozesse über dem östlichen Nordatlantik verbunden. Die neue quasi-Lagrangsche Methode zeigt, dass die mit dem Block verknüpfte PVA^{-} sich nicht lokal über Europa entwickelte, sondern weit entfernt von der Region vor der Ostküste der Vereinigten Staaten zum ersten Mal identifiziert wurde und nach Europa propagierte. Während der Überquerung des Nordatlantiks durchlief die PVA^{-} mehrere Episoden abrupter Verstärkung, hauptsächlich durch

feuchte Prozesse im Zusammenhang mit der Aktivität von sogenannten 'Warm Conveyor Belts' (WCB). Diese Erkenntnis bestätigt eine frühere Hypothese von Grams et al. (2018), dass die WCB-Aktivität stromaufwärts des beginnenden Blocks entscheidend für den Aufbau von Blocking im März 2016 war. Eulersche Diagnosen würden die trocken-dynamische Propagation der PVA$^-$ betonen und somit den erheblichen feuchten Beitrag in der Ferne der blockierten Region übersehen. Durch die Fokussierung auf die physikalischen Prozesse, die für den Beginn von Blocking relevant sind, ermöglicht die neuartige quasi-Lagrangsche Methode eine Entflechtung der trockenen und feuchten Beiträge.

Die systematische Auswertung der Dynamik von Blocking zeigt in dieser Arbeit zum ersten Mal, dass sich PVAs$^-$ entfernt von der Region entwickeln und in die blockierte Region hineinwandern. Es wurden zwei Pfade identifiziert, über die PVAs$^-$ aus dem Westen (stromaufwärtiger Pfad) und aus dem Osten (retrograder Pfad) in die blockierte Region propagieren. Die PVAs$^-$ werden in den Tagen vor dem Blocking überwiegend durch Feuchtprozesse verstärkt. Allerdings unterscheidet sich der Zeitpunkt, sodass retrograd-wandernde PVAs$^-$ die maximale Verstärkung früher erfahren als stromaufwärts propagierende PVAs$^-$. Infolgedessen erfolgt die westwärts gerichtete Propagation von PVAs$^-$ nicht rein barotrop, sondern ist das Resultat des Zusammenspiels mit feuchten Prozessen, welche die PVA$^-$ an der westlichen Flanke verstärken und sie somit nach Westen verschieben. Die Pfade der PVAs$^-$ und die jeweilige zugrundeliegende Dynamik waren zuvor nicht bekannt und liefern einen neuen Blickwinkel auf Blocking. Rund um die maximale Ausprägung des Regimes enthüllt die quasi-Lagrangsche Methode einen Zusammenhang zwischen dem Lebenszyklus des Regimes und dem Lebenszyklus der PVA$^-$. Feuchtprozesse dominieren die Verstärkung und Aufrechterhaltung der PVA$^-$ vor dem Regime-Maximum, während quasi-barotrope Dynamik maßgeblich zum Abbau nach dem Regime-Maximum beiträgt. Der Zerfall des Regime-Lebenszyklus geht mit einer starken Abschwächung der PVA$^-$-Amplitude einher und vor allem mit der Propagation von PVAs$^-$ aus der Region heraus. Erneut enthüllt die Methode zwei Pfade von PVAs$^-$ nach Westen und Osten, was zeigt, dass einige PVAs$^-$ zu nachfolgenden blockierten Regimen beitragen. Generell sind die Unterschiede in der Dynamik zwischen den blockierten Regimen geringer im Vergleich zu den Unterschieden zwischen den PVA$^-$ Pfaden. Dabei sticht Blocking über Grönland im Vergleich zu den anderen Regimen beim Aufbau von Blocking heraus. Erstens dominiert der retrograde Pfad von PVAs$^-$ für GL, was nicht der Fall ist für EuBL, ScBL und AR. Und zweitens spielen feuchte Prozesse für PVAs$^-$ bei GL unabhängig vom Pfad eine ähnliche Rolle, während sie für stromaufwärts propagierende PVAs$^-$ von EuBL, ScBL und AR einen deutlich höheren Beitrag leisten. Diese Variation resultiert aus der Position des Blocks relativ zur typischen Zugbahn von Tiefdruckgebieten und zeigt die Empfindlichkeit der Dynamik von Blocking gegenüber dem genauen Ort von Blocking.

Insgesamt versöhnt diese Arbeit zum ersten Mal unterschiedliche Perspektiven und Theorien zu Blocking in der Region über dem Nordatlantik und Europa und liefert eine neuartige quasi-Lagrangsche PV-Methode mit Potenzial für zukünftige Arbeiten zur Dynamik von Blocking.

Preface

The PhD candidate confirms that the research presented in this thesis contains significant scientific contributions by herself.

This thesis reuses material from the following publication:

> Hauser, S., Teubler, F., Riemer, M., Knippertz, P., and Grams, C. M., 2023: Towards a holistic understanding of blocked regime dynamics through a combination of complementary diagnostic perspectives, *Weather and Climate Dynamics*, **4** (**2**), 399–425.

The research leading to these results was performed within the subproject A8 “Dynamics and predictability of blocked regimes in the Atlantic-European region” of the Transregional Collaborative Research Center SFB/TRR 165 “Waves to Weather” funded by the German Research Foundation. The Helmholtz Partitioning and the piecewise PV inversion described in Section 4.3 were carried out and provided by W2W project colleague Dr. Franziska Teubler from the Johannes Gutenberg University in Mainz. The analyses in Hauser et al. (2023b) were – apart from the Eulerian perspective – performed by the candidate, who also wrote the manuscript, with advice from Jun.- Prof. Dr. Christian M. Grams, Prof. Dr. Peter Knippertz and PD. Dr. habil. Michael Riemer.

The candidate confirms that appropriate credit has been given within the thesis where reference has been made to the work of others. This copy has been supplied on the understanding that this is copyright material and that no quotation from the thesis may be published without proper acknowledgment.

Contents

1 Introduction

Extreme weather events pose significant challenges to societies worldwide, with impacts on various sectors, including human health, infrastructure, ecosystems, and the economy. The term ’extreme weather’ encompassed a wide range of types, ranging from small-scale thunderstorm events to large-scale heat waves or cold spells (Kautz et al., 2022). Two prominent examples of extreme weather events on the large scale are the European heat waves in 2003 and 2010 that led to extreme droughts, devastating forest fires, substantial losses in agricultural production, and fatalities across Europe (e.g., Mitchell et al., 2016). In early winter 2020/2021, a cold spell hit China that resulted in new minimum temperature records at multiple observational weather stations (Yao et al., 2022). Especially recently, extreme events exceeded partly long-standing records by large margins (Fischer et al., 2021), such as the unprecedented Western North American heat wave in 2021 (Fig. 1.1a), which surpassed the previous all-time heat record by 5 K for Canada (e.g., Oertel et al., 2023). Another example is the flooding event over Central Europe in July 2021, which led to regional devastation and is among the five costliest disasters of the last half century in Europe (Mohr et al., 2023). Despite the diversity of such extreme weather events, they all share the commonality of a certain large-scale flow pattern, which is dominated by a stationary high-pressure system.

Stationary, long-lived high-pressure systems occasionally disrupt the mean westerly flow and ‘block‘ the propagation of midlatitude synoptic-scale weather systems (e.g., Rex, 1950). This flow configuration is referred to as atmospheric blocking and has been identified as precursor to the extreme events mentioned above. Thereby, the term ’blocking’ does not comprise only the blocking anticyclone (often referred to as block) itself, but also the circulation pattern in which the block forms the dominant part. The type and location of extreme weather linked to blocking depends on the exact location of the block (Brunner et al., 2018) such that it is important to accurately predict these flow patterns to provide early warning of possible extreme weather. Back in the 1980s, operational forecasts by the European Centre for Medium-Range Weather Forecasts (ECMWF) frequently missed the onset of blocking beyond 3–4 days in advance (Tibaldi and Molteni, 1990). Despite the improvements in the representation of atmospheric processes in models, enhanced observational capabilities, and refined forecasting techniques, state-of-the-art numerical weather prediction models still struggle with the correct representation of blocking, where especially the formation and maintenance of the blocking pattern poses a difficulty (e.g., Ferranti et al., 2015; Matsueda and Palmer, 2018). Especially over Europe, occasional episodes of very poor forecasts of the large-scale flow pattern have been linked to the onset of a blocking pattern (e.g., Rodwell

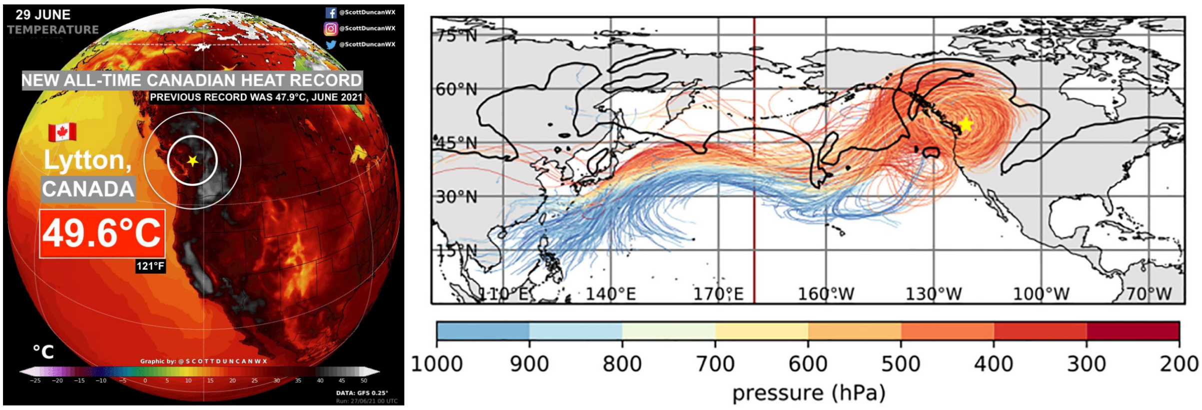

(a) (b)

Figure 1.1: (a) Reprinted twitter post from Duncan (2021) on the all-time Canadian heat record of 49.6 °C in Lytton (Canada) on 29 June 2021, which has been linked to the Western North American heat wave in 2021. (b) 10-day backward trajectories initialized within the upper-tropospheric ridge over North America on 29 June 00 UTC, which are located below 800 hPa 10 days earlier. Around 20 % of the total 1,249 trajectories ascend from the lower troposphere into the upper-tropospheric ridge. Reprinted from Oertel et al. (2023).

et al., 2013; Magnusson, 2017). Not only do weather models struggle to predict blocking, but also subseasonal and climate models face a systematic underestimation of the blocking frequency, in particular over the North Atlantic (e.g., Quinting and Vitart, 2019; Davini et al., 2021). Apart from uncertainties in the initial conditions and limitations of weather models, the complex underlying atmospheric dynamics contribute to the difficulty in predicting blocking.

The dynamics of blocking have been studied for decades, with the focus on the onset, maintenance, and decay of blocking (e.g., Woollings et al., 2018). Despite a wide variety of blocking dynamic concepts, a unified, process-based conceptual understanding addressing all aspects of the blocking life cycle is missing (e.g., Woollings et al., 2018; Lupo, 2021). Often, the dynamics are linked to a complex interplay between various processes on different temporal and spatial scales. In particular, a distinction is made between dry and moist dynamics (Fig. 1.2). Dry dynamics have been considered as main processes for blocking development for a long time (e.g., Shutts, 1983; Nakamura et al., 1997; Yamazaki and Itoh, 2013). From the perspective of potential vorticity (PV) as a key variable for midlatitude dynamics, the quasi-adiabatic transport of low-PV air masses along the amplified upper-tropospheric jet into the block has been linked to dry dynamics (blue arrow in Fig. 1.2). However, in the last decade, there has been a growing interest in the role of moist processes for blocking, described by the cross-isentropic transport of low-PV air into the block (red arrow in Fig. 1.2). Multiple studies in recent years have emphasized the presence and importance of latent heat release in modifying the midlatitude flow towards a blocking pattern (e.g., Pfahl et al., 2015; Steinfeld and Pfahl, 2019). For example, around 20 % of the air parcels ending up in the block linked to the Western North American heat wave in 2021 experienced latent heating and made an essential moist contribution to the establishment of the stationary large-scale block over

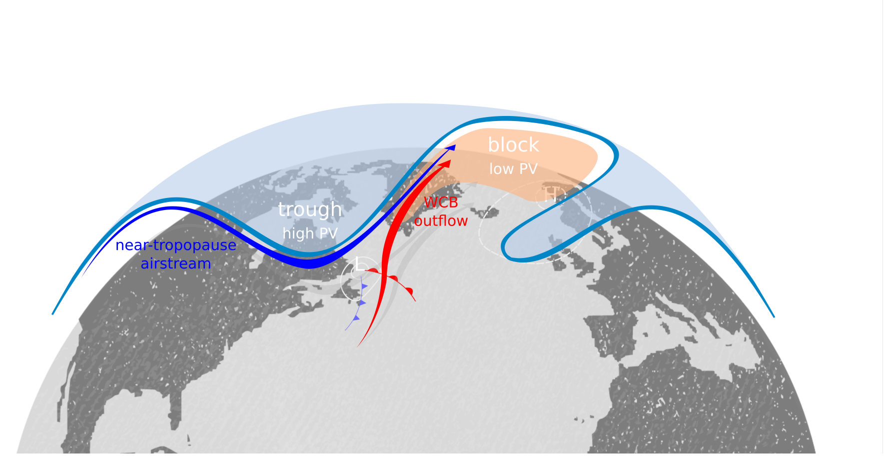

Figure 1.2: Schematic illustration of the dry and moist processes involved in the formation and maintenance of atmospheric blocking. Anomalous air masses with low PV are carried into the upper-level block through two distinct processes: (1) air masses are transported through ascending airstreams, characterized by intense latent heat release ahead of an extratropical cyclone (indicated by the red airstream), and (2) air masses can be transported quasi-adiabatically along the amplified upper-level jet, close to the tropopause, with minimal radiative cooling (represented by the blue airstream). Reprinted from Steinfeld et al. (2022).

Western North America (Fig. 1.1b). The studies on the importance of dry and moist dynamics are often isolated and could not be united so far. As different perspectives collide, some theories produce even contradictory results (e.g., Shutts, 1983; Pfahl et al., 2015). With an increase in available moisture in a warmer climate, moist processes for blocking become more important, with a high potential for intensified and longer-lasting episodes of blocking (Steinfeld et al., 2022). Consequently, the roles of dry and moist processes in blocking dynamics need to be considered together in a common framework in order to clarify the question of the relative importance of dry and moist dynamics, which is of high relevance to improve the representation of blocking in climate models.

In the last years, novel methods have been proposed, which enable the investigation of blocking from a different perspective. For the first time, a year-round weather regime definition has been developed by Grams et al. (2017) in the North Atlantic-European region. Weather regimes represent quasi-stationary, persistent, and recurrent large-scale circulation patterns in midlatitudes (e.g., Vautard, 1990), and allow a separate consideration of blocking in different subregions. As regional differences of blocking frequency biases in numerical weather prediction models (e.g., Quinting and Vitart, 2019) suggest that the underlying processes linked to blocking might be sensitive to the location of the block, a separate investigation of blocking in different regions is essential. Recently, Teubler and Riemer (2021) have studied the contributions of different processes to the amplitude evolution of troughs and ridges in the Northern Hemisphere with a framework based on PV. This framework enabled the quantification of dry and moist processes for the development of large-scale Rossby waves.

This thesis aims to shed light onto the dynamics of blocking in the North Atlantic-European region, thereby unifying different and stand-alone theories on blocking dynamics in a consistent framework. Blocking is, for the first time, investigated from a weather regime perspective (Grams et al., 2017), which allows disentangling the importance of dry and moist processes in the dynamics of four different blocking patterns. The thesis is structured as follows: Chapter 2 provides background knowledge on the phenomenology of atmospheric blocking, the concept of large-scale weather regimes, and midlatitude atmospheric dynamics from a PV perspective. The research questions are developed on the basis of this background information in Chapter 3. The data sets and methods that are used throughout the thesis are introduced in Chapter 4. The development and detailed description of the novel framework is the content of Chapter 5. Insights into the blocking dynamics are gained in Chapters 6–8, which present the main results of the thesis. Finally, overarching findings of the thesis are discussed, and an outlook is provided in Chapter 9.

2 Background

This chapter provides an overview of midlatitude dynamics (Sect. 2.1), the phenomenology and theories of atmospheric blocking (Sect. 2.2), and North Atlantic-European weather regimes (Sect. 2.3). This is followed by a detailed description of potential vorticity (PV) as the key variable in this thesis (Sect. 2.4). All sections introduce some historical aspects, and discuss recent scientific developments in the fields. Over the course of the chapter, the individual topics are linked, and research gaps are identified.

2.1 Midlatitude atmospheric dynamics

Midlatitude atmospheric dynamics refers to the complex processes that occur in the Earth's atmosphere in the geographic regions that lie between the subtropics and the polar regions, typically between 30 ° and 60 ° latitude in both the Northern and Southern Hemispheres. The weather and climate in the midlatitudes are generally determined by the large-scale atmospheric flow dominated by prevailing westerlies, as a result of the interaction between the Earth's rotation, associated variations in solar heating, the pressure gradient force, and the Coriolis force. More specifically, pressure differences between the subpolar low-pressure zone and the subtropical high-pressure zone, caused by the Hadley, Ferrell, and Polar Cell forming the global atmospheric circulation, and the Coriolis effect force winds to blow from west to east in the midlatitudes (e.g., Held and Hou, 1980). The westerlies form narrow, fast-flowing air currents at high altitudes - the jet streams - around the Earth's midlatitudes at the boundary between the troposphere and the stratosphere. The jet streams can be roughly described as being in a state of 'thermal wind balance', where the vertical variation in wind velocity (often referred to as vertical wind shear) is directly related to the horizontal differences in temperature gradient. In particular for midlatitude atmospheric dynamics, these jet streams are the crucial components as they play an essential role in shaping weather and climate patterns (e.g., Schneider, 2006; Martin, 2006).

In midlatitudes, two different types of jet streams exist. One is the subtropical jet stream, which represents a narrow band of strong winds that forms at the poleward edge of the Hadley cell (~30 ° latitude) and flows from west to east in the upper troposphere near the boundary between the tropics and midlatitudes (e.g., Newton and Persson, 1962). The polar jet, also known as the midlatitude or eddy-driven polar jet, forms a further narrow band of strong winds flowing from west to east in the upper troposphere that is typically located between ~30 ° and 60 ° latitude. Although both jet types form primarily as a result of the thermal wind balance, the eddy-driven polar jet is supported by convergence of eddy momentum

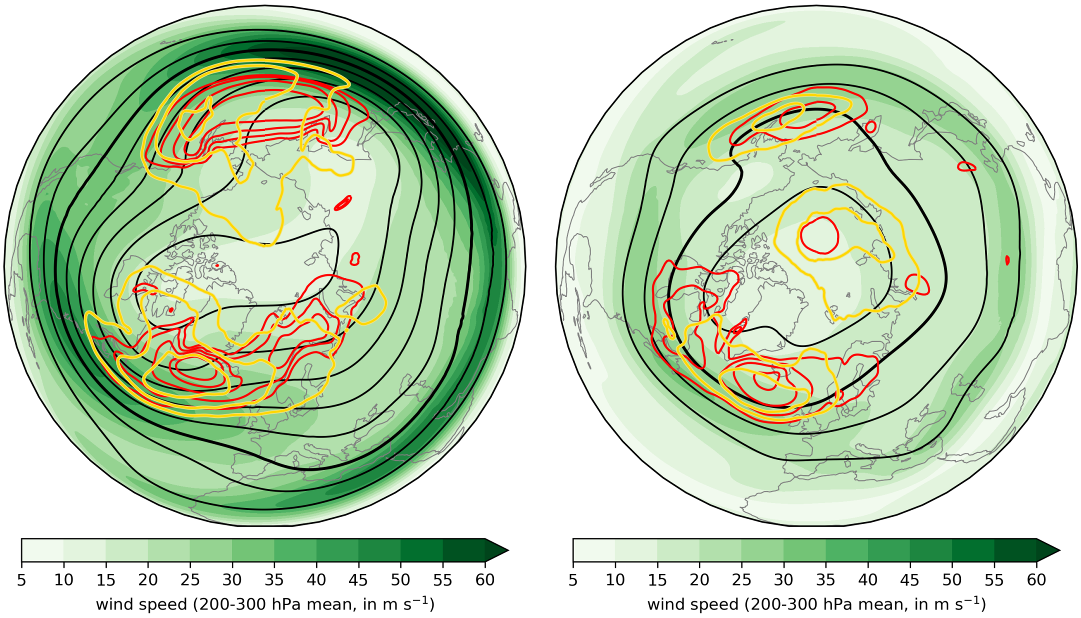

(a) winter (DJF)

(b) summer (JJA)

Figure 2.1: Overview of the large-scale extratropical circulation and embedded weather systems for (a) winter (December–February) and (b) summer (June–August). Vertically-averaged wind speed between 200 and 300 hPa (shading, in m s^{-1}), Z500 in black contours (in gpm from 5000 to 5700 in steps of 100 gpm), blocking frequency following the algorithm of Schwierz et al. (2004) in yellow contours (in steps of 0.05, 0.07, 0.09, 0.11), and cyclone frequency following the algorithm of Wernli and Schwierz (2006) in red contours (in steps of 0.2, 0.25, 0.3, 0.35, 0.4). Note that the climatological cyclone frequencies south of 30 °N were removed due to the noisy signals that are in particular created by topography and the monsoon over the Asian continent.

flux by baroclinic, transient eddies (Held, 1975). Even though the two jet types owe their existence to different formation mechanisms, a clear separation is not always possible (e.g., Winters et al., 2020). From a climatological perspective, two maxima in wind speed related to the jet streams are located over the western ocean basins of the North Pacific and North Atlantic (Fig. 2.1). The jet streams feature slightly different characteristics depending on the season, with higher wind speeds in winter than in summer due to a larger temperature contrast between the equator and the subtropics. The weakened meridional temperature gradient in summer leads not only to weaker wind speeds, but also to a poleward shift of the polar jet (Fig. 2.1b). Topography and the land-sea contrast can frequently cause planetary-scale longitudinal variations from the zonal symmetry of a strong wind band (Wills et al., 2019). These stationary waves are visible in the geopotential height field in the mid-troposphere as equatorward displacements over the eastern coasts of the North Pacific and North Atlantic and poleward displacements over Western Europe and Alaska (Fig. 2.1).

The undulations of the zonally-oriented westerly winds on the large scale are also referred to as Rossby Waves (Rossby, 1940), with the jet streams acting as Rossby waveguides (e.g., Wirth et al., 2018). Rossby waves shape the movement, strength, and duration of midlatitude synoptic-scale weather systems, which play a key role in the meridional redistribution of heat flux, momentum, and moisture over large distances (e.g., Holton and Hakim, 2012). As weather systems move along with the jet, they gain momentum and extract energy from it, pointing together with the formation of the eddy-driven jet to a two-way interaction. The path and intensity of the jet stream are closely linked to the growth and decay of weather systems, such that these systems tend to emerge in areas where the jet stream is accelerating (e.g., Wallace et al., 1988). As a result, the pathways of extratropical cyclones and anticyclones, commonly known as midlatitude storm tracks (e.g., Hoskins and Valdes, 1990), typically align with the position of the jets (Fig. 2.1). In summer and winter, the regions of high extratropical cyclone activity are located in the vicinity of the jet streams over the ocean basins, with a particular northward tilt over the North Atlantic towards Northern Europe in winter (Fig. 2.1a). Anticyclones, or high pressure systems, are interspersed within the prevailing westerly flow and interrupt the occurrence of cyclones. Occasionally, the situation arises that an anticyclone becomes stationary and persistent. This phenomenon is referred to as atmospheric blocking (Rex, 1950) and occurs most frequently on the eastern edge of the jet streams, in particular over the eastern North Atlantic and the eastern North Pacific (Fig 2.1).

2.2 Atmospheric blocking

2.2.1 Phenomenology

Atmospheric blocking describes a flow configuration in mid and high latitudes with a dominant, stationary, and long-lived high pressure systems which hinders the eastward progression of synoptic-scale weather systems (e.g., Rex, 1950; Steinfeld and Pfahl, 2019). The stationary high pressure system - frequently referred to as the 'block' - disrupt and decelerates the zonal westerly flow (e.g., Nakamura and Huang, 2018). Due to the persistence and stationarity, blocking can affect continent-size regions for several days and has a clear societal impact. By the modulation of synoptic-scale weather systems that determine surface weather, blocking is often associated with extreme weather events (Kautz et al., 2022). Thereby, the type of extreme weather depends heavily on the location of the block (Matsueda, 2009). Blocking can therefore be associated with flooding (e.g., Houze et al., 2011; Lenggenhager et al., 2019), heat waves and resulting droughts in summer (e.g., Alvarez-Castro et al., 2018), cold spells in winter (e.g., Sillmann et al., 2011; Luo et al., 2016), and storms (e.g., Grams et al., 2017).

Although a particular flow pattern has to fulfill several criteria to be classified as a blocking pattern, there is a high internal variability that results in very different blocking types. Figure 2.2 shows the variety of circulation patterns that are all referred to as atmospheric blocking in the North Atlantic region. These configurations, nonetheless, are not limited to the North Atlantic region and occur also in the North Pacific (e.g., Breeden et al., 2020). The most common patterns associated with blocking are the omega block (Fig. 2.2b) and the dipole block (Fig. 2.2e), also known as a 'Rex block' (Rex, 1950). The omega block pattern resembles the Greek letter Ω where typically a huge anticyclone is flanked by cyclones upstream (southwest) and downstream (southeast). In contrast, dipole block circulations are characterized by two adjacent highs and lows with a high sitting on the poleward side of the low, which leads to the reversal of the usual meridional flow. Further, blocking configurations feature the occurrence of 'Rossby wave breaking' (RWB) events (Pelly and Hoskins, 2003), which describe the breaking of Rossby waves, when the amplitude becomes very large and the wave becomes unstable (Masato et al., 2012). Anticyclonic and cyclonic RWB are shown in Figure 2.2c,d. Despite the assignment of blocking patterns to one of the mentioned categories, it cannot be excluded that a blocking event exhibits more than only one of these configurations over its life cycle (Lupo, 2021).

A variety of objective methods exist for the identification and quantification of atmospheric blocking, each of which captures different patterns of blocking (cf. Pinheiro et al., 2019). Consequently, resulting climatologies of atmospheric blocking depend heavily on the respective method and exhibit discrepancies in the comparison, reflecting the diversity of the term 'atmospheric blocking' (Woollings et al., 2018; Davini et al., 2012). The index of Tibaldi and Molteni (1990) identifies blocking in longitudes where the gradient of geopotential height at 500 hPa (Z500) is reversed, resulting in a timeline of a 1D binary blocking index. Further and more recent definitions of blocking capture the occurrence of blocking based on 2D anticyclonic anomaly features identified by, for example, quasi-stationary positive anomalies of Z500 (e.g., Liu et al., 2018). Similarly, other studies detect 2D features from upper-level fields of PV (e.g., Schwierz et al., 2004), which is a key variable in dynamical meteorology and introduced in Section 2.4. Tyrlis and Hoskins (2008) studied the aspects of the Northern hemispheric blocking climatology and found two hotspots in fairly well agreement with the blocking climatology in Figure 2.1 (yellow contours). The first hotspot covers a large region from the eastern North Atlantic through Europe to Central Asia, and the second hotspot ranges from the central to the eastern North Pacific. Within these hotspots, there are a variety of region-specific and seasonally occurring blocking configurations of which the detection and dynamical understanding is not yet clear (Sousa et al., 2021).

It is of particular interest to predict atmospheric blocking in advance due to the link to extreme weather events. In general, blocking represents a key challenge for forecast models (e.g., Davini and D'Andrea, 2016). In particular, the onset is hard to predict, as blocking mostly develops rapidly out of a zonally oriented flow (Ferranti et al., 2015; Büeler et al., 2021). Rodwell et al. (2013) even hypothesized that some of the largest forecast errors over Europe are associated with the transition to blocking. One example is the onset of a blocking event over Northern Europe in March 2016, which was associated with one of the worst forecast busts at ECMWF (Magnusson, 2017; Grams et al., 2018). Investigations of this case revealed that the ensemble forecast failed to correctly represent the amplitude of the ridge, which was the result of the misrepresentation of an upper-level trough near Newfoundland (Magnusson, 2017). This trough triggered synoptic activity linked to diabatic processes in the North Atlantic region, which

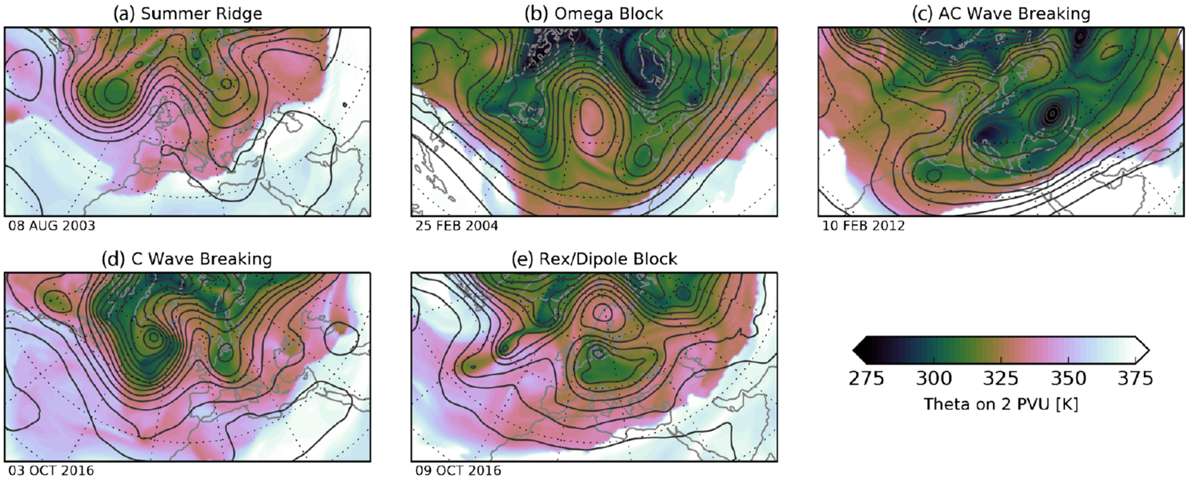

Figure 2.2: Variety of circulation patterns associated with atmospheric blocking in the North Atlantic. Potential temperature θ (shading, in K) on the dynamical tropopause (=2 PVU, cf. Sect. 2.4) and Z500 (black contours, every 60 m) for different dates indicated at the bottom pf each panel. The abbreviations AC and C stands for anticyclonic and cyclonic, respectively. Figure adapted from Woollings et al. (2018).

was misrepresented in the ensemble forecast, and consequently amplified existing forecast errors downstream (Grams et al., 2018). Recently, a study corroborated in a more systematic analysis that errors in the evolution of large-scale blocking are strongly tied to synoptic-scale forecast errors (Wandel, 2022), which further supports the assumption of Magnusson (2017) and Grams et al. (2018) that instabilities in the flow, and, in particular, diabatic outflow are important drivers of uncertainty in blocking. For the blocking over Northern Europe in March 2016, a co-occurrence of the amplifying ridge linked to the block and diabatic processes was found, suggesting that diabatic processes played a role for the amplification of the ridge (Grams et al., 2018). However, the interaction was not fully explored in these studies and still remains an open question.

For the prediction of blocking on sub-seasonal time scales, Quinting and Vitart (2019) revealed that different models underestimate the blocking frequency over the Atlantic-European sector. This negative bias becomes weaker for higher resolution model runs, suggesting that, among other things, processes at smaller scales are important for a block to evolve. In recent years, there has been growing interest on how the occurrence of blocking and its link to extreme weather will change in a warmer climate, and still remains an open question (e.g., Woollings et al., 2018). The response of blocking frequency to climate change seems to be weak, highly dependent on the blocking detection method and region, and in particular driven by more internal variability (e.g., Masato et al., 2013; Barnes et al., 2014; Woollings et al., 2018).

2.2.2 Theories

The phenomenon of atmospheric blocking has been studied extensively since the 1950s (Berggren et al., 1949; Rex, 1950). Existing work on the dynamics of blocking predominantly addresses various aspects of a particular part of the blocking life cycle stage (onset, maintenance, or decay). Although there are numerous studies on the dynamics of blocking, a unique and comprehensive understanding of processes that occur for the full life cycle of blocking events is still missing and remains an open issue (Woollings et al., 2018).

The **onset of blocking** has been investigated most intensively compared to the maintenance and decay of blocking, and is often connected to a complex interaction of multiple processes on different temporal and spatial scales. Following Tyrlis and Hoskins (2008), the theories can be split up into planetary and local theories. The former includes theories on the importance of wave dynamics (Austin, 1980), wave resonance to a given forcing (Petoukhov et al., 2013), the role of topography in the initiation of blocking on the planetary scale (Charney and DeVore, 1979; Grose and Hoskins, 1979), and the impact of tropical heating (Henderson et al., 2016) and sea surface temperatures on large scale Rossby wave dynamics (O'Reilly et al., 2016). A notable study in this context by Nakamura and Huang (2018) discusses the onset of a block by the convergence and the subsequent constrained zonal propagation of wave activity as a jet stream 'traffic jam'. On smaller spatial scales, studies highlight the role of upstream cyclones for the establishment of blocking (e.g., Colucci, 1985; Nakamura and Wallace, 1990, 1993), mostly by isentropic advection of lower tropospheric air along sloped isentropes. One example is the formation of a block in October 2016 over Scandinavia, where this isentropic poleward advection occurred due to a quasi-stationary rapidly growing cyclone southwest of Iceland (Schäfler et al., 2018). While the theories mentioned so far are more related to 'dry' dynamics, studies in recent years emphasize the importance of moist-diabatic processes in modifying the midlatitude flow in the upper troposphere (Grams et al., 2011; Pfahl et al., 2015; Steinfeld and Pfahl, 2019; Teubler and Riemer, 2021). In particular, Pfahl et al. (2015) found, based on a Lagrangian method, that latent heat release is of first-order importance for blocking formation. Latent heat release in the midlatitudes occurs mostly within ascending air streams, known as warm conveyor belts (WCBs; Wernli, 1997). WCBs resemble coherent air streams that occur in the vicinity of extratropical cyclones, where they transport air from the lower into the upper troposphere in an intense cross-isentropic airflow, and lead to divergent outflow near the tropopause (Madonna et al., 2014; Pfahl et al., 2014). This divergent outflow can interact with and modify the upper-tropospheric wave structure, leading to the formation or amplification of a ridge. Steinfeld and Pfahl (2019) showed in a climatological study that diabatic processes, linked to the release of latent heating in ascending air streams, often precede the formation and re-strengthening of blocking. Overall, the processes presented for blocking formation are not mutually exclusive, might occur simultaneously, and exhibit differences depending on the exact location and season, which characterizes the onset of blocking as a rather complex interplay of various processes (e.g., Miller and Wang, 2022).

Apart from the blocking onset, many studies have looked at mechanisms for **blocking maintenance**. Generally, a quasi-stationary behavior of a block can be achieved if the westward propagation of a Rossby wave pattern and the eastward advection by the background flow cancel out (Altenhoff et al., 2008). The most commonly discussed process responsible for the maintenance and thus longevity of blocks describes the feedback of synoptic-scale eddies on the block (e.g., Mullen, 1987; Shutts, 1983; Yamazaki and Itoh, 2013; Suitters et al., 2023). A conceptional picture on the interaction between synoptic-scale eddies and a blocking flow configuration is provided in Figure 2.3. One mechanism has been proposed by Yamazaki and Itoh (2009), which describes the attraction and absorption of synoptic anticyclones by the blocking high, also referred to as 'selective absorption mechanism' (Fig. 2.3a). This mechanism is proposed and investigated in the absence of diabatic processes, and relates more to a dry-dynamical maintenance process. The absorption of anticyclonic eddies reinforces the block and its intensity, which allows for a longer persistence. At the same time, the block rejects cyclonic eddies through differential vorticity advection (Fig. 2.3b). A further mechanism for the interaction has been proposed by Shutts (1983) and represents an eddy-straining mechanism for the maintenance of blocking that is applicable for dipole blocks. Forced by diffluent flow upstream, transient eddies are stretched and split into two branches, poleward and equatorward. The low pressure system south of the blocking high in the dipole block configuration is maintained by cyclonic vorticity forcing on the equatorward side. Conversely, anticyclonic forcing from eddies strengthens the blocking high on its poleward side (Fig. 2.3c). Further mechanisms have been proposed to play a role in blocking maintenance, such as the role of tropical forcing (Schneidereit et al., 2012), the repeated occurrence of interactions of the block with cyclones (Tsou and Smith, 1990; Lupo, 1997), the interaction between the planetary and synoptic scales (Burkhardt and Lupo, 2005), and the presence of cyclonic RWB, which favors the longevity of blocks (Drouard et al., 2021). A recent study by Martineau et al. (2022) revealed that the 3D blocking structure, which has often been described as a baroclinic feature, often exhibits a slight phase shift between the upper-level wave and the low-level temperature wave. This results in net horizontal fluxes of heat that amplify and maintain the existing block. Finally, as for the blocking onset, latent heat release mostly linked to the presence of WCBs contributes to an episodic re-strengthening of the block (Steinfeld and Pfahl, 2019).

Compared to the onset and maintenance stage of a block, the **decay of blocking** has been the least studied in terms of dynamics (Lupo, 2021). Changes in the large-scale circulation pattern lead to the decay of a block (Colucci and Baumhefner, 1998). During the decay, the blocking high experiences a decrease in size and intensity (Steinfeld and Pfahl, 2019), becomes highly distorted (Croci-Maspoli et al., 2007), and usually propagates downstream and equatorward (Nakamura et al., 1997). Often, through advection by other systems, the blocking high can be absorbed back into the subtropics downstream, which results in the dissipation of the blocking pattern (Hoskins, 1997). Viewed from a wave activity point of

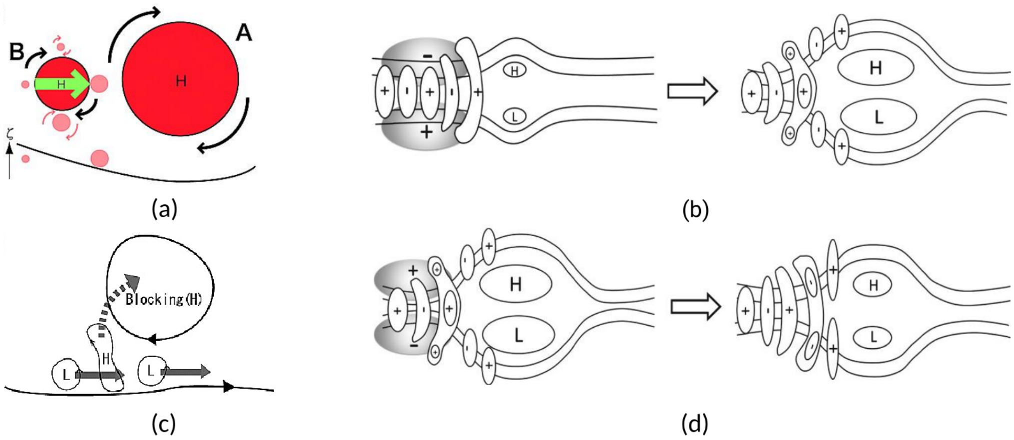

Figure 2.3: Conceptual figures on the interaction processes between synoptic-scale eddies and the blocking pattern. (a) Attraction and separation between binary anticyclonic eddies: blocking high is A, synoptic high is B. Red shading are areas of low vorticity induced by A. Black arrows point to the advection direction of vorticity and the green arrow shows the advection direction of B. (b) Selective absorption mechanism (Yamazaki and Itoh, 2009), where only synoptic-scale anticyclonic eddies (H) are absorbed by the blocking high while cyclones (L) drift further downstream. (c) Conceptual picture of the eddy-blocking matching mechanism for the interaction between synoptic-scale eddies from upstream and a dipole-type block during the intensification phase. Positive (+) and negative (-) anomalies of the eddy vorticity forcing are denoted by shading. High and low pressure centers are highlighted as 'H' and 'L', respectively. The panel on the left in (c) represent the initial condition, and the right panel shows the state a few days after the intensification. (d) same as (c) but for the decay phase. Figures (a)-(b) are adapted from Yamazaki and Itoh (2009) and Figures (c)-(d) are adapted from Luo et al. (2014).

view, the blocked region experiences a lack of wave activity flux entering and a simultaneous release of accumulated wave activity flux out of the vicinity of the block, leading to the decay (e.g., Nakamura et al., 1997; Narinesingh et al., 2020; Shi and Nakamura, 2021). Furthermore, many studies point to the lack of synoptic-scale support that would act as a maintenance mechanism (e.g., Lupo and Bosart, 1999; Burkhardt and Lupo, 2005). However, feedback from high-frequency eddies can still impose anticyclonic forcing and thereby re-strengthen the well-established block during the decay phase (Nakamura et al., 1997), such that other processes, in particular the downstream propagation of the anomaly, dominate blocking decay. However, Luo et al. (2014) even found that the one-way interaction of the eddy-straining mechanism (cf. Shutts, 1983) can work the other way around with a certain configuration of eddy vorticity forcing upstream, such that a blocking pattern decays (Fig. 2.3d). From the perspective of non-conservative processes, radiation plays a role in the structural modification of blocks, in particular due to long-wave radiative cooling above (Hoskins et al., 1985; Hoskins, 1997; Chagnon et al., 2013). The gradual decay of blocks can be caused by the slower increase above a radiative cooling maximum compared to the decrease above the latent heating maximum. Finally, the latent heat contribution is reduced to the lowest values during blocking decay, pointing to a significant decline in the contribution of moist processes (Steinfeld and Pfahl, 2019) and divergent outflow (Mullen, 1987). The decline in moist processes can be caused when (i) the block propagates away from localized heating sources, or (ii) when the block enters a region with smaller latent heat contributions (Steinfeld and Pfahl, 2019; Steinfeld et al.,

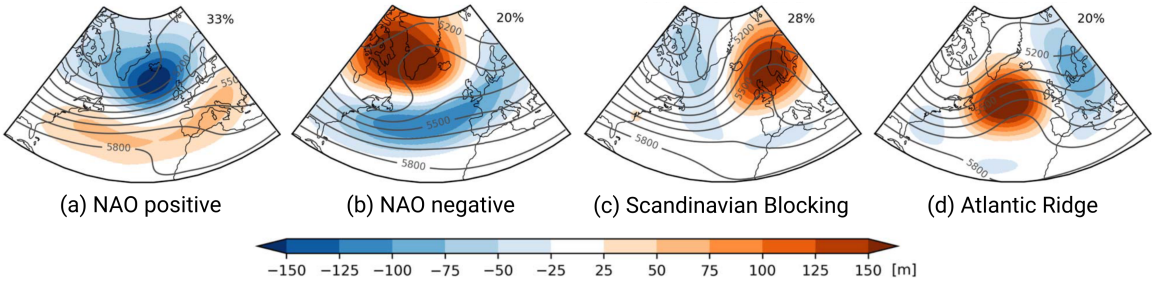
(a) NAO positive

(b) NAO negative

(c) Scandinavian Blocking

(d) Atlantic Ridge

Figure 2.4: The patterns of the classical four weather regimes in the North Atlantic-European region (90 °W–30 °E, 20 °–80 °N) after Cassou (2008) applied to ERA5 data (DJF, 1979–2018): (a) NAO positive, (b) NAO negative, (c) Scandinavian Blocking, (d) Atlantic Ridge. Anomalies of Z500 are shown in shading (in gpm) and grey contours depict absolute values of Z500 (in gpm) in intervals of 100 gpm. The percentage of total days categorized in each regime is displayed for each regime. Reprinted from Wiel et al. (2019).

2020).

In summary, this synopsis of blocking and associated dynamical theories shows that a significant body of literature exists. However, there are still huge gaps in the knowledge, despite progress in recent years. In particular, the individual theories cannot be directly linked and even contrast, such as in the example of the selective absorption mechanism of Yamazaki and Itoh (2013) for adiabatic flow and the importance of latent heat release in ascending air streams (e.g., Pfahl et al., 2015). Furthermore, within the hot spot of blocking ranging from the eastern North Atlantic to Central Asia, there is a lot of variability in blocking configurations that is also regionally confined. The different configurations together with the underlying dynamics have hardly been investigated so far, but are of enormous importance, since the exact location of the block is crucial for the impact of blocking. One way to depict preferred locations of blocking is presented below, with a focus on the North Atlantic-European region.

2.3 North Atlantic-European weather regimes

Intraseasonal variability of the atmosphere, which is often linked to low-frequency variability, encompasses variation in the large-scale circulation and leads to the modulation of weather systems. Weather regimes represent these low-frequency, large-scale circulations and describe quasi-stationary, persistent, and recurrent atmospheric circulation states that depict extratropical variability on larger atmospheric scales (Vautard, 1990; Michelangeli et al., 1995; Cassou, 2008). These patterns are often dominated by an anticyclonic circulation anomaly and hence characterized by atmospheric blocking. Weather regimes have generally been studied in various regions around the globe, for example, over North America (Vigaud et al., 2018; Lee et al., 2019b; Robertson et al., 2020), or over East Asia during winter (Matsueda and Kyouda, 2016). However, weather regimes in the North Atlantic-European region have been studied by far the most intensive.

Very early on in the mid-twentieth century, recurring large-scale patterns were empirically determined and their utility recognized. Baur et al. (1944) subjectively created a catalog of 29 central European weather types (called 'Grosswetterlagen') based on daily synoptic charts in the period 1881—1943. This catalog has been maintained for more than 70 years by the German Weather Service. A slightly less subjective approach was taken by Rex (1950) who introduced the phenomenon of atmospheric blocking and studied various blocking events in the North Atlantic and North Pacific regions. Motivated by the fact that the variability between the blocking events has been small, Rex (1951) introduced a European weather regime associated with blocking activity over the eastern North Atlantic. From 1988 on, first statistical-dynamical approaches were used to define weather regimes (Vautard and Legras, 1988; Vautard, 1990). Several regimes were identified in Vautard and Legras (1988) that were split up into two families of zonal and blocking types. Applied to 37 winter periods, Vautard (1990) found nine significant weather regime patterns over the North Atlantic that were later reduced to four regimes. Two of the four regimes are the zonal regime and the Greenland anticyclonic regime (Fig. 2.4a,b) and resemble the positive and negative phase of the North Atlantic Oscillation (NAO), respectively. The remaining two regimes are the blocking regime and the Atlantic ridge regime (Fig. 2.4c,d), both dominated by anticyclonic regime anomalies.

Subsequent studies from the 1980s on have further developed the classical four regime definition of Vautard (1990) or even created new regime definitions for the North Atlantic-European region. Many weather regime definitions exist to this date, and differ by method, season, and time period (e.g., Hannachi et al., 2017). The majority of regime definitions are based on statistical techniques such as cluster analysis (e.g., Michelangeli et al., 1995; Cassou et al., 2004) or principal component analysis (e.g., Vautard, 1990) of geopotential height anomalies or mean sea level pressure. Thereby, all methods try to fulfill the following properties of regimes: quasi-stationarity, persistence and recurrence (Michelangeli et al., 1995). For the quasi-stationarity criterion, the large-scale motion needs to be stationary with a vanishing time derivative, which requires a net balance of zero of forces acting on the pattern. The recurrence characteristic leads to the definition of regimes as patterns with the highest occurrence frequency, which is often obtained by phase space analysis or cluster analysis (e.g., Legras et al., 1987). Lastly, the persistence is a further criterion for the definition of weather regimes, which states that the circulation anomalies of a pattern must be persistent for a certain period of time. However, despite further development in statistical-dynamical techniques in the past decades, the classification of the four regimes is still the most used definition of weather regimes in the North Atlantic-European region (e.g., Cassou, 2008). In terms of season, there is a distinct majority of definitions for weather regimes in winter (e.g., Vautard, 1990; Ferranti et al., 2015) than for summer (e.g., Cassou et al., 2005). However, Grams et al. (2017) introduced a novel year-round valid weather regime definition in the North Atlantic-European region, which has been used recently for further research on various aspects highlighted below (e.g., Grams et al., 2018; Beerli and Grams, 2019; Büeler et al., 2021).

Because of their persistence of typically longer than 10 days, weather regimes can affect continent-size regions for several days and modulate the location and intensity of synoptic-scale weather systems that further determine surface weather (Yiou and Nogaj, 2004). Particularly persistent regimes can lead to heatwaves in summer (e.g., Spensberger et al., 2020), cold spells in winter (e.g., Ferranti et al., 2018), and precipitation extremes (e.g., Yiou and Nogaj, 2004; Lenggenhager et al., 2019). Furthermore, weather regimes can create conditions for the clustered occurrence of cyclones, which is linked to extreme weather (Hauser et al., 2023a). By modulating temperature, cloud cover, and wind speed, weather regimes affect the energy market due to fluctuations in yield from renewable energy, such as solar power and wind power (e.g., Grams et al., 2017; Beerli and Grams, 2019; Wiel et al., 2019). Due to the large number of impacts, it is of particular importance to predict these large-scale flow patterns at an early stage.

The small number of weather regime patterns can help to 'bridge the gap' between the temporal scales of weather forecasts and climate predictions, and shed light onto sub-seasonal forecast ranges that have been referred to as the 'predictability' desert (Robertson et al., 2020). Differences in sub-seasonal forecast skill of the weather regimes highlight that certain regimes are more predictable than others. Generally, the most predictable regime types are the positive and negative phases of the NAO. Conversely, regimes that feature a dominant anticyclonic circulation anomaly, often referred to as 'blocked regimes', exhibit lower predictability (Ferranti et al., 2018; Matsueda and Palmer, 2018; Büeler et al., 2021). Specific regime transitions are well predicted, such as the transition from a block over Scandinavia to the negative phase of the NAO, which is characterized by a high persistence and therefore high intrinsic predictability (e.g., Ferranti et al., 2018). Various studies found that low-frequency phenomena like the El Niño Southern Oscillation (ENSO), the Madden-Julian Oscillation (MJO), and the stratospheric polar vortex (SPV) in winter can modify the predictability skill of weather regimes (e.g., Cassou, 2008; Henderson et al., 2016; Büeler et al., 2020), which raises the question of the underlying dynamics of weather regimes.

In the last years, various studies have addressed whether regimes are merely useful statistical classifications, or have a physical grounding (e.g., Faranda et al., 2016; Hochman et al., 2021). Faranda et al. (2016) examined the transition between zonal and blocked flows in dynamical systems theory and linked some of the blocked regimes to unstable points rather than stable equilibria. In contrast, cyclonic regimes exhibit enhanced flow stability and persistence. Based on recent developments in dynamical system theory, Hochman et al. (2021) approached the physical grounding of seven year-round weather regimes defined by Grams et al. (2017) in winter. They found, in agreement with Faranda et al. (2016), strong evidence of most regimes being physically meaningful, which corresponds to a good agreement between the statistical classification and the dynamical system analysis and underpins the broad relevance of weather regimes.

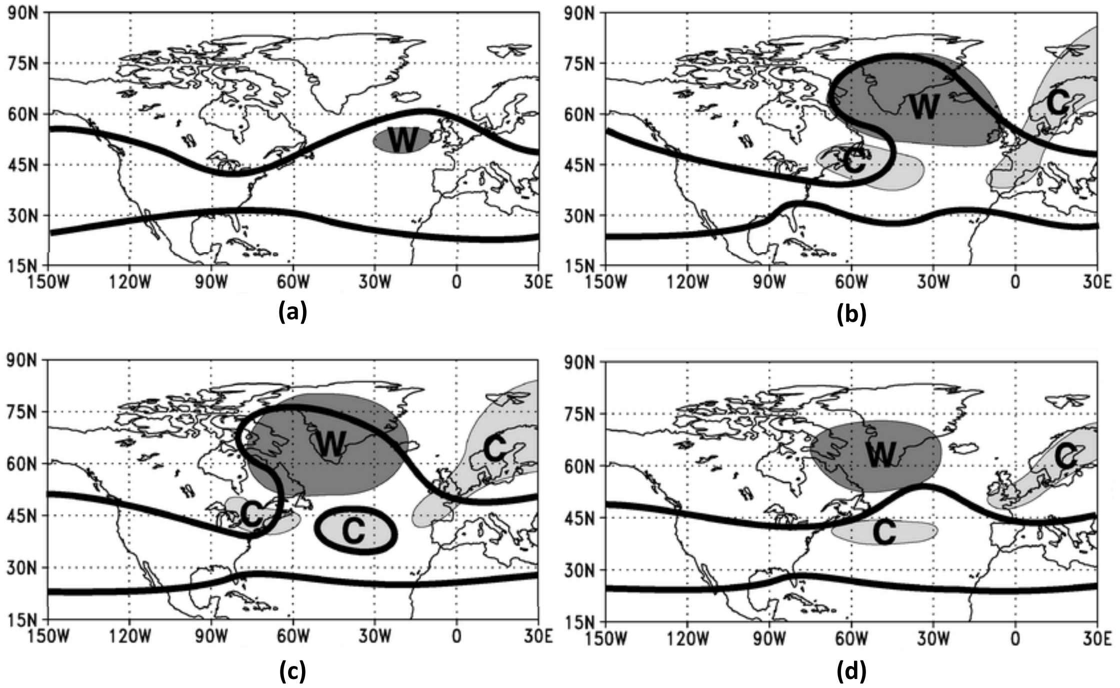

Figure 2.5: Schematic diagram of the flow patterns and features of the negative phase of the NAO for different periods (each 3–5 days) within a negative NAO event. Panel (c) represents the time when the NAO reaches its absolute maximum. Thick black contours are for the total flow (southern contour: 305 K, northern contour: 335 K). Dashed curves indicate trough axes and the shaded areas with the labels 'W' and 'C' refer to warm and cold air as anomalies, respectively. Adapted from Benedict et al. (2004).

In general, the dynamics of weather regime growth and decay, as well as the transitions from one into another regime, have been studied intensively. A variety of theories on blocking dynamics were mentioned in Section 2.2, which also apply here, as weather regimes that feature a dominant anticyclonic anomaly are related to blocking (Stan and Straus, 2007). From a regime perspective, Legras et al. (1987) and Vautard (1990) studied the precursor and successor patterns of the classical four winter regimes and highlight the transition from zonal to blocking, and the transition from blocking to Greenland anticyclone. Further insights into the dynamics of weather regimes were gained in the past 20 years with the work from Michel and Rivière (2011), Feldstein (2003), and Benedict et al. (2004), who all investigated weather regime dynamics from a streamfunction perspective. Feldstein (2003) examined the growth and decay of the positive and negative NAO patterns. He points to a Rossby wave train from the North Pacific to the east coast of North America before the positive NAO phase, and, in contrast, an in situ development for the negative NAO phase. Furthermore, Feldstein (2003) found that transient eddy fluxes are of importance in the growth of the NAO. A synoptic view on the NAO by Benedict et al. (2004) complemented the previous findings of Feldstein (2003) that synoptic-scale waves trigger NAO events. An analysis on the types of RWB and weather regimes revealed a strong link between anticyclonic RWB and the positive NAO phase, and between cyclonic RWB and the negative NAO phase (Benedict et al., 2004;

Michel and Rivière, 2011). In particular for the negative NAO phase, which represents the Greenland anticyclone weather regime, the formation of a ridge over the eastern North Atlantic is evident several days before the maximum of the negative NAO phase (Fig. 2.5). A cyclonic RWB event characterizes the large-scale flow in the few days before the NAO maximum, leading to a high amplified flow south of Greenland. Benedict et al. (2004) further found that the NAO is maintained by the breaking of upstream synoptic-scale waves, and that the lack of synoptic-scale disturbances leads to the decay of the NAO. Michel and Rivière (2011) extended the analysis on RWB of Benedict et al. (2004) to the four classical weather regimes and highlighted that each weather regime exhibits a distinct pattern of RWB frequencies. Their results for the two NAO-related weather regimes (zonal, Greenland anticyclone) are in agreement with the results of Benedict et al. (2004). Furthermore, Michel and Rivière (2011) found an occurrence of anticyclonic RWB for the Atlantic ridge regime and both RWB types for the blocking regime. They additionally analyzed regime transitions and identified two types of precursors, which are related to (1) non-linear interactions between low-frequency and high-frequency eddies, and (2) linear propagation of low-frequency eddies. For the two preferred transitions mentioned above, Michel and Rivière (2011) showed that the occurrence of cyclonic RWB south of Greenland trigger the transition from blocking to Greenland anticyclone. For the transition from zonal to blocking, it is an interplay between both - a low-frequency wave train coming from upstream and the decrease of RWB over Europe.

In conclusion, weather regimes describe a large part of the midlatitude large-scale variability of the flow and the links to impacts and underlying dynamics from a low-frequency perspective have been the content of various studies in the past. However, the relationship between synoptic-scale weather systems and how they modify the low-frequency anomalies of weather regimes is still not fully understood. The blocked regimes can serve as a fundament to investigate the dynamics of different blocking configurations, as different regional blocking patterns are distinguished over the North Atlantic-European region from the perspective of weather regimes. Yet, a framework for considering blocking dynamics from a regime perspective is missing.

2.4 Potential vorticity (PV) perspective

2.4.1 Definition of PV and climatological distribution

Potential vorticity (further abbreviated with PV) is a key variable for dynamical meteorology, as it provides a coherent theoretical framework to analyze the dynamics of the midlatitudes and combines kinematic and thermodynamic properties of the atmospheric flow in one single quantity (Hoskins et al., 1985). The most widespread formula for PV is known as the Ertel PV (Ertel, 1942) and is defined in height coordinates as

$$q = \frac{1}{\rho} \eta \cdot \nabla \theta, \tag{2.1}$$

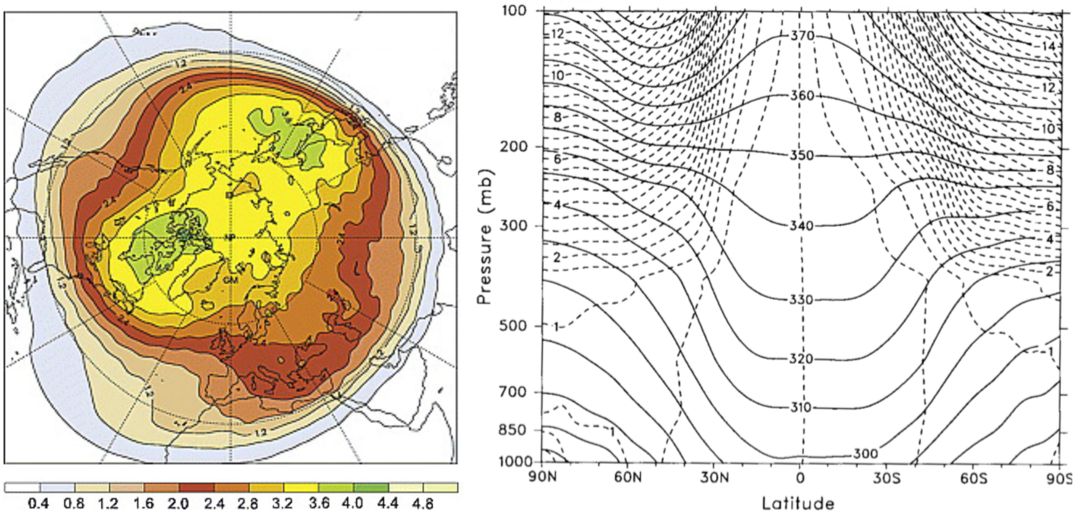

(a) (b)

Figure 2.6: Overview on climatological horizontal and vertical distribution of PV and potential temperature (θ). (a) Climatology of vertically-averaged PV between 500 and 150 hPa based on ERA15 DJF period 1979–1993 (in PVU, shading). Reprinted from Schwierz et al. (2004). (b) Zonally averaged PV (dashed contours) and θ (solid contours) distribution for DJF. Reprinted from Bluestein (1993).

where θ is the potential temperature, ρ is the density, and η the vector of the absolute vorticity $\eta = \nabla \times \mathbf{v} + 2\Omega$, where $\nabla \times \mathbf{v}$ is the relative vorticity and 2Ω the planetary vorticity. Note that ∇ is the three-dimensional nabla operator, $\mathbf{v}$ the three-dimensional wind field, and Ω the angular velocity of the Earth's rotation. PV is commonly expressed in Potential Vorticity Units (PVU), where 1 PVU corresponds to 10^{-6} m^2 s^{-1} K kg^{-1}. The Ertel PV can also be expressed in isentropic coordinates, as analyses of midlatitude weather systems are often conducted on surfaces of θ (isentropic surfaces). In its isentropic form, PV is defined by

$$q = -g\frac{\partial \theta}{\partial p}(\zeta_\theta + f) = \frac{(\zeta_\theta + f)}{\sigma}, \tag{2.2}$$

with the gravitational acceleration g, the pressure p, the vertical component of the relative vorticity on isentropic surfaces ζ_θ, and the Coriolis parameter f = $2\Omega sin(\phi)$ with the latitude ϕ. The isentropic density σ is related to the static stability, such that $\sigma^{-1} = -g(\partial\theta/\partial p)$.

In the troposphere, PV varies with latitude, height, and the presence of weather systems (Fig. 2.6). Near the equator, PV is generally low due to weak horizontal temperature gradients and weak Coriolis effects. PV increases towards the midlatitudes, where stronger horizontal temperature gradients exist (Fig. 2.6b). In the vertical direction, PV tends to increase with height in the troposphere. This is because the vertical gradient of potential temperature is generally positive in the troposphere, leading to an increase in PV with height. However, the actual distribution can be complex due to the influence of weather systems, jet

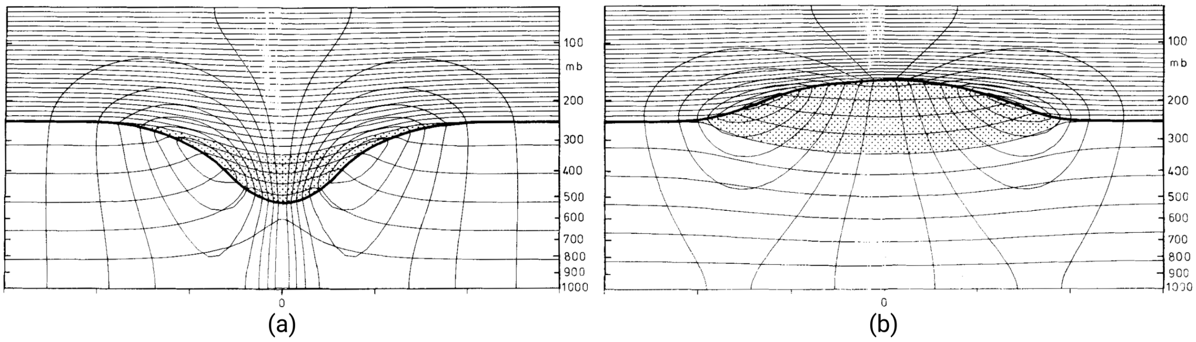

Figure 2.7: Vertical cross-section of an isentropic positive PV anomaly (a) and a negative PV anomaly (b) in the upper troposphere. The PV anomalies are shown as area of stippling and are centered in the figure (radius around the center: 2500 km). The thick black line points to the dynamical tropopause. The two sets of thin lines in black represent the transverse velocity ($\Delta v = 3\,ms^{-1}$) and the isentropes ($\Delta\theta = 5\,K$). The zero isotach is omitted. Reprinted from Hoskins et al. (1985).

streams, and further atmospheric features.

In the stratosphere, PV is generally higher compared to the troposphere, as the stratosphere is characterized by strong stable stratification and relatively low horizontal temperature gradients. A vertical average of PV between 150 and 500 hPa shows a general increase in PV with latitude due to the increase in stability, which can be attributed to the lower tropopause height at higher latitudes, such that tropospheric and stratospheric PV values are mixed in comparison to lower latitudes (Fig. 2.6a). The sharpest increase in PV is located in the transition zone between the troposphere and the stratosphere. Consequently, the tropopause can be recognized as a PV surface, since this region denotes the boundary between low PV values in the troposphere and high PV values in the stratosphere. Nowadays, the 1.5 or 2.0 PVU surface is referred to as the dynamical tropopause (e.g., Martius et al., 2010; Röthlisberger et al., 2018). In the absence of non-conservative processes, stratospheric air typically descends when it is displaced towards the equator adiabatically whereas tropospheric air ascends polewards (Fig. 2.6b).

2.4.2 Properties of PV

The use of PV in dynamic meteorology has been demonstrated as a powerful tool to analyze the interaction and dynamics of weather systems. The three key characteristics of PV that make PV a unique are summarized in the following:

1. **Conservation of PV**

   In the absence of diabatic processes and friction, the PV of an air parcel is materially conserved following the fluid motion on isentropic surfaces:

$$\frac{Dq}{Dt} = \frac{\partial q}{\partial t} + \mathbf{v} \cdot \nabla q = 0 \tag{2.3}$$

Here $\frac{Dq}{Dt}$ is the material derivative, i.e. the temporal change of the PV within an air parcel, which moves with the flow $\mathbf{v}$. Adiabatic conditions normally prevail in the free troposphere, where moist processes are restricted to confined regions. However, assuming these criteria, the PV of an air parcel is exclusively advected with the flow. The local change of PV with time $\left(\frac{\partial q}{\partial t}\right)$ describes the PV tendency at a fixed location and under adiabatic conditions can only be caused by advection of air masses of lower or higher PV:

$$\frac{\partial q}{\partial t} = -\mathbf{v} \cdot \nabla q = 0 \tag{2.4}$$

2. Invertibility principle

Another advantage of the PV is the ability to invert the PV distribution in order to isolate associated temperature, pressure and balanced wind fields. This requires that the PV distribution, an equilibrium condition, suitable boundary conditions, and the potential temperature at the ground are given. Thus, the balanced flow in terms of streamfunction and the mass distribution can be determined from PV. (Davis, 1992).

Anomalies of PV are often investigated as deviations from the surrounding PV (or climatological PV). Figure 2.7 shows the balanced wind fields and the location of isentropes of isolated PV anomalies in the upper troposphere. Positive PV anomalies are linked to a cyclonic wind field, and the compressed isentropes within the anomaly point to the increased stability (Fig. 2.7a). In contrast, an anticyclonic wind field is linked to negative PV anomalies with a reduced stability within the anomaly (Fig. 2.7a). Temperature anomalies at the surface behave similarly to PV anomalies, such that warm anomalies are located beneath positive PV anomalies, and cold anomalies are located beneath negative PV anomalies (Hoskins et al., 1985). Although anomalies are inverted separately, they have a broad impact on the flow configuration far beyond the area of the PV anomaly.

3. Non-conservation of PV

PV is not conserved in the presence of non-conservative processes like friction, radiative processes, surface fluxes, and diabatic heating and cooling. The associated changes in potential temperature lead to the modification of PV, such that the equation of the local change in PV reads as (Hoskins et al., 1985):

$$\frac{\partial q}{\partial t} = -\mathbf{v} \cdot \nabla q + \frac{1}{\rho}(\eta \cdot \nabla \dot{\theta}) + \frac{1}{\rho}(\nabla \times \mathbf{F}) \cdot \nabla \theta \tag{2.5}$$

The second term on the right-hand side of Equation 2.5 describes the change in PV due to diabatic heating with $\dot{\theta}$ as the diabatic heating rate. The third term includes frictional forces $\mathbf{F}$ and their effect on the PV along an air parcel.

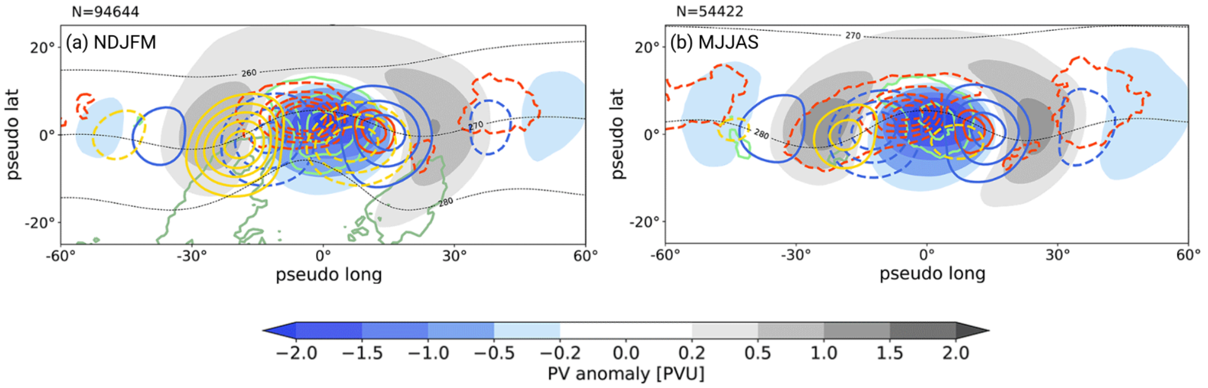

Figure 2.8: Centered spatial composites of negative PV anomalies as part of RWPs (shading, in PVU) and individual PV tendencies (contours) for NDJFM (a) and MJJAS (b). Different colored contours point to the individual PV tendency terms: Quasi-barotropic PV tendencies in blue contours in steps of ±(1, 2, 3, 4, 5) PVU d^{-1}, baroclinic interaction PV tendencies in yellow contours in steps of ±(0.1,0.15,0.2,0.25,0.3) PVU d^{-1}, and divergent PV tendencies in red contours in steps of ±(0.2, 0.4, 0.6, 0.8, 1) PVU d^{-1}. As proxy for latent heat release in the lower to mid-troposphere, the convergence of the integrated vapor transport between 1000 and 500 hPa is used if relative humidity is larger than 80 % (±(0.02, 0.04, 0.06, 0.08, 0.1) kg m^{-2} d^{-1}, divergence displayed in dark green). Solid and dashed contours of PV tendencies refer to positive and negative values, respectively. The mean temperature between 850 and 800 hPa is shown in dashed black lines in steps of 260, 270 and 280 K and indicates the location of warm (northward extension of contour) and cold (southward extension of contour) anomalies in the lower troposphere. The isentropic level for PV anomalies and PV tendencies follows the seasonal cycle. Reprinted from Teubler and Riemer (2021).

2.4.3 PV thinking for midlatitude dynamics

The key characteristics listed in Section 2.4.2 make PV a powerful variable. In particular, the 'PV thinking' of Hoskins et al. (1985) has become an established way to study atmospheric dynamics with a focus on the extratropics. Rossby waves with alternating cyclonic and anticyclonic vorticity anomalies are a fundamental component of the dynamics of the synoptic-scale and large-scale flow in the midlatitudes and have been studied a lot in the past from the PV perspective (e.g., Rossby, 1940; Hoskins et al., 1985).

Recently, a novel PV-θ-framework has been developed by Teubler and Riemer (2016) to diagnose the dynamics of Rossby wave packets (RWP). Rossby waves are not ubiquitous and exhibit starting and ending points such that a sequence of alternating cyclonic and anticyclonic anomalies is defined as a RWP (e.g., Wirth et al., 2018). As a characteristic, RWPs are associated with maxima in amplitude in the longitudinal center of the RWP and decaying amplitudes towards the edges of the RWP. The PV-θ-framework of Teubler and Riemer (2016) aims to examine the evolution of RWPs by the amplitude evolution of the troughs and ridges, linked to RWPs and identified on isentropic levels. By a partitioning of the full wind field, the PV-tendency equation is split up into individual contributions to the amplitude evolution. A major advantage of the PV-θ-framework is that, in addition to processes linked to more 'dry' dynamics, the impact of moist processes can be diagnosed. This contrasts to established 'dry' frameworks used to investigate RWP dynamics. The PV-θ-framework of Teubler and Riemer (2016) has been successfully applied to a 40-year reanalysis period of RWPs and led to a quantitative analysis of RWP dynamics

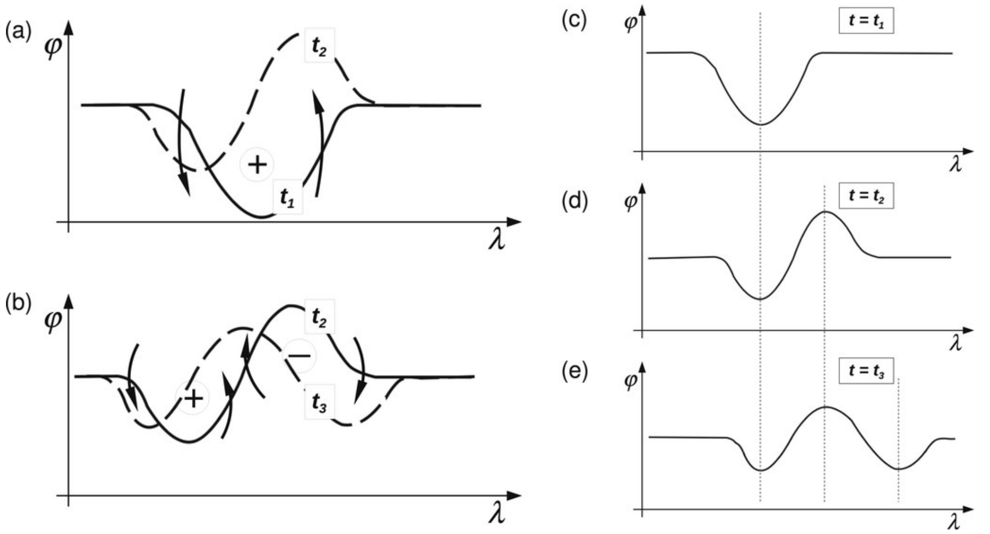

Figure 2.9: Schematic description of barotropic downstream development from a PV thinking perspective in a latitude-longitude map ($\varphi - \lambda$) for different times ($t_1 < t_2 < t_3$). Black lines depict contours of PV for early times (solid) and later times (dashed). The PV gradient of the background PV is directed to the north. PV anomalies are represented in (a) and (b) with plus and minus signs, and the arrows point to the wind field associated with the PV anomalies. The time intervals from t_1 to t_2 and from t_2 to t_3 are shown in (a) and (b), respectively. Panels (c) to (e) represent schematically a case with a stationary phase of the troughs and ridges. Reprinted from Wirth et al. (2018).

(Teubler and Riemer, 2021). In the following, the key-processes that influence the development of RWPs and appear in the individual PV tendency terms are explained in detail. Centered composites of ridges within RWPs at the time of maximum amplitude by Teubler and Riemer (2021) are shown in Figure 2.8 and shortly discussed.

Relative to the background flow, Rossby waves propagate downstream as the envelope of the Rossby wave propagates faster to the east than the single embedded troughs and ridges to the west (e.g., Chang, 1993). This leads not only to an eastward shift of the Rossby waves, but also to the development of new vorticity anomalies at the eastern endpoint, often referred to as 'downstream development'. The PV thinking introduced by Hoskins et al. (1985) can descriptively explain this downstream development of RWPs from a PV perspective. Assuming a northward facing background PV gradient, Figure 2.9a depicts a single trough that corresponds to an isolated positive PV anomaly with a cyclonic wind field. Low PV air is advected on the eastern flank to the north, and high PV air is advected southwards on the western flank. Consequently, this leads to a westward shift of the trough but also to the generation of a new ridge east of the initial trough ($t_1 \rightarrow t_2$). Another time step later, the trough-ridge couplet that forms a RWP is again shifted westwards due to the meridional advection of PV induced by the wind fields associated with the trough and ridge (Fig. 2.9b, $t_2 \rightarrow t_3$). In the meantime, another new trough forms on the eastern flank. By adding a westerly basic flow with the same magnitude as the westward phase velocity of ridges and troughs, the essential characteristics of downstream development are acquired (Fig. 2.9c-e):

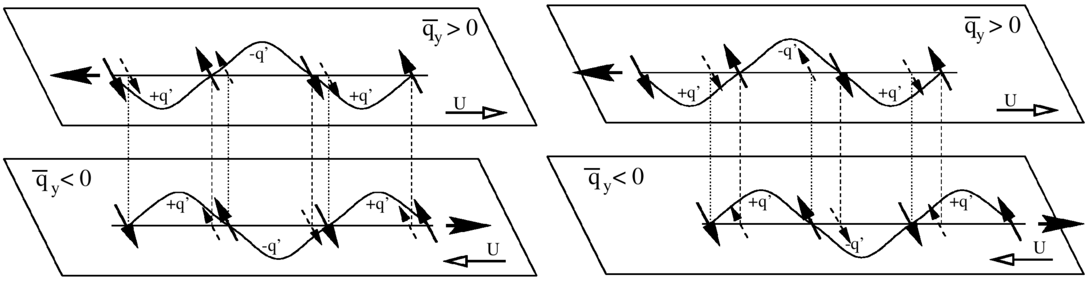

(a) (b)

Figure 2.10: Schematic sketch on the interaction between an upper-tropospheric and lower-tropospheric Rossby wave for (a) a phase shift of the upper and lower PV anomalies between 0 and $\pi/2$, and (b) a phase shift of the upper and lower PV anomalies between $\pi/2$ and π. $\bar{q}_y$ is the mean PV gradient, U(z) the mean wind (blank arrows), and -q' and +q' are negative and positive PV anomalies, respectively. Wavy lines point to the meridional shift of a PV contour, and the zonally oriented arrows indicate the direction of propagation of the Rossby waves. The remaining solid arrows point to the wind associated with the Rossby waves at its level. The dashed arrows show the effect of the induced wind at the level of the other Rossby wave. Reprinted from Heifetz et al. (2004).

new PV anomalies are generated downstream of existing PV anomalies (e.g., Hoskins et al., 1985). At the same time, PV anomalies are weakened upstream on the trailing edge of the RWP. In general, the process behind downstream development can lead to both weakening and amplification of the anomalies within a RWP, if the following two conditions are fulfilled: (1) the RWP consists of several sequential anomalies, and (2) there is an asymmetry between the upstream and downstream anomalies. Such a situation is displayed in the spatial composite of Teubler and Riemer (2021) for ridges within a RWP in extended winter (Fig. 2.8a, blue contours). Illustrated is a more pronounced trough downstream than upstream, which leads to higher positive PV tendencies on the eastern flank than negative PV tendencies on the western flank of the ridge. In this thesis, this process is referred to as **quasi-barotropic wave propagation**, analogous to Teubler and Riemer (2016).

Baroclinic instability describes the growth of initial small disturbances and plays a key role in the development of low and high pressure systems. As RWPs interact with processes in the upper troposphere and also lower tropospheric dynamics, PV anomalies associated with an upper-tropospheric RWP are influenced by PV anomalies near the surface (Eady, 1949). The mutual interaction between upper-level and lower-level PV anomalies can be explained with the two-layer model of Eady (1949) and is schematically shown in Figure 2.10. Thus, two PV waves are considered: one wave in the upper troposphere and one wave in the lower troposphere, where the latter can be considered a temperature wave with warm anomalies (positive PV anomalies) and cold anomalies (negative PV anomalies). Each wave is connected to a wind field, which acts on the initial level but also extends vertically to the level of the other wave, such that the wind field advects the associated wave and the PV at the level of the other wave. The strength of the wind field at the level of the other wave depends on its own wavelength and the intervening vertical layering. The meridional component induced by the wave on its own level leads to the PV advection at the flanks and causes a shift. With a suitable phase shift of $0 < \Delta\phi < \pi$ between

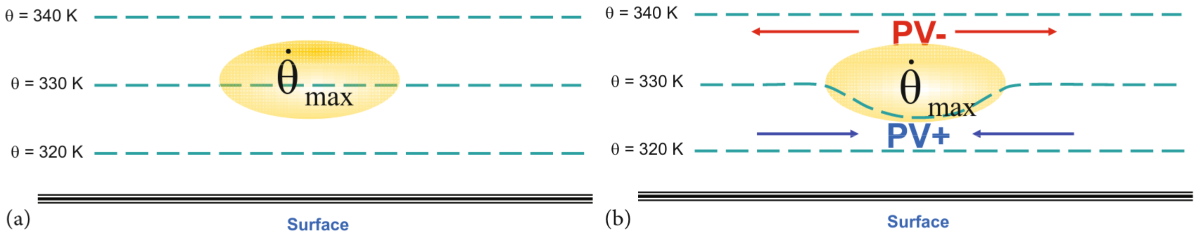

Figure 2.11: Diabatic redistribution of PV in the vicinity of mid-tropospheric latent heat release ($\dot{\theta}$): (a) heating region (yellow shading) superimposed with initially flat isentropes (dashed green) and (b) altered isentrope configuration, PV anomalies (denotes as PV+ and PV-), and divergent flow vectors. Reprinted from Lackmann (2012).

the two waves, the wind field at the level of the other wave is oriented in such a way that the advection of the PV by this wind field becomes maximal within the anomaly, leading to an amplification of the anomalies. For a phase shift between $0 < \Delta\phi < \pi/2$, the wind field not only amplifies the anomaly, but also supports the intrinsic phase propagation of each wave – i.e., the phase propagation against the base current increases (Fig. 2.10a). This also has the effect that the phase shift between the two waves is further increased. For a phase shift between $\pi/2 < \Delta\phi < \pi$ (Fig. 2.10b), growth again takes place, but the westward propagation of the upper-level wave is reduced. In summary, the vertical interaction between the upper-level and lower-level PV anomalies leads to a mutual amplification of the upper-level and lower-level PV anomalies when a certain phase shift is present. This is the essence of baroclinic instability. For the ridges within the RWP study of Teubler and Riemer (2021), a phase shift is evident in extended winter such that negative PV tendencies co-occur on average with ridges, leading to an amplification due to baroclinic growth (Fig. 2.8a, yellow contours). For extended summer, the PV tendencies are less pronounced, as baroclinic growth is much weaker in summer than in winter (Fig. 2.8b). In this thesis, this process is further referred to as **baroclinic interaction**, analogous to Teubler and Riemer (2016).

Non-conservative processes like friction, radiative transfer, cloud latent heat release, and turbulent mixing have a non-negligible impact on the PV distribution and can cause material PV changes or indirectly trigger changes in the flow nearby (Grams et al., 2011; Chagnon et al., 2013; Spreitzer et al., 2019). In particular, near the tropopause, diabatic processes have a strong effect on PV and can therefore affect Rossby wave propagation (Davis et al., 1993). Diabatic processes lead to positive PV tendencies above and negative PV tendencies below the tropopause (Chagnon et al., 2013). Positive PV anomalies within the stratosphere are the result of longwave radiation, which typically shows strong signals at the tropopause because of the strong moisture gradients. Negative PV tendencies below the tropopause are mainly caused by convection and clouds. The isentropes are compressed below the maximum of the latent heating rate and expanded above, which results in a change in vertical stability and leads to the generation of PV anomalies (Fig. 2.11). In general, PV is generated below the maximum heating and reduced above, which causes a generation or even intensification of existing negative PV anomalies close to the tropopause (Fig. 2.11b). With respect to the influence of diabatic processes on PV, WCBs have

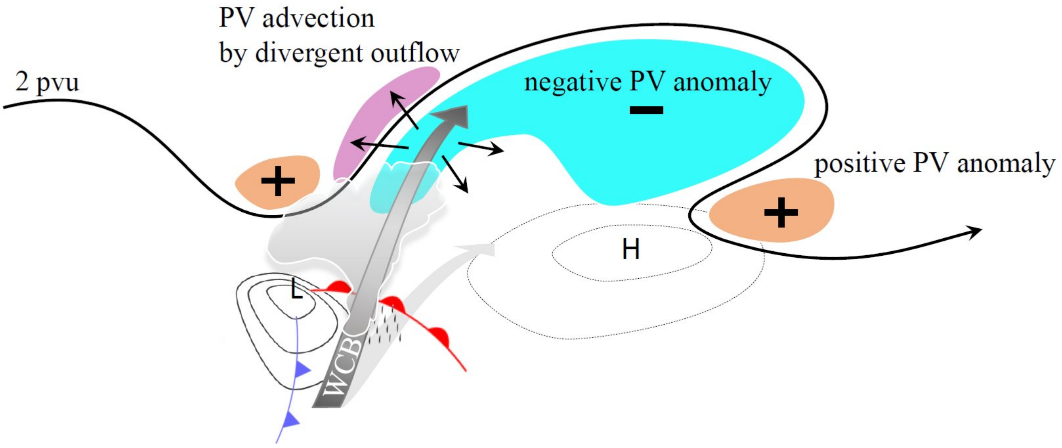

Figure 2.12: Conceptual picture of the divergent outflow associated with a WCB embedded in the extratropical circulation. The synoptic-scale cyclone is labeled with 'L', the rapidly-ascending air stream (WCB) is highlighted as gray arrow, and the area of an upper-level ridge (as negative PV anomaly) is indicated by cyan shading. Upper-tropospheric divergent wind is shown with black arrows, and the interaction with the tropopause is displayed in magenta shading. Reprinted from Steinfeld (2019).

come into scientific focus in recent years as latent heat release in midlatitudes is most prominently linked to WCBs (e.g., Madonna et al., 2014; Pfahl et al., 2014). In the ridge composite study of Teubler and Riemer (2021), a proxy was used for latent heat release, which revealed a systematic release of latent heat within the ridge, most likely linked to WCBs in extratropical cyclones (Fig. 2.8, green contours). Again, the weaker latent heat release in summer is linked to the reduced baroclinicity. The overall effect of non-conservative processes on PV is in the remainder of this thesis referred to as **non-conservative modification**.

Diabatic processes can also have an important indirect influence on the development of Rossby waves, mostly from upper-tropospheric divergence (Davis et al., 1993). Especially in the context of ascending air masses (WCBs), the release of latent heat enhances the vertical motion, and thus the outflow and divergent wind (Fig. 2.12). Upper-tropospheric divergence caused by diabatic heating below usually leads to the increase of ridges in the upper troposphere, and therefore makes an important contribution to the reinforcement of ridges as part of a RWP (e.g., Davis et al., 1996; Riemer and Jones, 2010; Grams et al., 2013). Moreover, the westward component of the divergent wind acts against the phase velocity of the trough, such that its propagation can be slowed down, and thus the large-scale structure can be changed (e.g., Riemer and Jones, 2014). Previous work has highlighted that this indirect diabatic contribution has a larger effect than the direct contribution (e.g., Teubler and Riemer, 2016, 2021). In the ridge composite of Teubler and Riemer (2021), negative PV tendencies linked to upper-tropospheric divergence maximize within ridges, leading to an overall amplification (Fig. 2.8). Negative PV tendencies occur, on average, in the northwestern part of the ridge, while positive and weakening tendencies for ridges are located in the eastern part. This process linked to upper-tropospheric divergence is further referred to as **divergent**

outflow in this thesis.

In summary, the processes that govern RWP amplitude evolution comprise quasi-barotropic wave propagation, baroclinic interaction, diabatic modification by non-conservative processes, and divergent outflow, which are all included in the PV-θ-framework of Teubler and Riemer (2016). This allows quantifying the importance of dry and moist dynamics. At the end of the previous section, it was stated that the weather regime perspective forms a fundament for considering blocking dynamics at different locations, but lacks a framework in which the dynamics can be investigated. The PV-θ-framework of Teubler and Riemer (2016, 2021), which is based on PV thinking, offers this framework.

3 Research questions

The literature review in Chapter 2 indicates that, despite considerable progress in the past years, the underlying dynamics of atmospheric blocking are still not fully understood. Due to the potential large-scale impacts of blocking, an in-depth knowledge about the processes is of tremendous importance for the blocking prediction. Decades ago, stationary anticyclones as dominant features of the blocking pattern were considered to be barotropic and to originate from dry dynamics. This view is mainly based on a Eulerian perspective. In recent years, a Lagrangian perspective was used to draw more attention to moist processes, the role of which was found to be just as important for the initiation of blocking flow patterns. To this date, these perspectives (dry vs. moist dynamics) are largely consistent on their own, but yield contradictionary results regarding the relative importance of dry and moist dynamics. Despite the plethora of blocking identification methods and individual studies, which are restricted to a single aspect of blocking dynamics related to a certain stage of blocking, a unified comprehensive understanding of the full blocking phenomenology from the formation to the dissipation is still missing.

This thesis aims to develop a common framework to unify different perspectives on blocking dynamics (Fig. 3.1), and to shed light onto open questions regarding the blocking life cycle. To this end, the PV-θ-framework of Teubler and Riemer (2016), originally developed for troughs and ridges within RWPs, and the year-round weather regime definition of Grams et al. (2017) are combined in order to develop a novel approach to disentangle the contributions of dry and moist processes for different blocked regime patterns in the North Atlantic-European region. Based on the gaps of knowledge identified in Chapter 2, the main research questions (RQs) for this thesis are formulated.

In Chapter 5, a PV framework is developed to bridge Eulerian and Lagrangian perspectives. A major further advancement and combination of Eulerian and Lagrangian methods (e.g., Schwierz et al., 2004; Pfahl et al., 2015; Teubler and Riemer, 2016) allow for the development of a novel framework to unify existing perspectives and theories. This framework constitutes the foundation of subsequent analyses on blocking dynamics in this thesis. With the focus on upper-tropospheric, negative PV anomalies linked to blocks, the framework sheds light on the dynamics and evolution of these features from a quasi-Lagrangian perspective. The following questions are addressed:

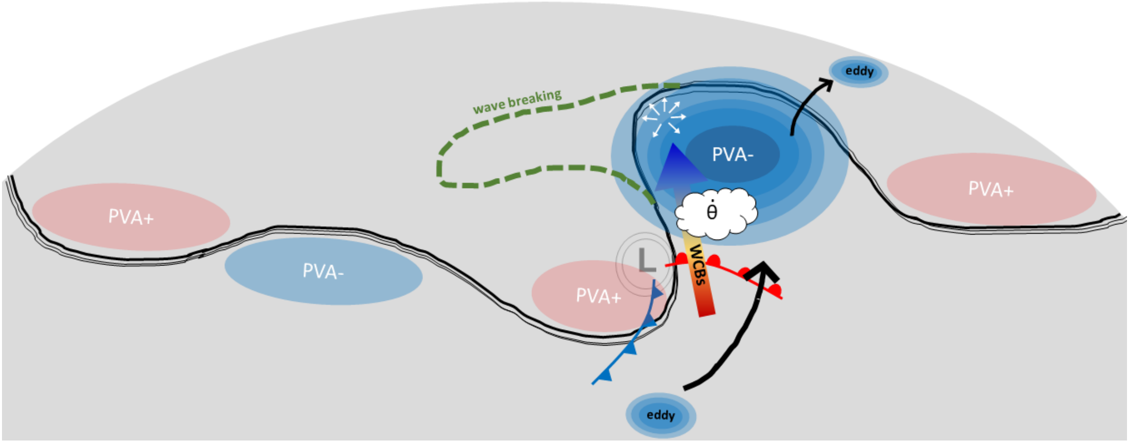

Figure 3.1: Schematic summary of topics and processes discussed in this thesis. Black lines represent the wave guide as contours of PV in the upper troposphere. Shaded areas point to upper-level PV anomalies. Feeding eddies and split-up eddies of the same polarity are highlighted in small blue shaded areas northeast and southwest of the 'block'. RWB is schematically indicated with the green dashed contour. The position of an extratropical cyclone is demonstrated by the 'L' with associated cold and warm fronts. A WCB is displayed as a colored arrow pointing northwards towards the block. The white cloud points to heating within the WCB in the mid-troposphere. Divergent outflow is indicated with white arrows.

RQ-1 How can the PV-θ-framework of Teubler and Riemer (2016) be used for the investigation of blocked weather regime dynamics?

RQ-2 How does the novel quasi-Lagrangian PV framework compare to previous Eulerian and Lagrangian approaches?

The quasi-Lagrangian PV framework is, for the first time, applied to a European Blocking (EuBL) event in March 2016, which was associated with a severe forecast bust in the North Atlantic-European region (Magnusson, 2017; Grams et al., 2018). Ensemble forecasts predicted higher temperatures than observed due to an underestimation of the extent and amplitude of a ridge that built up over Northern Europe (Magnusson, 2017). This underestimation has been linked to a misrepresentation of an upper-level trough over the western North Atlantic that initiated WCB activity (Grams et al., 2018). The dynamics of this case obtained from the novel quasi-Lagrangian perspective are the content of Chapter 6. The question of particular interest that could not be answered yet with classical Eulerian and Lagrangian approaches is:

RQ-3 What is the relative role of moist dynamics and WCB activity during the onset of the EuBL regime life cycle in March 2016? Can the hypothesized dominance of moist dynamics by Grams et al. (2017) be confirmed?

Motivated by the first application of the quasi-Lagrangian PV framework to a case study, a systematic analysis is performed on different blocking configurations in the North Atlantic-European region during the period 1979–2021. The results are presented first for the Greenland blocking type in Chapter 7, followed by a synopsis of all blocking types in Chapter 8. Motivated by recent studies on the dynamics of blocking onset (e.g., Nakamura and Huang, 2018; Steinfeld and Pfahl, 2019; Miller and Wang, 2022), the quasi-Lagrangian PV framework is used for a systematic investigation of blocking onset dynamics to address the following question:

RQ-4 What are the dominant processes governing the amplitude evolution of relevant PV anomalies, and where and when do they occur relative to the blocking onset?

The emerging debate in recent years whether moist processes contribute to the formation of blocking has been resolved since the study by Pfahl et al. (2015). Based on their finding that moist processes are at least as important as dry dynamics for the occurrence of especially strong and long-lived blocks, further investigations were triggered. A systematic climatological analysis by Steinfeld and Pfahl (2019) revealed the importance of moist processes for the formation of blocking, but also for the maintenance of an existing block. However, a systematic analysis on the importance of moist process relative to different dry dynamical processes has not been carried out yet over an entire life cycle of a block from the onset until the decay. The following RQ is considered in the results chapters 7 and 8 from the perspective of the novel quasi-Lagrangian framework:

RQ-5 How important are moist processes in the development of the blocked regimes, and where do they occur?

Various studies linked the interaction of synoptic-scale eddies with a block to a maintenance mechanism of blocking (e.g., Shutts, 1983; Yamazaki and Itoh, 2009). In particular, the selective absorption mechanism by Yamazaki and Itoh (2009) states that blocks are maintained by the absorption of eddies with the same polarity. The quasi-Lagrangian framework can look at this mechanism in a novel way. Applied to one blocking type, this analysis reveals insights into the following question:

RQ-6 How do interactions of PV anomalies linked to a block with other small-scale anticyclonic eddies influence its evolution?

Blocking maintenance is a key process as it determines the duration of blocking events. A recent study of Drouard et al. (2021) investigated the question of the differences in the dynamics for long and short blocking episodes, where they found differences in the occurrence of RWB from a Eulerian perspective.

Still, the relative importance of dry and moist processes in the maintenance is unclear, which motivates an investigation from the quasi-Lagrangian perspective. Using the regime life cycle definition for weather regimes by Grams et al. (2017), it is possible to objectively determine the maximum manifestation of a blocked flow pattern. The question that arises in this context is:

RQ-7 Does the PV anomaly life cycles have a connection with the regime life cycles at the time of the regime maximum stage? And which processes cause a regime life cycle not to be further maintained?

Compared to the significant body of literature on blocking formation and maintenance, only few studies examined the decay of blocking (Lupo, 2021). The quasi-Lagrangian framework can shed light onto the dynamics leading to the breakdown or the transition of a blocked regime. As blocking is suggested to decay in the absence of a maintenance process (e.g., Hoskins, 1997), Chapter 8 investigates the dynamics around the decay life cycle stage of blocked regimes to address the following question:

RQ-8 Is the end of a blocked regime life cycle evoked by the weakening of the PV anomalies, and how does it relate to regime transitions?

Woollings et al. (2018) point to the variety of blocking flow configurations that all fall into the term of ’atmospheric’ blocking. Different blocking configurations, with focus on the exact position of the block, can be disentangled by looking at blocking from a weather regime perspective (Grams et al., 2017). After specific questions have been addressed concerning the dynamics of different life cycle stages of a blocked regime, one final and overarching question is:

RQ-9 What are the most important differences in dynamics between the various blocked regime types?

Prior to addressing these RQs, Chapter 4 presents the data sets and basic methods employed throughout the thesis.

4 Data sets and basic methods

This chapter presents the data sets and already existing methods that are used in this thesis. First, the ERA5 reanalysis data set is introduced, which forms the basis of all investigations (Sect. 4.1). This is followed by an introduction of the year-round weather regime definition in the North Atlantic-European region of Grams et al. (2017) in Section 4.2. The partitioning of the full wind field as part of the PV-θ-framework of Teubler and Riemer (2016) is presented in Section 4.3. The description of a Lagrangian tool for the computation of air parcel trajectories is provided in Section 4.4. Two different methods to identify WCBs are the content of Section 4.5, namely a Lagrangian identification and a Eulerian identification. Other diagnostics that address very specific aspects will be introduced in the corresponding results chapters.

4.1 ERA5 reanalysis data

Reanalyses provide a convenient basis for the investigation of atmospheric dynamics in weather and climate science (e.g., Kidston et al., 2010). The creation of reanalyses involves data assimilation, a process where observations from a variety of sources and current numerical weather prediction model forecasts are combined for the best possible estimate of atmospheric conditions. If the numerical weather prediction model and the type of observational data are adopted without modification over several decades, a long-term, comprehensive data set (= reanalysis) at regular intervals results that is attractive due to its convenient format for climatological investigations (Parker, 2016).

The latest ERA5 reanalysis data set by ECMWF (Hersbach et al., 2020) forms the basis data for all investigations in this thesis. This reanalysis data set covers the period from 1950 onward and is performed with the model cycle Cy41r2. It uses a 4D-var ensemble for data assimilation, which represents a major improvement compared to the former ERA-Interim reanalysis data set (Dee et al., 2011). The spatial resolution is 31 km (TL639) in the horizontal, and the data set contains 137 model levels in the vertical. The maximum possible output frequency is 1 hour. For the investigations in this thesis, three-hourly reanalysis data are used for the period January 1, 1979 – December 31, 2021, remapped from the original TL639 spectral resolution to a regular latitude-longitude grid with a horizontal resolution of 0.5°. Model level data of ERA5 enable a high vertical resolution, which is in particular of use for the definition of upper-tropospheric PV anomalies (cf. Sect. 5.1) and for the estimation of non-conservative processes for the case study presented in Chapter 6. Mean temperature and wind tendencies at model levels from

ERA5 short-range forecasts serve to estimate non-conservative processes with a spatial resolution of 0.5 ° in the horizontal and a temporal resolution of 1 hour. The ERA5 data set provides these tendencies accumulated over the previous hour, from which 3-hourly mean values are calculated around analysis time (e.g., taking the mean of data valid at 2, 3 and 4 UTC for the analysis at 3 UTC). Furthermore, basic atmospheric variables available in the ERA5 data set are derived based on the standard output and interpolated on pressure or isentropic levels.

4.2 Year-round North Atlantic-European weather regimes

The year-round weather regime definition of Grams et al. (2017) marks a central point in this thesis, as it enables a novel perspective on atmospheric blocking in the North Atlantic-European region. A detailed introduction to the definition of the seven year-round regimes and their patterns, the objective life cycle definition, and transitions between regimes is given below.

Definition

Following the technical setup of Grams et al. (2017), the year-round definition of weather regimes based on Z500 is adapted to ERA5. Anomalies of Z500 are calculated based on a 90-day running mean climatology for the time period January 1979 – December 2019 with a temporal resolution of 6 hours and a spatial resolution of 0.5° in the horizontal. The Z500 anomaly fields are passed through a 10-day low-pass filter (Lanczos filter; Duchon, 1979) to underline low-frequency variability beyond synoptic timescales. As the low-frequency Z500 anomalies have a specific seasonal cycle in their amplitude, a normalization of the anomalies is performed such that further steps in the definition of weather regimes are not dominated by signals in winter when Z500 anomalies are generally stronger and show a higher variability than in summer. To obtain the normalization weights, a running temporal standard deviation is computed at each grid point in the time window +/- 15 days around each calendar time and year in the period 1979–2019. The spatial average of this standard deviation is computed within the domain used for the EOF analysis (80 °W–40 °E, 30 °N—90 °N) and yields the final normalization weights for each calendar time. Then, the low-frequency Z500 anomalies are divided by the normalization weight at the respective calendar time. EOF analysis is performed in the EOF domain based on 6-hourly low-frequency Z500 anomalies, and subsequently k-means clustering is applied to the seven leading EOFs that explain around 74.4 % of the variability. The optimal number of clusters is determined and results in seven year-round weather regimes defined as the cluster means. The seven weather regimes consist of three cyclonic regime types (Zonal Regime – ZO, Scandinavian Trough – ScTr, Atlantic Trough – AT) and four anticyclonic regime types (Atlantic Ridge – AR, European Blocking – EuBL, Scandinavian Blocking – ScBL, Greenland Blocking – GL).

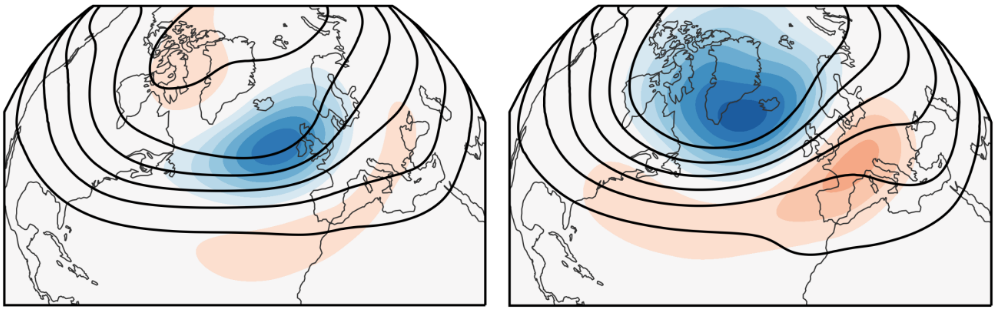

(a) Atlantic Trough (AT),13.2%	(b) Zonal Regime (ZO),16.3%

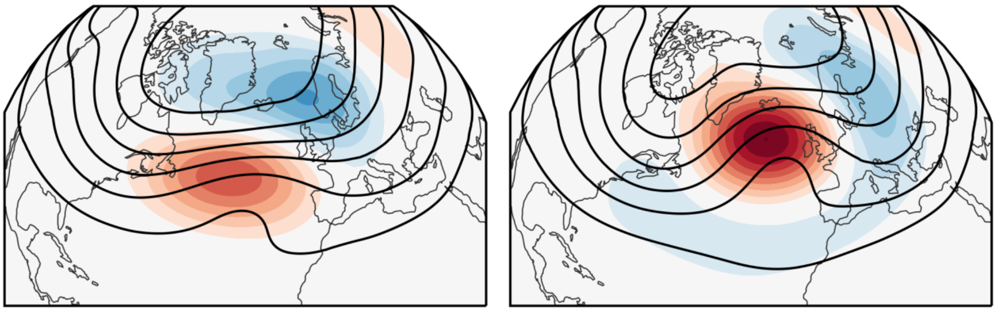

(c) Scandinavian Trough (ScTr),14.2%	(d) Atlantic Ridge (AR),13.4%

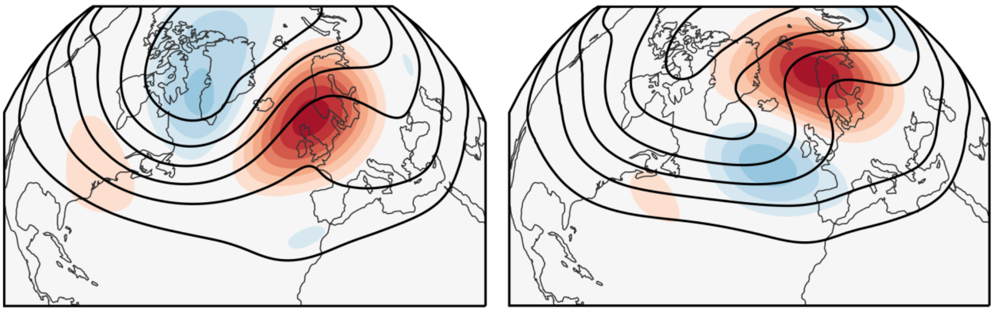

(e) European Blocking (EuBL),13.8%	(f) Scandinavian Blocking (ScBL),14.8%

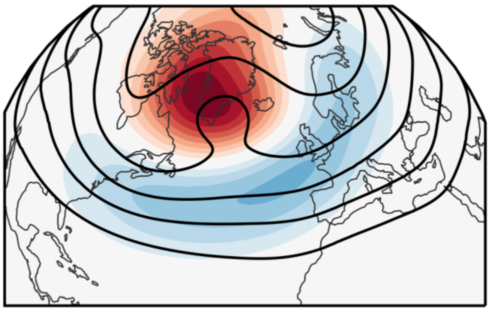

(g) Greenland Blocking (GL),14.4%

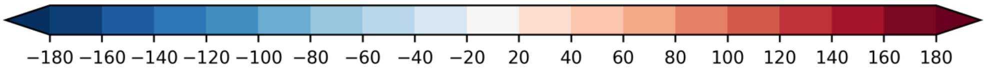

Geopotential height anomalies at 500hPa (in gpm)

Figure 4.1: The seven North Atlantic-European year-round weather regimes in ERA5. Mean low-pass filtered (10 days) Z500 anomalies (shading, in gpm) and mean absolute Z500 (in gpm, from 5300 to 5800 in steps of 100 gpm) based on the EOF clustering for the period 1979–2019. Regime names, abbreviations, and the explained variances (in %) are indicated in the captions of the subfigures.

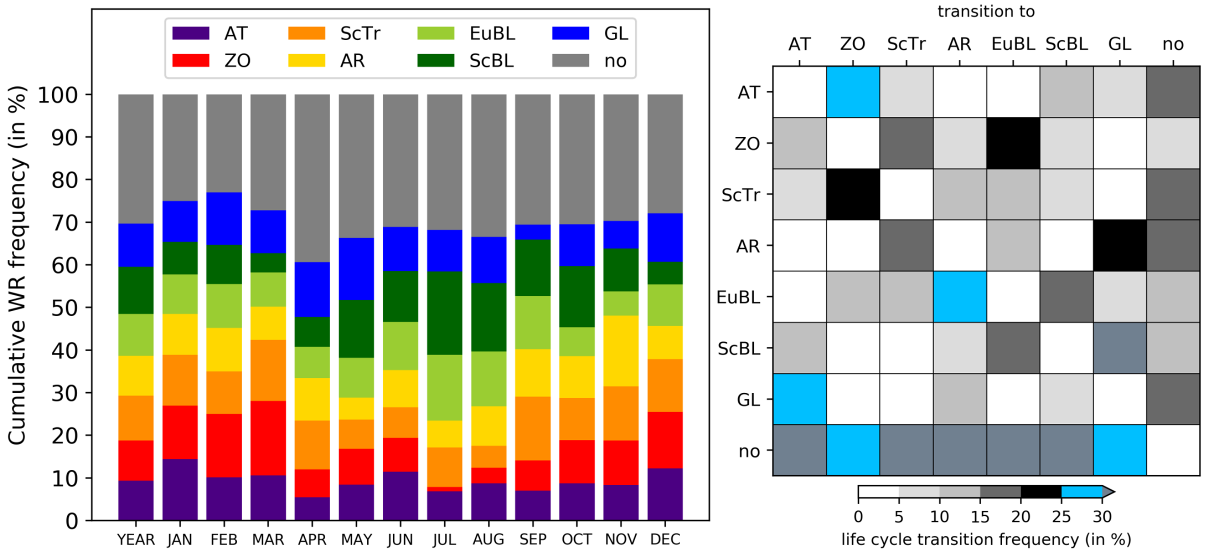

(a) (b)

Figure 4.2: (a) Cumulative weather regime frequency (in %) for each month in the time period 1979–2021 and year-round (first bar from left) based on the dominant weather regime defined for each time step. (b) Regime life cycle transition frequencies (in %) from a regime (y-axis) into another regime (x-axis).

The patterns of the seven year-round weather regimes are displayed in Figure 4.1. AT exhibits a dominant negative Z500 anomaly east of Ireland and a westerly, upper-level flow over the North Atlantic-European region is evident (Fig. 4.1a). Negative Z500 anomalies around Iceland and positive Z500 anomalies over continental Europe dominate the large-scale pattern of ZO and constitute the positive phase of the NAO (Fig. 4.1b). The strong westerly flow over the eastern North Atlantic is deflected to the north over Europe due to an enhanced ridge over continental Europe. ScTr is characterized by negative Z500 anomalies over Scandinavia, which points to a broad trough over northern and Eastern Europe (Fig. 4.1c). A positive Z500 anomaly is located over the North Atlantic, indicating a weak ridge.

The four anticyclonic regimes are dominated by a positive Z500 anomaly that is flanked by weaker negative Z500 anomalies, such that these regimes are further referred to as blocked regimes. Strong positive Z500 anomalies dominate the pattern of AR south of Iceland. These are linked to a strong ridge west of Ireland, which blocks the usual westerly flow and leads to northwesterly winds over Western and Northern Europe (Fig. 4.1d). EuBL exhibits a strong positive Z500 anomaly over the North Sea, linked to a blocking ridge over Western and Central Europe. Upstream, negative Z500 anomalies point to a trough over the Labrador Sea leading to north-easterlies over the North Atlantic (Fig. 4.1e). During ScBL, the positive Z500 anomaly is located over northern Scandinavia, flanked by a negative Z500 anomaly over the eastern North Atlantic (Fig. 4.1f). Over Europe, the upper-level flow is split into westerlies over the Mediterranean Sea and a poleward shifted flow around the dominant positive Z500 anomaly. GL resembles the negative phase of the NAO, with a dominant positive Z500 anomaly over Greenland and a region of negative Z500 anomalies extending from the western North Atlantic into Europe (Fig. 4.1g). This is linked to an equatorward deflection of the prevailing westerly flow.

Monthly weather regime frequencies based on the dominant weather regime for each time step are given in Figure 4.2a. Over the year (first column), the seven weather regimes share an equal frequency of around 8-12 %, while around 30 % of all days are linked to none of the seven regime types and fall into a 'no-regime' category, representing a climatological mean pattern with no distinct Z500 anomalies (Grams et al., 2017). Cyclonic regimes are more frequent in winter months, with the highest variations visible in ZO. In summer, the blocked regimes dominate with the highest frequency values for ScBL.

Weather regime index and regime life cycle definition

Following Michel and Rivière (2011) and Grams et al. (2017), a weather regime index I_{WR} is computed to make a quantitative statement about the similarity of an instantaneous Z500 field to one of the seven weather regimes. It is defined as

$$I_{WR}(t) = \frac{P_{WR}(t) - \overline{P_{WR}}}{\sqrt{\frac{1}{NT}\sum_{t=1}^{NT}[P_{WR}(t) - \overline{P_{WR}}]^2}} \qquad \text{with} \qquad P_{WR}(t) = \frac{\sum_{(\lambda,\varphi)\in EOF} \Phi^L(t,\lambda,\varphi)\Phi^L_{WR}(\lambda,\varphi)\cos\varphi}{\sum_{(\lambda,\varphi)\in EOF}\cos\varphi}, \tag{4.1}$$

where NT is the total number of time steps within a climatological sample (all times in 1979–2019) and (λ, φ) is the respective longitude/latitude within the EOF domain. $P_{WR}(t)$ is a scalar measure that describes the projection of the filtered anomaly $\Phi^L(t,\lambda,\varphi)$ to the EOF cluster mean $\Phi^L_{WR}(\lambda,\varphi)$ within the EOF domain. $\overline{P_{WR}}$ is the climatological mean of the projection P_{WR} such that I_{WR} is computed as the deviation of $P_{WR}(t)$ from $\overline{P_{WR}}$ normalized by the standard deviation. Even though the weather regimes are defined based on the 1979–2019 data period, I_{WR} can also be computed beyond this data period for each of the seven regime and each three-hourly time step in the ERA5 period considered here.

Based on I_{WR}, objective weather regime life cycles and associated life cycle stages are obtained. Figure 4.3b shows the evolution of the I_{WR} for August–November 2016 with marked regime life cycles (bold I_{WR} lines) and associated life cycle stages for two selected life cycles in this period (vertical lines). First, local maxima of I_{WR} with I_{WR} >= 1.0 are determined as preliminary maximum stages of possible weather regime life cycles. Second, preliminary onset and decay dates are defined as first and last time steps around all maximum stages, where $I_{WRL} > 1.0$. Finally, regime life cycles are defined as periods bounded by an onset and a decay time if the difference $\Delta t = t_{decay} - t_{onset}$ amounts to at least five days to ensure sufficient persistence of the regime. In case two local maximum stages of the same regime share the same onset or decay time (e.g., ScBL regime life cycle in October 2016, Fig. 4.3b), two regime life cycles are combined if the additional following conditions apply: (i) the mean I_{WR} between the two maximum stages is >= 1.0, and (ii) the time difference between the two maxima $\Delta t_{max} = t_{max1} - t_{max2}$ is smaller than 100 days. The combined regime life cycle is then characterized by the earliest onset and

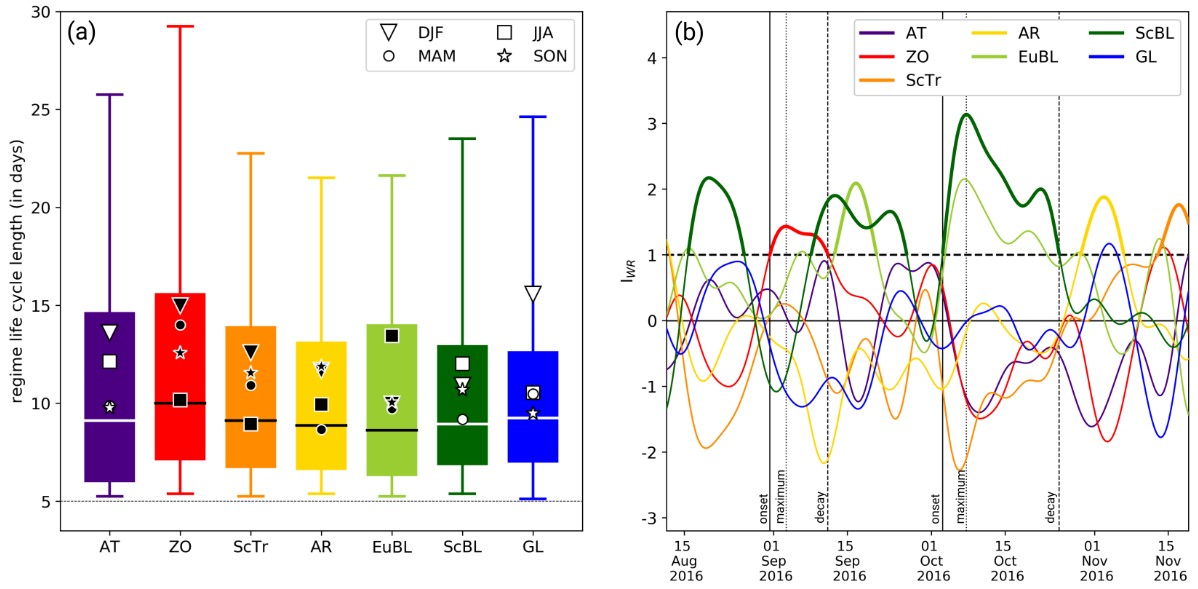

Figure 4.3: (a) Regime life cycle lengths for all seven weather regimes cycles in the period 1979–2021 (in days). The markers point to the mean regime life cycle length for the respective season. The whiskers extend to the 5th and 95th percentile. (b) I_{WR} for all seven weather regimes for the period 11 August – 18 November 2016. Thick lines point to active regime life cycles. The vertical lines mark the objectively determined regime life cycle stages for two selected regime life cycles (ZO and ScBL): onset (solid), maximum (dotted), and decay (dashed).

latest decay time. The maximum stage corresponds to the time, when I_{WR} is highest during the new life cycle period. This definition of weather regime life cycles allows more than one regime to be active at the same time, where 'active' here means that the I_{WR} for more than one regime exceeds 1.0 for at least five days. For strong and meaningful regime life cycles, it applies that the regime must have the highest I_{WR} out of all seven regimes for at least one time step in the active regime life cycle (e.g., not fulfilled for the I_{WR} of EuBL in October 2016, Fig. 4.3b), such that an in-depth analysis of clear life cycle stages (onset, maximum, decay) is possible.

Table 4.1 shows the number of regime life cycles for the period 1979–2021. The number of regime life cycles varies slightly among regime types with the most life cycles for ScBL, dominated by the increased occurrence of ScBL in summer, and the fewest life cycles for ZO, with only 18 life cycles in summer. The number of regime life cycles in Table 4.1 compared to the monthly weather regime frequencies displayed in Figure 4.2a raises the question of how, for example, a high occurrence frequency of GL in winter is compatible with only a few regime life cycles. This is an effect of the life cycle duration, which is shown for all regimes in Figure 4.3a. All regime life cycles exhibit a mean duration of around 8–10 days, with the most long-lasting regime life cycles for ZO, and the shortest life cycles for EuBL. Seasonal differences point to more long-lived cyclonic regimes in winter, and longer life cycles of the two blocked regimes EuBL and ScBL in summer. ZO and GL, which represent the two NAO phases, have the longest life cycles in winter with a mean duration of around 15 days.

Table 4.1: Number of weather regime life cycles after Grams et al. (2017) for all seven regimes and for different seasons: December–February (DJF), March–May (MAM), June–August (JJA), September–November (SON). Regime life cycles are assigned to the season with which the largest temporal overlap exists.

	Atlantic Trough (AT)	Zonal regime (ZO)	Scandinavian Trough (ScTr)	Atlantic Ridge (AR)	European Blocking (EuBL)	Scandinavian Blocking (ScBL)	Greenland Blocking (GL)
year-round	173	148	184	177	183	192	177
DJF	45	48	43	42	47	33	31
MAM	42	41	51	42	43	40	58
JJA	40	18	34	43	51	67	52
SON	46	41	56	50	42	52	36

Weather regime transitions

The change from one weather regime to another is called a regime transition, and each regime life cycle is checked for transitions prior to, during and after the regime life cycle. The time period four days before onset to onset (= 96 hours) is examined for the last active regime to determine the transition from a possible previous regime to the current regime life cycle. If no active regime is detected within those four days, a transition from the ’no-regime’ category is registered. A transition from the current active regime life cycle into another regime life cycle is determined when the life cycle does not show the highest I_{WR} of all seven regimes anymore. If the subsequent regime with the highest I_{WR} is active (all life cycle criteria are fulfilled), a transition into this regime occurs. Otherwise, a transition into the current life cycle itself takes place.

The regime transition frequencies for all regime life cycles in the period 1979–2021 are shown in Figure 4.2b. Often, the seven weather regimes develop out of the ’no-regime’ category. This is not necessarily the case for ZO and GL that exhibit the most frequent regime transition from AT to ZO, and from ScBL to GL. Further frequent transitions occur from GL to AT, and from EuBL to AR.

4.3 Partitioning of the full wind field

This subsection describes the partitioning of the full wind field $\mathbf{v}$ using Helmholtz partitioning and piecewise non-linear PV inversion. This serves as preparation for the partitioning of the advective processes of the PV tendency equation later in Section 5.5. First, the Helmholtz partitioning is used to split up the full wind field $\mathbf{v}$ into its irrotational ($\mathbf{v}_\chi$) and non-divergent ($\mathbf{v}_\psi$) wind components, such that

$$\mathbf{v} = \mathbf{v}_\chi + \mathbf{v}_\psi = \nabla\chi + \mathbf{k}\times\nabla\psi \qquad (4.2)$$

is valid with the velocity potential χ and the streamfunction ψ. Following Lynch (1989), a unique partition into the divergent, rotational, and harmonic ($\mathbf{v}_{harm}$) components of the wind field is performed,

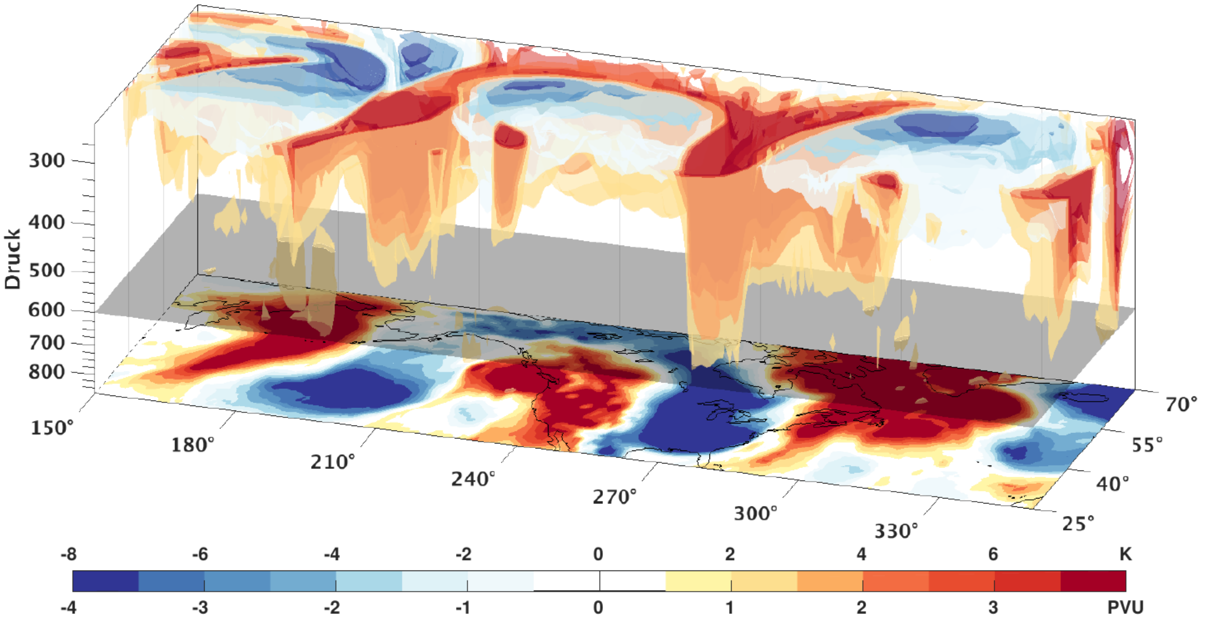

Figure 4.4: Demonstration of the separation of anomalies for the piecewise PV inversion. 3D perspective of PV anomalies (slightly transparent shading, in PVU) and temperature anomalies on the lower boundary (shading, in PVU) for 28 October 2008 00 UTC. PV anomalies are only displayed between 850 hPa and 250 hPa. The selected pressure surface that separates the upper and lower anomalies (600 hPa) is grayed out. Reprinted from Teubler (2018).

as the partitioning into non-divergent and irrotational components is ambiguous on a limited domain (Riemer et al., 2008). In this case, the following applies:

$$\mathbf{v} = \mathbf{v}_\chi + \mathbf{v}_\psi + \mathbf{v}_{harm}. \tag{4.3}$$

Using cyclic boundary conditions in the zonal direction, Dirichlet boundary conditions for the velocity potential, and Neumann boundary conditions for the streamfunction in the meridional direction, $\mathbf{v}_{harm}$ is very small. In this work, the divergent part of the wind ($\mathbf{v}_{div}$) includes the harmonic component and is thus determined over

$$\mathbf{v}_{div} = \mathbf{v} - \mathbf{v}_\psi = \mathbf{v}_\chi + \mathbf{v}_{harm}. \tag{4.4}$$

The characteristic feature of invertibility of PV is exploited to further partition the non-divergent wind field ($\mathbf{v}_\psi$). Therefore, a PV inversion is run based on non-linear balance (Charney, 1955; Davis and Emanuel, 1991; Davis, 1992). In order to understand the influence of near-surface processes on upper-level PV anomalies and the effect of upper-level dynamics on upper-level PV anomalies separately, a 'piecewise' PV inversion is performed. PV anomalies are split up into upper-tropospheric PV anomalies (including upper-boundary θ-anomalies) and lower-tropospheric PV anomalies (including lower-boundary θ-anomalies). The level for dividing these two PV anomaly groups is chosen to be between 600 and 650 hPa because midlatitude, mid-tropospheric PV anomalies around this level are smaller compared to upper-tropospheric and lower-tropospheric PV anomalies. This ensures that PV anomalies are not intersected (see example in Fig. 4.4). Rarely occurring exceptions to this are recurving tropical cyclones, deep tropopause folds and midlatitude cyclones with deep-tropospheric PV towers. The setup for the PV inversion is the horizontal domain 25 °N– 80 °N and -180 ° to 180 ° in longitude (periodic to reduce boundary effects). A separate inversion of the anomalies results in wind fields associated with the respective anomalies. For the non-linear piecewise PV inversion, the subtraction method by Davis (1992) is used. If PV is partially removed from the field during PV inversion, the associated changes in PV would result in changes in the vertical stability and relative vorticity. Therefore, the PV in the inversion region must be redistributed. The numerical solution of the inversion problem is performed on pressure surfaces between 900 hPa and 100 hPa (Δp = 50 hPa).

The background state of PV (q_0) and the horizontal wind ($\mathbf{v}_0$) are defined as a running mean climatology centered on the respective calendar time. The climatology is created first for each time step for the period 1980–2019, and then a running mean is built over the +/- 15 days around each time step. Note that the background wind field $\mathbf{v}_0$ is balanced in good approximation and therefore divergence-free. PV anomalies (q') are identified as deviations from this background q_0, such that $q' = q - q_0$ is valid. For each time step within ERA5, three PV inversions are carried out that are shortly explained in the following:

(1) **Full PV inversion** The PV inversion of the full PV field (q) is performed and directly yields the balanced wind field $\mathbf{v}_{bal}$.

(2) **PV inversion with subtracted upper-tropospheric PV anomalies** The PV to be inverted consists of the background q_0 in the upper troposphere and of the full PV field in the lower troposphere ($q - q'_{up}$). The resulting wind field is subtracted from the balanced wind $\mathbf{v}_{bal}$ (1) and is referred to as $\mathbf{v}'_{up}$ from now on.

(3) **PV inversion with subtracted lower-tropospheric PV anomalies** The PV to be inverted consists of the background q_0 in the lower troposphere and of the full PV field in the upper troposphere ($q - q'_{low}$). The resulting wind field is subtracted from the balanced wind $\mathbf{v}_{bal}$ and is referred to as $\mathbf{v}'_{low}$ from now on.

All three wind fields from PV inversion ($\mathbf{v}_{bal}$, $\mathbf{v}'_{up}$, $\mathbf{v}'_{low}$) are balanced and therefore non-divergent. The wind fields are interpolated to isentropic levels ranging from 315 K to 355 K in steps of 5 K. This is done with a log-linear interpolation (Ziv and Alpert, 1994) with the assumption that temperature varies linearly with the natural log of pressure. In this context, it should be briefly mentioned that the wind fields interpolated on isentropic levels are not necessarily non-divergent anymore. More on this follows in Section 5.5. The split up of the horizontal wind $\mathbf{v}$ finally reads as

$$\mathbf{v} = \mathbf{v}_0 + \mathbf{v}'_{div} + \mathbf{v}'_{up} + \mathbf{v}'_{low} + \mathbf{v}'_{res}. \tag{4.5}$$

Here, $\mathbf{v}'_{res}$ is the residual wind field that arises due to (i) characteristics inherent in piecewise PV inversion (e.g., nonlinearities and imperfect knowledge of boundary conditions), (ii) numerical inaccuracies, and (iii) the interpolation of wind fields from pressure to isentropic levels. Note that $\mathbf{v}'_{res}$ is calculated via $\mathbf{v}'_{res} = \mathbf{v} - \mathbf{v}'_{div} - \mathbf{v}'_{low} - \mathbf{v}'_{up} - \mathbf{v}_0$. The partitioning of the horizontal wind field in Equation 4.5 is later required for the derivation of the PV tendency equation for the quasi-Lagrangian framework.

4.4 Trajectory calculation

Air parcel trajectories are of high importance in atmospheric sciences (Sprenger and Wernli, 2015). In this thesis, to investigate the history and pathway of single air parcels that end up in a negative upper-tropospheric PV anomaly, the LAGRangian ANalysis TOol (LAGRANTO) is used. It was originally developed by Wernli and Davies (1997) and has been updated by Sprenger and Wernli (2015). Initiated from a starting position, LAGRANTO uses the three-dimensional wind fields $\mathbf{u} = (u, v, w)$ from ERA5 model level data to evaluate the position of an air parcel for the next time step.

Analogous to Pfahl et al. (2015), the diabatic history of air parcels is investigated with a set of three-day backward trajectories that end up in the upper-tropospheric PV anomalies associated with the EuBL regime life cycle (Chapt. 6). For each time step, trajectory calculations are launched for each grid point within a negative PV anomaly ($\Delta x = 0.5\,°$) on nine pressure levels between 500 and 150 hPa (Δp = 50 hPa). Following Pfahl et al. (2015) and Steinfeld and Pfahl (2019), potential temperature θ is traced along the trajectories and classify the three-day backward trajectories based on their net change of θ along the trajectory. If the criterion $\Delta\theta_{h,max} > 2\,K$ is fulfilled, the respective trajectory falls into the category of heated trajectories.

4.5 Warm Conveyor Belt identification methods

Most intense latent heating in the extratropics occurs in warm conveyor belts (WCBs) in the vicinity of extratropical cyclones (e.g., Wernli, 1997). In this thesis, the occurrence of WCB activity is investigated and serves as a proxy for moist processes for different regime life cycle stages. Two identification methods of WCBs are applied in this thesis. The first method describes the well-established Lagrangian identification of WCBs that is used for the EuBL regime life cycle in March 2016 (Chapt. 6). However, the Lagrangian method is computationally quite expensive. Therefore, a novel Eulerian identification tool for WCBs is applied to the full ERA5 data set (1979–2021) for the climatological investigation of all four blocked regimes in Chapters 7 and 8.

Lagrangian perspective

In their study, Madonna et al. (2014) introduce a Lagrangian method to identify WCBs by the calculation of trajectories with LAGRANTO. Following Madonna et al. (2014), two-day forward trajectories

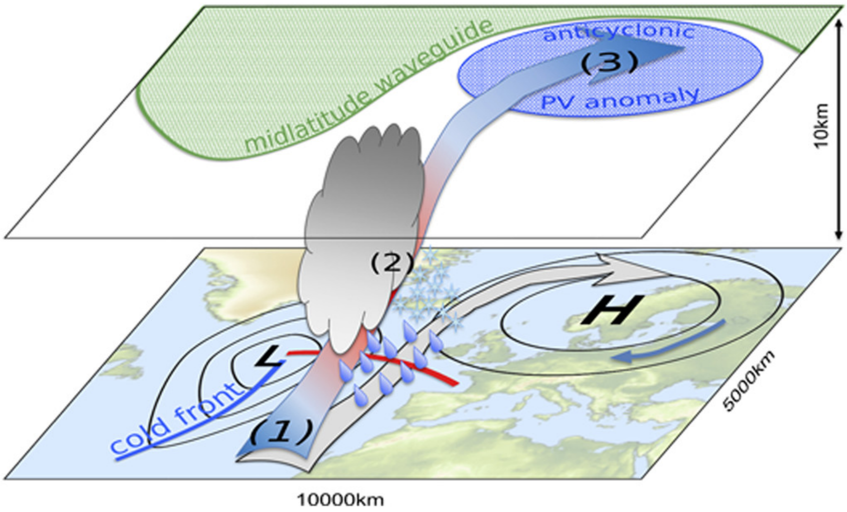

Figure 4.5: Schematic illustration of a warm conveyor belt and its conceptual relation to a large-scale flow configuration. A low pressure system is marked with 'L' and the associated fronts are shown as colored lines (cold front: blue; warm front: red). Typical WCB trajectories are highlighted by shadowed arrows that additionally show the typical PV values along the trajectory (low PV values: blue, high PV values: red). The gray arrow indicates the shadow of the WCB on the ground for a better representation of its geographical location. Blue hatching shows the upper-tropospheric anticyclonic PV anomaly associated with the surface high pressure system (labeled as 'H'. The different WCB stages are labeled with the numbers: 1) WCB inflow, 2) WCB ascent, and 3) WCB outflow. Reprinted from Quinting and Grams (2022).

are started in the lower troposphere. For the purpose of this thesis, WCBs are defined by using two-day backward trajectories from the upper troposphere. This offers the advantage to calculate trajectories directly from upper-tropospheric PV anomalies.

For the EuBL regime life cycle in March 2016 (Chapt. 6), a set of two-day backward trajectories is started every three hours on 13 equidistant vertical levels between 400 and 100 hPa in the Northern Hemisphere on a horizontal equidistant grid of $\Delta x = 100$ km. WCB trajectories are then identified as air parcels that descend for at least 600 hPa within the two days from $t_1 = 0$ h to $t_2 = -48$ h. In contrast to Madonna et al. (2014), the filtering of trajectories to avoid double counting and the criterion that the ascent must take place in the vicinity of an extratropical cyclone are omitted. Different stages of the WCB are distinguished by the assignment of WCB air parcel locations into three different layers (Fig. 4.5), following the classification of Schäfler et al. (2014): WCB inflow in the lower troposphere ($p > 800$ hPa), WCB ascent in the mid-troposphere ($800\,\text{hPa} > p > 400$ hPa), and WCB outflow ($p < 400$ hPa).

Eulerian perspective

The identification of WCBs with Lagrangian air parcel trajectories requires data with high temporal and spatial resolution and is associated with rather expensive computations. For the climatological analysis of the four blocked regimes in the period 1979–2021, the EuLerian Identification of ascending AirStreams

(ELIAS 2.0) is utilized (Quinting and Grams, 2022). This novel framework uses convolutional neural networks (CNNs) fed with instantaneous gridded fields to predict footprints of WCBs (one CNN model for each of the three WCB stages). The selection of input data for the CNNs is based on outcomes of a previous study, where the four most important predictors for each of the three stages of the WCB (inflow, ascent, outflow) were identified by a step-wise forward selection approach (Quinting and Grams, 2021). For the WCB inflow, the most important predictors are 700 hPa thickness advection, 850 hPa meridional moisture flux, 1000 hPa moisture flux convergence, and 500 hPa moist PV. Relative vorticity at 850 hPa, relative humidity at 700 hPa, thickness advection at 300 hPa and the meridional moisture flux at 500 hPa are predictors for WCB ascent. For WCB outflow, 300 hPa relative humidity, 300 hPa irrotational wind speed, 500 hPa static stability, and 300 hPa relative vorticity are the four most important predictors. Additionally, the 30-day running mean Lagrangian-based WCB climatology is employed as a fifth predictor to include the varying WCB occurrence frequency across seasons to successfully apply the CNNs models for a year-round WCB identification. The training of the CNNs is based on 12-hourly ERA-Interim data (Dee et al., 2011) from 1980–1999, and the CNNs are applied to 3-hourly ERA5 data from 1979–2021. The output of the CNNs can be interpreted as a conditional probability for WCBs ranging from 0 to 1. Following Quinting and Grams (2021), a grid-point dependent decision threshold is applied for the final decision if certain probability is associated with any of the three WCB stages. This threshold is determined for each day of the year and for each WCB stage, such that the bias between the Lagrangian-based and CNN-based WCB climatology is minimal.

5 A novel quasi-Lagrangian PV framework

This chapter introduces a novel quasi-Lagrangian PV framework, which facilitates for the first time a consistent investigation of blocked regime dynamics. The framework disentangles the contributions of dry and moist processes to blocked weather regime life cycles. The major steps towards the novel framework are: (1) identification and tracing of upper-tropospheric PV anomalies (Sect. 5.1–5.3), (2) attribution of PV anomalies to individual blocked regime life cycles defined by Grams et al. (2017) (Sect. 5.4), and (3) adaption of the PV-θ-framework of Teubler and Riemer (2016) on the PV anomalies to investigate their amplitude evolution (Sect. 5.5).

5.1 Vertically averaged PV

The approach for the definition of upper-tropospheric PV anomalies is closely related to the two-dimensional PV-based blocking identification proposed by Schwierz et al. (2004). Their blocking definition is based on upper-tropospheric PV anomalies linked to blocking, and aims to incorporate the effect of salient, quasi-isolated features of low PV, or in terms of anomalies, negative upper-tropospheric PV anomalies. Here, analogously to their procedure, PV is calculated on ERA5 model levels to obtain the most accurate calculation possible with reanalysis data. Following Schwierz et al. (2004), a vertical (weighted) mean is performed between the lower stratosphere (150 hPa) and the mid troposphere (500 hPa). This procedure effectively produces horizontal fields that depict the pattern of the vertically-averaged PV (short: VAPV) for a given time. An example is shown in Figure 5.1 for the maximum stage of the EuBL regime life cycle in March 2016. The VAPV field reveals a low-PV area over the northeastern North Atlantic, pointing to the highly amplified ridge associated with the EuBL regime life cycle (Fig. 5.1a). A cross-section through this area indicates an elevated tropopause with low PV values up to 200 hPa (Fig. 5.1b).

For the determination of the negative PV anomalies traced in the quasi-Lagrangian PV framework, the calculation of a climatology is required. In contrast to Schwierz et al. (2004), a 30-day running mean climatology is used instead of a monthly climatology to avoid jumps in the climatology that occur during transitions between months. In a first step, an absolute climatology is calculated for each calendar time ($\Delta t = 3h$) based on the time period 1980–2019. Then, a 30-day running mean is formed based on this data of +/- 15 days around each calendar time that results in the climatology $VAPV_0$. Finally, anomalies of vertically-averaged PV (VAPV') are constructed based on this 30-day running mean climatology, such that $VAPV' = VAPV - VAPV_0$. Once the anomalies are obtained, Schwierz et al. (2004)

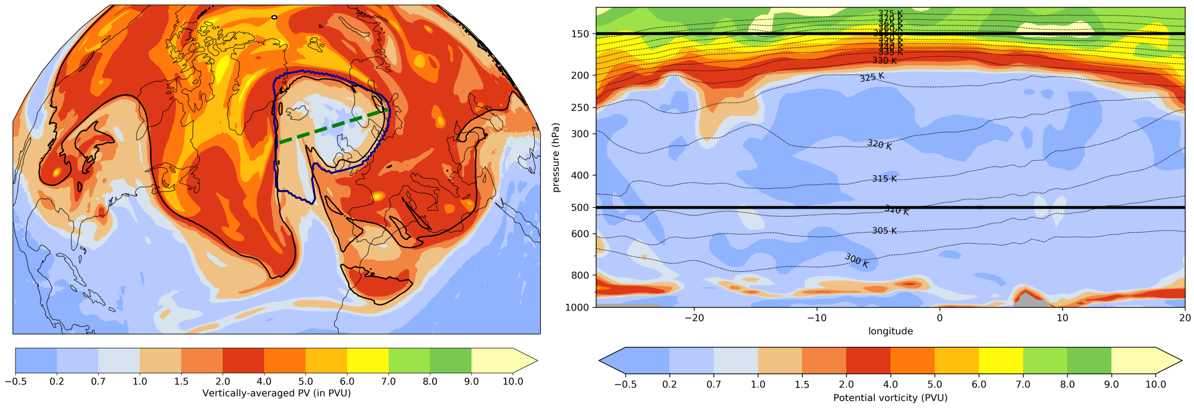

(a) (b)

Figure 5.1: (a) VAPV (500–150 hPa, shading, in PVU) for 13 March 2016 18 UTC (maximum stage for the EuBL regime life cycle in March 2016). The thick black line is the 2 PVU contour at 325 K. The identified negative PV anomaly associated with the EuBL regime life cycle is shown by the dark blue line. (b) Vertical cross-section for the location marked in (a) as green dashed line. PV is displayed in shading (in PVU), contours show potential temperature every 5 K. Grey shading near the surface points to orography. The two horizontal lines at 500 and 150 hPa demonstrate the region used for the VAPV calculation.

apply a two-day time filter to smooth out high frequency signals, as their interest is on the detection of blocking anticyclones as a persistent low-frequency signal. However, since the interest here lies in transient PV anomalies that represent the anticyclonic regime part of blocked weather regimes, the strong smoothing procedure is omitted. Nevertheless, a spatial smoothing with a radius of influence of 150 km is performed. For the smoothing, all grid points located within the radius are considered and the weights for the points linearly depend on the distance from the central grid point. This yields the final field of VAPV'.

5.2 Identification of negative upper-tropospheric PV anomaly features (PVAs$^-$)

Various thresholds are reported in literature to define negative upper-tropospheric PV anomalies as individual objects. The original definition of Schwierz et al. (2004) used a threshold of -1.3 PVU to identify upper-tropospheric PV anomalies associated with blocking in winter. The same threshold was used by Croci-Maspoli et al. (2007) for year-round investigations of blocking. However, Pfahl and Wernli (2012) added a weaker threshold of -0.7 PVU to account for weaker blocks. The strong seasonal variability in $VAPV_0$ makes it difficult to compare VAPV' objects identified with a fixed threshold in different seasons. As VAPV' are weaker in summer than in winter, a fixed threshold would result in different sized objects, although the actual amplitude might be less of dynamical relevance. At the same time, a threshold of less than 0.0 PVU is needed to focus on spatially confined VAPV' objects.

The objective is to find a suitable threshold to define negative PV anomaly features as 2D objects, which is consistent across seasons. This threshold needs to fulfill the following requirements: (i) The threshold

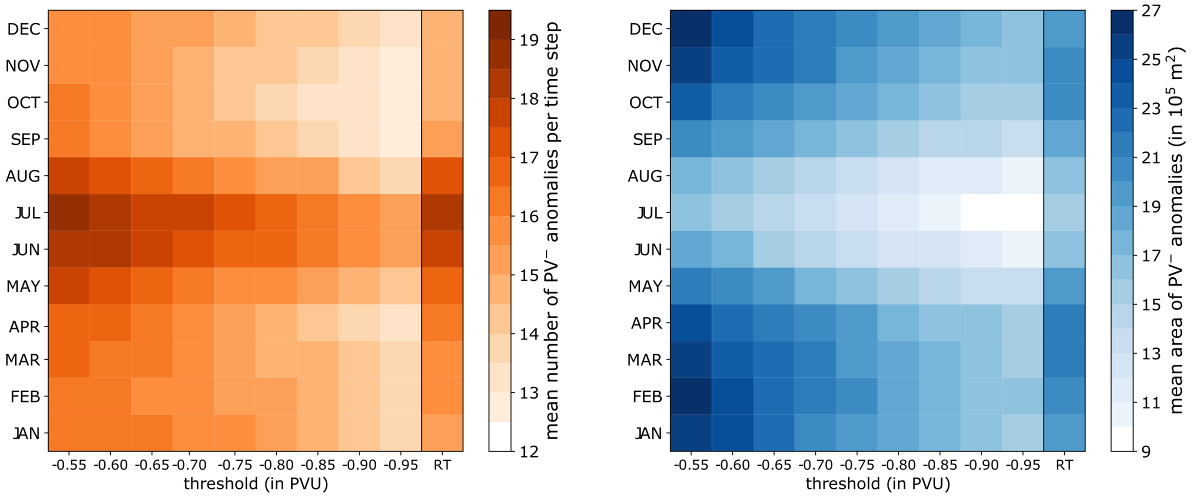

(a) (b)

Figure 5.2: Sensitivity of (a) mean number of negative PV (PV$^-$) anomalies and (b) mean area of PV$^-$ anomalies (in 10^5 m^2) for all months. Data basis is January 1979 – December 2019. The analyses are shown for fixed thresholds ranging from -0.55 PVU to -0.95 PVU in steps of 0.05 PVU. Analyses based on the final running threshold (RT; shown in Fig. 5.3a, dark blue line) are included in the last column of each subplot.

should encompass the negative PV anomaly feature as completely as possible to close the integrated PV tendency budget that is introduced later, (ii) the identification of a single contiguous object, which comprises multiple negative PV anomaly features spanning a very large region, should be avoided, and (iii) the threshold should fulfill the points (i) and (ii) regardless of the season in which the anomaly identification is performed. Since the interest lies in the entire life cycle of negative PV anomaly features, a weaker threshold than in Schwierz et al. (2004) is targeted.

For the EuBL case study presented in Section 6, the subjectively identified threshold of -0.8 PVU fulfills the conditions (i) and (ii) and is chosen for the analysis. It is anticipated that the integrated PV anomaly budget captures the observed amplitude evolution well, thus justifying the choice of the threshold value for this particular case study. In order to examine the impact of a fixed threshold on identified negative PV anomaly features when applied over the entire year, Figure 5.2 displays the mean number of PV anomaly features and the mean area of PV anomaly features in the Northern Hemisphere per time step for each month separately. A threshold analysis is performed for different fixed thresholds ranging from -0.55 PVU to -0.95 PVU in steps of 0.05 PVU. The threshold analysis reveals that significantly more and in particular smaller features in size occur compared to the winter months for a fixed threshold of -0.8 PVU (Fig. 5.2). This suggests that the selected threshold is too strong for anomalies in summer, such that multiple small local maxima within a region of negative PV anomalies are mistakenly as individual objects. Independent of the selected threshold, more negative PV anomaly features are identified in the summer months compared to the winter months, when the threshold is kept constant throughout the year (Fig. 5.2a). Additionally, the analysis indicates that the average area of all negative PV anomaly features

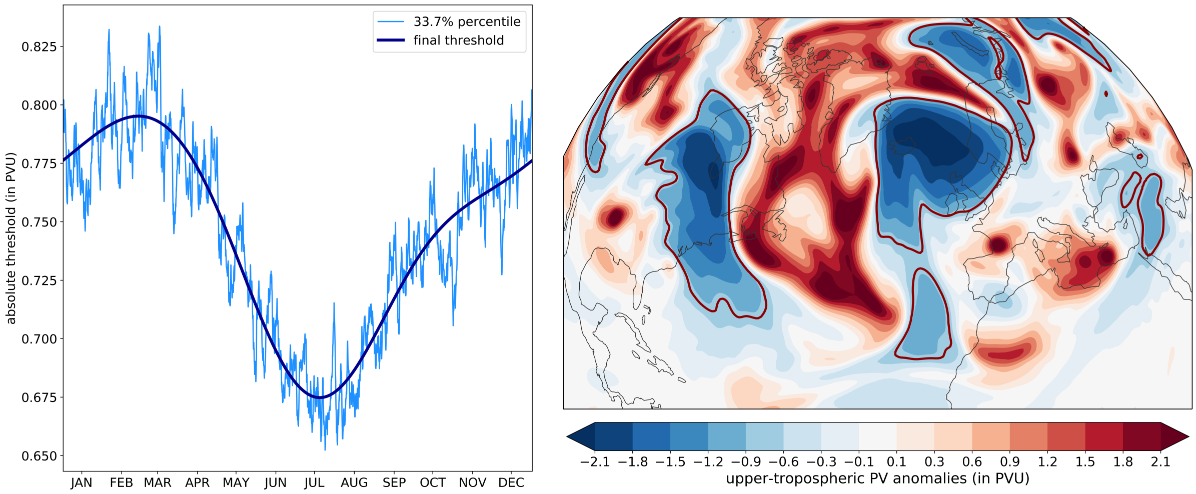

(a) (b)

Figure 5.3: (a) Final running threshold for the identification of negative PV anomaly features. The light blue line shows the threshold that corresponds to the 33.7 % percentile for each calendar day (1980–2019). The final threshold (smoothed with Fast Fourier Transformation) is shown in the bold, dark blue line. Note that the absolute threshold is displayed to emphasize the strength of the threshold. (b) An illustrative example of the VAPV' field (shading, in PVU) and associated identified negative PV anomaly features (thick dark red contours) for the maximum stage of the EuBL regime life cycle (March 13, 2016 18 UTC).

in summer is smaller compared to the area covered by negative PV anomaly features in winter (Fig. 5.2b).

Based on these results, the analysis is extended by looking for a threshold that varies throughout the year to account for the seemingly weaker negative PV anomaly features in summer. Assuming that a threshold of -0.8 PVU is a good choice for March 1st, the percentile is determined that corresponds to this threshold when taking into account all PV anomalies < 0.0 PVU on the Northern Hemisphere (0–90 °N) from 1980–2019 for this date. The -0.8 PVU threshold value matches the 33.7 % percentile, which is then taken to identify the associated threshold for each additional calendar day in the year.

Figure 5.3a displays the mean value that matches the percentile for each calendar day throughout the year. Despite a high year-to-year variability (light blue curve), the percentile value exhibits an annual cycle. In order to avoid abrupt changes of the threshold value, the curve, which is reminiscent of a sinusoidal curve, is smoothed with the Fast Fourier Transformation. This leads to the final running threshold (dark blue). The threshold, which varies throughout the year, exhibits an absolute minimum seen in summer (mid-July) and a maximum in late winter/early spring (mid-March). Interestingly, using the threshold corresponding to the 33.7 % percentile at each calendar day results in a relatively equal fraction of the number and area covered by all negative PV anomalies in the Northern Hemisphere over the year (last column in Fig. 5.2a,b). Consequently, for the systematic year-round investigation of blocked weather regimes, this variable threshold is used and applied to all 3-hourly VAPV' fields between January 1979 and December 2021. In the following, the identified upper-tropospheric, negative PV anomalies

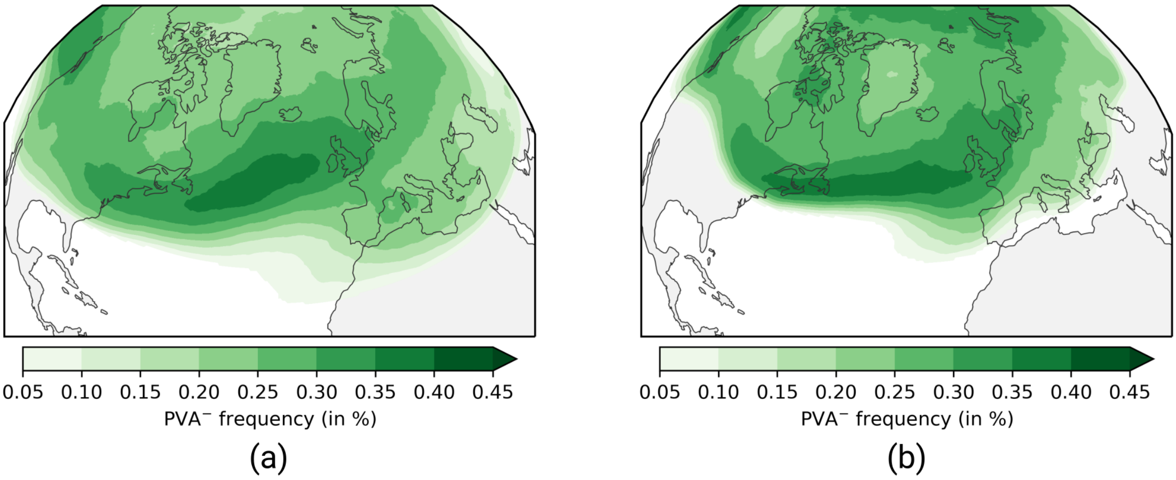

Figure 5.4: Snapshots of the 30-day running mean climatology of PVAs$^-$ (1980–2019) for (a) January 15, 00 UTC and (b) July 15, 00 UTC illustrated as occurrence frequency. Values below an occurrence frequency of 0.05 are removed.

from this quasi-Lagrangian perspective are referred to as PVAs$^-$. For visual illustration, Figure 5.3b shows the VAPV' field and the identified PVAs$^-$ with the fixed threshold of -0.8 PVU for the time of the maximum stage of the EuBL regime life cycle. Despite the non-zero threshold, the variable threshold reasonably encompasses the PVAs$^-$. In total, this yields numerous PVAs$^-$, since small PVAs$^-$ are not filtered out. Again, a minimum criterion is rejected in order to be able to trace the PVA$^-$ to its origin as well as its life cycle end.

In order to assess the climatological frequency of PVAs$^-$ in different seasons and to compute instantaneous anomalies, a 30-day running mean climatology of PVAs$^-$ is calculated for the time period 1980 – 2019 for PVAs$^-$ that are bounded by the variable threshold. Figure 5.4 shows the climatological frequency occurrence for 15 January and 15 July as representative time steps for winter and summer, respectively. In both seasons, a maximum in frequency is co-located with the storm track region over the North Atlantic. In summer, the occurrence frequency of PVAs$^-$ at midlatitudes is higher, possibly due to the general higher number of PVAs$^-$ despite the lowering of the threshold in summer. During winter, PVAs$^-$ are present at lower latitudes than in summer due to the equatorward shift of the jet stream in winter. Despite some differences between the seasons, the general occurrence frequency maximum over the North Atlantic storm track is a joint characteristic, and relatively little seasonal variation in the number of PVAs$^-$ is evident compared to previously reported differences in the blocking occurrence based on fixed thresholds (cf. Pfahl and Wernli, 2012, their Fig. 2).

5.3 Tracking of PVAs$^-$

Analogous to Schwierz et al. (2004), the individually identified PVAs$^-$ in the Northern Hemisphere are tracked via checking for a spatial overlap of subsequent time steps. Some modifications are made here, since the interest lies on fast-moving, transient PV anomalies and not exclusively blocks as quasi-stationary features. The tracking algorithm uses a reduced minimum spatial overlap of two PVAs$^-$ that is set to > 0.0 % for the 3-hourly data, compared to 70 % for 6-hourly data in Schwierz et al. (2004). When individual PVAs$^-$ are tracked, the PVAs$^-$ can distort so strongly that they split up ('splitting events'). Similarly, two PVAs$^-$ can also merge over time ('merging events'). In order to be able to reasonably track the PVAs$^-$ as long as possible, the original contour overlap algorithm of Schwierz et al. (2004) has been modified in such a way that it recognizes and takes into account splitting and merging events. A further refinement is that no minimum track length is set, such that all tracked PVAs$^-$ are kept independent of their track length.

The main functionality of the advanced tracking algorithm is schematically depicted in Figure 5.5. For each time step t, it inputs the identified PVAs$^-$ on the Northern Hemisphere for time t and time $t - \Delta t$. For each PVA$^-$ at time $t - \Delta t$, the algorithm checks if a PVA$^-$ at time t overlaps spatially. In case that only one PVA$^-$ exhibits a spatial overlap, a rather simple assignment can be made at first, which leads to the continuation of the track (Fig. 5.5b). Sometimes, two or even more PVAs$^-$ reveal a spatial overlap with a PVA$^-$ at the time before (Fig. 5.5c). This indicates a splitting event wherein a decision is made of which PVA$^-$ feature to continue tracking. For the decision, the amplitude of the PVA$^-$ is included, which is defined as the integrated VAPV' field over the PVA$^-$ area. The PVA$^-$ that exhibits the strongest amplitude is selected as the continuation of the track. The remaining split PVAs$^-$ represent starting points of new tracks. In the opposite case, a merging event can occur when the same PVA$^-$ at time t shows a spatial overlap for two separate PVAs$^-$ at time $t - \Delta t$ (Fig. 5.5d). Again, the integrated amplitude strength decides for which PVA$^-$ the track is continued, and the tracks of the remaining PVAs$^-$ end with the merging event. Note that the algorithm is able to detect splitting and merging events at the same time for the same PVA$^-$. In a last step, PVA$^-$ at time t that do not show an overlap with any PVA$^-$ at time $t - \Delta t$ are marked as starting points of a newly created PVA$^-$ tracks, which points to the local development of a PVA$^-$ (Fig. 5.5a). Equivalently, PVA$^-$ at time $t - \Delta t$ that have no overlap with PVA$^-$ at time t are labeled as completed tracks and represents PVAs$^-$ that dissipated. The information of splitting and merging events along a track and the associated track-IDs of splitting and merging PVAs$^-$ are stored for later applications. This allows PVAs$^-$ to be traced back over multiple track IDs to their local origin time and place of origin, as well as the determination of their dissipation time and place at the end of their lifetime.

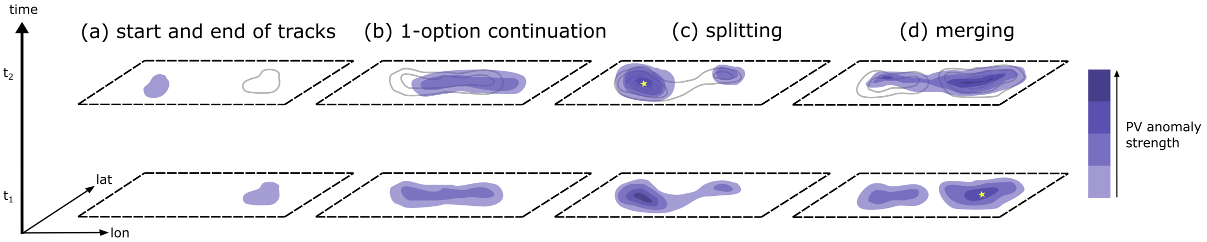

Figure 5.5: Schematic of the 2D tracking algorithm applied to PVAs$^-$ in the quasi-Lagrangian perspective. The sketch demonstrates the creation of PVAs$^-$ tracks from one time step t_1 to the next $t_2 = t_1 + \Delta t$ for different situations: (a) start and end of a track, (b) 1-option continuation, (c) splitting, and (d) merging. The gray thin lines in the upper row at t_2 indicate the position and amplitude of the PVA$^-$ at t_1 to show the overlap more visually. Yellow dots in panels (c) and (d) indicate which track ID is continued after splitting and merging events. Reprinted from Hauser et al. (2023b).

5.4 Assignment of PVAs$^-$ to blocked regimes

In order to study the dynamics of blocked regimes, the interest here is exclusively on PVAs$^-$ that actively contribute to the regime life cycles. For this purpose, a criterion is required to consider only the PVAs$^-$ that are located within the region of interest. Figure 5.6 shows the composite of VAPV' field for the four blocked weather regimes and indicates the areas where negative values of VAPV' prevail on average. By taking the -0.3 PVU contour (further referred to as 'regime mask'), a region is defined where PVAs$^-$ are on average located during the blocked regime. Since minor differences in the composite between seasons occur and the intention is to use a uniform year-round valid regime mask, this rather small threshold of -0.3 PVU was chosen such that it is guaranteed that at least a single PVA$^-$ overlaps with the regime mask during a regime life cycle. The regime mask for EuBL is located over Northern Europe, encloses the UK and Scandinavia, and reaches to the northwest until Iceland (Fig. 5.6a). The North Europe region east of Iceland is associated with the regime mask of ScBL with its center at high latitudes near Tromsø in Norway (Fig. 5.6b). The regime mask of AR covers a huge part of the eastern North Atlantic at midlatitudes from Greenland to the UK (Fig. 5.6c). Finally, for GL, the regime mask lies with its center over the southern tip of Greenland and extends from Iceland to the eastern edge of Hudson Bay (Fig. 5.6d).

Two degrees of freedom exist for the assignment of PVAs$^-$ to active life cycles, which are the spatial overlap of the PVAs$^-$ with the regime mask and the duration of the overlap. The first criterion is that the PVAs$^-$ cover a certain fraction of the regime mask during the regime life cycle. A relative minimum overlap of 10 % was chosen, which means that the PVAs$^-$ must cover at least 10 % of the regime mask area. This ensures that all PVAs$^-$ that could be of relevance are actually considered. The second criterion aims to capture only PVAs$^-$ that also make a persistent contribution. Therefore, a minimum duration of the overlap (<10 %) must persist for at least 12 hours. This corresponds to at least a 10 % contribution in terms of time, considering that regime life cycles require a minimum duration of 5 days (cf. Sect. 4.2). With these two criteria, PVAs$^-$ that fulfill both are referred to as 'contributing' PVAs$^-$.

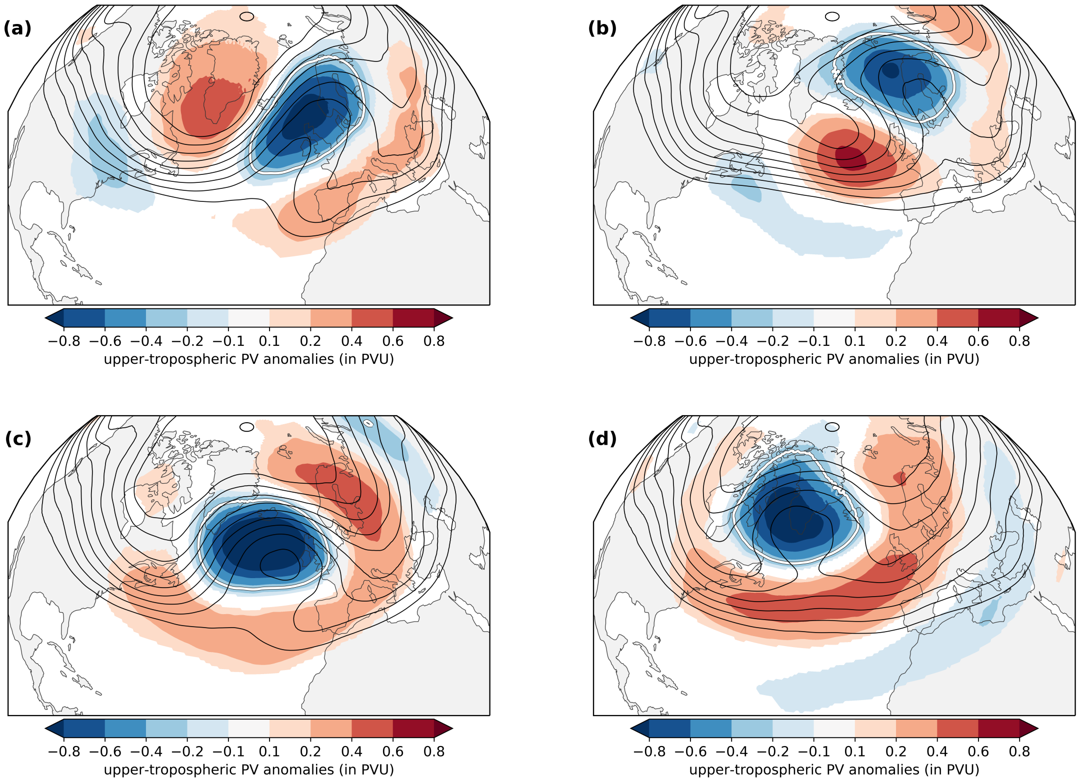

Figure 5.6: VAPV' composite between 500 and 150 hPa (shading, in PVU) for all days within an active blocked regime life cycle: (a) EuBL, (b) ScBL, (c) AR, and (d) GL. Solid black lines indicate contour lines of VAPV (from 1.5 to 3.5 PVU in steps of 0.25). Colored contour lines indicate the regime masks as defined by the -0.3 PVU contour in the VAPV' composite for each regime.

Applied to all blocked regime life cycles in the considered ERA5 period (1979–2021), the number of contributing PVAs$^-$ for each life cycle is determined (Fig. 5.7). In around 80 % of the cases, more than one single PVA$^-$ meets the conditions to contribute to the regime life cycle. This departs from the classical view in which a blocking event is associated with a single blocking anticyclone and, in this case, a single PVA$^-$. Still, as outlined in Section 2.2, this finding is in line with the selective absorption mechanism proposed by Yamazaki and Itoh (2009). This work investigates the dynamics of blocked weather regimes, where the regime perspective allows for more transience than the blocking algorithm of Schwierz et al. (2004). Whereas the large-scale pattern must be quasi-stationary, persistent, and recurrent from a regime perspective, it does not automatically eliminate transient behavior of synoptic-scale PV anomalies. The positive correlation between the life cycle length and the number of contributing PVAs$^-$ based on the Pearson correlation coefficient (0.53 for GL, 0.61 for AR, 0.65 for ScBL, and 0.78 for EuBL) suggests that several PVAs$^-$ are necessary for maintaining a long-lived blocked regime life cycle. This is consistent with the studies of Shutts (1983) and Yamazaki and Itoh (2013), who point to the positive feedback of synoptic-scale eddies on the blocking anticyclone as a possible maintenance mechanism for blocking. However, with the refined tracking algorithm for PVAs$^-$, a situation can arise

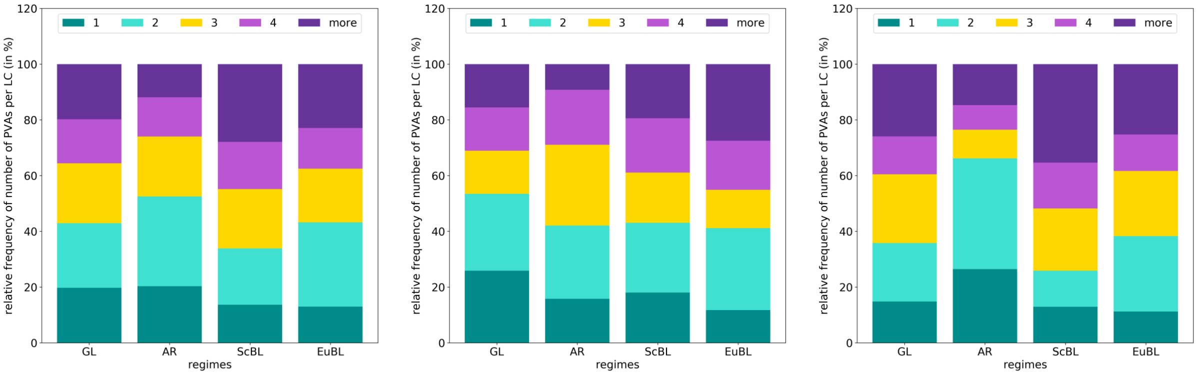

(a) year-round (b) NDJFM (c) MJJAS

Figure 5.7: Number of contributing PVA$^-$ tracks to all blocked regime life cycles: (a) year-round, (b) extended winter (NDJFM), and (c) extended summer (MJJAS). Note that exclusively PVA$^-$ tracks that show a spatial overlap of at least 10 % with the respective regime mask for at least four time steps within the regime life cycle are considered in the count.

where an existing PVA$^-$ splits into two parts, both of which remain in the regime mask for some time.

Differences in the number of contributing PVAs$^-$ emerge between the individual blocked regimes and between seasons (Fig. 5.7). From a year-round perspective, AR stands out, as 50 % of all regime life cycles are associated with a maximum of two PVAs$^-$ and only a small fraction of life cycles are linked to four or even more contributing PVAs$^-$ (Fig. 5.7a). Considering the two extended seasons, it is evident that winter dominates the year-round signal, where more than 60 % of the life cycles are characterized by a maximum of two PVAs$^-$ (Fig. 5.7b,c). ScBL stands out due to the high number of contributing PVAs$^-$ (Fig. 5.7a). Only 15 % of the ScBL regime life cycles are associated with a single PVA$^-$ and, especially in summer, more than half of the regime life cycles exhibit four or more PVAs$^-$ suggesting a more transient behavior of the associated PVAs$^-$ (Fig. 5.7c). A high fraction of EuBL regime life cycles is related to two contributing PVAs$^-$, even though there are more life cycles characterized by more than two PVAs$^-$ (Fig. 5.7a). In winter, there is a slight tendency of more contributing PVAs$^-$ than in summer for EuBL regime life cycles (Fig. 5.7b,c). Last, no category in the number of contributing PVAs$^-$ stands out specifically (Fig. 5.7a). Only when the distribution for summer and winter are considered separately, it becomes apparent that in winter the GL life cycles tend to be associated with fewer PVAs$^-$ than in summer (Fig. 5.7b,c).

As shown before, multiple PVAs$^-$ can contribute to a single regime life cycle, which makes a systematic evaluation of regime life cycle dynamics from a quasi-Lagrangian PV perspective rather difficult. To consider and simultaneously track multiple concurrent PVAs$^-$ within a regime life cycle would result in a complex analysis that confuses rather than truly elucidates the dynamics for the systematic investigation of blocked regime dynamics. The three objectively determined regime life cycle stages (onset, maximum, and decay; Sect. 4.2) are unique and can circumvent this problem to a certain degree by introducing an

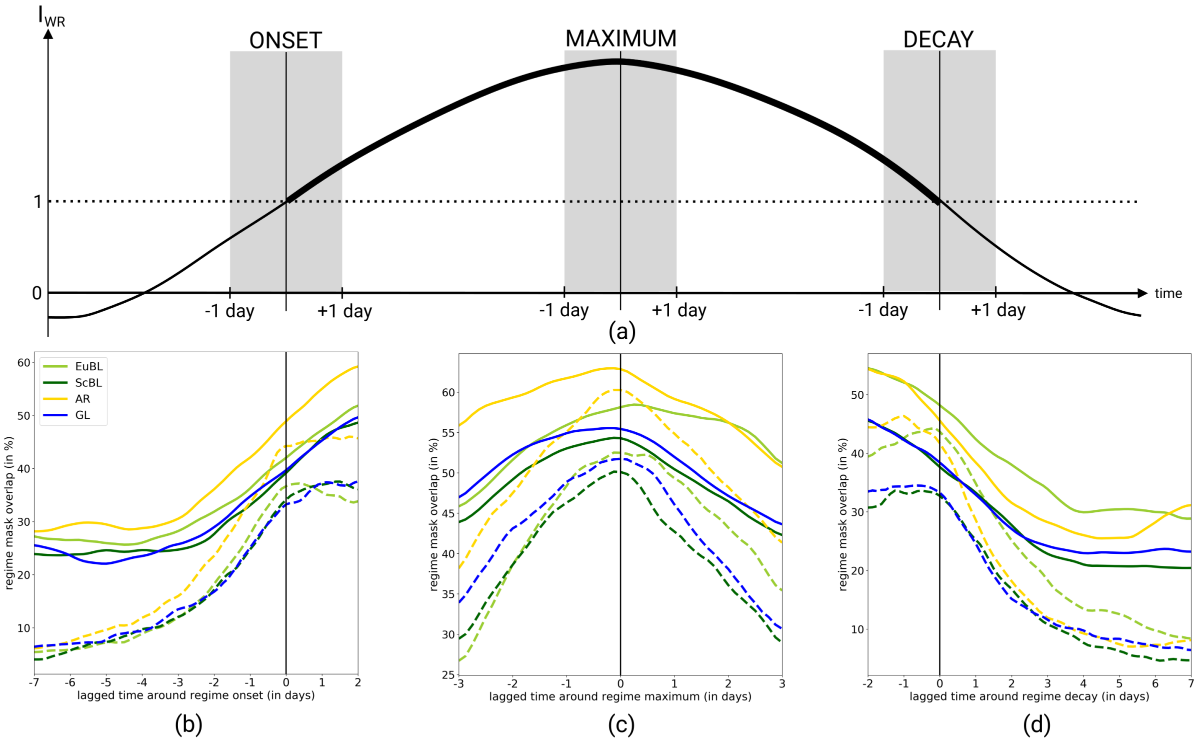

Figure 5.8: (a) Schematic illustration on the allocation of PVAs$^-$ to the three different regime life cycle stages (onset, maximum, and decay). The schematic figure shows an idealized regime life cycle (bold black curve) based on the I_{WR} as a function of time. Vertical lines point to the three life cycle stages. Grey shading marks the time interval of two days (+/- one day around the life cycle stages). The I_{WR} = 1.0 line is shown as a horizontal line in gray. Note that the regime life cycle lengths highly vary, such that the regime life cycle stages serve as anchor point in time for the systematic analysis. (b)-(d) Lagged composite of the share of the regime mask (in %) that is overlapped by all PVAs$^-$ without any criterion (solid lines) and the mean share of the regime mask that is overlapped by the selected life cycle stage PVA$^-$ (dashed lines) for the four blocked regimes and the different life cycle stages: (b) onset, (c) maximum, and (d) decay. The black vertical line shows the time of the life cycle stage. The curves in (b)-(d) are slightly smoothed by taking into account the two neighboring values (running mean window of +/- three hours).

evaluation that is oriented by regime life cycle stage. Thereby, one PVA$^-$ is determined for each regime life cycle stage that resembles the dominating anticyclonic circulation of the blocked regime for the specific regime stage. Technically, the assignment is performed as follows: In a time window of +/- one day around each of the regime life cycle stages (onset, maximum, decay), the PVA$^-$ is selected that most frequently exhibits the largest spatial overlap with the regime mask within the two-day window (Fig. 5.8a). In the mean, the selected PVA$^-$ resembles the total overlap of PVAs$^-$ close to the regime life cycle stage (Fig. 5.8b-d) for all blocked regimes, which justifies the selection of a single PVA$^-$ object as the dominant anomaly at the respective life cycle stage. With some temporal distance to the regime life cycle stage, the overlap of the selected PVA$^-$ decreases faster than the total overlap of all PVAs$^-$ with the regime mask. On the one hand, this could indicate that the selected PVA$^-$ exclusively describes the occurrence around the regime life cycle stage. On the other hand, it could suggest a propagation of the selected PVA$^-$, for example, into the regime mask before regime onset (Fig. 5.8b) or out of the regime mask after regime decay (Fig. 5.8d).

5.5 Integrated amplitude evolution metric based on PV tendencies

In this section, the PV-θ-framework of Teubler and Riemer (2016, 2021) is further developed and adapted to the quasi-Lagrangian PVAs$^-$. The following adjustments made to the PV-θ-framework and possible limitations in the method are documented in separate subsections:

- Derivation of a suitable PV tendency equation for the amplitude evolution of tracked PVAs$^-$
- Estimation of a boundary term, which considers the change in the area along PVA$^-$ tracks
- Closeness of the budget and discussion of error sources and inaccuracies
- Partitioning of the change in PV background into different processes, which is a refinement of the original PV-θ-framework

Derivation of a suitable tendency equation

With the integrated amplitude evolution metric introduced by Teubler and Riemer (2016), it is possible to investigate the importance of different processes to the amplitude evolution of ridges and troughs within RWPs. Therefore, the amplitude is defined as the spatially integrated PV anomaly on isentropic surfaces. In this thesis, the metric is refined and further developed for the application on traced PVAs$^-$ from a quasi-Lagrangian PV perspective. Since a distinction is made between different processes that contribute to the amplitude change of a PVAs$^-$, an examination of a wide range of individual spatial maps would be too intricate. With the integrated metric, the spatial information is compressed.

Generally, a PV anomaly can evolve in time by (i) the change in the strength of the PV anomaly, and ii) the change in its area. In the following, to account for both contributions, the total derivative of the area integral of the PV anomaly is considered as the integrated PVA$^-$ amplitude. Using the Leibniz integral rule, the amplitude evolution is given by

$$\frac{d}{dt}\int_{A(t)} q'\,dA = \int_{A(t)} \frac{\partial q'}{\partial t}\,dA + \oint_{S(t)} q'(\mathbf{v}_s \cdot \mathbf{n})\,dS, \tag{5.1}$$

where $A(t)$ refers to the PV anomaly area for a specific time t, $S(t)$ is the curve that defines area $A(t)$, $\mathbf{n}$ is the normal vector in the outward direction of the boundary $S(t)$, and $\mathbf{v}_s$ is the motion of $S(t)$. The first term on the right-hand side (hereafter RHS) of Equation 5.1 describes the contribution to the change of amplitude strength. The second term specifies the changes in area of the anomaly under integration.

The equation for the local change in PV anomaly in the presence of non-conservative processes (Eq. 2.5) is inserted in the RHS of Equation 5.1. Following Teubler and Riemer (2021, their Eq. 3), the non-conservative PV modification (second and third term on RHS of Eq. 2.5), further referred to as $\mathcal{N}$, is given as

$$\mathcal{N} = -\dot{\theta}\frac{\partial q}{\partial \theta} + \frac{1}{\sigma}\left[(\nabla_\theta \times \mathbf{v} + f\mathbf{k}) \cdot \nabla_\theta \dot{\theta} + \mathbf{k} \cdot (\nabla_\theta \times \dot{v})\right], \tag{5.2}$$

with $\mathbf{k} = (0,0,1)$ the unit vector perpendicular to an isentropic surface, $\dot{\theta}$ the non-conservative heating rate, and $\dot{v}$ the sources and sinks of non-conservative momentum (e.g., friction or gravity wave drag).
In the following, the focus is set exclusively on the first term on the RHS of Equation 5.1. The advection term is transformed using the chain rule $\mathbf{v} \cdot \nabla q' = \nabla \cdot (\mathbf{v}q') - q'(\nabla \cdot \mathbf{v})$ and with the use of the relation $q = q_0 + q'$ it yields the following equation:

$$\begin{aligned}
\int_{A(t)} \frac{\partial q'}{\partial t}\, dA &= \int_{A(t)} \frac{\partial q}{\partial t}\, dA - \int_{A(t)} \frac{\partial q_0}{\partial t}\, dA \\
&= \int_{A(t)} \left[-\mathbf{v} \cdot \nabla q + \mathcal{N}\right] dA - \int_{A(t)} \frac{\partial q_0}{\partial t}\, dA \\
&= -\int_{A(t)} \mathbf{v} \cdot \nabla (q_0 + q')\, dA + \int_{A(t)} \mathcal{N}\, dA - \int_{A(t)} \frac{\partial q_0}{\partial t}\, dA \\
&= \underbrace{-\int_{A(t)} \mathbf{v} \cdot \nabla q_0\, dA}_{I.advection} + \underbrace{\int_{A(t)} q'(\nabla \cdot \mathbf{v})\, dA}_{II.divergence} - \underbrace{\int_{A(t)} \nabla \cdot (\mathbf{v}q')\, dA}_{\substack{III.anomaly\,flux\\ divergence}} + \underbrace{\int_{A(t)} \mathcal{N}\, dA}_{\substack{IV.non-conservative\\ PV\,modification}} \underbrace{- \int_{A(t)} \frac{\partial q_0}{\partial t}\, dA}_{\substack{V.change\,in\,PV\\ background}}
\end{aligned} \tag{5.3}$$

The first term (I) on the RHS of Equation 5.3 (last row) describes the advection of background PV (q_0) and is closely related to linear wave propagation, which plays an important role in the formation and amplification of PVAs$^-$. The divergence term (term II) describes the change in area of the PVA$^-$ that can occur as a result of divergent or convergent flow within the PVA$^-$. Term III contains the information about the divergence of the PV anomaly flux ($\mathbf{v}q'$), which in turn depicts the net flux of q' across the boundary of the PVA$^-$ area. The non-conservative PV modification term (IV) describes the influence of diabatic processes within the PVA$^-$. Lastly, term (V) on the RHS of Equation 5.3 shows the local change in q_0 that is by definition very small and in good approximation negligible.

In a next step, the individual wind fields from the division of the full wind field $\mathbf{v} = \mathbf{v}_0 + \mathbf{v}'_{div} + \mathbf{v}'_{low} + \mathbf{v}'_{up} + \mathbf{v}'_{res}$ (Eq. 4.5) are inserted in the first two terms (I and II) of Equation 5.3. By definition, the wind fields arising from the PV inversion and $\mathbf{v}_0$ are divergence-free, such that the divergence term (II.) with the wind fields $\mathbf{v}_0, \mathbf{v}'_{up}$, and $\mathbf{v}'_{low}$ can be omitted. However, the wind fields are interpolated from pressure levels to isentropic levels such that it is no longer assured that the isentropic wind fields are completely divergence-free. Hence, the divergence term (II) of the three balanced wind fields ($\mathbf{v}_0, \mathbf{v}'_{up}$, and $\mathbf{v}'_{low}$) is not necessarily zero. The introduction of $\mathbf{v}'_{res}$ counteracts the problem, such that the following applies:

$\nabla \cdot (\mathbf{v} - \mathbf{v}'_{div}) \approx 0 \approx \nabla \cdot (\mathbf{v}_0 + \mathbf{v}'_{low} + \mathbf{v}'_{up} + \mathbf{v}'_{res})$. For the case study in Chapter 6 and the systematic investigation for GL life cycles in Chapter 7, Figure A.2 confirms that the individual divergence terms linked to $\mathbf{v}'_{up}$, $\mathbf{v}'_{low}$, $\mathbf{v}'_0$, and $\mathbf{v}'_{res}$ are not zero individually but in sum cancel out. As the divergence terms of the balanced wind fields and $\mathbf{v}'_{res}$ are an artifact of the interpolation to isentropic surfaces and do not bring a physical meaning here, they are not further considered. After inserting the individual wind fields in Equation 5.3, putting all back in Equation 5.1, grouping individual terms and sorting by relevance, the final form of the equation that describes the amplitude evolution reads as:

$$\begin{aligned} \frac{d}{dt}\int_{A(t)} q'\,dA = & \underbrace{\int_{A(t)} -\mathbf{v}'_{up}\cdot\nabla q_0\,dA}_{UP} + \underbrace{\int_{A(t)} -\mathbf{v}'_{low}\cdot\nabla q_0\,dA}_{LOW} \\ & + \underbrace{\int_{A(t)} -\mathbf{v}'_{div}\cdot\nabla q_0\,dA}_{DIV_{adv}} + \underbrace{\int_{A(t)} q'(\nabla\cdot\mathbf{v}'_{div})\,dA}_{DIV_{div}} \\ & + \underbrace{\int_{A(t)} -\mathbf{v}_0\cdot\nabla q_0\,dA}_{BGA} + \underbrace{\int_{A(t)} -\mathbf{v}'_{res}\cdot\nabla q_0\,dA}_{RES} \\ & + \underbrace{\int_{A(t)} \mathscr{N}\,dA}_{NON-CONS} - \underbrace{\int_{A(t)} \frac{\partial q_0}{\partial t}\,dA}_{dq0dt} \\ & \underbrace{\left[-\int_{A(t)} \nabla\cdot(\mathbf{v}q')\,dA + \oint_{S(t)} q'(\mathbf{v}_s\cdot\mathbf{n})\,dS\right]}_{\mathscr{B}nd}. \end{aligned} \tag{5.4}$$

The term describing the divergence of the PV anomaly flux (III. in Eq. 5.3) indirectly denotes an area change, such that the term is considered together with the second term in Equation 5.1 and is further referred to as a boundary term $\mathscr{B}$nd.

Description of the individual PV tendency terms

The first term in Equation 5.4 ($-\mathbf{v}'_{up}\cdot\nabla q_0$) is closely related to barotropic wave dynamics as it represents the advection of upper-tropospheric PV by the wind field associated with upper-tropospheric PV anomalies, referred to as intrinsic wave propagation. Amplification and decay of PV anomalies highly depend on the asymmetry in the amplitude of PV anomalies upstream and downstream. This process is further referred to as UP.

The term $-\mathbf{v}'_{low}\cdot\nabla q_0$ describes the modification of upper-tropospheric PV anomalies by the wind fields associated with lower-tropospheric PV anomalies, which denotes baroclinic interaction in the PV-θ -framework. The phase relation between the upper and lower-tropospheric PV is decisive for the influence of lower-tropospheric PV anomalies on the amplitude of upper-tropospheric PV anomalies. Only when the low-level PV anomalies lead the upper-level wave pattern by less than one-half wavelength, an amplification of upper-tropospheric PV anomalies can be expected. This term is hereafter abbreviated with LOW.

Two terms arise with the divergent wind field that are associated with a change in the upper-tropospheric PV anomaly amplitude due to (i) the advection of background PV with the divergent wind field ($-\mathbf{v}'_{div} \cdot \nabla q_0$), and (ii) the divergence of the divergent wind within the PV anomaly as contribution to the area change of the PV anomaly ($q'(\nabla \cdot \mathbf{v}'_{div})$). The PV tendency due to (i) depends strongly on the location of the maximum divergent/convergent flow relative to the maximum PV gradient, and is usually an order of magnitude smaller compared to term (ii). Term (ii) leads to an amplification of negative PV anomalies when divergence occurs within an area of negative PV anomalies. Both terms (i and ii) and considered separately in the following and are referred to as DIV_{adv} and DIV_{div}, respectively.

The term $-\mathbf{v}_0 \cdot \nabla q_0$ describes the advection of background PV with the background flow as part of barotropic dynamics, and has been considered, together with UP, as a quasi-barotropic PV tendency term in Teubler and Riemer (2016). In the following, this term is further referred to as BGA, which stands for background advection. The influence of BGA is investigated separately in this work and therefore not considered with UP. The advection of background PV by the residual wind field ($-\mathbf{v}'_{res} \cdot \nabla q_0$) is hard to describe in a physical sense, as it includes the part of the framework that cannot be explained by the wind fields obtained from Helmholtz partitioning and piecewise PV inversion. However, for the sake of completeness, this term is incorporated in the evaluations and abbreviated with RES. As already mentioned above in the derivation of the tendency equation, non-conservative processes ($\mathscr{N}$) and the change in the background PV ($\partial q_0/\partial t$) contribute to the amplitude evolution of PV anomalies and are referred to as NON-CONS and $\partial q_0/\partial t$ in the remainder of this work, respectively.

Calculation of integrated PV tendency terms

To evaluate the different contributions to the amplitude evolution of a PVA$-$, the various PV tendency terms in Equation 5.4 are integrated over the area enclosed by the PVA$-$. Therefore, the contour of the PVA$-$ is put on selected isentropic surfaces, as the amplitude evolution is investigated on isentropic surfaces. In order to study the amplitude evolution in the close vicinity of the tropopause, the choice of the appropriate isentropic surface is of high importance and depends on the time of the year. Following the recommendations of Röthlisberger et al. (2018), a suitable selection is 320 K in December, January, February, March; 325 K in April, November; 330 K in May, October; 335 K in June, September; and 340 K in July, August. For each time step, the vertical mean of three isentropic levels is chosen (+/- 5 K around the varying central value).

The non-conservative PV modification $\mathscr{N}$ (cf. Eq. 5.2) is estimated only for the EuBL case study in March 2016 with the available wind and temperature tendencies linked to radiation and parametrizations.

Estimation of the boundary term

As described in Equation 5.1, the total change in PVA$^-$ amplitude includes a term that represents the change in area. Together with the term that describes the divergence of the PV anomaly flux (term III in Eq. 5.3), they make up the boundary term $\mathscr{B}$nd, defined as

$$\begin{aligned} \mathscr{B}nd &= -\int_{A(t)} \nabla \cdot (\mathbf{v}q')\,dA + \oint_{S(t)} q'(\mathbf{v}_s \cdot \mathbf{n})\,dS \\ &= \oint_{S(t)} q'(\mathbf{v}_s - \mathbf{v})\,d\mathbf{S} \end{aligned} \tag{5.5}$$

with d**S** = **n** dS, where the divergence term of the PV anomaly flux has been transformed in the second row using the Gauss's theorem. In Teubler and Riemer (2016), individual troughs and ridges are characterized by positive and negative PV anomalies that are bounded by $q' = 0$, such that $\mathscr{B}$nd vanishes. For the application of anomalies that are bounded by $q' = 0$ on their northern and southern edge, $\mathbf{v}_s$ could be estimated from the longitudinal displacement between two consecutive dates, which facilitates a physically meaningful and reliable assessment of $\mathbf{v}_s$. However, the PVAs$^-$ in this work are identified differently and with an anomaly-based threshold of $\neq 0.0$ PVU such that the PVAs$^-$ are often not completely bounded by a $q' = 0$ contour or may even be connected with like-signed, neighboring PV anomalies. As a result, $\mathscr{B}$nd is no longer negligible. For the PVAs$^-$ in this work, an estimation of $\mathscr{B}$nd needs to be carried out.

The area integral describing the divergence of the anomaly flux (first term on RHS of Eq. 5.5) is uniquely determinable. However, the movement of the boundary enclosing the PVA$^-$ ($\mathbf{v}_s$) in the second term on the RHS of Equation 5.5 is generally unknown and complicates the calculation of $\mathscr{B}$nd. In particular, $|\mathbf{v}_s|$ becomes very large when splitting and merging events occur. Using Gauss's theorem, the integral over the closed contour can be transformed into an area integral. As $\nabla \cdot \mathbf{v}_s$ implies a change of the anomaly area ΔA, the sub term in $\mathscr{B}$nd associated with $\mathbf{v}_s$ is estimated as

$$\oint_{S(t)} q'(\mathbf{v}_s \cdot \mathbf{n})\,dS = \int_{A(t)} \nabla \cdot (q'\mathbf{v}_s)\,dA \approx \overline{q}' \cdot \Delta A, \tag{5.6}$$

where $\overline{q}'$ is the average value of q' along the boundary S of the PVA$^-$ on the respective isentropic surface. The change in area ΔA describes the observed area change as $\Delta A(t) = (A(t+\Delta t) - A(t))$ with $\Delta t = 3\,h$.

Closeness of the PV tendency budget

The aggregate of all processes quantified in Eq. 5.4 is referred to in the following as the diagnosed amplitude change. To assess how closed the diagnostic PV budget is, i.e., to what degree the individual processes describe the observed PVA amplitude evolution, the diagnosed amplitude change is compared with the actual observed amplitude change. In analogy to Teubler and Riemer (2016), the observed amplitude change is calculated from the difference of the area-integrated PVA$^-$ amplitude between two time steps (here: Δt = 3 h):

$$\frac{d}{dt}\int_{A(t)} q'\,dA\bigg|_{obs} = \frac{1}{\Delta t}\left(\int_{A(t+\Delta t)} q'dA - \int_{A(t)} q'dA\right) \tag{5.7}$$

The closeness of the PV tendency budget depends on various factors. First, processes such as turbulent mixing as part of the non-conservative modification term are neglected within the diagnostic framework. Second, the uncertainties from the partitioning of the wind fields are reflected in the tendencies and thus contained in the calculated values. Third, the overall comparison of instantaneous tendencies with a finite difference of 3 hours always bears inaccuracies. Fourth, PV tendency terms are limited to the region between 25 °N and 80 °N, such that the PVA amplitude evolution of PV anomalies that extend out of this region cannot be fully described. Last, and most importantly, a main reason for the differences between diagnosed and observed amplitude change is an abrupt change in the anomaly area A, which usually occurs when parts of the PV anomaly split up or other PV anomalies merge into an existing PVA$^-$. This effect of splitting or merging is explicitly reflected in $\mathscr{B}$nd. Therefore, the determination of $\mathscr{B}$nd is of high importance to ensure that the PV tendency budget is closed.

Consideration of the change in PV background

By selecting the PV background q_0 as the 30-day running mean climatology (1980–2019), it is given that the local change in q_0 from one time step to the next is small enough such that $\partial q_0/\partial t \approx 0$ holds. For a consistent picture with the separation of $\partial q/\partial t$ into the different processes contributing to the change in the PVA$^-$ amplitude, the aim is to split up the smaller term $\partial q_0/\partial t$ too, such that the climatological footprint can be considered for each term in Equation 5.4. This is of particular importance for the systematic evaluation of year-round regime life cycles, as the climatological footprint changes over the year. In the following, this further modification of the original framework by Teubler and Riemer (2016) is presented for the integrated amplitude analysis and used for all systematic blocked regime evaluations.

A mean operator (<>) is introduced that consists of averages between 1980–2019 for each calendar time and a subsequent running mean (+/- 15 days). The background calculation for q and the wind field **v** follows this method such that <q> = q_0 holds. With this, by using the PV tendency equation (Eq. 2.5), the following applies for the change in q_0:

$$\frac{\partial q_0}{\partial t} = < \frac{\partial q}{\partial t} > = - < \mathbf{v}\cdot\nabla q > + < \mathscr{N} > . \tag{5.8}$$

By using the relations $q = q_0 + q'$, $\mathbf{v} = \mathbf{v}_0 + \mathbf{v}'$ and $\mathscr{N} = \mathscr{N}_0 + \mathscr{N}'$, and the application of the chain rule, Equation 5.8 reads as:

$$\begin{aligned}\frac{\partial q_0}{\partial t} &= - < (\mathbf{v}_0 + \mathbf{v}') \cdot \nabla(q_0 + q') > + < (\mathscr{N}_0 + \mathscr{N}') > \\ &= - < \mathbf{v}_0 \cdot \nabla q_0 > - < \mathbf{v}_0 \cdot \nabla q' > - < \mathbf{v}' \cdot \nabla q_0 > - < \mathbf{v}' \cdot \nabla q' > + < \mathscr{N}_0 > + < \mathscr{N}' > \\ &= -\mathbf{v}_0 \cdot \nabla q_0 - < \nabla \cdot (\mathbf{v}_0 q') > + < q'(\nabla \cdot \mathbf{v}_0) > - < \mathbf{v}' \cdot \nabla q_0 > \\ &- < \nabla \cdot (\mathbf{v}' q') > + < q'(\nabla \cdot \mathbf{v}') > + \mathscr{N}_0,\end{aligned} \tag{5.9}$$

with the assumption that $< \mathscr{N}_0 > = \mathscr{N}_0$ and that $< \mathscr{N}' > \approx 0$. After combining the terms such that similar terms as in Equation 5.4 arise, the following is obtained:

$$\frac{\partial q_0}{\partial t} = - < \mathbf{v}' \cdot \nabla q_0 > + < q'(\nabla \cdot \mathbf{v}) > - < \nabla \cdot (\mathbf{v} q') > + \mathscr{N}_0 - \mathbf{v}_0 \cdot \nabla q_0. \tag{5.10}$$

After inserting the individual wind fields contained in the full wind field $\mathbf{v} = \mathbf{v}_0 + \mathbf{v}' = \mathbf{v}_0 + \mathbf{v}'_{div} + \mathbf{v}'_{up} + \mathbf{v}'_{low} + \mathbf{v}'_{res}$ into Equation 5.10, the final version of $\partial q_0 / \partial t$ reads as

$$\begin{aligned}\frac{\partial q_0}{\partial t} &= - < (\mathbf{v}'_{low} + \mathbf{v}'_{up} + \mathbf{v}'_{div} + \mathbf{v}'_{res}) \cdot \nabla q_0 > + < q'(\nabla \cdot (\mathbf{v}_0 + \mathbf{v}'_{low} + \mathbf{v}'_{up} + \mathbf{v}'_{div} + \mathbf{v}'_{res})) > \\ &- < \nabla \cdot (\mathbf{v} q') > + \mathscr{N}_0 - \mathbf{v}_0 \cdot \nabla q_0.\end{aligned} \tag{5.11}$$

In comparison with the terms contained in Equation 5.4, it turns out that apart from the second term in $\mathscr{B}$nd (Eq. 5.5), each term contains a climatological footprint term that is subtracted from the absolute PV tendency term. With the same assumption as above that $\nabla \cdot (\mathbf{v} - \mathbf{v}'_{div}) \approx 0 \approx \nabla \cdot (\mathbf{v}_0 + \mathbf{v}'_{low} + \mathbf{v}'_{up} + \mathbf{v}'_{res})$, most of the divergence terms drop out. By sorting the terms logically and inserting Equation 5.11 into

Equation 5.4, the final equation for the amplitude evolution of PVAs$^-$ with the partitioned PV background change term ($\partial q_0/\partial t$) is:

$$\begin{aligned}
\frac{d}{dt}\int_{A(t)} q'\,dA = & \underbrace{-\int_{A(t)} \mathbf{v}'_{up}\cdot\nabla q_0\,dA - \int_{A(t)} < -\mathbf{v}'_{up}\cdot\nabla q_0 > dA}_{UP} \underbrace{-\int_{A(t)} \mathbf{v}'_{low}\cdot\nabla q_0\,dA - \int_{A(t)} < -\mathbf{v}'_{low}\cdot\nabla q_0 > dA}_{LOW} \\
& \underbrace{-\int_{A(t)} \mathbf{v}'_{div}\cdot\nabla q_0\,dA - \int_{A(t)} < -\mathbf{v}'_{div}\cdot\nabla q_0 > dA}_{DIV_{adv}} + \underbrace{\int_{A(t)} q'(\nabla\cdot\mathbf{v}'_{div})\,dA - \int_{A(t)} < q'(\nabla\cdot\mathbf{v}'_{div}) > dA}_{DIV_{div}} \\
& \underbrace{-\int_{A(t)} \mathbf{v}'_{res}\cdot\nabla q_0\,dA - \int_{A(t)} < -\mathbf{v}'_{res}\cdot\nabla q_0 > dA}_{RES} + \underbrace{\int_{A(t)} \mathscr{N}\,dA - \int_{A(t)} \mathscr{N}_0\,dA}_{NON-CONS} \\
& \left[\underbrace{-\int_{A(t)} \nabla\cdot(\mathbf{v}q')\,dA - \int_{A(t)} < -\nabla\cdot(\mathbf{v}q') > dA + \oint_{S(t)} q'(\mathbf{v}_s\cdot\mathbf{n})\,dS}_{\mathscr{B}nd}\right].
\end{aligned} \tag{5.12}$$

Discussion of the climatological footprints

For the sake of completeness, the patterns of the climatological footprint fields contained in Equation 5.12 are discussed briefly. The patterns for every time step changes during the year, as they exclusively show the mean patterns for a 30-day running mean period (1980–2019). There is no detailed analysis of all patterns for different seasons, as this would go beyond the scope of this thesis. Instead, this subsection provides an insight into the footprint patterns for a selected time in winter (January 15, 00 UTC). For a comparison, the mean patterns for summer (July 15, 00 UTC) are displayed in Figure A.3.

The climatological footprint of UP ($-\mathbf{v}_{up}\cdot\nabla q_0$) reveals positive PV tendencies on the upstream and negative PV tendencies on the downstream flank of a climatological trough over the eastern half of the US in winter (Fig. 5.9a). This picture is in agreement with PV thinking for linear Rossby waves (e.g., Fig. 17 in Hoskins et al., 1985) and would lead to a westward shift of the trough. Additional positive PV tendencies are found over the Mediterranean Sea with a maximum near Gibraltar, where they contribute to a westward phase propagation of the ridge over the eastern North Atlantic, which is linked to the stationary waves in winter (cf. Fig. 2.1a). In contrast, the pattern of LOW ($< -\mathbf{v}_{low}\cdot\nabla q_0 >$) exhibits nearly a reversed picture of UP, with positive PV tendencies on the downstream and negative PV tendencies on the upstream flank of the trough over the eastern United States (US) (Fig. 5.9b). The cold temperature anomaly over the continent (not shown) related with the trough is associated with an anticyclonic wind field in the lower troposphere. This leads to the northward advection of background PV on the upstream flank and southward advection of background PV on the downstream flank in the upper troposphere. Over the Mediterranean, negative PV tendencies of LOW point to the presence of a surface

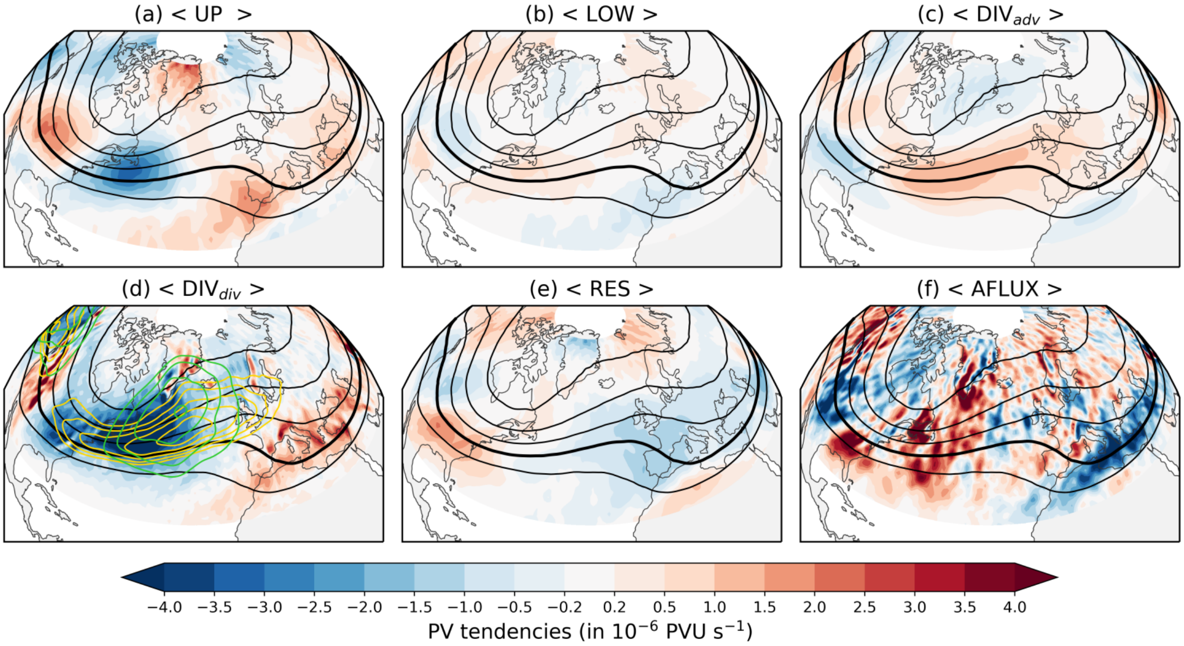

Figure 5.9: Climatological footprints of PV tendency terms (shading, in 10^{-6} PVU s^{-1}) centered on January 15, 00 UTC: (a) advection of PV background with upper-tropospheric wind field ($-\mathbf{v}_{up} \cdot \nabla q_0$; UP), (b) advection of PV background with lower-tropospheric wind field ($-\mathbf{v}_{low} \cdot \nabla q_0$; LOW), (c) advection of PV background with divergent wind field ($-\mathbf{v}_{div} \cdot \nabla q_0$; DIV$_{adv}$), (d) divergence term of divergent wind field ($q'(\nabla \cdot \mathbf{v}_{div})$; DIV$_{div}$), (e) advection of background PV with residual wind field ($-\mathbf{v}_{res} \cdot \nabla q_0$; RES), and (f) the divergence of the PV anomaly flux as part of the boundary term $\mathscr{B}$nd ($-\nabla \cdot (\mathbf{v}q')$). PV tendency terms are shown as isentropic mean between 315 and 325 K in steps of 5 K. Black contours show PV contours at 320 K (from 1-5 PVU in steps of 1 PVU). The 2-PVU-contour that points to the location of the dynamical tropopause is displayed in bold. The green and yellow contour lines in (d) show the climatological frequency of WCB outflow based on the Eulerian WCB metric (cf. Sect. 4.5) and negative upper-tropospheric PV anomalies (cf Sect. 5.1), respectively. Contour intervals for the WCB outflow frequency range from 8–14 % (in steps of 2 %) and range from 28–38 % (in steps of 2 %) for the frequency of negative PV anomalies. Note that both climatology fields are smoothed slightly.

cold anomaly, the wind fields of which leads to a northward advection of background PV and works against the westward phase propagation. Along the North Atlantic storm track region, the climatological footprint of DIV$_{adv}$ ($< -\mathbf{v}_{div} \cdot \nabla q_0 >$) indicates an elongated band of positive PV tendencies, pointing to a general weakening of negative and a strengthening of positive upper-tropospheric PV anomalies (Fig. 5.9c). As this region overlaps with the climatological footprint of WCB outflow (green contours, Fig. 5.9d), this seems counterintuitive at first, since the primary expectation is that enhanced divergent winds aloft related to WCBs are often associated with a radial outflow of low PV. However, as divergence in the wind field occurs north of the maximum PV gradient q_0 (e.g., WCB outflow on the northwestern edge), it leads to positive PV tendencies south of it and negative PV tendencies north of it. This is visible by negative PV tendencies of DIV$_{adv}$ over Greenland (Fig. 5.9c). Negative PV tendencies of DIV$_{div}$ ($< q'(\nabla \cdot \mathbf{v}_{div}) >$) prevail over the western North Atlantic, with the highest absolute values in the Gulf Stream region (Fig. 5.9d). A glance at the mathematical expression of the term reveals that negative PV tendencies appear only when negative PV anomalies co-occur with divergence or positive

PV anomalies co-occur with convergence in the upper troposphere. Since the climatologies of WCB outflow and negative PVA$^-$ frequency show high values over the western North Atlantic, it is reasonable to assume that it is mainly the combination of negative PV anomalies and divergence in combination with WCB activity that leads to the negative PV tendencies in DIV$_{div}$. The climatological footprint of RES ($< -\mathbf{v}_{res} \cdot \nabla q_0 >$, Fig 5.9e) is hard to explain from a physical processes perspective. As a reminder, $\mathbf{v}_{res}$ includes the part of the wind fields that is not contained in the other split up wind fields that in sum should make up the full wind field $\mathbf{v}$, mainly due to numerical inaccuracies. In general, it appears that in the case of the trough over the US, a northward component of the wind is missing in the split up of $\mathbf{v}$ by Helmholtz partitioning and PV inversion. Over Western Europe, a southward component is missing, which results in positive and negative PV tendencies of RES, respectively. The climatological footprint of the term that describes the divergence of the PV anomaly flux ($-\nabla \cdot (\mathbf{v}q')$) and belongs to $\mathscr{B}$nd is the most patchy pattern of all terms shown in Figure 5.9. This term shows negative PV tendencies in case of a radial outward pointing (divergent) flux of negative PV anomalies, which seems to be present in the Mediterranean Sea and over the central US. An area of positive PV tendencies is visible over the western North Atlantic, where upper-level convergence within areas of positive PV anomalies leads to the amplification of PV in place.

5.6 Summary

This chapter presented the development of the novel quasi-Lagrangian PV framework based on the blocking detection algorithm of Schwierz et al. (2004), the year-round weather regime definition of Grams et al. (2017), and the PV-θ-framework of Teubler and Riemer (2016). The quasi-Lagrangian PV framework, illustrated schematically in Figure 5.10, contains the following steps, which help to disentangle the dynamics of blocked regimes from a new angle:

(1) **Identification and tracking of upper-tropospheric negative PV anomalies**
PV anomalies are identified in fields of VAPV’ (relative to a 30-day running mean climatology) between the middle and upper troposphere. Based on a PV anomaly threshold, which varies throughout the year, negative PV anomalies are identified as features (PVAs$^-$). A novel contour-overlap tracking algorithm, which recognizes and quantifies splitting and merging, is applied to trace PVAs$^-$. This leads to PVA$^-$ tracks describing the PVAs$^-$ from their origin to the time when they dissipate (Fig. 5.10, upper level).

(2) **Assignment of PVAs$^-$ to blocked regime life cycles**
Based on the VAPV’ composite patterns of the four blocked regimes, regions are defined in which negative PV anomalies are typically present during an active regime (further referred to as regime masks). This allows PVAs$^-$ to be assigned as actively contributing PVAs$^-$ if they share spatial overlap with the regime mask (Fig. 5.10, middle level).

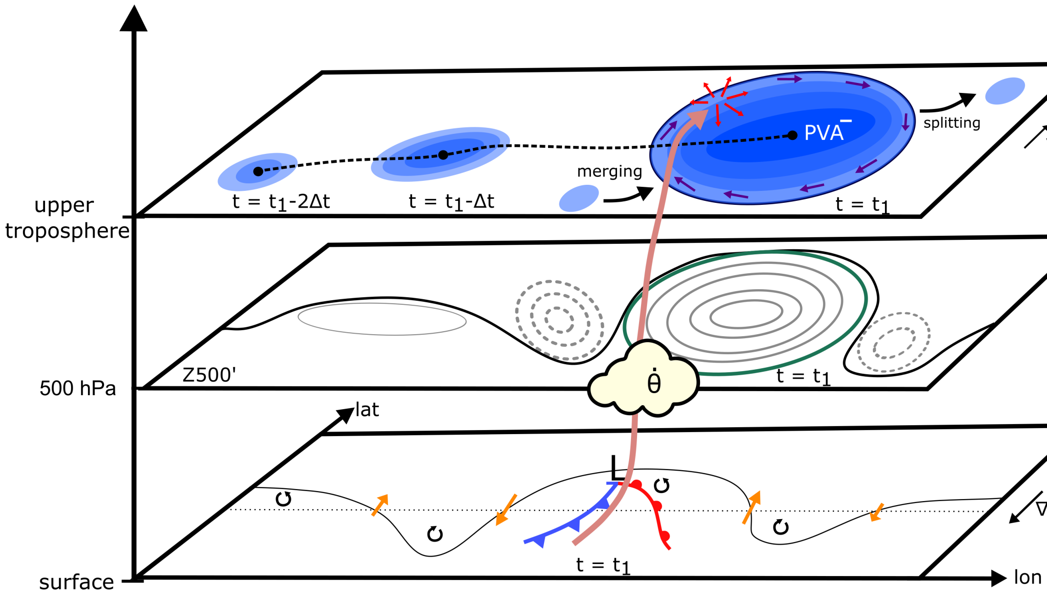

Figure 5.10: Schematic summary of the quasi-Lagrangian PV framework. The upper level indicates the identification and tracking of PVA$^-$ (blue shadings, dashed black line is track) and the ability of the tracking algorithm to detect splitting and merging along the track. The wind field induced by the PVA$^-$ is shown in dark violet arrows, pointing to the UP PV tendency term. The middle level shows a blocked regime pattern with the waveguide (black solid line) and Z500 anomalies in gray contours (positive - solid; negative - dashed). The regime mask is indicated by the green contour. In the lowest level, the black lines show the temperature wave near the surface. Orange arrows point to the flow induced by the temperature wave, pointing to the LOW PV tendency term. An extratropical cyclone ('L') is shown with its fronts on the surface. The arrow (salmon color) covering all levels is the WCB linked to latent heat release in the mid-troposphere ($\dot{\theta}$) and divergent outflow in the upper troposphere (diverging red arrows), indicating the DIV$_{div}$ and DIV$_{adv}$ PV tendency terms.

(3) **Process contributions to the amplitude evolution of PVAs$^-$**

The PV-θ-framework of Teubler and Riemer (2016), which was originally developed for ridges and troughs within RWPs, is adapted to the definition of PVAs$^-$ as transient features. Thereby, a new way to consider the area change of PVAs$^-$ is refined. Split up into the different PV tendency terms, the advanced version of the PV-θ-framework enables insights into the relative contributions of dry and moist dynamics in the amplitude evolution of PVAs$^-$ (Fig. 5.10, lower and upper level).

Next, this novel quasi-Lagrangian framework is tested and applied to a EuBL regime life cycle.

6 Insights into the European Blocking regime life cycle in March 2016

The novel quasi-Lagrangian PV framework introduced in Chapter 5 is applied here, for the first time, to a single EuBL regime life cycle that occurred in spring 2016. The onset of the strong blocking over Europe in March 2016 was associated with large errors in ECMWF's high-resolution forecast in the medium range and led to one of the three worst forecast busts with exceptional low forecast skill in the period 2014-2016 over Europe (Magnusson, 2017). An initial error was detected over the western North Atlantic, linked to a misrepresentation of a cyclone that triggered strong diabatic WCB activity over the North Atlantic region (Grams et al., 2018). The errors in synoptic activity over the western North Atlantic were communicated into regions far downstream that resulted in wrong forecasts of the upper-level circulation pattern over Europe. Previous studies investigated the dynamics of regimes and blocked regimes, in particular from a classical Eulerian perspective, and highlighted the dry dynamics for the formation of a block (e.g., Austin, 1980). In agreement, a low-frequency Eulerian perspective on the EuBL regime life cycle in March 2016 revealed the dominance of dry processes that built up the EuBL regime pattern (Hauser et al., 2023b). In particular, the advection of PV anomalies into the North Atlantic-European region led to the onset of the regime pattern in March 2016. These results contrast with studies in recent years that have increasingly identified an important contribution from moist processes for the formation and maintenance of blocking (e.g., Pfahl et al., 2015). In Steinfeld and Pfahl (2019), a systematic evaluation of air masses that end up in upper-tropospheric blocking anticyclones from a pure Lagrangian perspective revealed a leading role of moist processes for long and intense blocking episodes. Hence, the relative importance of dry and moist dynamics is sensitive to the chosen perspective.

Using a case study which was sensitive to moist-baroclinic development during the onset stage, the purpose of this chapter is to test whether the novel quasi-Lagrangian perspective can capture and quantify all processes – i.e., the importance of dry-dynamical and moist-dynamical processes – in a unified approach. The quasi-Lagrangian perspective that follows PVAs^{-} and investigates the contributions to the PVA^{-} amplitude evolution (Fig. 6.1b) is compared to the classical pure Lagrangian perspective, where the origin and history of air parcel that end up in the PVAs^{-} are analyzed (Fig. 6.1c). Linked to the results from the Eulerian perspective (Fig. 6.1a) in Hauser et al. (2023b), a holistic view of the dynamical evolution of the EuBL regime life cycle in March 2016 can be achieved. However, the particularly novel aspect is the quasi-Lagrangian perspective, which helps to bridge the gap between the Lagrangian and

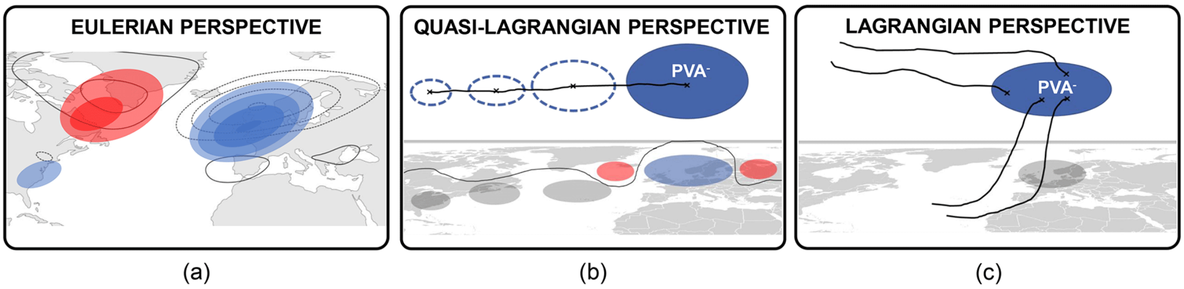

(a) (b) (c)

Figure 6.1: Schematic overview of three perspectives on the PV dynamics of blocked weather regime life cycles: (a) Eulerian perspective, (b) quasi-Lagrangian perspective, and (c) Lagrangian perspective. The framework linked to the Eulerian perspective quantifies the PV dynamics by projecting different upper-tropospheric PV tendency terms onto the mean regime pattern. Black contours schematically show the PV anomaly pattern for EuBL (solid for positive, dashed for negative PV anomalies). Red and blue shading shows exemplary positive and negative PV anomalies at a fixed point in time, respectively. The quasi-Lagrangian perspective follows PVAs$^-$, assigns them to active regime life cycles, and investigates the PVA$^-$ amplitude evolution. The solid black line connects the center of mass positions of a traced PVA$^-$ (dashed blue contours at different times). The PVA$^-$ is part of a RWP, as displayed by the sequence of negative (blue shading) and positive (red shading) PV anomalies. The thin black line on the map schematically shows the position of the waveguide. The Lagrangian perspective calculates backward trajectories out of the negative PVA$^-$ defined in the quasi-Lagrangian perspective, and focuses on the diabatic and non-diabatic history of air parcels that end up in the PVA$^-$. The black lines represent schematically backward trajectories from the PVA$^-$ (starting points marked with a black cross). Adapted from Hauser et al. (2023b).

Eulerian perspectives.

The chapter is structured as follows. First, the large-scale PV evolution of the regime life cycle is discussed (Sect. 6.1). The novel quasi-Lagrangian PV perspective (schematic overview in Fig. 6.1a) introduced in detail in Chapter 5 is applied to the EuBL regime life cycle in Section 6.2. Lagrangian backward trajectories enable a Lagrangian view (schematic overview in Fig. 6.1b) on the dynamics by the investigation of the history of air parcels associated with the PVA$^-$ (Sect. 6.3). A short synopsis of the two perspectives (quasi-Lagrangian and Lagrangian) and the Eulerian perspective as third perspective (Hauser et al., 2023b) is given in Section 6.4. The chapter closes with a summary (Sect. 6.5).

Note that the results appearing in this chapter are partly published in Hauser et al. (2023b).

6.1 Large-scale PV evolution

Based on the temporal evolution of the I_{WR}, the EuBL regime life cycle linked to the forecast bust occurred from March 9, 18 UTC to March 18, 00 UTC (Fig. 6.2, light green thick line) and exhibited a total length of around nine days. The large-scale flow in the 15 days before the EuBL onset could not be assigned to any of the seven regimes, hence the onset did not arise from a preceding regime. Figure 6.3 presents snapshots of the large-scale circulation based on upper-level PV for selected time steps around the EuBL regime life cycle. Intersection points of WCB trajectories (cf. Sect. 4.5) with the isentropic

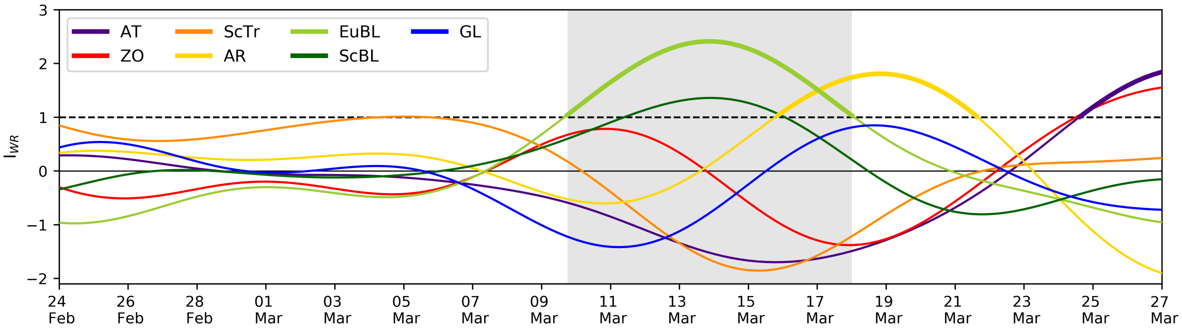

Figure 6.2: I_{WR} for year-round weather regime definition from February 24, 00 UTC–March 27, 00 UTC for all seven Euro-Atlantic regimes. Thick lines represent active regime life cycles. Gray shading indicates the period of the active EuBL regime life cycle from March 9, 18 UTC–March 18, 00 UTC. Adapted from Hauser et al. (2023b).

layer 320 K indicate the occurrence of WCB outflow on the upper-tropospheric flow and provide first insights into the potential influence of moist processes.

The large-scale circulation pattern is characterized by a high amplitude ridge over the North Atlantic five days prior to EuBL onset (Fig. 6.3a). This ridge is flanked by a broad trough reaching downstream to Spain over Western Europe that occupies the region where a quasi-stationary ridge is expected later during the EuBL regime life cycle. Upstream of the North Atlantic ridge, an incipient negative PV anomaly (yellow contour) develops at the southern flank of the trough near the US East Coast. Later in this chapter, the quasi-Lagrangian perspective will identify this PV anomaly as the main contributing PVA$^-$ during the EuBL regime life cycle that is further referred to as PVA$^-_{EuBL}$. The prevalence of WCB intersection points covering the PVA$^-_{EuBL}$ suggest an important role of WCB outflow and therefore moist processes in the formation of this anomaly. Over the next two days, the PVA$^-_{EuBL}$ dramatically amplifies ahead of a narrowed and elongated trough along the US East Coast and extends to the east, where it replaces the high-amplitude ridge over the North Atlantic (Fig. 6.3b). During the same period, the large-amplitude trough downstream has slowly moved from western to Central Europe. Still, WCB outflow within PVA$^-_{EuBL}$ points to a further strengthening of the PVA$^-_{EuBL}$ amplitude by moist processes. Around one day before EuBL onset, the trough upstream reaches far to the south, exhibits a cut-off character, and wraps up cyclonically (Fig. 6.3c). The PVA$^-_{EuBL}$, which still sits over the eastern North Atlantic upstream of the EuBL regime mask, slowly propagates towards Europe and extends over a large latitude span from Morocco to the north of Greenland around one day after EuBL onset (Fig. 6.3d). The trough downstream has also shifted even further to the south. At the time of the maximum I_{WR} of the EuBL regime life cycle (13 March 18 UTC; Fig. 6.2), the PVA$^-_{EuBL}$ exhibits a compact shape and nearly covers the full EuBL regime mask (Fig. 6.3e). Similar to the times before, WCB intersection points co-occur with the PVA$^-_{EuBL}$ once again and indicate a contribution of moist processes. Towards the end of the EuBL regime life cycle, an amplified pattern characterized by a high number of synoptic waves is evident over the North Atlantic-European region (Fig. 6.3f). A strongly pronounced trough lies over

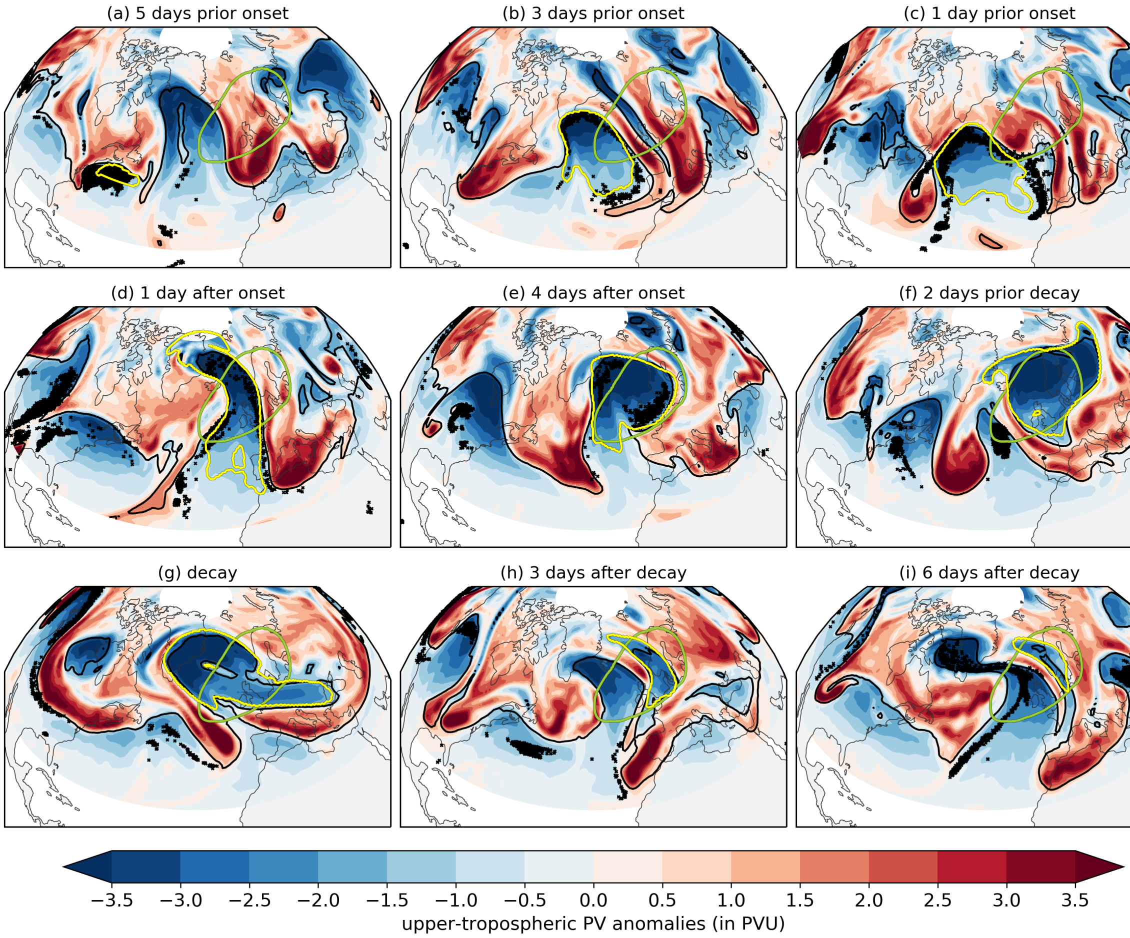

Figure 6.3: Large-scale evolution of the EuBL regime life cycle in March 2016. Isentropic mean PV anomalies (315–325 K, shading, in PVU) and the 2 PVU contour as measure of the dynamical tropopause (solid black line) are displayed for selected times around the onset and decay. The yellow contour line in each subplot represents the traced quasi-Lagrangian PV anomaly associated with the regime life cycle. The fixed light green contour is the regime mask for EuBL (see Sect. 5.4, Fig. 5.6a). Black crosses mark WCB intersection points with the 320 K +/- 2.5 K isentropic layer for the respective time step. Adapted from Hauser et al. (2023b).

the central North Atlantic, and the PVA^{-}_{EuBL} begins to deform. For the first time, no WCB intersection points are co-located within the PVA^{-}_{EuBL}. Strong deformations of the PVA^{-}_{EuBL} are visible at the time of regime decay (Fig. 6.3g). Still, the trough upstream reaches far into the south and is elongated from northwest to southeast. The large-scale flow pattern at this time resembles the pattern of AR, reflected in the high projection of the I_{WR} for AR and the concurrent active life cycle of AR (Fig. 6.2). Three days after the EuBL decay, the large-scale pattern has changed significantly, and a new ridge has formed over the eastern North Atlantic that overlaps with the southwestern part of the EuBL regime mask (Fig. 6.3h). In the meantime, the former ridge linked to the PVA^{-}_{EuBL} has significantly lost in area and strength and is pushed towards Scandinavia. The PVA^{-}_{EuBL} is still visible in the regime mask as a small remnant 6 days after regime decay (Fig. 6.3i). Upstream of the PVA^{-}_{EuBL}, a strong amplification of the newly formed ridge is taking place that is accompanied by high WCB activity within the ridge. Over the next 24 hours, the PVA^{-}_{EuBL} weakens even further until it dissipates completely on March 25 (not shown).

In summary, the development of the EuBL regime life cycle in March 2016 is related to the eastward propagation of the PVA^{-}_{EuBL} into Europe during the days before regime onset. The presence of WCB activity before the onset and within the regime life cycle suggests that moist processes contribute to the regime buildup, and that a lack thereof might be linked to the weakening and decay of the regime. Most importantly, the large-scale circulation reveals that the dominant PVA^{-}_{EuBL} over Europe does not form locally.

6.2 Quasi-Lagrangian PV perspective

This section presents insights into the EuBL regime life cycle from a quasi-Lagrangian perspective that traces PVAs^{-} linked to a blocked regime life cycle and investigates their evolution (cf. Chapt. 5). At first, the track of the main contributing PVA^{-} (further referred to as PVA^{-}_{EuBL}) is presented and the occurrence of splitting and merging is analyzed. Afterward, the processes that determine the amplitude evolution of the PVA^{-}_{EuBL} are quantified.

6.2.1 Development of the main contributing PVA^{-}

Figure 6.4 shows the temporal evolution of the total spatial share of the regime mask that is covered by traced PVAs^{-} and the PV anomaly amplitude evolution within the regime mask around the EuBL regime life cycle. The total overlap by PVAs^{-} increases before the onset and peaks between 14 – 16 March, nearly simultaneously with the I_{WR} for EuBL. At the same time, the maximum in PV anomaly amplitude is diagnosed within the regime mask (Fig. 6.4). After March 16, the overlap by PVAs^{-} decreased before the decay of the regime life cycle (Fig. 6.4). If exclusively PVAs^{-} are considered that cover at least 10 % of the regime mask area for a minimum duration of 12 hours, a single PVA^{-} is found that dominated the EuBL regime life cycle in March 2016 and is further referred to as PVA^{-}_{EuBL}. The good agreement between the total overlap of PVAs^{-} with the regime mask (black dashed line in Fig. 6.4) and the overlap of the main contributing PVA^{-}_{EuBL} (blue solid line in Fig. 6.4) demonstrates that the PVA^{-}_{EuBL} reflects the main development of the anticyclonic regime pattern of EuBL to a high degree and justifies the exclusive analysis of the PVA^{-}_{EuBL} in the following.

The PVA^{-}_{EuBL} that dominated the EuBL regime life cycle formed five days before the EuBL onset and vanished seven days after EuBL decay. The novel tracking algorithm identified the PVA^{-}_{EuBL} from March 4–25 that exhibited a total lifetime of nearly 21 days. The full track of the PVA^{-}_{EuBL} based on the center of mass position is displayed in Figure 6.5a and reveals the initial identification of the PVA^{-}_{EuBL} over the US East Coast five days before regime onset. Over time, the PVA^{-}_{EuBL} propagated rapidly over the North Atlantic northeastwards towards Europe, where it entered the regime mask shortly before the regime

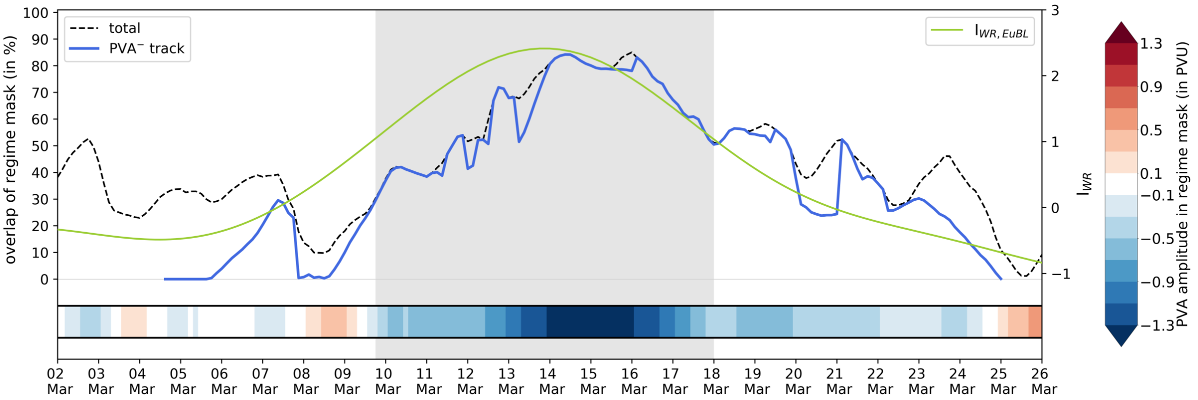

Figure 6.4: Evolution of the PV anomaly amplitude within the regime mask (horizontal bar in lower part of figure, in PVU), the total overlap of negative PV anomalies within the regime mask (black dashed line), the overlap with the regime mask for PVA^-_{EuBL} (blue solid line), and the I_{WR} for EuBL (cf. Fig. 6.2). Note that the regime mask is displayed in Fig. 6.3. The gray shading shows the time period of the active regime life cycle.

onset. It then became quasi-stationary over Northern Europe (illustrated by the frequency maximum in shading) with the onset of the regime life cycle on March 9, 2016. During the full active EuBL regime life cycle, the center of mass of the PVA^-_{EuBL} was located within the regime mask. Towards the end of the regime life cycle and after the decay, the PVA^-_{EuBL} started to migrate towards the northeast and finally vanished on 25 March over western Russia (black cross at eastern regime mask boundary in Fig. 6.5a).

Abrupt changes of the center of mass position along the PVA^-_{EuBL} track (Fig. 6.5a) result from splitting and merging PVAs$^-$. The merging of a PVA$^-$ into the PVA^-_{EuBL}, or the split off from the PVA^-_{EuBL}, can lead to sudden changes of the PVA^-_{EuBL} amplitude and area, depending on the extent of splitting or merging PVA$^-$. This, in turn, impacts the position of the PVA^-_{EuBL}'s center of mass. The novel tracking algorithm in the quasi-Lagrangian perspective is designed to detect and quantify the effect of these events, and an overview of all splitting and merging events along the PVA^-_{EuBL} track is given in Figure 6.5b. In addition, Figure 6.6 shows the occurrence frequency of splitting and merging, and provides spatial information about the PVAs$^-$ that split up or merge into the PVA^-_{EuBL}.

Considering all splitting and merging events without a minimum size criterion, more than 20 splitting and 20 merging events occur along the traced PVA^-_{EuBL}. However, for approximately half of the events, the impact on the PVA^-_{EuBL}'s area and area-integrated amplitude is small, with a relative area change of less than 15 % (Fig. 6.5b). Other events, however, are accompanied by a significant change in area and amplitude and lead to large jumps in the PVA^-_{EuBL} track. One example is the prominent northward jump of the track and the subsequent southward jump around March 7 (Fig. 6.5a). Within a short period of time, the PVA^-_{EuBL} briefly merges with another PVA$^-$ that extends north into Arctic latitudes (Fig. 6.6a, green cross over northern Greenland). This indicates a size corresponding to more than 40 % of the PVA^-_{EuBL} (Fig. 6.5b, green dot), explaining the sudden jump of the center of mass in the track. Only 6

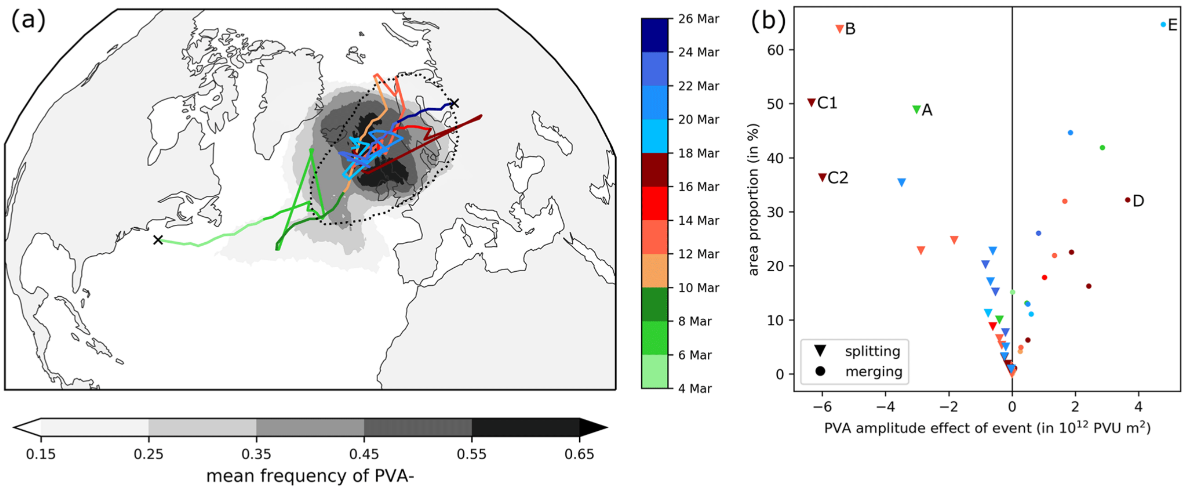

Figure 6.5: (a) Track of the PVA^-_{EuBL} (colored line) based on the center of mass from March 4, 15 UTC – March 25, 00 UTC. The time information is given in color shades with green colors for the period before regime onset, red colors for the active regime life cycle (onset – decay), and blue for the period after regime decay. Jumps in the PVA^-_{EuBL} track are linked to abrupt changes in the center of mass and occur due to splitting and merging events. Grey shading shows the mean frequency of the PVA^-_{EuBL} (in %) during the time of the track. The black dotted contour highlights the regime mask of EuBL (cf. Fig. 5.6). (b) Scatter plot that indicates the association between the PVA^-_{EuBL} amplitude effect of a splitting (triangle) or a merging (dot) event (in 10^{12} PVU m^2) and the area proportion of the splitting/merging PVA^- and the PVA^-_{EuBL} (in %). The markers represent splitting (triangle) and merging (dot) events. The color of the marker reveals the time of the event. Particular events discussed in the text are labeled with capital letters and numbers. Reprinted from Hauser et al. (2023b).

hours later, the northern part splits off again (green triangle, labeled with 'A') and propagates towards the northeast (Fig. 6.6b, green cross/dot), which leads to the southward jump in the PVA^-_{EuBL} track. Three major splitting events occur in the first half of the active regime life cycle (12–13 March) that lead to jumps in the center of mass position towards the south (Fig. 6.5a, event B). Two of the three split up PVAs^- from the PVA^-_{EuBL} move towards the northeast (Fig. 6.6b, crosses/dots over Russia), whereas the remaining PVA^- separates to the south of the PVA^-_{EuBL} and stays in this area. A merging event on 16 March is associated with the sudden eastward jump of the track outside the regime mask, where the PVA^-_{EuBL} briefly merges with a filament of low PV air over Asia that splits up again but remains over the Asian continent (Fig. 6.5b, event D; Fig. 6.6b, dark red cross/dot over Asia). Towards the end of the regime life cycle, two splitting events occur that lead to substantial relative changes in the PVA^-_{EuBL} area (Fig. 6.5b, events C1 and C2). A last example is the major merging event on 19 March, where a PVA^-, that exhibits a size over 60 % of the area of PVA^-_{EuBL}, merges into the existing anomaly (Fig. 6.5b, light blue dot labeled with 'E'). This merging PVA^- originates from the western North Atlantic and merges into the PVA^-_{EuBL} from the west (Fig. 6.6a, light blue cross over North Atlantic).

Following the origin and destination of merging and splitting PVAs^-, merging PVAs^- anomalies tend to reach the PVA^-_{EuBL} from the southwest, while splitting PVAs^- preferentially migrate to the northeast after they split up from the PVA^-_{EuBL}. Figure 6.6 shows the occurrence frequency of splitting and merging

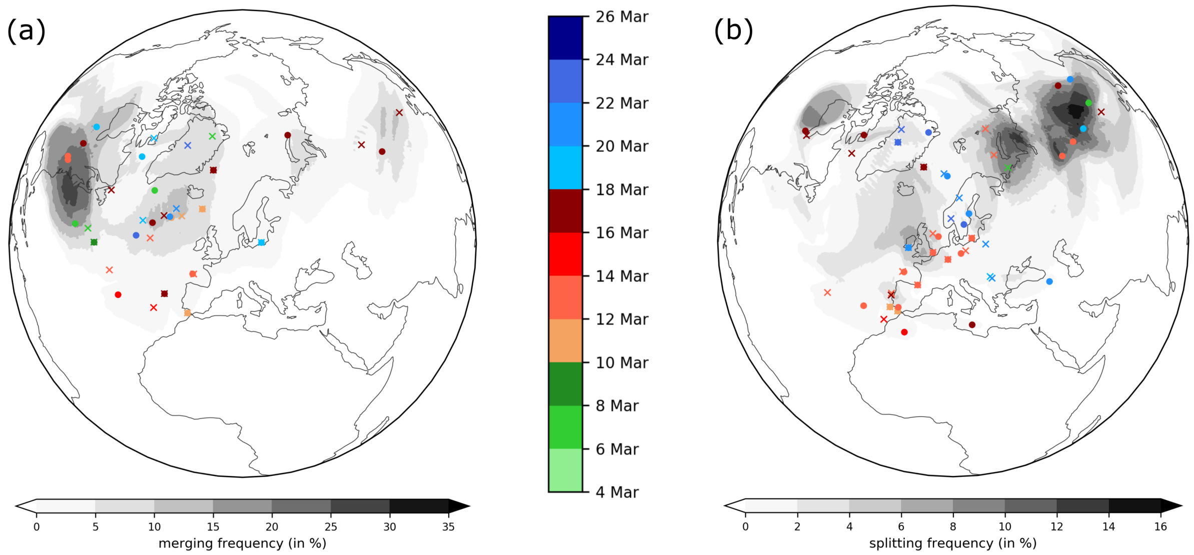

Figure 6.6: Occurrence frequency (in %) of PVAs$^-$ that merge into (a) or separate from (b) the PVA$^-_{EuBL}$. All splitting and merging events are considered that take place during the life cycle of the PVA$^-_{EuBL}$. For the calculation per event, the PVA^- is traced back three days in case of merging or from the splitting event to three days later if possible. Crosses show the position (based on the center of mass) of the PVA^- before they merge into the PVA$^-_{EuBL}$ (panel a) or at the time of splitting from the PVA^-_{EuBL} (panel b). Points mark the position of the PVAs$^-$ at most three days before the merging event or at most three days after the splitting event. In case of a shorter lifetime of the PVA^-, the last possible (splitting) or first possible (merging) position is shown. The color indicates the time in the life cycle at which the respective event occurs. Reprinted from Hauser et al. (2023b).

PVAs$^-$ and marks each particular event individually. Two maxima in the merging frequency are found, with a more pronounced maximum near the US East Coast and another one in high latitudes over the central North Atlantic (Fig. 6.6a). The variety of center of mass positions of merging PVAs$^-$ before the actual event emphasize the origin of merging PVAs$^-$ from upstream. The track of PVAs$^-$ that split up from the PVA$^-_{EuBL}$ exhibits higher variability (Fig. 6.6b). Around the decay of the EuBL regime life cycle, the majority of splitting PVAs$^-$ are linked to a split up of the PVA$^-_{EuBL}$ on the northern flank that is linked to a northward propagation of the PVAs$^-$. However, earlier within the regime life cycle, some splitting events lead to a more southeastward propagation, suggesting that parts of the PVA$^-_{EuBL}$ split up to the south. Overall, splitting and merging events can have a substantial impact on the center of mass position of the PVA$^-_{EuBL}$, which influences the course of the track. However, for the first time, the occurrence of these events can be quantified such that sudden jumps can be checked for splitting and merging, and linked to these events.

The evolution of the PVA$^-_{EuBL}$ life cycle shares strong similarities with the evolution of the EuBL regime life cycle, in particular the nearly simultaneous occurrence of the maximum I$_{WR}$ and the maximum amplitude of the PVA$^-_{EuBL}$ around 14 March (Fig. 6.2, Fig. 6.7). More generally, the life cycle of the PVA$^-_{EuBL}$ can be split up into three phases, independent of the EuBL regime life cycle: (i) the buildup and initial amplification of the PVA$^-_{EuBL}$, (ii) the stagnation in development, and (iii) the weakening and dissipation

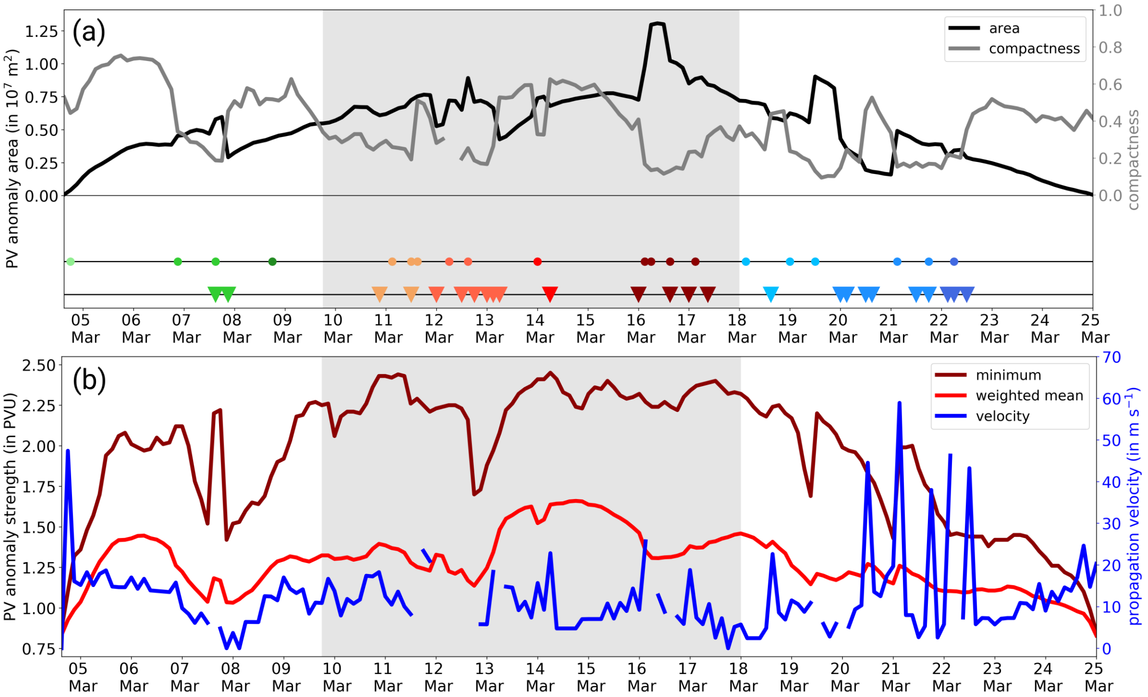

Figure 6.7: Temporal evolution of PVA^{-}_{EuBL} characteristics for the lifetime of the PVA^{-}_{EuBL}. (a) area (black, in 10^7 m^2, left y-axis) and compactness factor $C_{IPQ} = 4\pi\mathscr{A}/P^2$ with the area $\mathscr{A}$ and the perimeter P (gray, defined between 0 and 1, right y-axis). Colored symbols along the two horizontal lines in the lower half of the panel mark the occurrence of splitting (triangles) and merging (dots) events. The color of the markers points to the timing of these events (cf. colorbar in Fig. 6.5). (b) minimum value within PVA^{-}_{EuBL} (dark red, in PVU, left y-axis), weighted mean value within PVA^{-}_{EuBL} (light red, in PVU, left y-axis), and propagation velocity (blue, in m s^{-1}, right y-axis). Note that non-physical values that occur for the compactness factor and the propagation velocity were removed. Adapted from Hauser et al. (2023b).

of the PVA^{-}_{EuBL}. The first phase describes the initial growth of the PVA^{-}_{EuBL} area and amplitude from the first identification on March 4 until 12 March, when multiple splitting and merging events take place (Fig. 6.7a,b). This phase is characterized by a rapid amplification of the PVA^{-}_{EuBL} strength and a fast propagation towards Europe (cf. Fig 6.5a). The second phase from March 12 – 16 describes a period of time with a near constant PVA^{-}_{EuBL} area (Fig. 6.7a,b). Few sudden jumps in the temporal evolution of characteristic variables indicate the high frequency of splitting and merging during this period. Additionally, splitting and merging events are more pronounced in the temporal evolution of the PVA^{-}_{EuBL} minimum instead of the mean PVA^{-}_{EuBL} value. This indicates whether a splitting or merging event has a marked effect on the anomaly and exceeds or falls below the previous minimum. The propagation velocity exhibits small values, linked to the quasi-stationarity behavior of the PVA^{-}_{EuBL} during the active EuBL regime life cycle. The third and last phase runs from March 16 to the end of the PVA^{-}_{EuBL} life cycle on March 25. During this period, the area and the amplitude of the PVA^{-}_{EuBL} is decreasing (Fig. 6.7a,b). Shortly before the dissipation of the anomaly, the propagation velocity increases, again, suggesting a final acceleration of the PVA^{-}_{EuBL}.

An objective description of the compactness of a PVA^- is achieved with the compactness measure of Osserman (1978) who defines the compactness as $\mathrm{C}_{IPQ} = 4\pi\mathscr{A}/\mathrm{P}^2$ with the area $\mathscr{A}$ and the perimeter P. The compactness measure is defined between 0 and 1 in which values closer to 1 present a more compact shape of the PVA^-. Applied to the PVA^-_{EuBL}, the compactness factor reveals that splitting events often lead to a gain of compactness, whereas merging events lead to a loss of compactness. For the first phase of the PVA^-_{EuBL} life cycle, the compactness factor is rather high, pointing to a compact shape of the PVA^-_{EuBL} (Fig. 6.7a). However, in the second phase from March 12–16, the compactness factor exhibits multiple jumps because of splitting and merging events, and shows less compactness compared to the first phase. In the third phase of the PVA^-_{EuBL} lifetime, the low compactness factor, paired with the multiple occurrence of splitting and merging, suggests a strong deformation of the PVA^-_{EuBL} that leads to the weakening of the anomaly.

In summary, the EuBL regime life cycle in March 2016 was linked to a single PVA^- (PVA^-_{EuBL}) that originated from the US East Coast, amplified on the way towards Europe, and experienced multiple splitting and merging events along the track. Within the active EuBL regime life cycle, the PVA^-_{EuBL} became stationary and amplified even more. Towards the end of the regime life cycle and the PVA^-_{EuBL} life cycle, the PVA^-_{EuBL} started to degrade in amplitude and area, heavily deformed, and finally dissipated over western Russia.

6.2.2 Detailed view on the amplitude evolution of the PVA^-

Amplitude evolution

To quantify the processes that govern the amplitude evolution of the PVA^-_{EuBL}, Equation 5.4 is evaluated on isentropic levels (mean of the 315–325 K isentropic layer). Note that the version of the integrated amplitude evolution is selected that performs no division of the change of the PV background (cf. Sect. 5.5). A comparison between the observed amplitude change based on the VAPV' (150–500 hPa) and the mean isentropic-layer PV anomaly (315–325 K) reveals a very good quantitative agreement (Fig. 6.8a). This justifies the integration of the PV tendencies over the PVA^-_{EuBL} area originally defined on the VAPV' field. The overall higher mean values for the isentropic-based amplitude results from the fact that the isentropic layer is thinner and selected in such a way that it captures the maximum manifestation of the negative PV anomaly signal. The selection of the thinner isentropic layer changes with season, such that it can be kept thin in comparison to the year-round valid and fixed pressure-based layer. Deviations in the course of the amplitude can be predominantly attributed to the extent of the PVA^-_{EuBL} north of 80 °N (marked red line in Fig. 6.8a) where no isentropic data from the piecewise PV inversion are available (cf. Sect. 4.3).

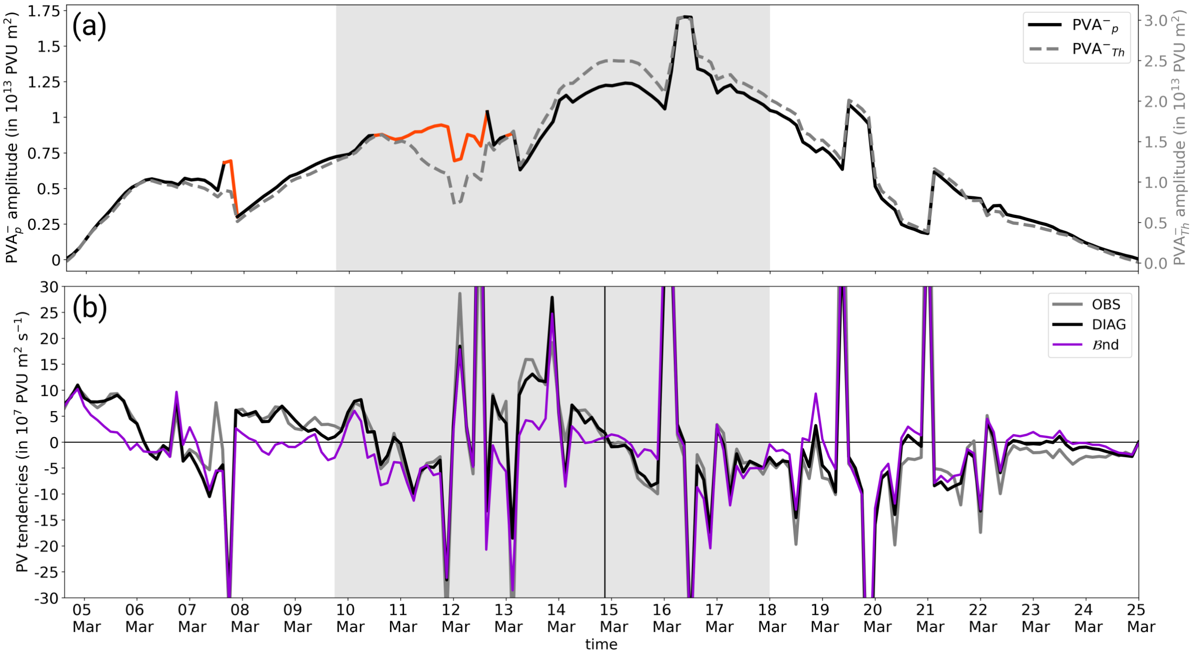

Figure 6.8: (a) Comparison of the PVA^{-}_{EuBL} amplitude evolution based on a pressure-layer mean (500 – 150 hPa, black lines) and an isentropic layer mean (315 – 325 K, gray dashed line) in PVU m^2. The sequences highlighted in orange mark times when the PVA^{-}_{EuBL} extends north of 80 °N and thus outside the domain used for the PV tendency diagnostic. (b) Comparison of the observed (OBS, gray) and diagnosed (DIAG, black) amplitude change for the PVA^{-}_{EuBL}. The boundary term $\mathscr{B}$nd is shown in dark violet. The gray shading points to the active EuBL regime life cycle. The vertical black line in (b) indicates where the active EuBL life cycle is divided into two for the investigation of the net effect of the tendency terms in Figure 6.9. Note that the amplitude is shown in absolute values and that the signs of the amplitude change were reversed such that positive values point to a strengthening of the PVA^{-}_{EuBL} amplitude. Adapted from Hauser et al. (2023b).

Figure 6.8b shows the observed change in PVA^{-}_{EuBL} amplitude and the diagnosed change in PVA^{-}_{EuBL} amplitude as the sum of all processes in Equation 5.4 integrated over the PVA^{-}_{EuBL}. The diagnosed PV tendency follows the observed PV tendency to a very high degree, which indicates that the integrated amplitude budget in Equation 5.4 is reasonably closed. The boundary term $\mathscr{B}$nd, which describes the contributions to the amplitude evolution via the change in PVA^{-}_{EuBL} area, sometimes dominates the overall change in the PVA^{-}_{EuBL} amplitude, in particular when the observed PVA^{-}_{EuBL} amplitude change reveals prominent spikes during the lifetime of the PVA^{-}_{EuBL}. The large values in $\mathscr{B}$nd arise because of abrupt changes in the PVA^{-}_{EuBL} area, which are linked to the splitting and merging events as discussed above. Occasionally, the diagnosed PV tendency does not reproduce the observed evolution sufficiently well. Some of these episodes are due to the restriction of the PV tendency diagnostics to south of 80 °N (March 7–8, March 12–14, cf. Fig. 6.8a). Other episodes with inconsistencies between the diagnosed and observed amplitude change exhibit a quick succession of splitting and merging events. Overall, however, the accuracy of the PV tendency budget evaluation appears sufficient.

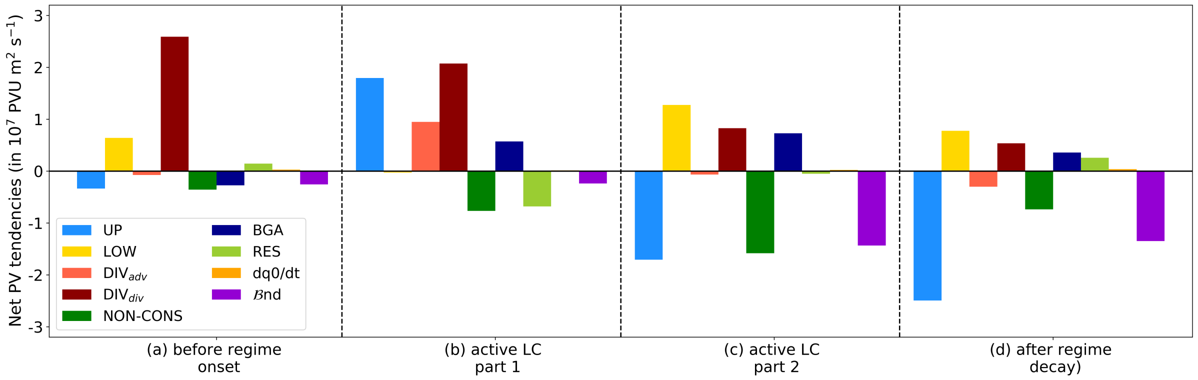

Figure 6.9: Net effect of PV tendencies on the amplitude evolution of the PVA$_{EuBL}^{-}$ for different periods within the PVA$_{EuBL}^{-}$ lifetime. All contributing PV tendency terms from Equation 5.4 are summed up over four different periods (from left to right): (a) before EuBL onset (March 4, 15 UTC – March 9, 15 UTC), (b) active EuBL life cycle part I (March 9, 18 UTC – March 14, 21 UTC), (c) active EuBL life cycle part II (March 15, 00 UTC – March 18, 00 UTC), and (d) after EuBL decay (March 18, 03 UTC – March 25, 00 UTC). To account for different lengths of the periods, the sums are divided by the number of time steps in the period. Adapted from Hauser et al. (2023b).

Contributions of dry and moist processes in the amplitude evolution

The temporal evolution of all area-integrated PV tendencies (except from $\mathscr{B}$nd) contributing to the overall change in the PVA$_{EuBL}^{-}$ amplitude is displayed in Figure 6.10. The full timeline is divided into four different phases to investigate (i) the buildup/amplification of the PVA$_{EuBL}^{-}$ before the EuBL onset, (ii) the further amplification within the regime life cycle, (iii) the starting decay process within the regime life cycle, and (iv) the weakening and dissipation of the PVA$_{EuBL}^{-}$ separately. Figure 6.11 displays spatial maps for selected time steps when a certain PV tendency term exhibits a clear maximum. The net effect of all contributing PV tendency terms on the PVA$_{EuBL}^{-}$ amplitude evolution for the four phases is illustrated in Fig. 6.9.

A net amplification of the PVA$_{EuBL}^{-}$ is evident during the first phase of the PVA$_{EuBL}^{-}$'s life cycle before the EuBL onset from March 4 – 9 (Fig. 6.9a). This amplification is largely dominated by the PV tendency term that describes the divergence with the divergent wind field ($q'(\nabla \cdot \mathbf{v}'_{div})$; DIV$_{div}$) and also dominates the net amplifying effect for this phase. In contrast, the PV tendency that describes the advection of background PV with the divergent wind field ($-\mathbf{v}'_{div} \cdot \nabla q_0$; DIV$_{adv}$) contributes nearly negligible to the amplitude evolution and only has a slight weakening effect on the amplitude evolution before the EuBL onset. Two distinct episodes of intensification due to DIV$_{div}$ occur on March 4–6 and March 7–9 (Fig. 6.10a). Figure 6.11a shows the sum of both, DIV$_{div}$ and DIV$_{adv}$, and reveals that the dominant strengthening tendency acts along the western edge of the PVA$_{EuBL}^{-}$ for the first intensification phase on March 5. As further discussed in Section 6.3, both episodes are associated with prominent WCB activity, providing some evidence that the pronounced amplification due to DIV$_{div}$ is, in this case, coupled to latent heat release. Thus, it can be considered an indirect diabatic impact. Both intensifi-

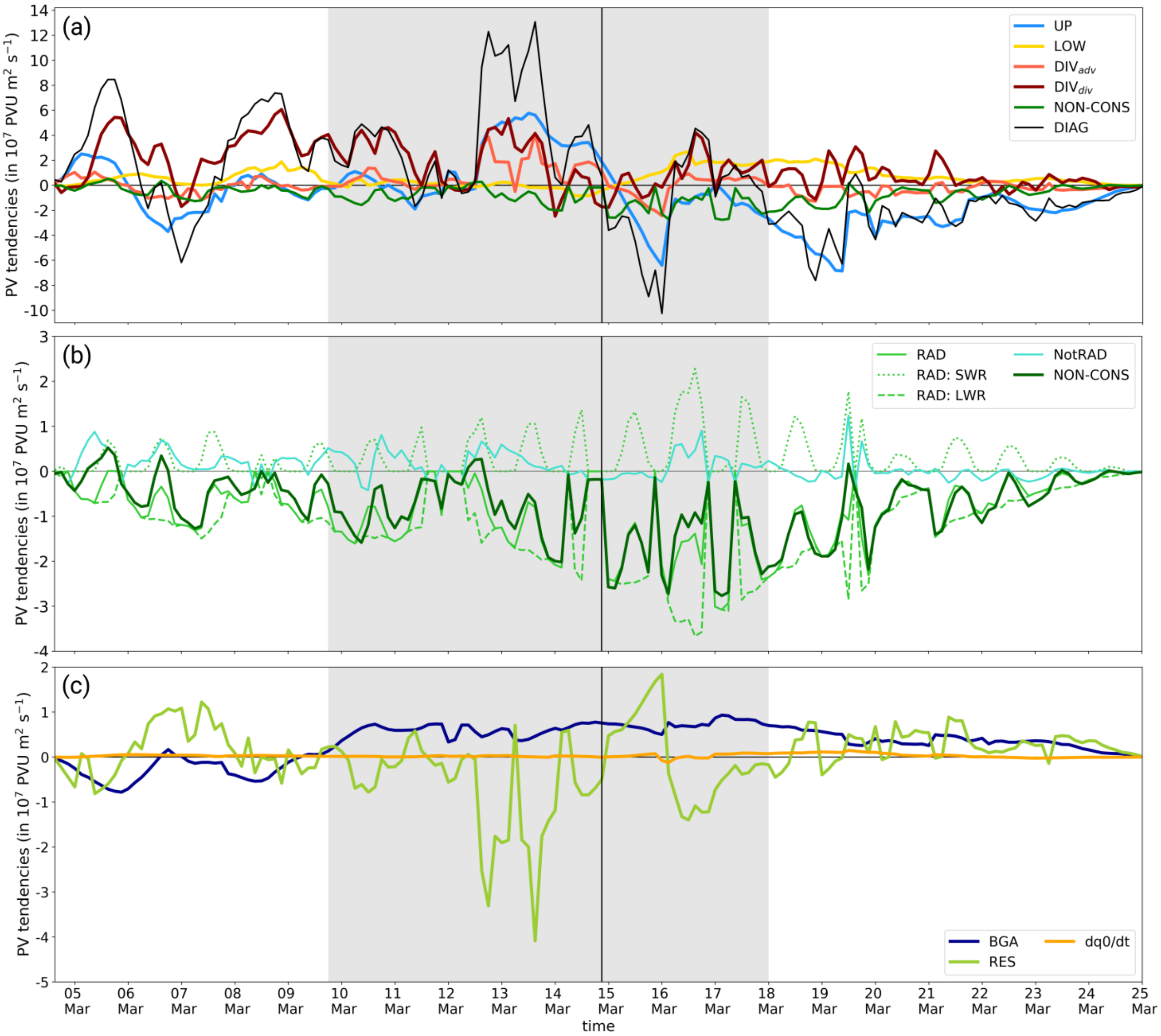

Figure 6.10: Process contributions to the amplitude evolution of the PVA$^-_{EuBL}$ associated with the EuBL regimes life cycle in March 2016. (a) UP ($-\mathbf{v}'_{up}\cdot\nabla q_0$), LOW ($-\mathbf{v}'_{low}\cdot\nabla q_0$), DIV$_{adv}$ ($-\mathbf{v}'_{div}\cdot\nabla q_0$), DIV$_{div}$ ($q'(\nabla\cdot\mathbf{v}'_{div})$), NON-CONS (cf. Eq. 2.5), and DIAG = UP + LOW + DIV$_{adv}$ + DIV$_{div}$ + NON-CONS. (b) Division of NON-CONS into its various components: non-radiative part (NotRAD) and radiative part (RAD). The radiative term is further partitioned into the non-conservative PV tendency by shortwave radiation (RAD: SWR) and by longwave radiation (RAD: LWR). (c) BGA ($-\mathbf{v}_0\cdot\nabla q_0$), RES ($-\mathbf{v}'_{res}\cdot\nabla q_0$), and $\partial q_0/\partial t$. The sign convention here is that positive tendencies signify a strengthening of PVA$^-_{EuBL}$ amplitude. The period of the active EuBL life cycle is shown in all panels in gray shading, and the vertical black line in (a) and (b) marks the date used to split up the EuBL life cycle in two episodes for the analysis presented in Figure 6.9. Note the different y-axis ranges between (a), (b) and (c). Adapted from Hauser et al. (2023b).

cation episodes (March 4–6 and March 7–9) exhibit local maxima in the baroclinic PV tendencies that describe the advection of background PV with the wind fields associated with lower-tropospheric PV anomalies ($-\mathbf{v}'_{low} \cdot \nabla q_0$; LOW). In particular, LOW contributes to the strengthening of the amplitude around 9 March, likely due to the warm anomaly near the surface that co-occurs with the PVA$^-_{EuBL}$ in the upper troposphere (Fig. 6.11b). The co-occurrence of LOW and DIV$_{div}$ with positive contributions to the amplification of the PVA$^-_{EuBL}$ indicates moist-baroclinic coupling (e.g., Teubler and Riemer, 2021). Quasi-barotropic PV tendencies, which describe the advection of background PV with the wind field associated with upper-tropospheric PV anomalies ($-\mathbf{v}'_{up} \cdot \nabla q_0$; UP), govern the very early amplification of the PVA$^-_{EuBL}$ (Fig. 6.10a). This suggests that the trough sitting over the US East Coast makes an important contribution to the formation of the incipient PVA$^-_{EuBL}$ through northward advection of low PV air into the downstream region. The net impact of UP during the first phase is small and negative (Fig. 6.9a), likely due to the period of negative UP around March 7 (Fig. 6.10a). The net impact of $\mathscr{B}$nd during the first phase is slightly negative (Fig. 6.9a). Although the PVA$^-_{EuBL}$ area is growing and experiences various merging events from its first detection until the EuBL onset, the aforementioned splitting event on March 7 (Fig. 6.5b, green triangle) seems to dominate the net effect (Fig. 6.9a). The contribution of the PV tendency term that describes the advection of background PV by the background wind field ($-\mathbf{v}_0 \cdot \nabla q_0$; BGA) is very small as well as the advection of background PV with the residual wind field ($-\mathbf{v}'_{res} \cdot \nabla q_0$; RES) and the PV tendency term that describes the local change in background PV ($\partial q_0 / \partial t$).

The second phase of the PVA$^-_{EuBL}$ life cycle extends from March 9 18 UTC – March 14 21 UTC and comprises the first part of the active EuBL regime life cycle, which is associated with a further amplification of the PVA$^-_{EuBL}$ amplitude (Fig. 6.8b). Furthermore, the choice of March 14 21 UTC delineates two periods with several splitting and merging events within the active EuBL regime life cycle. The further continued amplification of the PVA$^-_{EuBL}$ during this phase is dominated by DIV$_{div}$, DIV$_{adv}$ and UP (Fig. 6.9b). Especially for the first amplification episode around March 10 – 11, DIV$_{div}$ dominates the amplitude growth (Fig. 6.10a). For the second amplification around March 13 – 15, DIV$_{div}$, and in particular UP, show the highest contributions. The high contribution of UP can be linked to a trough upstream that reaches far to the south, and thereby low PV air from the south gets advected towards the north on the western flank of the PVA$^-_{EuBL}$ (Fig. 6.11c). The net effect of DIV$_{div}$, DIV$_{adv}$ and UP is positive in the first phase of the active regime life cycle, with the strongest net effect in DIV$_{div}$ (Fig. 6.9b). This points to the importance of moist processes. LOW has a negligible impact in this phase, with no net effect at all. The net effect of $\mathscr{B}$nd is again negative and rather small, as for the first phase prior to onset. A variety of splitting and merging events take place (Fig. 6.5b) that lead to huge values of $\mathscr{B}$nd that describes the PVA$^-_{EuBL}$ area change by the movement of the boundary. The major splitting event on March 13 (Fig. 6.5b, the orange triangle in the upper left of the figure) is most likely responsible for the net weakening effect of $\mathscr{B}$nd. BGA contributes positively to the amplification throughout the time, which leads to an overall positive and non-negligible net effect (Fig. 6.9b). Note that the rather high

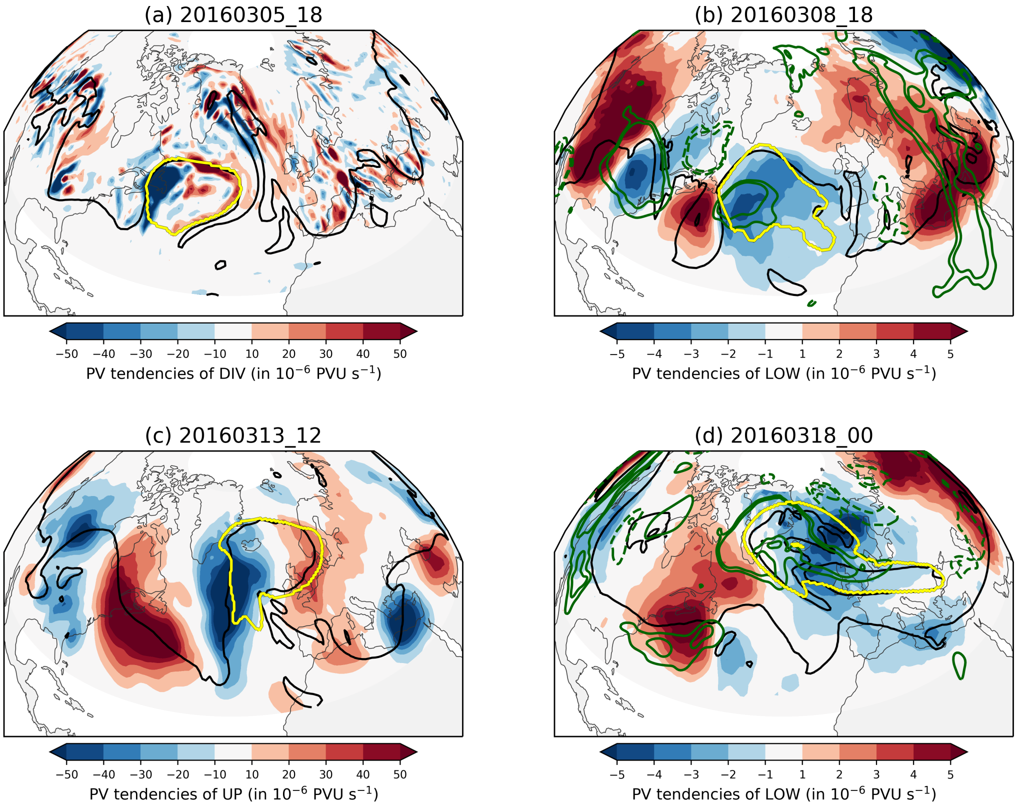

Figure 6.11: PV tendency maps for selected time steps and selected variables during the lifetime of the PVA^{-}_{EuBL}: (a) 5 March 2016 18 UTC, (b) 8 March 2016 18 UTC, (c) 13 March 2016 12 UTC, and (d) 18 March 2016 00 UTC. PV tendencies of DIV (as $\mathrm{DIV}_{div} + \mathrm{DIV}_{adv}$), LOW and UP are displayed in shading. The yellow contour marks the PVA^{-}_{EuBL} for the respective time. The thick black contour is the 2-PVU line from an isentropic mean layer (315-325 K). The green contours in (b) and (d) point to temperature anomalies at 850 hPa based on a 30-day running mean climatology (1979-2019) for +/- 6 and 8 K (positive: solid, negative: dashed). Temperature anomalies are smoothed by a Gaussian filter with $\sigma = 2$.

signal of *RES* might be attributed to the fact that the PVA^{-}_{EuBL} area extends north of the PV inversion region where boundary effects of the piecewise PV inversion arise (Fig. 6.9b, Fig. 6.10c).

The third phase of the PVA^{-}_{EuBL} life cycles comprises the second part of the active blocked regime life cycle from March 15 – 18, which describes the beginning reduction of the PVA^{-}_{EuBL} amplitude and heralds the eventual decay. Thereby, UP is the leading process in the weakening of the amplitude (Fig. 6.9c). This contrasts the first part of the active life cycle, in which UP makes a major contribution to the strengthening of the PVA^{-}_{EuBL}. LOW, which was negligible during the first part of the active life cycle, becomes persistently positive after UP becomes negative on March 15, and thus constitutes the main contribution to counteracting the weakening of the PVA^{-}_{EuBL} in the second part of the regime life cycle (Fig. 6.10a). The positive contribution of LOW leading to the amplification of PVA^{-}_{EuBL} indicates incipient downstream moist-baroclinic development. DIV_{adv} shows only small contributions and a negligible net effect (Fig. 6.9c). The amplitude strengthens again around 16 – 17 March due to the positive contributions of especially DIV$_{div}$, which results in a positive net contribution of DIV$_{div}$. However, the net effect of DIV$_{div}$ is smaller compared to the first phase of the regime life cycle. BGA has a negligible but consistently positive effect on the PVA$^{-}_{EuBL}$ amplitude (Fig. 6.9c, Fig. 6.10c), resulting in an overall positive net effect to the strengthening of the PVA$^{-}_{EuBL}$ amplitude. In contrast to the two phases before, $\mathscr{B}$nd has a very strong negative net effect in the second part of the active regime life cycle (Fig. 6.9c). Generally, strong deformation of the PVA$^{-}_{EuBL}$ occurs during this phase (cf. Fig.6.7a) that is accompanied by several splitting and merging events. These contribute to sudden noticeable changes in amplitude but also to substantial relative changes in the area of the PVA$^{-}_{EuBL}$ (cf. Fig. 6.5b).

The fourth phase of the PVA$^{-}_{EuBL}$ life cycle includes the final decay phase of the PVA$^{-}_{EuBL}$ from March 18 – 25, with a strong weakening of the amplitude that is led by UP and $\mathscr{B}$nd (Fig. 6.9d). Most PV tendencies exhibit similar characteristics as during the second part of the active regime life cycle. The dominant contribution of UP to the weakening of the amplitude is likely linked to the beginning deformation of the PVA$^{-}_{EuBL}$ after the regime decay. Shortly after decay, DIV$_{div}$ and LOW make positive contributions to the maintenance of the PVA$^{-}_{EuBL}$ (Fig. 6.10a). LOW exhibits its highest positive contributions around March 18 that are likely connected to the positive temperature anomaly beneath the anomaly near the surface (Fig. 6.11c). However, the contributions of LOW and DIV$_{div}$ decay strongly in the last days before the end of the PVA$^{-}_{EuBL}$ life cycle (Fig. 6.10a, Fig. 6.9d). $\mathscr{B}$nd again exhibits a strong negative net effect after regime decay, pointing to a degrading contribution as the PVA$^{-}_{EuBL}$ decreases in size towards the end of the PVA$^{-}_{EuBL}$ life cycle (cf. Fig.6.7a). Several splitting and merging events take place, with the number of splitting events predominating (Fig. 6.5b).

Direct diabatic impact on amplitude evolution

The direct diabatic PV tendency (NON-CONS) describes the direct impact of non-conservative processes that is predominately negative and smaller than the impact of the advective PV tendencies throughout the PVA$^{-}_{EuBL}$ life cycle (Fig. 6.10a,b). Longwave radiation dominates this direct diabatic weakening of the PVA$^{-}_{EuBL}$ (Fig. 6.10b), as expected from idealized considerations (Zierl and Wirth, 1997). This is consistent with Teubler and Riemer (2021), who found that longwave radiative cooling weakens ridges within RWPs. Teubler and Riemer (2021) provided a rough estimate that one-third of the longwave radiative tendencies may be associated with cloud-radiative effects, whereas the majority of the signal was interpreted as a large-scale 'background' signal. In addition, these authors demonstrated that the longwave radiative tendency roughly scales with the amplitude of PV anomalies, which is consistent with the observed minimum of the tendencies at the peak time of PVA$^{-}_{EuBL}$ during the second part of the active EuBL regime life cycle. Shortwave radiation counteracts the weakening and exhibits a distinct diurnal cycle. In contrast, the non-radiative diabatic tendencies are mostly positive. The dominant amplifying diabatic tendencies within ridges are due to latent heat release (e.g., Chagnon et al., 2013; Teubler and

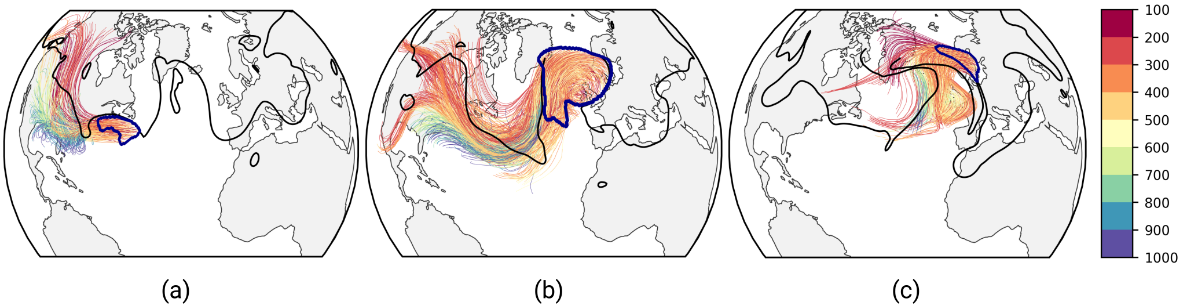

(a) (b) (c)

Figure 6.12: Three-day backward trajectories (colored lines) started within the PVA^-_{EuBL} for three different times: (a) 4 March 21 UTC (shortly after first identification), (b) 13 March 15 UTC (within the EuBL regime life cycle, and (c) 24 March 06 UTC (shortly before the PVA^-_{EuBL} vanished). Colors along the trajectories show the pressure (in hPa). The black line illustrates the 2 PVU contour at the isentropic level of 320 K. The dark blue contour marks the PVA^-_{EuBL}. Note that in (a) and (c) every tenth trajectory is shown, whereas every 50 trajectory is shown in (b) due to the large amount of trajectories.

Riemer, 2021), suggesting that latent heat release has a small positive direct impact on the onset of the EuBL regime life cycle in March 2016. However, the overall net impact of all direct diabatic tendencies on the amplitude evolution is negative and smaller than the net impact of the advective tendencies (Fig. 6.9).

Summary

In summary, the EuBL regime life cycle in March 2016 was associated with a single PVA^- (PVA^-_{EuBL}) that was first identified off the US East Coast five days before regime onset. Moving towards Northern Europe, the PVA^-_{EuBL} underwent several splitting and merging events. DIV_{div} dominates all amplification episodes of the PVA^-_{EuBL} with a further substantial contribution by UP within the active regime life cycle. Shortly before regime decay, UP becomes more important and dominates the weakening of the PVA^-_{EuBL}. This is counteracted by LOW, which becomes most relevant during the second half of the life cycle. The dominant role of DIV_{div} in the amplification of the PVA^-_{EuBL} before the EuBL onset quantitatively supports the findings by Magnusson (2017) and Grams et al. (2018), who argued more qualitatively, that divergent WCB outflow was crucial for the onset of the block.

6.3 Lagrangian perspective

As seen from the quasi-Lagrangian perspective, PV tendencies associated with the divergent wind field make major contributions to the amplification of the PVA^-_{EuBL} before the onset and within the EuBL regime life cycle. This highlights the importance of moist processes during the onset and maintenance of the blocked regime pattern. This section investigates the role of moist processes from a purely Lagrangian perspective. Three-day backward trajectories are started within the PVA^-_{EuBL} from the quasi-Lagrangian framework, similar to the method of Pfahl et al. (2015). For the set of three-days backward trajectories, diabatically 'heated trajectories' are defined as trajectories that experience a heating of $\Delta\theta > 2\,\mathrm{K}$ along their way to the PVA^{-}_{EuBL}. WCB outflow at each time step is identified based on two-day backward trajectories fulfilling the criterion that the air parcels ascend at least 600 hPa within that time. Fig. 6.13 compares DIV (as sum of DIV_{div} and DIV_{adv}) from the quasi-Lagrangian perspective integrated over the PVA^{-}_{EuBL} area (red) with the fraction of heated trajectories (black) and the fraction of WCB outflow (shading).

Some link exists between amplitude-enhancing DIV tendencies and the occurrence of moist-synoptic activity for the lifetime of the PVA^{-}_{EuBL}. Most peaks of strengthening DIV tendencies co-occur with increased WCB activity within the PVA^{-}_{EuBL} area and a high share of heated trajectories that end up in the PVA^{-}_{EuBL} (Fig. 6.13a). All three quantities are positively correlated over the lifetime of the PVA^{-}_{EuBL}, with a Pearson correlation coefficient of 0.44 between DIV and the fraction of heated trajectories, 0.57 between DIV and the fraction of WCB outflow, and 0.73 between the fraction of heated trajectories and the fraction of WCB outflow. These positive correlations support the common expectation that the modification of the tropopause by upper-tropospheric divergent flow is enhanced by latent heat release in WCBs and represent a direct co-occurrence of WCBs and reinforcing DIV within the PVA^{-}_{EuBL}. A link between DIV and WCBs is further supported by the fact that the prominent peaks of DIV ($> 3 \cdot 10^{7}$ PVU m^{2} s^{-1}, gray horizontal line in Fig. 6.13a) occur simultaneously with a WCB outflow fraction of at least 20 %. For the presented case, it can thus be demonstrated with a high degree of certainty that DIV is indeed an indirect moist impact and that the WCB outflow dynamically modifies the tropopause. In some periods within the PVA^{-}_{EuBL} life cycle (e.g., March 21–23), a high fraction of heated trajectories is present, but DIV is relatively low or even contributes to amplitude weakening (Fig. 6.13a). One explanation is that the timing, and, in particular, the exact location where diabatic heating occurs along the three-day trajectory is essential, as this ultimately shapes the effect on the PV distribution within the PVA^{-}_{EuBL}. Thus, if the trajectory experiences the ascent and thus the period of maximum heating early enough to reach the upper troposphere outside the PVA^{-}_{EuBL} and migrates nearly horizontally into the anomaly, the effect on the amplitude amplification is much smaller than if the trajectory experiences its ascent directly in the immediate vicinity of the PVA^{-}_{EuBL}.

Figure 6.12 shows the evolution of the air parcel position and pressure along three-day backward trajectories started within the PVA^{-}_{EuBL} in the mid to upper troposphere for different time steps. In accordance with the values in Figure 6.13, a higher share of air parcels ascend in the initial development and maintenance of the PVA^{-}_{EuBL} as during the last hours before the PVA^{-}_{EuBL} vanishes. Shortly after the initial development of the PVA^{-}_{EuBL}, approximately half of the trajectories that end up in the PVA^{-}_{EuBL} are located in the lower troposphere over the southern United States that ascend within the two days into the upper-tropospheric PVA^{-}_{EuBL} (Fig. 6.12a). The remaining trajectories are already located in the upper troposphere, suggesting that air parcels are isentropically advected into the PVA^{-}_{EuBL}. A similar distribution

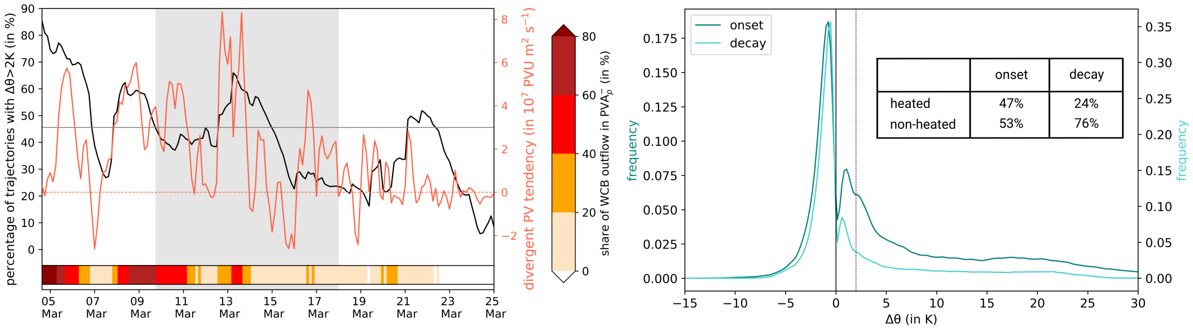

	onset	decay
heated	47%	24%
non-heated	53%	76%

(a)

(b)

Figure 6.13: Results of the Lagrangian perspective on the PV dynamics of the EuBL regime life cycle in March 2016. (a) Evolution of DIV = DIV_{adv} + DIV_{div} (red line), the fraction of heated ($\Delta\theta > 2$ K) three-day backward trajectories starting in PVA^-_{EuBL} (black), and the fraction of WCB outflow within the in PVA^-_{EuBL} area (red shading, horizontal bar). Note that the divergent PV tendencies are integrated within the PVA^-_{EuBL} area for grid points with PV anomaly < 0 PVU on the respective isentropic surfaces while WCB outflow and the backward trajectories are included for all grid points within the PVA^-_{EuBL} area and latitudes < 80 °N and > 25 °N. The gray shaded area denotes the time of the active EuBL regime life cycle. See the text for the explanation of the thin gray horizontal line. (b) Frequency distribution of maximum heating and cooling rates along three-day backward trajectories starting in PVA^-_{EuBL} +/- one day around the onset (dark turquoise) and decay (light turquoise) of the EuBL. The vertical line (black, dashed) corresponds to the 2 K value. The table provides information on the proportion of heated ($\Delta\theta > 2$ K) and non-heated ($\Delta\theta < 2$ K) trajectories. Reprinted from Hauser et al. (2023b).

of trajectories is valid for the air parcels that end up in the PVA^-_{EuBL} within the active EuBL life cycle when DIV_{div} exhibits a peak contribution to the strengthening of the PVA^-_{EuBL} amplitude (Fig. 6.12b). Some air parcels are located in the lower troposphere in the vicinity of the eastern North Atlantic and ascend along the eastern flank of the trough over the central North Atlantic. However, many air parcels are already in the upper-troposphere three days before and reach the PVA^-_{EuBL} by isentropic advection along the wave guide. Shortly before the PVA^-_{EuBL} vanishes, the share of air parcels that are located in the lower troposphere and ascend in the following two days is low, which suggests a lack of moist processes (Fig. 6.12c). This is consistent with the even diagnosed negative contributions from DIV that point to an overall dominating upper-level convergence within the PVA^-_{EuBL}.

The evolution of the pressure along the three-day backward trajectories in Figure 6.12 give a glimpse on different heating and cooling rates for individual time steps. The maximum heating and cooling rates along the three-day backward trajectories started from the PVA^-_{EuBL} are investigated in Figure 6.13b for onset (+/- one day) and decay (+/- one day) separately. As in Steinfeld and Pfahl (2019), a broad heating regime exists that is associated with values as high as $\Delta\theta > 20$ K and a narrow non-heated regime with values as low as $\Delta\theta <$ -5 K. Most three-day backward trajectories (53 % around the onset and 76 % around the decay) experience diabatic cooling before they arrive in the PVA^-_{EuBL}, most likely due to longwave radiative cooling. Figure 6.14 shows the spatial origin of trajectories that end up three days later in the PVA^-_{EuBL} and reveals that a high fraction of the diabatically-cooled parcels are located upstream of the PVA^-_{EuBL} in the mid or upper troposphere and likely reach the PVA^-_{EuBL} by adiabatic advection

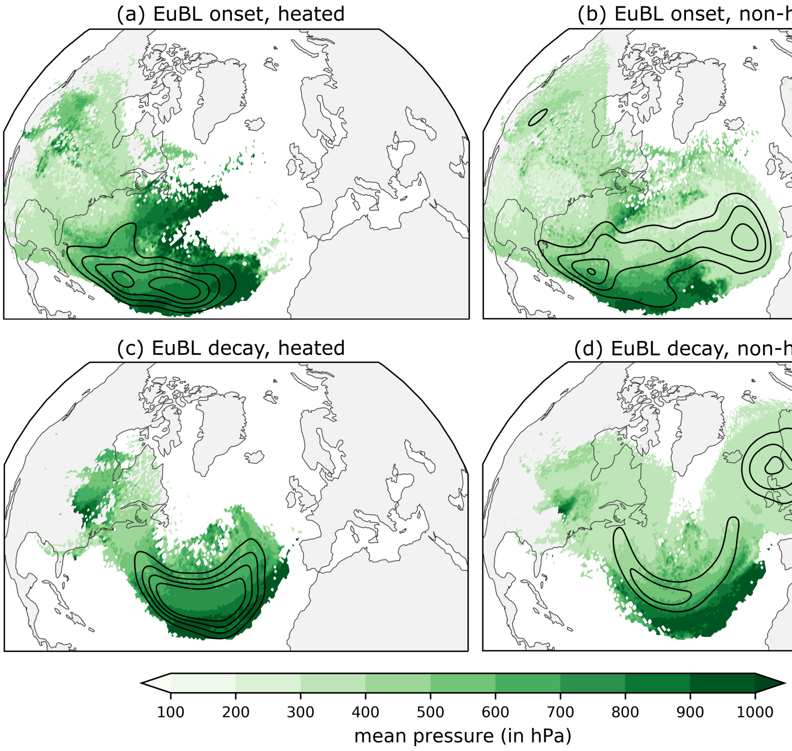

Figure 6.14: Origin of air parcels that end up in the PVA^-_{EuBL} around the EuBL onset (upper row) and the decay (lower row). The origin of air masses is shown separately for diabatically heated trajectories ($\Delta\theta > 2\,\mathrm{K}$) and non-heated trajectories. All three-day backward trajectories out of the PVA^-_{EuBL} in the time window +/- one day (Δt = 3h) around the EuBL onset and decay are considered. The pressure of the air parcels associated with the trajectory (in hPa) is shown at time t = -3 days in green shading. If several air parcels are at the same grid point (by considering several times), the mean pressure is displayed. The occurrence frequency is shown in black contours for the heated trajectories in steps of 1.5, 2.5, 3.5 and 4.5 10^{-2} and for the non-heated trajectories in steps of 1.0, 1.5, 2.0, 2.5 10^{-2}. For a clearer visualization, the fields are Gaussian-filtered with $\sigma = 4$. Reprinted from Hauser et al. (2023b).

(Fig. 6.14b). In addition to the adiabatic advection of air parcels from upstream, some recirculating air parcels are located in the upper troposphere in the close vicinity of the PVA^-_{EuBL}.

The substantially increased fraction of heated trajectories around onset (47 %) as compared to around decay (24 %) in Figure 6.13b demonstrates the importance of diabatic heating for the development and strengthening of the PVA^-_{EuBL} in an earlier stage of the life cycle from the Lagrangian perspective. Concerning the spatial origin of the heated trajectories, the southern North Atlantic is identified as a key source region around the EuBL onset and decay (Fig. 6.14a,c). The position of air parcels upstream of the PVA^-_{EuBL} in the lower troposphere suggests that air parcels will most likely experience latent heat release on their ascent to the upper-tropospheric PVA^-_{EuBL} in the following three days.

In summary, the Lagrangian perspective thus complements the insights from the quasi-Lagrangian perspective and links the amplitude-enhancing divergent PV tendency contribution from the quasi-Lagrangian perspective to the occurrence of latent heating, which is (mostly) associated with the occurrence of

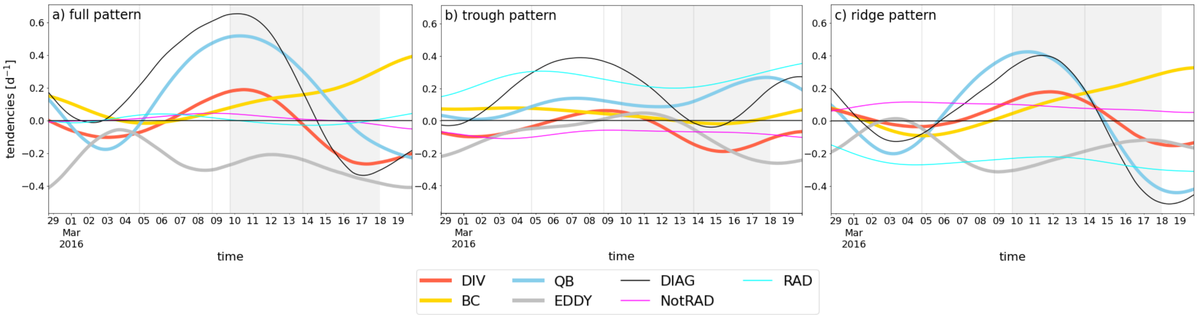

Figure 6.15: Eulerian perspective on the PV dynamics of the EuBL regime life cycle in March 2016. Projection of low-frequency PV tendencies (in d^{-1}) onto (a) the full regime pattern consisting of positive and negative PV anomalies, (b) only the positive PV anomalies (trough), and (c) only the negative PV anomalies of the regime pattern. The colored curves represent the following PV tendency terms: divergent PV tendencies (DIV, -$\mathbf{v}'_{div} \cdot \nabla$ q), quasi-barotropic (QB, - [$\mathbf{v}'_{up} \cdot \nabla q_0 + \mathbf{v}_0 \cdot \nabla q'$]), baroclinic (BC, -$\mathbf{v}'_{low} \cdot \nabla q_0$), and the convergence of eddy fluxes (EDDY, - $\nabla \cdot$ ($\mathbf{v}'_{rot} q'$) with $\mathbf{v}'_{rot} = \mathbf{v}'_{up} + \mathbf{v}'_{low} + \mathbf{v}'_{res}$). The contribution due to non-conservative processes is shown for radiation (RAD, turquoise) and non-radiative processes (NotRAD, pink) separately. The full diagnosed tendency (DIAG) is defined as DIAG = DIV + QB + BC + EDDY + RAD + NotRAD. The gray shaded area denotes the time of the active EuBL regime life cycle. Adapted from Hauser et al. (2023b).

WCBs. Consequently, this confirms the hypothesis of Grams et al. (2018) that moist processes linked to WCB activity played an important role in the formation of the block.

6.4 Comparison to a Eulerian perspective

The PV-θ-framework of Teubler and Riemer (2016) has been adjusted for a Eulerian perspective on weather regime dynamics. Similar PV tendency terms to the ones in this thesis are projected onto the mean regime pattern from the PV perspective. This enables the quantification of processes that favor a certain regime pattern (positive projected PV tendencies) and processes that work against a regime pattern (negative projected PV tendencies). Figure 6.15 shows the individual contributions of different processes to the evolution of the EuBL regime pattern during the EuBL regime life cycle in March 2016. Linear wave dynamics linked to the quasi-barotropic PV tendency term dominate the regime pattern evolution around the EuBL onset, indicating that the downstream advection of PV anomalies is of crucial importance for the onset of the regime (Fig. 6.15a). Divergent PV tendencies favor the regime pattern around EuBL onset, but are of less importance. Even a split up into positive and negative PV anomalies of the EuBL pattern reveals a dominance of linear wave dynamics (Fig. 6.15b,c). This clashes with the insights obtained from the quasi-Lagrangian and Lagrangian perspective in Sections 6.2.2 and 6.3 that moist processes played a crucial role in the formation of the EuBL in March 2016.

The three perspectives - Eulerian, quasi-Lagrangian, and Lagrangian - elucidate different aspects of the EuBL regime life cycle that initially contrast with each other. The reason why the moist processes do not emerge more clearly in the Eulerian perspective stems from the methodology and Eulerian thinking itself. Only the processes within the typical regime pattern are considered, i.e. in the case of the ridge over Europe. Therefore, the Eulerian perspective misses the processes that occur outside this region, and, in particular, the development of the PVA^{-}_{EuBL} identified from the quasi-Lagrangian perspective. Therefore, the Eulerian framework fails to capture the importance of moist processes in the evolution of the PVA^{-}_{EuBL}, which especially emerge clearly from a Lagrangian thinking. However, the Eulerian framework reveals the PVA^{-}_{EuBL} propagation to Europe in the PV tendency term, which describes the advection of PV anomalies into the region. Thus, the different perspectives do not contradict each other, but highlight aspects from different angles.

6.5 Summary

This chapter gave, for the first time, an in-depth insight from a quasi-Lagrangian PV perspective into the dynamics of an EuBL regime life cycle that occurred from 9–18 March 2016 and was associated with one of the largest forecast bust at ECMWF between 2014 and 2016. The novel PV framework revealed that the PVA^{-}_{EuBL}, which was associated with the regime life cycle, was advected into Europe and did not build up locally. Multiple pulses of latent heating (reflected by the PV tendency term of DIV_{div}) led to an amplification of the traced PVA^{-}_{EuBL} during its propagation from the US East Coast towards Europe. Even within the first days of the regime life cycle, DIV_{div} and UP tendencies contributed to a further amplification before the regime started to decay. The decay of the regime life cycle was associated with a co-occurrence of the PVA^{-}_{EuBL} weakening led by tendencies of UP. In addition, strong deformation of the PVA^{-}_{EuBL}, in combination with splitting events, caused the PVA^{-}_{EuBL} to vanish nine days after regime decay. A pure Lagrangian perspective confirmed the link of divergent PV tendencies and moist processes (such as latent heating) and highlighted the increased presence of moist processes during the onset and the reduced presence of moist processes around the decay of the EuBL regime life cycle. This agrees with the results of Pfahl et al. (2015) and Steinfeld and Pfahl (2019), who found during a systematic climatological investigation that moist-diabatic processes play an important role during the onset of blocking. The lack of moist processes during the decay of the EuBL regime life cycle fits well with the hypothesis of Hoskins (1997) that the disruption by the advection of other systems and the lack of a maintenance process can be associated with the decay of a block.

The insights obtained confirm the initial suggestion by Grams et al. (2018) that the onset of EuBL was associated with moist processes and, in particular, the presence of WCBs. Compared to a Eulerian perspective in Hauser et al. (2023b), the quasi-Lagrangian framework has been shown to do exactly what it was designed to do: to bridge the gap between the Lagrangian and Eulerian perspectives.

7 Dynamics of Greenland blocking onset

The previous chapter highlighted the use of the novel quasi-Lagrangian framework, which allows studying the dynamics of a full blocking life cycle from the perspective of regimes, and in particular from a new angle that combines Eulerian and Lagrangian theories. After the successful test of the framework on the EuBL regime life cycle in March 2016, the systematic application to numerous regime life cycles in the period 1979–2021 is now carried out for one out of four blocked regimes. Greenland Blocking (GL) is strongly anti-correlated with the NAO (Fig. B.1), which represents the most prominent pattern of climate variability in the extratropical North Atlantic region. In the Northern Hemisphere, GL is the most long-lasting blocking circulation pattern in the Northern Hemisphere (e.g., Drouard et al., 2021), which can dramatically accelerate the melting of the Greenland Ice Sheet by increased surface temperatures (Hermann et al., 2020; Hanna et al., 2021). Not only Greenland is affected by this type of blocking but also adjacent or even remote regions. As such, Simonson et al. (2022) point to the link of GL and the increased precipitation during summer over the northeastern US as a consequence of increased moisture flux from the south into higher latitudes. Across Europe, GL can be associated with periods of widespread low production of wind and solar power and high electricity demand (Otero et al., 2022), and has substantial impacts on the health system in the UK (Charlton-Perez et al., 2019). The southward shifted storm track over the North Atlantic during GL leads to increased winds over southwestern Europe (Grams et al., 2017). A more recent study pointed to the clustered occurrence of extratropical cyclones during GL that hit Iberia and potentially lead to extreme weather events in this area (Hauser et al., 2023a). Therefore, a better understanding of the underlying dynamics is necessary to improve the forecast of GL to provide valuable information for a wide range of applications ranging from agriculture and health over energy to transportation and disaster risk management.

This chapter is confined to the onset of GL and starts with an introduction of the GL regime life cycles by the investigation of the large-scale PV evolution leading to GL onset (Sect. 7.1). The quasi-Lagrangian PV framework is applied to all GL regime life cycles in the chosen ERA5 period to investigate the origin of PVAs$^-$ that trigger the GL onset (Sect. 7.2). Equivalent to the detailed investigation of the EuBL regime life cycle in the previous chapter, Section 7.3 characterizes the amplitude evolution of the PVAs$^-$ and disentangles the role of dry and moist processes in the amplification and weakening. A more detailed insight into the role of moist processes is presented in Section 7.4. Lastly, the role of splitting and merging events along the PVA$^-$ tracks is analyzed in Section 7.5).

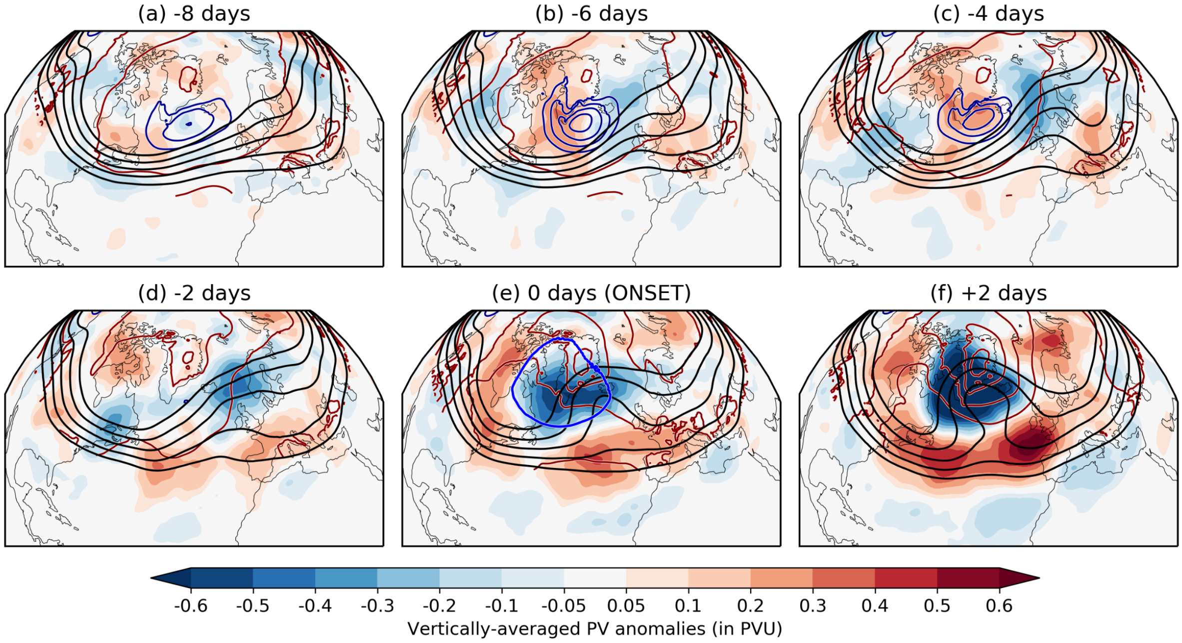

Figure 7.1: Year-round composite of VAPV' (shading, in PVU), Z500 (black contours) from 5350 to 5550 gpm in steps of 50 gpm, and mean sea level pressure for low pressure (blue contours, from 1000 to 1008 hPa in steps of 2 hPa) and high pressure (red contours, from 1015 to 1030 hPa in steps of 5 hPa) for selected time steps relative to GL onset (in days). The fields represent 24 hours running means (+/- 6 hours around the central date). The regime mask of GL based on VAPV' (cf. Fig. 5.6d) is displayed in (e) as a blue contour.

7.1 Large-scale PV evolution

Figure 7.1 presents the large-scale evolution of GL regime life cycles centered on the 177 regime life cycle onset dates between 1979–2021. The main characteristics in the large-scale flow leading to GL are discussed based on the field of VAPV' between 500 and 150 hPa, Z500 and mean sea level pressure (MSLP).

Around eight days before GL onset, a zonally-oriented circulation prevails over the North Atlantic (Fig. 7.1a). An area of low pressure is located over the central North Atlantic and suggests the presence of extratropical cyclones linked to the favorable zonal flow conditions. Positive PV anomalies are found over Central Europe, linked to a trough that is visible in Z500. Within the next two days, the low pressure region over the central North Atlantic further deepens and is now co-located with positive PV anomalies on its western flank (Fig. 7.1b). Downstream, over Europe, the flow starts to further amplify with a ridge that builds up over Western Europe upstream of the trough over Central Europe. Four days before GL onset, the ridge over Western Europe is well established and flanked by two troughs, upstream over the western North Atlantic and downstream over southeastern Europe (Fig. 7.1c). Still, low pressure prevails upstream of the ridge centered south of Greenland and points to the role of extratropical cyclones that act as precursor cyclones for the formation of GL (cf. McLeod and Mote, 2015).

The large-scale circulation patterns suggest the split up of the flow into two distinct branches over Europe shortly before the onset of GL (Fig. 7.1d). The northern brunch is located over Island and Scandinavia and co-occurs with negative PV anomalies, while the southern brunch is linked to positive PV anomalies over Southern Europe. Upstream of Europe, negative PV anomalies are located along the US East Coast in close vicinity of Greenland. The area of low pressure over the central North Atlantic is not visible anymore and marks the end of potential extratropical cyclone activity. A ridge pointing to the formation of a blocking situation is evident at the time of the GL onset over the central North Atlantic (Fig. 7.1e). Negative PV anomalies linked to this ridge are located within the regime mask of GL (blue contour) and indicate the established anticyclonic large-scale pattern that represents GL. High MSLP over GL shows that the anticyclonic circulation in the upper troposphere has manifested as a high pressure anticyclone near the surface. Negative PV anomalies in the lower midlatitudes indicate the southward shift of the storm track downstream of Greenland, which is typical for GL (cf. Woollings et al., 2010). Two days after GL onset (Fig. 7.1f), the surface high over Greenland has amplified and the typical GL pattern as seen in the composite in Figure 5.6d has fully established. The prominent ridge as anticyclonic circulation anomaly is well pronounced as an area of negative upper-tropospheric PV anomalies centered on the southern tip of Greenland, and is flanked by troughs over the northeastern United States and Western Europe.

In summary, the large-scale circulation over the North Atlantic-European region develops within a short time period from a nearly zonal flow over the North Atlantic into the blocked flow with negative upper-tropospheric PV anomalies linked to the anticyclonic circulation anomaly in the upper troposphere over Greenland. The questions on how the negative PV anomalies over Greenland develop and where they originate is the subject of the following section.

7.2 Pathways of onset PVAs$^-$

The various snapshots of the large-scale flow in the days before GL shown in the previous chapter demonstrated the mean picture on how GL forms. However, recent studies investigated the different evolution of the large-scale circulation over the extratropical North Atlantic, leading to distinct ice sheet melting and snowfall patterns over Greenland (e.g., Hermann et al., 2020; Pettersen et al., 2022). In particular, the study of Preece et al. (2022) focused on the diversity of blocked flow patterns during GL episodes in summer linked to the response to the Greenland ice shield. The authors highlight a cyclonic wave breaking pattern with a ridge over Iceland and an Omega blocking pattern centered over the Baffin Bay as the most frequent pattern during GL episodes in summer. These two patterns are associated with different impacts on the surface over Greenland as the position of the blocking anticyclone has a decisive influence by governing the interaction between the path of moisture advection, the topography of Greenland, and large-scale subsidence linked to the surface anticyclone. A crucial question here is therefore whether, from a quasi-Lagrangian point of view, GL forms in different ways and, more in detail, where the anomalies originate that represent the dominant anticyclonic anomaly in the upper troposphere during GL.

The behavior and in particular the track of the PVAs^{-} from the quasi-Lagrangian framework (cf. Sect. 5.3) around GL onset are investigated to address this question. The anomalous frequency of PVAs^{-} is calculated relative to a 30-day running mean climatology (1979–2019) centered on the respective calendar day (cf. Fig. 5.4). Figure 7.2 shows the frequency of PVAs^{-} for selected time steps relative to GL onset (left column) and the normalized anomalous frequency of PVAs^{-} (middle and right column) to detect unusual signals and thus deviations from the climatology in different regions. The method conducted in Section 5.4 to identify the PVAs^{-} contributing to a regime life cycle has revealed that often multiple PVAs^{-} are involved, such that a systematic analysis becomes complex. Hence, for simplification, a single PVA^{-} for each GL regime life cycle is determined as the PVA^{-} that exhibits the highest and most frequent spatial overlap of the GL mask (cf. Fig. 5.6d) around GL onset. The selected PVAs^{-} are further referred to 'onset PVAs^{-}' and their frequency is shown in black contours in Figure 7.2.

The backtracking of PVAs^{-} triggering the onset of GL indicates varying origin regions of the anomalies in the days before the regime onset. At the time of the onset and even two days later, onset PVAs^{-} are located over Greenland within the regime mask (Fig. 7.2j,m). Tracing back the onset PVAs^{-} in time, the single frequency maximum over Greenland splits up into two local maxima two days before the onset (Fig. 7.2g). Some of the onset PVAs^{-} are located over the Norwegian Sea downstream of Greenland, and other onset PVAs^{-} appear near the US East Coast upstream of Greenland. Around four days before GL onset, the two frequency maxima of onset PVAs^{-} become more distinct. At the same time, a local minimum in PVA^{-} frequency is evident over Greenland, indicating that PVAs^{-} contributing to the onset do not build up locally over Greenland. The spatially distinct two frequency maxima for onset PVAs^{-} suggest that the path to Greenland is not uniform from this quasi-Lagrangian perspective.

Motivated by these findings, the characteristics of PVAs^{-} are investigated that emerge from upstream and downstream before GL onset. For each PVA^{-}, the center of mass position is calculated for each time step (recall that Δ t = 3 hrs) based on the VAPV' field (cf. Sect. 5.1). The longitude of the center of mass position of the regime mask in the VAPV' field composite (cf. Fig. 5.6d, ϕ_{GL} = 51.5 °W) serves to distinguish the upstream and downstream located onset PVAs^{-} before the onset of GL. If the majority of the PVA^{-}'s center of mass positions are located east of ϕ_{GL}, the onset PVAs^{-} and subsequently the regime life cycle is assigned to a category that is further referred to as 'retrogression pathway'. Vice versa, if the onset PVA^{-} is predominantly located west of ϕ_{GL}, then it is assigned to a category referred to as 'upstream pathway'.

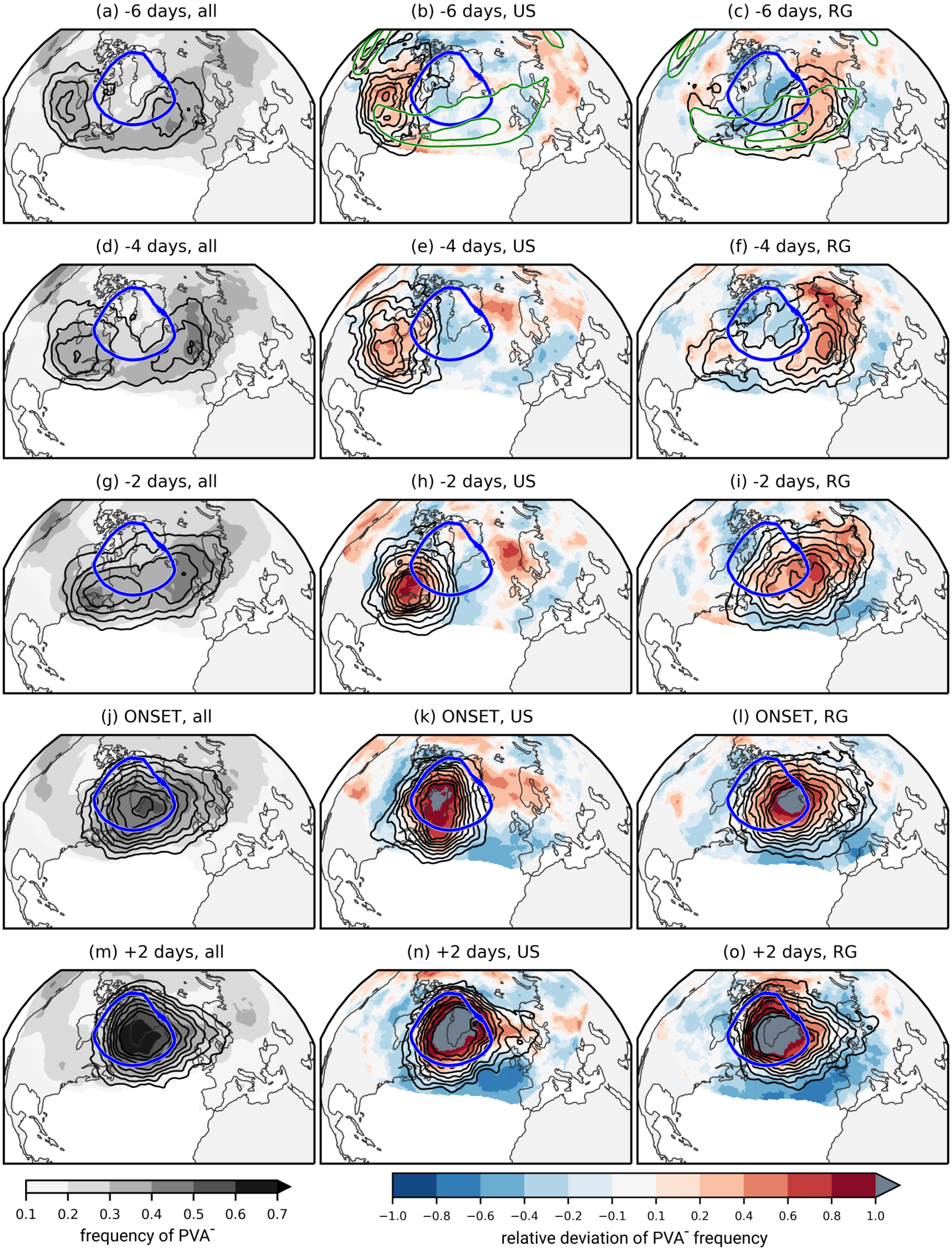

Figure 7.2: (left column) Frequency of PVAs^{-} (gray shading) and frequency of onset PVAs^{-} (black contours, from 0.1 to 0.45 in steps of 0.05) for selected time steps around GL onset. (middle and right column) Normalized anomalous frequency of PVAs^{-} (shading) for the upstream pathway (referred to as US; middle column) and the retrogression pathway (referred to as RG; right column) for the same time steps selected in the left column. The climatological frequency of PVAs^{-} (green shading, for 0.3 and 0.35) is shown in green contours in panel plots (b) and (c). Black contours represent the frequency of onset PVA^{-} for the respective pathway from 0.1 to 0.45 in steps of 0.05. The blue contour marks the regime mask of GL based on VAPV' (cf. Fig. 5.6d). The normalized anomalous frequency of PVAs^{-} exhibits high values in the subtropics and are masked when the climatological PVA^{-} frequency falls below 0.2. To increase the sample size of the composite, the fields +/- 6 hours around each time lag are included and Gaussian filtering (with $\sigma = 1$) is applied for smoother contours.

Table 7.1: Number of GL life cycles that are associated with the two pathways of PVAs$^-$ to Greenland prior to GL onset. Relative shares of the number of regime life cycles that fall into the different pathways are given additionally in brackets (in %).

	year-round	DJF	NDJFM	MAM	JJA	MJJAS	SON
All	177	31	58	58	52	81	36
Retrogression	102 (58 %)	24 (77 %)	38 (66 %)	34 (59 %)	27 (52 %)	46 (57 %)	17 (47 %)
Upstream	75 (42 %)	7 (23 %)	20 (34 %)	24 (41 %)	25 (48 %)	35 (43 %)	19 (53 %)

The partitioning of the onset PVAs$^-$ into the two pathway categories before GL onset and seasonal statistics are shown in Table 7.1. The retrogression pathway occurs more frequent (58 %) than the upstream pathway (42 %) from a year-round perspective. Split into different seasons, both pathways occur almost equally often for spring, summer, and autumn with occurrence frequencies of the retrogression pathway of 59, 52 and 47 %, respectively. Winter contrasts with the other seasons as the retrogression pathway is dominant with a frequency of 77 %, indicating that a retrograding behavior of PVAs$^-$ that trigger a GL onset in winter is quite common.

The different pathways of onset PVA$^-$ and associated signals of normalized anomalous PVA$^-$ frequency are illustrated in Figure 7.2 (middle and right column) to reveal anomalous behavior of PVAs$^-$ that do not represent the onset PVA$^-$. Both pathways exhibit differences in the position of onset PVAs$^-$, but especially in the anomalous frequency of PVA$^-$ in the extratropical North Atlantic. Around six days prior to GL onset, the onset PVAs$^-$ following the upstream pathway are located over the mainland of North America, where they are associated with an anomalous high frequency of PVAs$^-$ (Fig. 7.2b). In the next days, the onset PVAs$^-$ migrate to the northeast towards Greenland. Two days before GL onset, the onset PVAs$^-$ reach the southwestern edge of the climatological regime mask of GL, where they initiate the anticyclonic regime part of the GL pattern (Fig. 7.2h). Onset PVAs$^-$ are prevalent in the climatological regime mask at the time of the onset, with a slight shift towards the western half, and the region of the Labrador Sea and western Greenland (Fig. 7.2k). In the following days, the onset PVAs$^-$ spread over the area of the GL regime mask, which is visible in the anomalous high deviation of the PVA$^-$ frequency (> 1) that indicates more than a doubling of the climatological frequency (Fig. 7.2n). At the same time, the frequency of PVA$^-$ around Greenland decreases (anomalously few PVA$^-$), indicating not only the suppression of PVA$^-$ but also the stationarity of the full GL regime pattern.

A different picture emerges for onset PVAs$^-$ that retrograde towards Greenland before the GL onset. Onset PVAs$^-$ are located over the eastern North Atlantic six days before GL onset (Fig. 7.2c). Within the next two days, the frequency of onset PVAs$^-$ has further increased and has even shifted to higher latitudes, apparent as a region of anomalously high PVA$^-$ frequency (Fig. 7.2f). The onset PVAs$^-$ continue to migrate westward towards Greenland and enter the regime mask of GL from the southeast with an anomalous high frequency of PVAs$^-$ along the eastern edge of the regime mask shortly before the

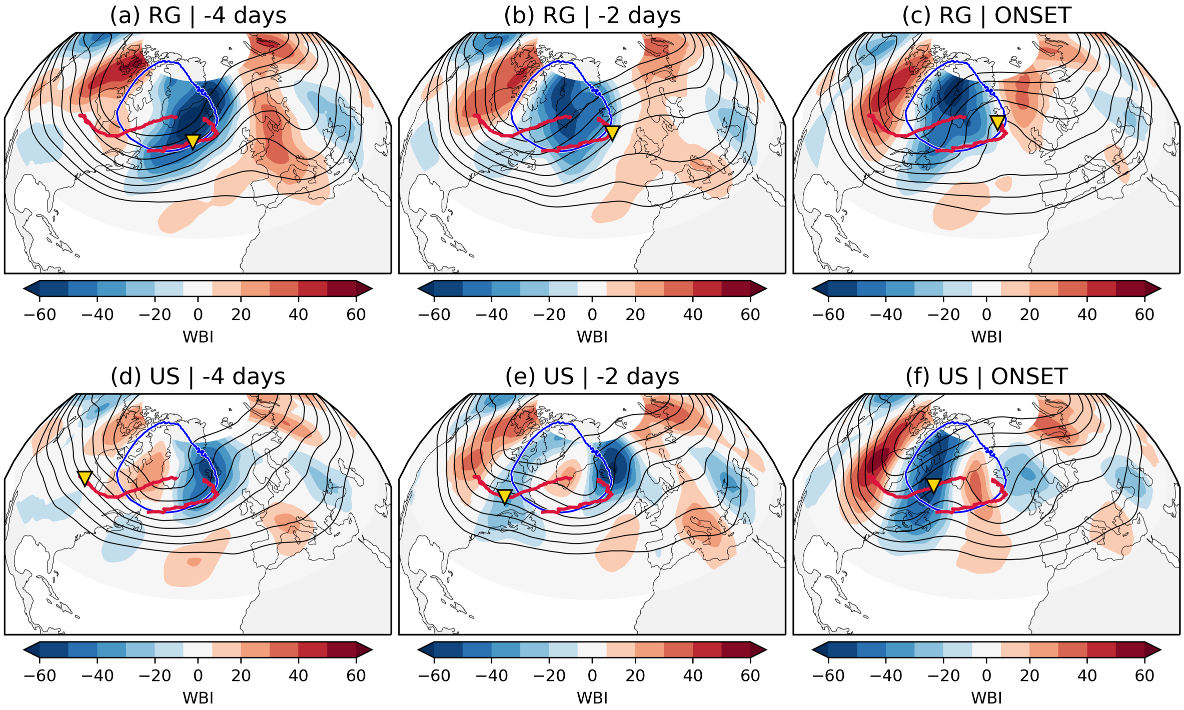

Figure 7.3: RWB index (WBI, shading) for selected time lags before and at GL onset for the retrograding onset PVAs⁻ (RG, upper row) and the PVAs⁻ from upstream (US, lower row). Black contours show Z500 (from 5250 to 5600 gpm in steps of 50 gpm). The blue contour represents the regime mask of GL. The two lines point to the mean tracks of each pathway within the time period -7 days to +2 days around GL onset. The yellow triangle marks the time and therefore the mean center of mass location of onset PVAs⁻ for the time shown.

onset (Fig. 7.2i,l). It is noticeable that the frequency of onset PVAs⁻ for retrograde migrating PVAs⁻ is more meridionally pronounced compared to the more compact onset PVAs⁻ from upstream. Two days after GL onset, both pathways exhibit a similar pattern despite the difference in evolution before the GL onset (Fig. 7.2o).

Although the propagation of the onset PVA⁻ determines the pathway category of a regime life cycle, it remains possible that other PVAs⁻ that further contribute to the GL onset reach Greenland by the other pathway. Indeed, Figure 7.2b indicates an anomalous high frequency of PVAs⁻ downstream over Russia six days before GL onset. In the following days, the signal even strengthens, and a maximum is visible between Iceland and Scandinavia two days before GL onset (Fig. 7.2e,h). From the onset, the two clear maxima in the anomalously high PVAs⁻ frequency can no longer be separated, which is due to the convergence of both signals over Greenland (Fig. 7.2k,n). This points to the simultaneous propagation of contributing PVAs⁻ from upstream and downstream before GL onset in some regime life cycles. Also in the retrogression pathway, a slightly enhanced PVA⁻ frequency is evident upstream over northeastern North America, pointing to a simultaneous occurrence of both pathways (Fig. 7.2, right column).

Link of pathways to RWB

The retrogression of existing PVAs$^-$ to Greenland before GL onset was already observed early from a Eulerian perspective (e.g., Vautard, 1990). Croci-Maspoli et al. (2007) found a preference of retrograding blocks during the negative NAO phase and linked this behavior to slow-moving waves on the planetary and low-frequency scale. Benedict et al. (2004) investigated the role of breaking waves for the initiation and maintenance of the two NAO phases and pointed to the importance of cyclonic RWB. More recently, Preece et al. (2022) found a frequent blocked pattern that is characterized by cyclonic RWB, where the anticyclone approaches Greenland from the east during GL episodes in summer. This raises the question of how signals from RWB differ in the two pathways in the days before GL onset, and if they exhibit similar characteristics as in previous studies. A simplified version of the RWB index of Davini et al. (2012) is used here to examine the occurrence of cyclonic and anticyclonic RWB independent of blocking occurrence. The index calculates for each grid point the horizontal gradient of Z500 measured 8 ° south of each grid point. The larger the RWB index, the stronger the horizontal geopotential gradient. Negative values indicate cyclonic RWB (Z500 increases eastward) and positive values point to anticyclonic RWB (Z500 decreases eastward). The temporal development of the RWB index for the two pathways is shown in Figure 7.3.

The various patterns in the RWB index between the two pathways suggest different processes in the formation of GL. For retrograding onset PVAs$^-$, the quasi-stationary pattern of the RWB index during the four days before GL onset points to a rather stationary flow with a small wave number (Fig. 7.3, upper row). Negative RWB index values within the regime mask four days before GL onset reveal the occurrence of cyclonic RWB from the eastern North Atlantic towards Greenland (Fig. 7.3a). Over time, the signal of cyclonic RWB propagates westward into the GL regime mask, which demonstrates the progress of the cyclonic RWB event. At the time of GL onset, the maximum in the negative RWB index is co-located with the GL regime mask (Fig. 7.3c). This matches the results of Benedict et al. (2004), who found that the negative phase of the NAO is the remainder of cyclonic RWB events over the North Atlantic. In addition, the distinct signal of cyclonic RWB in the days before points to a reason for the dominant retrogression pathway in winter (cf. Tab. 7.1). The RWB occurrence exhibits a seasonality linked to the seasonal variation of the jet stream latitude, such that cyclonic RWB occurs more frequently when the jet is shifted equatorward (e.g., Woollings et al., 2008; Liu and Barnes, 2015). The more southerly location of the jet stream in winter compared to summer thus creates more favorable conditions for a retrogression of the onset PVAs$^-$, and could be one reason why the retrogression pathway dominates in winter.

In contrast, for the upstream pathway, changes in the RWB index pattern are evident over time towards GL onset (Fig. 7.3, lower row). A complex quadrupole structure of the RWB index is located over the

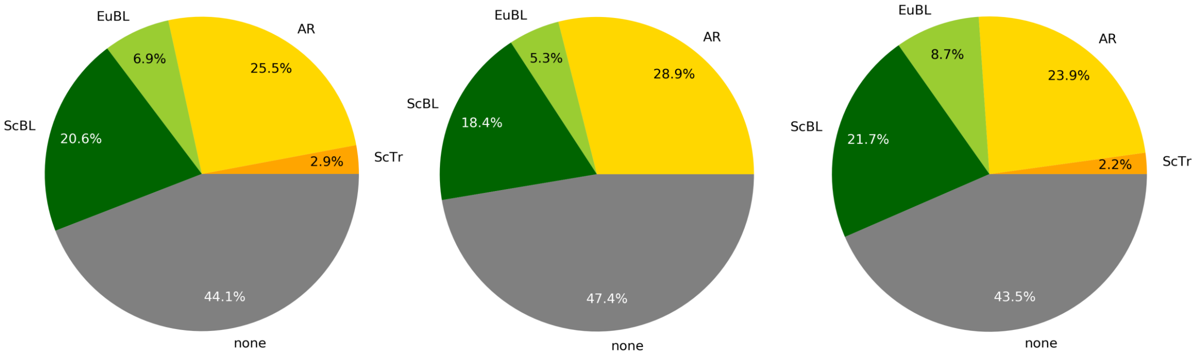

(a) Retrogression (year-round)
(b) Retrogression (NDJFM)
(c) Retrogression (MJJAS)

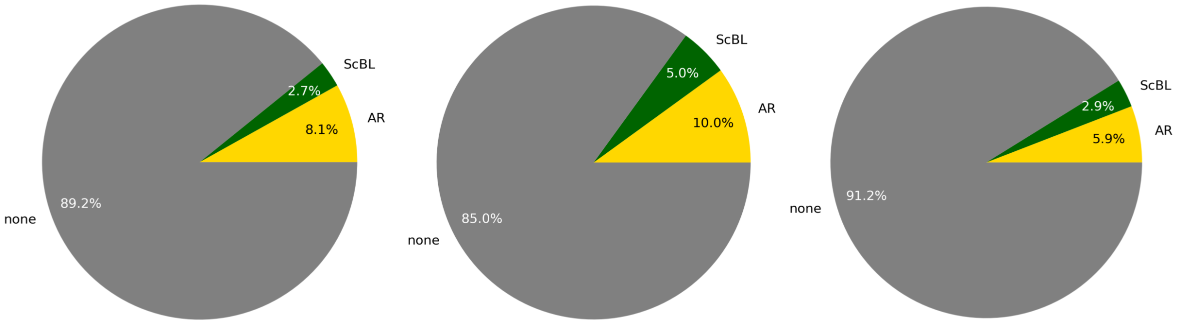

(d) Upstream (year-round)
(e) Upstream (NDJFM)
(f) Upstream (MJJAS)

Figure 7.4: Share of onset PVAs$^-$ (in %) that follow the retrogression (upper row) and the upstream (lower row) pathway and contributed to the regime life cycle before when the GL life cycle transitioned out from ScTr, AR, EuBL, or ScBL: (a,d) year-round, (b,e) extended winter, (c,f) extended summer. A contribution is counted when the onset PVAs$^-$ exhibits a minimum overlap with the regime mask of 10 % for at least four time steps within the regime life cycle of the dominant regime before. The ’none’ category includes the regime life cycles that transitioned from ZO, AT or none of the regimes or when onset PVAs$^-$ do not fulfill the contribution conditions.

North Atlantic four days before GL onset (Fig. 7.3d) which dissolves over time. Shortly before onset, two areas of cyclonic RWB are visible in the vicinity of Greenland (Fig. 7.3e). The first one is located along the US East Coast, co-located with the mean position of upstream onset PVAs$^-$ (yellow triangle). The second and dominating area of cyclonic RWB is located in high latitudes over the eastern North Atlantic. At the time of GL onset, the two minima in the RWB index remain but the strength of the mean RWB index between these two minima is reversed such that the signal over the US East Coast that propagated northeastward dominates and points to a more western location of the actual RWB event (Fig. 7.3f). This suggests that the major cyclonic RWB event associated with the GL onset in the upstream pathway is originating and building up almost locally southwest of Greenland. Meanwhile, a clear signal of a cyclonically-breaking wave from Europe is evident for the retrogression pathway already several days before the regime onset.

Link between pathways and regime contributions before GL onset

The two pathways provide indications of preferred regime transitions to GL. One of these regime transitions is from blocking over Europe to GL (e.g., Vautard, 1990; Michel and Rivière, 2011). This is supported by the RWB index composite for the retrograding onset PVAs$^-$ that strongly resembles the RWB pattern of the blocking regime of Michel and Rivière (2011, their Fig. 3b)) in the days before GL onset. The retrograding of onset PVAs$^-$ in the transition from other blocked regimes in the North Atlantic-European region to GL suggests that PVAs$^-$ can contribute to multiple blocked regimes. The pie plot in Figure 7.4 reveals for both pathways the share of onset PVAs$^-$ that contributed to another blocked regime before. Note that the ScTr regime is included in this analysis, with its anticyclonic circulation anomaly centered over the central North Atlantic (cf. Fig A.1a). The share is presented in addition for extended winter and summer separately to investigate whether differences exist between the seasons.

From a year-round perspective, more than 50 % of the onset PVAs$^-$ following the retrogression pathway have contributed to another blocked regime in the North Atlantic-European region before (Fig. 7.4a). Split up into the different blocked regime types, the preferred contributions are AR and ScBL pointing to a northwestward and westward retrogression of onset PVAs$^-$, respectively. This agrees well with the findings of Büeler et al. (2021) who state that the dominant transitions to GL from blocked regimes occurs from AR and ScBL (their Fig. 7). Still, some GL life cycles seem to evolve from EuBL and ScTr suggesting a northwest displacement of the onset PVAs$^-$. A higher fraction of onset PVAs$^-$ contributed to a blocked regime before GL onset for summer compared to winter (Fig. 7.4b,c). Although the contributions of onset PVAs$^-$ to AR and ScBL differ between the seasons, the sum of both contributions is identical for summer and winter. This indicates that the increased contributions to blocked regimes in summer arise from EuBL and ScTr. These insights are in agreement with the results obtained by Teubler et al. (2023), who performed an EOF analysis and *k*-means clustering on Eulerian PV anomaly maps prior to GL onset to come up with an upstream and retrogression pathway. They found that 65 % of the transitions from regime life cycles linked to dominant anticyclonic PV anomalies downstream of Greenland before onset are associated with blocked regimes. This agrees well with the finding here that around 60 % of onset PVAs$^-$ have contributed to another blocked regime before in the retrogression pathway. In contrast, onset PVAs$^-$ that follow the upstream pathway rarely contribute to a blocked regime before, which is due to the fact that the anticyclonic circulation anomaly of the other blocked regimes is located downstream of Greenland (Fig. 7.4d). The small shares for ScBL and AR likely arise due to meridional very elongated onset PVAs$^-$. However, and most importantly, the fact that upstream PVAs$^-$ usually do not contribute to a blocked regime before does not exclude transitions from a blocked regime to GL. It rather implies that the large majority of onset PVAs$^-$ have not contributed to a blocked regime over Europe before. The degree to which these results are related to preferred regime transitions is addressed in the systematic evaluation of all blocked regimes in Section 8.1.1.

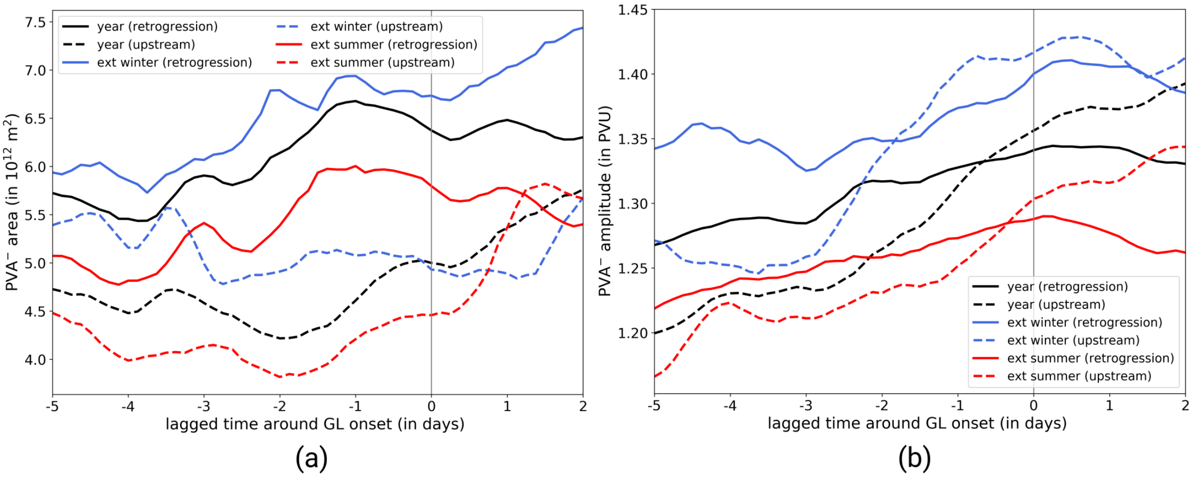

Figure 7.5: Mean temporal evolution of (a) the onset PVA$^-$ area (in 10^{12} m^2) and (b) the onset PVA$^-$ amplitude (in PVU, reversed sign) for the time relative to GL onset. The temporal evolution for onset PVAs$^-$ that follow the retrogression (solid) or upstream (dashed) pathway is shown in addition to the year-round perspective (black lines) for extended winter (blue lines) and extended summer (red lines) separately. The vertical line indicates the time of GL onset. Note that the lines are smoothed by taking into account the time steps +/- 6 hours around each time step relative to regime onset.

7.3 Amplitude evolution of onset PVAs$^-$

The previous section showed that PVAs$^-$, which contribute to the onset of GL, migrate on two distinct pathways towards Greenland. It is now of interest to shed light onto the characteristics, physical and dynamical processes associated with the onset PVAs$^-$, and to investigate whether the characteristics differ depending on the pathway. Equivalent to the PVA$^-$ that contributed to the EuBL regime life cycle in March 2016 (Chap. 6), the relative importance of different PV tendency terms to the amplitude evolution of onset PVA$^-$ is presented. Figure 7.5 shows the evolution of the PVA$^-$ area and amplitude around GL onset for the retrogression and upstream pathways. Due to seasonal differences in the occurrence of the PVA$^-$ pathways, analyses for extended winter and extended summer are presented in addition to the year-round composite.

Independent of the season, upstream PVAs$^-$ (dashed lines) exhibit a smaller area than retrograding PVAs$^-$ (solid lines in Fig. 7.5a). Until about two days before onset, the area of the upstream PVAs$^-$ hardly changes and only shortly before the onset a strong increase in area starts that continues into the active GL life cycle. In comparison, PVAs$^-$ that retrograde towards Greenland grow in size earlier, around -4 to -1 day before GL onset. Onset PVAs$^-$ that follow the retrogression pathway already decrease in size around onset. Focusing on the different seasons, the qualitative development is quite similar, and the main differences arise due to the fact that PVAs$^-$ are generally larger in area in winter than summer (cf. Chap. 5.2). Furthermore, retrograding PVAs$^-$ increase in size after the onset in winter, while in summer the area decreases steadily from one day before the onset.

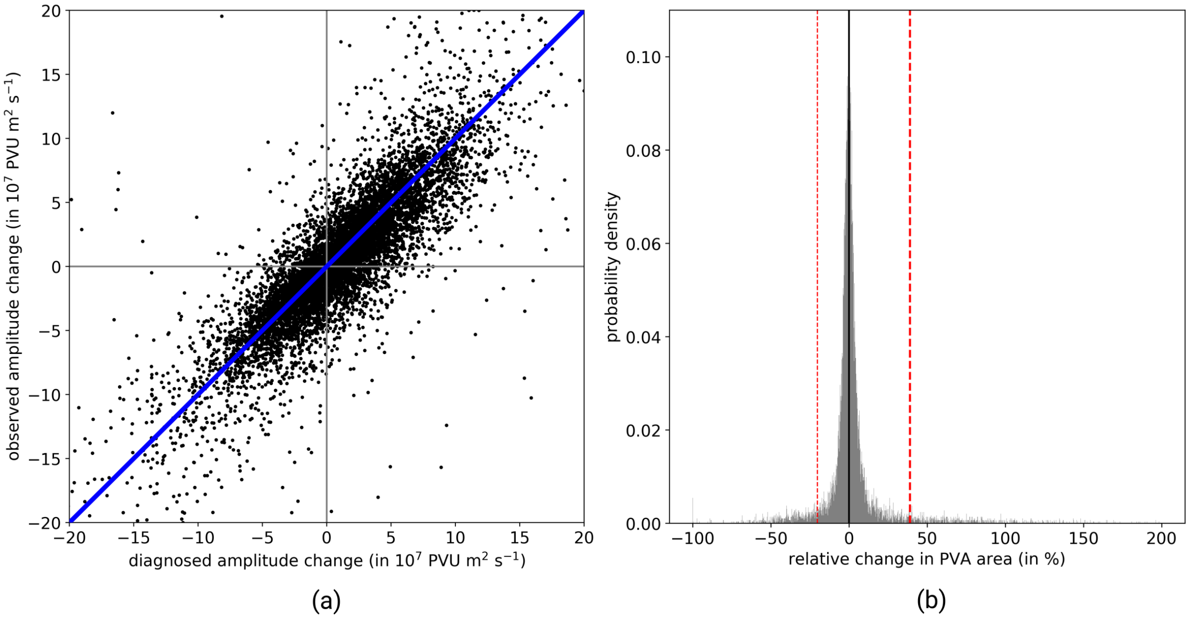

(a) (b)

Figure 7.6: (a) Relation between the observed and the diagnosed amplitude change (in 10^7 PVU m^2 s^{-1}) integrated over the onset PVAs$^-$ for every time step in the time period -7 to +2 days around GL onset. All scatters should be aligned along the blue solid line of slope 1 for a perfect correspondence. (b) Probability density of the relative area changes of onset PVAs$^-$ (in %) from one time step to the following one. The vertical lines (red, dashed) mark the 5 % and 95 % percentile. The relative changes in area in (b) are limited on the negative axis to -100 % which corresponds to a complete breakdown of the PVA$^-$.

The amplitude evolution of the onset PVAs$^-$ exhibits differences in the course of the amplitude between the two clusters (Fig. 7.5b). Retrograde migrating PVAs$^-$ experience a slow but steady amplification before onset that peaks around one day after GL onset. In contrast, the upstream PVAs$^-$ are associated with a sudden and rapid amplification that starts three days before onset. Until just before the onset, the retrograde migrating PVAs$^-$ feature a higher amplitude. After this point, the upstream PVAs$^-$ exhibit a stronger amplitude, growing further even during the active life cycle. Again, the different seasons reflect the qualitative progression of the temporal evolution of the area and amplitude, such that the real differences are clearly discernible between the two pathways rather than between the seasons.

The sudden and rapid amplification of the upstream PVAs$^-$ suggest that these PVAs$^-$ are diabatically driven and that moist processes make a contribution to the rapid growth in amplitude. As for the EuBL case study in the previous chapter, the individual PV tendency terms are spatially integrated over the area of the respective onset PVA$^-$ in order to understand which processes contribute to the amplitude evolution of onset PVAs$^-$. Note that the advanced version of the amplitude evolution (cf. Eq. 5.12) is selected as this version considers the change in PV background, which is negligible for a single case study but not for a year-round analysis of multiple regime life cycles. Figure 7.6a shows the relationship between the observed amplitude change measured on the isentropic PV anomaly field and the diagnosed amplitude change as sum of all PV tendencies. Each dot represents a time step around GL onset in the range -7

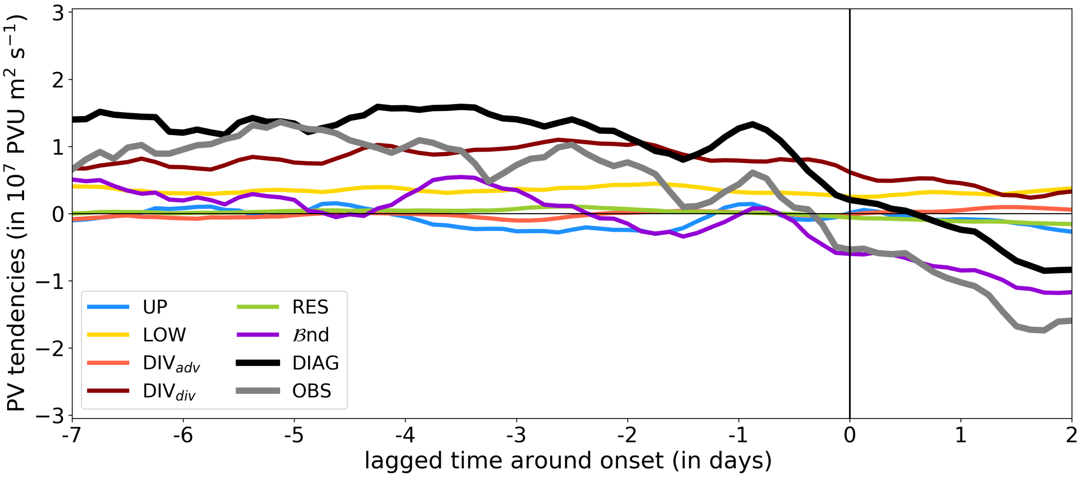

Figure 7.7: Integrated amplitude evolution of onset PVAs$^-$ around GL onset for the different PV tendency terms: UP (-$\mathbf{v}'_{up} \cdot \nabla q_0$), LOW (-$\mathbf{v}'_{low} \cdot \nabla q_0$), DIV$_{adv}$ (-$\mathbf{v}'_{div} \cdot \nabla q_0$), DIV$_{div}$ (q'($\nabla \cdot \mathbf{v}'_{div}$)), RES (-$\mathbf{v}'_{res} \cdot \nabla q_0$), and the boundary term $\mathscr{B}$nd. The thick black line shows the diagnosed amplitude evolution DIAG = UP + LOW + DIV$_{adv}$ + DIV$_{div}$ + RES + $\mathscr{B}$nd. The thick gray line indicates the observed amplitude evolution. Only the time steps are considered if the relative area change is <= 20 % from one to the following time step, as splitting and merging would lead to extraordinary values in the composite. Note that the lines are smoothed by taking into account the values +/- 6 hours around.

to +2 days for all 177 onset PVAs$^-$ independent of the pathway. There is a good agreement between the diagnosed and observed amplitude change, which is represented by the high Spearman correlation coefficient of 0.86. However, not all dots are arranged along the blue solid line with a slope of 1. Some reasons for the deviation of the diagnosed amplitude change are due to limitations in the method, which were discussed in detail in Section 5.5. Additionally, compared to the EuBL case study in Chapter 6, the non-conservative PV tendency term (NON-CONS) is not evaluated for the systematic analysis. As $\mathscr{B}$nd is estimated partly by the change in PVA$^-$ area, splitting and merging processes along the PVA$^-$ track lead to nonphysical $\mathscr{B}$nd values that dominate the full diagnosed PV tendency. Figure 7.6b shows the probability density of relative area changes from one time step to another one (in %) every three hours for all onset PVAs$^-$. The distribution indicates that most area changes along the onset PVA$^-$ tracks are rather small, pointing more to a natural growth of the anomaly rather than to merging or splitting of small-scale PVAs$^-$ from the onset PVA$^-$. Events that lead to a drastic change in area are rare, as in 90 % of all time steps investigated the relative change in area lies between -20 % and 40 % (red dashed lines in Fig. 7.6b). This justifies the filtering out of time steps with high values of the $\mathscr{B}$nd term. Section 7.5 investigates the role of splitting and merging events along the onset PVA$^-$ tracks in detail.

Figure 7.7 shows the mean integrated PV tendencies of all onset PVA$^-$ around the GL onset and reveals the contributions of different PV tendency terms to the amplitude evolution. Despite the analysis of the area change mentioned above, a uniform threshold for the relative area change is desirable, which will also be used later for the systematic evaluation of all four blocked regimes. A decision has been made

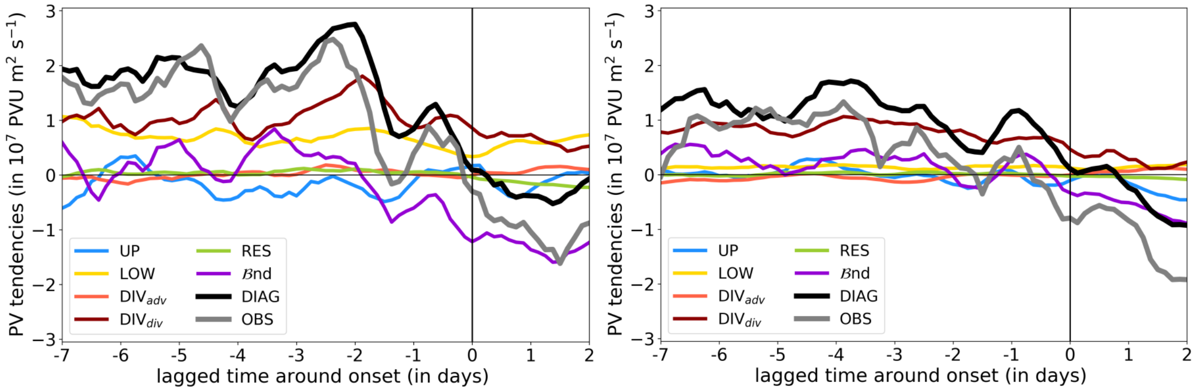

(a) extended winter (b) extended summer

Figure 7.8: Integrated amplitude evolution of onset PVAs$^-$ around GL onset for (a) extended winter (November–March), and (b) extended summer (May–September) for the different PV tendency terms: UP (-$\mathbf{v}'_{up} \cdot \nabla q_0$), LOW (-$\mathbf{v}'_{low} \cdot \nabla q_0$), DIV$_{adv}$ (-$\mathbf{v}'_{div} \cdot \nabla q_0$), DIV$_{div}$ (q'($\nabla \cdot \mathbf{v}'_{div}$)), RES (-$\mathbf{v}'_{res} \cdot \nabla q_0$), and the boundary term $\mathscr{B}$nd. The thick black line shows the diagnosed amplitude evolution DIAG = UP + LOW + DIV$_{adv}$ + DIV$_{div}$ + RES + $\mathscr{B}$nd. The thick gray line indicates the observed amplitude evolution. Only the time steps are considered if the relative area change is <= 20 % from one to the following time step, as splitting and merging would lead to extraordinary values in the composite. Note that the lines are smoothed by a rolling mean of +/- 6 hours.

on a lower but uniform threshold of 20 % (instead of -20 % and +40 %, cf. Fig. 7.6b) to reduce possible outliers linked to splitting and merging. Consequently, time steps in the composite that exhibit a relative area change of larger than +/- 20 % are excluded from this analysis to focus on the process-oriented changes in the PVA$^-$ amplitude.

As mentioned above, there is a good agreement between the diagnosed and observed amplitude evolution for the onset PVA$^-$ around the GL onset (Fig. 7.7). The PVA$^-$ amplitude increases before the GL onset and starts to weaken immediately after the onset. There is a slight offset between the diagnosed and observed amplitude change, which suggests that a process leading to a general weakening of the PVA$^-$ amplitude is missing. As mentioned above, this is likely the effect of the missing NON-CONS PV tendency term (cf. Eq. 2.5), which has been determined for the EuBL regime life cycle in March 2016 where it contributed to the attenuation of the PVA$^-$ amplitude. Teubler and Riemer (2021) calculated this term explicitly for the systematic evaluation of RWPs and showed that ridges are constantly weakened by non-conservative processes. Hence, a more closed budget is expected, taking into account NON-CONS. Moreover, larger offsets arise when the PVA$^-$ amplitude decreases and the PVA$^-$ additionally starts to break apart. As argued in Teubler and Riemer (2021), the diagnosed tendencies struggle to represent the actual development of PVA$^-$ during non-linear evolution and often overestimate the weakening of the PVA$^-$ amplitude.

The largest contribution to the amplification of onset PVAs$^-$ arises from the PV tendency term that describes the upper-level divergence of the divergent wind DIV$_{div}$ (Fig. 7.7). The dominance of DIV$_{div}$

suggests important contributions by moist processes to the onset of GL. This assumption will be explored in detail in the next subsection. DIV$_{div}$ exhibits highest values before the onset that slowly decrease after onset. The advection of background PV by the divergent term DIV$_{adv}$ shows only very small contributions to the amplitude evolution of the onset PVAs^{-} and is negligible. The baroclinic tendency term LOW contributes throughout and constantly to the strengthening of the onset PVAs^{-}, pointing to the baroclinic growth of the PVAs^{-}. The quasi-barotropic propagation term UP has a rather minor role but leads more often to the weakening of the onset PVA^{-} amplitude. Considering the onset PVA^{-} as part of an RWP, the negative contribution to the amplitude change from a quasi-barotropic perspective indicates that the trough downstream is more pronounced than the trough upstream. Hence, the PVA^{-} degradation on the eastern flank is stronger than the PVA^{-} buildup on the western flank. RES is of one magnitude smaller than the other advective terms and is negligible. $\mathscr{B}$nd predominantly shows positive values before and negative values after the GL onset. This points to a general increase in PVA^{-} area before and a decrease in area after onset.

The division of the year-round picture into winter and summer reveals a very similar qualitative progression of PV tendency terms (Fig. 7.8). However, the absolute values and thus contributions to the amplitude evolution are essentially different for the two terms, which leads to an overall stronger amplification of the onset PVAs^{-} in winter compared to summer before the GL onset. A higher contribution of DIV$_{div}$ is evident in winter compared to summer. This probably arises due to higher baroclinicity in winter and the more frequent occurrence of WCBs (Madonna et al., 2014), which occurred simultaneously with high contributions from DIV$_{div}$ during the EuBL regime life cycle in March 2016 (cf. Fig. 6.13). Compared to summer, LOW exhibits higher positive contributions in winter, which is again linked to the higher baroclinicity in winter (Fig. 7.8). Larger values of $\mathscr{B}$nd exist typically in winter and smaller values of $\mathscr{B}$nd in summer. This is consistent with the fact that PVAs^{-} are generally smaller and weaker in summer, which results in smaller changes in the area and subsequently smaller contributions in $\mathscr{B}$nd compared to winter.

Contributions to the amplitude evolution linked to pathways

Although the seasonal variations in baroclinicity lead to higher contributions of DIV$_{div}$ and LOW in winter than in summer, the breakdown of the amplitude evolution of onset PVAs^{-} into the seasons has shown that the qualitative course of the tendency terms remains equal. It is of further interest to investigate if the dynamics associated with the PVA^{-} amplitude evolution between the two pathways differ. First and equivalent to the underlying method in Figure 6.9 for the EuBL case study in Chapter 6, the major differences in the contributions to the amplitude evolution are discussed based on the net contributions in the days before the GL onset (Fig. 7.9). The discussion on the evolution of the integrated PV tendency terms for both pathways separately follows with Figure 7.10). Spatial maps are presented for selected times relative to GL onset to better understand the differences in the dynamics and the exact location of

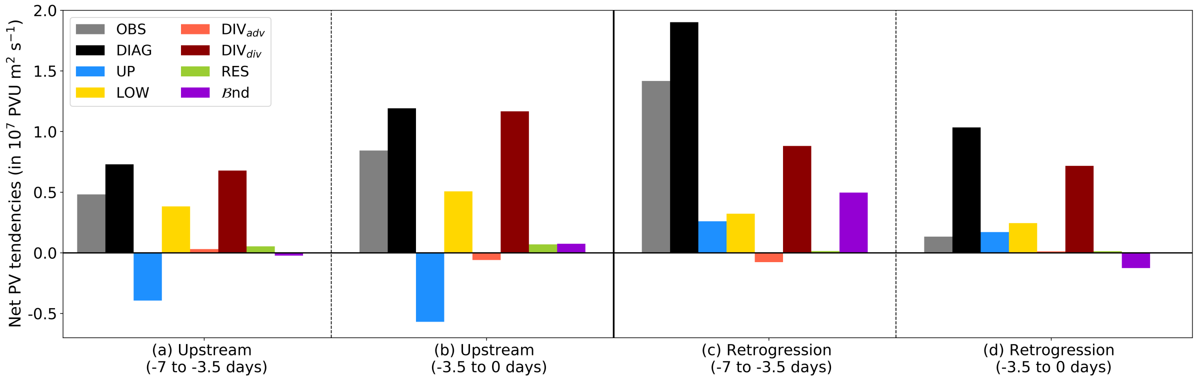

Figure 7.9: Net effect of the different contributions to the integrated amplitude evolution of onset PVAs$^-$ before GL onset for the upstream and retrogression pathway: UP (-$\mathbf{v}'_{up} \cdot \nabla q_0$), LOW (-$\mathbf{v}'_{low} \cdot \nabla q_0$), DIV$_{adv}$ (-$\mathbf{v}'_{div} \cdot \nabla q_0$), DIV$_{div}$ (q'($\nabla \cdot \mathbf{v}'_{div}$)), RES (-$\mathbf{v}'_{res} \cdot \nabla q_0$), and the boundary term $\mathscr{B}$nd. The black bar shows the diagnosed amplitude evolution as DIAG = UP + LOW + DIV$_{adv}$ + DIV$_{div}$ + RES + $\mathscr{B}$nd. The gray bar indicates the observed amplitude evolution. The net effect on the amplitude change is performed for tow time periods: -7 to -3.5 days relative to GL onset (a,c) and -3.5 days to GL onset (b,d). Only the time steps are considered if the relative area change is <= 20 % from one to the following time step.

PV tendencies relative to the PVAs$^-$ (Fig. 7.11, 7.12).

Four major differences are evident in the net onset PVA$^-$ amplitude evolution and associated contributions between the pathways. First, and as indicated in Figure 7.5b, the timing of the maximum amplification of onset PVA$^-$ differs between the pathways (Fig. 7.9). Retrograding PVAs$^-$ experience a higher net amplification in earlier times (-7 days to -3.5 days before onset, c) than shortly before the onset (-3.5 days to onset, d). In contrast, PVAs$^-$ following the upstream pathway exhibit a higher amplitude increase shortly before the onset than in earlier times. Second, in terms of contributions to the amplitude evolution, UP exhibits the most striking differences between the two pathways as it contributes to a weakening of the upstream PVA$^-$ amplitude (Fig. 7.9a,s) and to a strengthening of the retrograding PVA$^-$ amplitude (Fig. 7.9c,d). Third, DIV$_{div}$ is the leading contribution to the net amplitude increase and has a stronger effect shortly before GL onset for the upstream PVAs$^-$ (Fig. 7.9b) compared to earlier times (Fig. 7.9a). Vice versa, a higher net effect of DIV$_{div}$ is found for earlier times instead for the period -3.5 days to onset for retrograding PVAs$^-$ (Fig. 7.9c,d). And forth, LOW has a stronger amplifying net effect on the upstream PVAs$^-$ than on the retrograding PVAs$^-$ despite the fact that many regime life cycles are linked to this pathway in summer where baroclinicity is lower compared to winter.

A detailed consideration of the temporal evolution of the individual terms is important for a better understanding of the underlying dynamics, the timing and the exact location of the tendencies relative to the PVA$^-$. As indicated above, the largest difference in the contributions to the amplitude evolution of onset PVA$^-$ is visible in UP in the days before GL onset (Fig. 7.10). For the upstream pathway, the advection of background PV by the wind field associated with upper-tropospheric PV anomalies causes

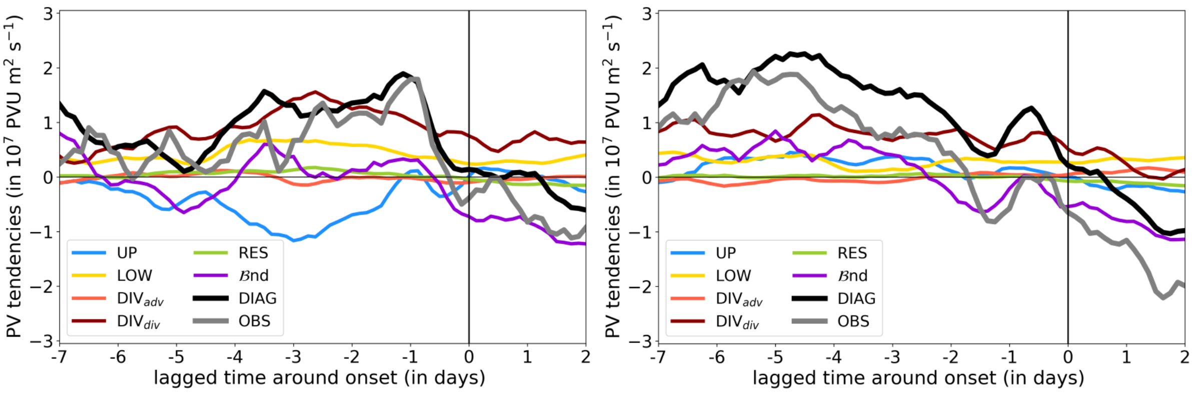

(a) upstream pathway

(b) retrogression pathway

Figure 7.10: Year-round integrated amplitude evolution of onset PVAs$^-$ around GL onset for (a) those following the upstream pathway, and (b) those following the retrogression pathway for the different PV tendency terms: UP (-$\mathbf{v}'_{up} \cdot \nabla q_0$), LOW (-$\mathbf{v}'_{low} \cdot \nabla q_0$), DIV$_{adv}$ (-$\mathbf{v}'_{div} \cdot \nabla q_0$), DIV$_{div}$ (q'($\nabla \cdot \mathbf{v}'_{div}$)), RES (-$\mathbf{v}'_{res} \cdot \nabla q_0$), and the boundary term $\mathscr{B}$nd. The thick black line shows the diagnosed amplitude evolution DIAG = UP + LOW + DIV$_{adv}$ + DIV$_{div}$ + RES + $\mathscr{B}$nd. The thick gray line indicates the observed amplitude evolution. Only the time steps are considered if the relative area change is <= 20 % from one to the following time step, as splitting and merging would lead to extraordinary values in the composite. Note that the lines are smoothed by a rolling mean of +/- 6 hours.

a strong weakening of the PVA$^-$ amplitude (Fig. 7.9a,b). This effect is strongest 2–3 days before onset and is associated with (i) a trough extending downstream to the central North Atlantic (linked to positive PV anomalies), and (ii) the general asymmetry between the anomalies upstream and downstream of the PVA$^-$ (Fig. 7.10a, Fig. 7.11f). From an RWP perspective, the upstream PVAs$^-$ are expected to be located at the trailing edge of an RWP over the North Atlantic. Shortly before the GL onset, the dominant weakening contribution of UP decreases in strength and even changes its sign, while exhibiting nearly negligible contributions 24 hours around GL onset (Fig. 7.10a). This can be attributed to the deepening of the upstream trough over the eastern US within a few days before GL onset, such that the negative tendencies of UP on the western flank of the PVA$^-$ strengthen and consequently counteract the positive PV tendencies of UP (Fig. 7.11g,h). For retrograding PVAs$^-$, in contrast, UP shows exclusively positive contributions to the amplification of onset PVAs$^-$ (Fig. 7.10b, Fig. 7.9a,b). Two days before GL onset, this effect is largest when the PVAs$^-$ are located in the eastern North Atlantic and flanked by a strong trough to the southwest that leads to strong negative PV tendencies on the western flank of the PVAs$^-$ area (Fig. 7.11c). A clear wave pattern downstream of the retrograding PVAs$^-$ is missing, such that the negative and hence amplifying PV tendencies prevail within the PVAs$^-$ (Fig. 7.11b-d). Thereby, the impression arises that the PVA$^-$ is located on the leading edge of an RWP. Over time, the trough downstream of the retrograding PVAs$^-$ over Scandinavia deepens (not shown) and the quasi-barotropic PV tendency contributes to a weakening of the PVAs$^-$ amplitude after GL onset (Fig. 7.10).

LOW amplifies the PVAs$^-$ prior to onset, independent of the pathway (Fig. 7.10). This points to the importance of baroclinic growth for the amplification of PVAs$^-$ and marks the according phase shift between the upper-tropospheric wave guide and the lower-troposphere temperature pattern. Differences

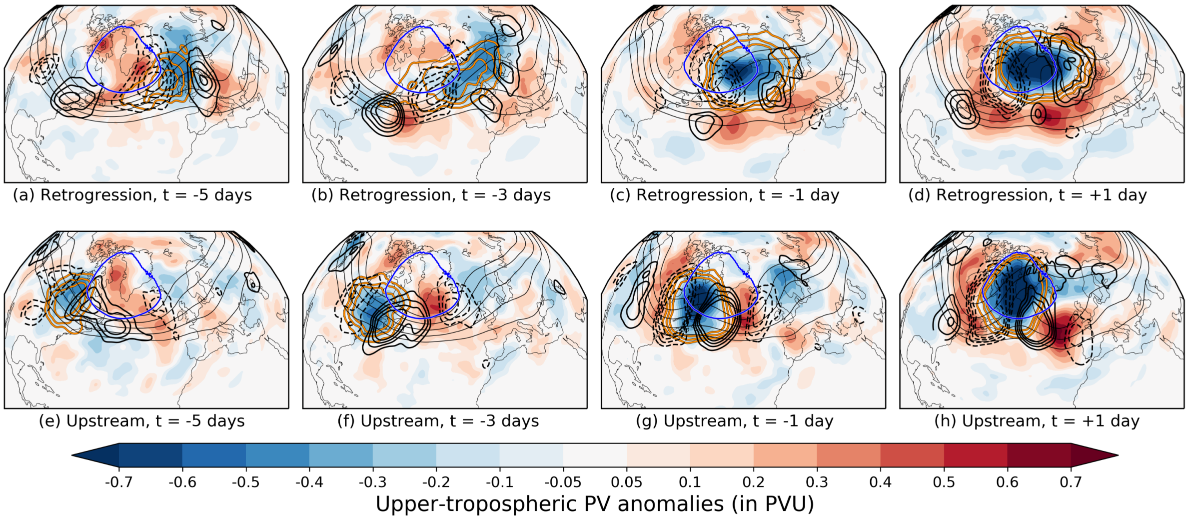
(a) Retrogression, t = -5 days
(b) Retrogression, t = -3 days
(c) Retrogression, t = -1 day
(d) Retrogression, t = +1 day
(e) Upstream, t = -5 days
(f) Upstream, t = -3 days
(g) Upstream, t = -1 day
(h) Upstream, t = +1 day

Figure 7.11: Year-round spatial composites of upper-tropospheric PV anomalies (shading, in PVU), PV tendencies of UP := $-\mathbf{v}'_{up} \cdot \nabla q_0$ (black contour lines in steps of +/- 4, 6, 8, 10, 12 10^{-6} PVU s^{-1}), Z500 (thin black lines in steps of 5350, 5400, 5450, 5500, 5550 gpm), and frequency of onset PVAs$^-$ contributing to GL (orange contour lines in steps of 0.2, 0.25, 0.3) for selected time steps relative to GL onset shown for the retrogression pathway (upper row) and upstream pathway (lower row). Positive PV tendencies are displayed in solid contour lines and negative PV tendencies are displayed in dashed contour lines. The regime mask of GL is indicated by the blue contour. Note that a time window of +/- 6 hours around the central time has been selected to slightly smooth the fields.

in the evolution of LOW between the two pathways exist in the period -4 days to -1 day before GL onset, where LOW exhibits stronger effects on the amplitude of upstream PVAs$^-$ than for the retrograding PVAs$^-$ (Fig. 7.9c,d). LOW is much more pronounced for the upstream cluster in a spatial composite sense (Fig. 7.12). One reason might be that retrograding PVAs$^-$ are more meridionally elongated and exhibit a larger area (cf. Fig. 7.5a), such that canceling effects occur in the composite due to a higher variability. Two days prior to GL onset, a warm surface anomaly is located just beneath the area where upstream PVAs$^-$ are located (Fig. 7.12g). With a cold anomaly directly located to the east (south of Greenland), it ensures the advection of low PV air towards the north, leading to an amplification of the upstream PVAs$^-$ on the eastern flank that predominates within the PVAs$^-$ in an integrated sense. Conversely, the warm anomaly on the surface is centered over Iceland for retrograding PVAs$^-$ two days before GL onset and extends far to the north (Fig. 7.12c). The rather weak contribution of LOW at the edges of the PVAs$^-$ lead in the integrated sense to only a very small positive effect on the amplification of the PVA$^-$ amplitude (Fig. 7.10, Fig. 7.9c,d).

The contribution of $\mathscr{B}$nd to the amplitude evolution of onset PVAs$^-$ differs between the two pathways. PVAs$^-$ that retrograde towards Greenland before the onset are associated with a positive contribution a few days before GL onset that turns negative two days before onset (Fig. 7.10b, Fig. 7.9c,d). This points to an early increase in the PVA$^-$ area that stagnates two days before GL onset, which fits the observed change in PVA$^-$ area (cf. Fig. 7.5a). Around and after GL onset, $\mathscr{B}$nd turns negative, suggesting a

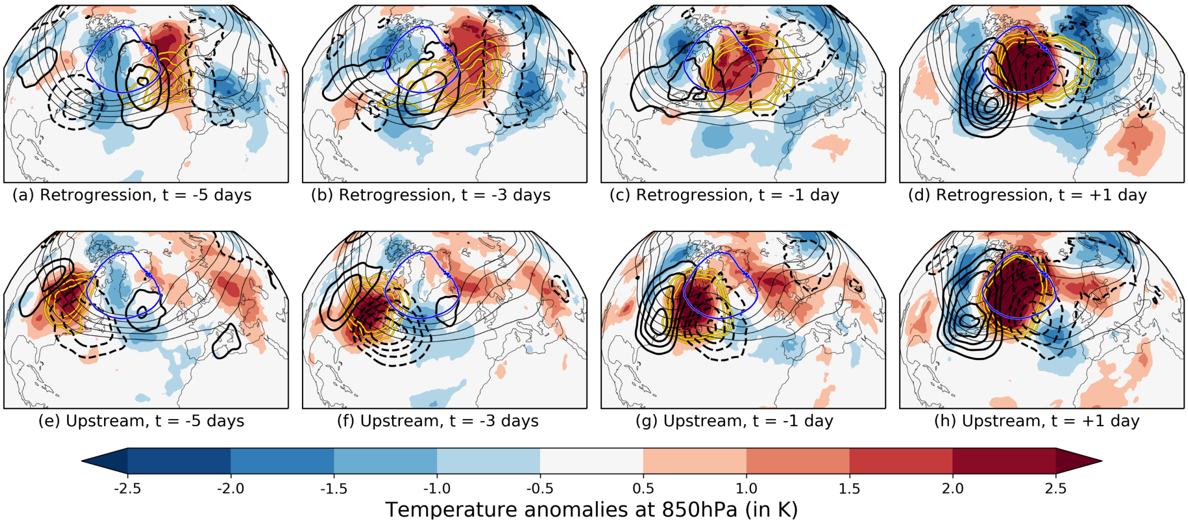

Figure 7.12: Year-round spatial composites of temperature anomalies at 850 hPa (shading, in PVU, relative to a 30-day running mean climatology 1980–2019), PV tendencies of LOW := $-\mathbf{v}'_{low} \cdot \nabla q_0$ (black contour lines in steps of +/- 0.4, 0.8, 1.2, 1.6, 2.0 $^{-6}$ PVU s^{-1}), Z500 (thin black lines in steps of 5350, 5400, 5450, 5500, 5550 gpm), and frequency of onset PVAs$^-$ contributing to GL (yellow contour lines in steps of 0.2, 0.25, 0.3) for selected time steps relative to GL onset shown for the retrogression pathway (upper row) and upstream pathway (lower row). Positive PV tendencies are displayed in solid contour lines and negative PV tendencies are displayed in dashed contour lines. The regime mask of GL is indicated by the blue contour. Note that a time window of +/- 6 hours around the central time has been selected to slightly smooth the fields.

shrinking in PVA$^-$ area. The course of $\mathscr{B}$nd runs exactly opposite, with negative values of $\mathscr{B}$nd that occur rather early for upstream propagating PVAs$^-$ (Fig. 7.10a). During the time of maximum amplification (-4 days to onset), $\mathscr{B}$nd exhibits positive values, pointing to a growth of the anomaly associated with the amplification. However, $\mathscr{B}$nd turns negative around GL onset for both pathways, which suggests a decline in PVA$^-$ area. Looking at Figure 7.5a, it does not fit the observed strengthening in the area even after the onset. A possible explanation could be that other PVAs$^-$ merge into the onset PVA$^-$. RES and DIV$_{adv}$ do not have a particular contribution to the amplitude evolution of onset PVAs$^-$ but are illustrated in Figures 7.10a and 7.9 for completeness.

The investigation of the different PV tendencies and their net contribution to the amplitude evolution revealed a key role of DIV$_{div}$ in the amplification of PVA$^-$ before the onset. For this reason, the following section will focus in detail on the role of moist processes in the formation of GL, as DIV$_{div}$ represents an indirect moist-dynamical contribution (cf. Teubler and Riemer, 2021).

7.4 Importance of moist processes for the amplification of onset PVAs$^-$

The importance of moist processes for blocking initiation has received a lot of attention in the last years (e.g., Pfahl et al., 2015; Steinfeld and Pfahl, 2019). This section discusses in detail the dominant relative contribution of DIV$_{div}$ for the amplitude evolution of onset PVAs$^-$. Equivalent to the Lagrangian

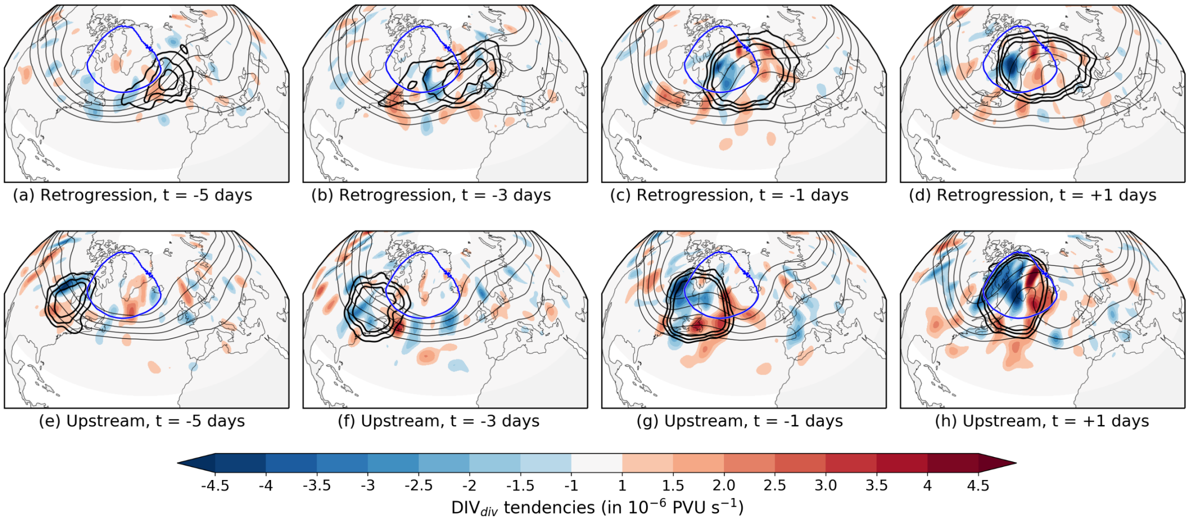
(a) Retrogression, t = -5 days
(b) Retrogression, t = -3 days
(c) Retrogression, t = -1 days
(d) Retrogression, t = +1 days
(e) Upstream, t = -5 days
(f) Upstream, t = -3 days
(g) Upstream, t = -1 days
(h) Upstream, t = +1 days

Figure 7.13: Year-round spatial composites of DIV$_{div}$ ($q'(\nabla \cdot \mathbf{v}'_{div})$, shading, in 10^{-6} PVU s^{-1}), Z500 (thin black lines in steps of 5350, 5400, 5450, 5500, 5550 gpm), and frequency of onset PVAs^{-} contributing to GL (black thick contour lines in steps of 0.2, 0.25, 0.3) for selected time steps relative to GL onset shown for the retrogression pathway (upper row) and upstream pathway (lower row). The regime mask of GL is indicated by the blue contour. Note that a time window of +/- 6 hours around the central time has been selected. Gaussian filtering has been applied to the frequency of onset PVAs^{-} ($\sigma = 2$), and a stronger smoothing has been applied to the spatial composite of DIV$_{div}$ ($\sigma = 4$).

perspective in the EuBL regime life cycle in March 2016 (cf. Chapt. 6), a further analysis examines air parcels out of the onset PVAs^{-} and investigates their vertical propagation, which gives an indication of whether they experience latent heating. This is complemented with a diagnostic on the occurrence of WCBs as proxy for moist processes (cf. Grams et al., 2011; Grams and Archambault, 2016). Overall, it is examined to what extent the signals from DIV$_{div}$ occur simultaneously with signals in the proxies for moist processes.

Independent of the pathway, the dominant contribution to the amplification of onset PVAs^{-} before GL onset arises from DIV$_{div}$ that describes the upper-level divergence with the divergent wind field and contributes throughout positively to the amplitude evolution (Fig. 7.9; Fig. 7.10). Figure 7.13 illustrates the spatial composite of DIV$_{div}$ for selected time steps relative to GL onset, and for the upstream and retrogression pathways. Strong amplifying contributions of DIV$_{div}$ at the northwestern corner of PVAs^{-} from upstream point to an amplification of the PVA^{-} several days before the GL onset (Fig. 7.13e). However, in an integrated sense, the overall contribution to the amplification of the PVAs^{-} appears slightly weaker due to the weakening contributions of DIV$_{div}$ on the southern flank of the PVAs^{-} (Fig. 7.10a). In the three days before onset, the contribution of DIV$_{div}$ to the amplification and the area share of amplifying DIV$_{div}$ values increase, which leads to a large and dominating net contribution of DIV$_{div}$ (Fig. 7.9b; Fig. 7.13f,g). The contribution of DIV$_{div}$ decreases after onset as weakening tendencies of DIV$_{div}$ strengthen on the

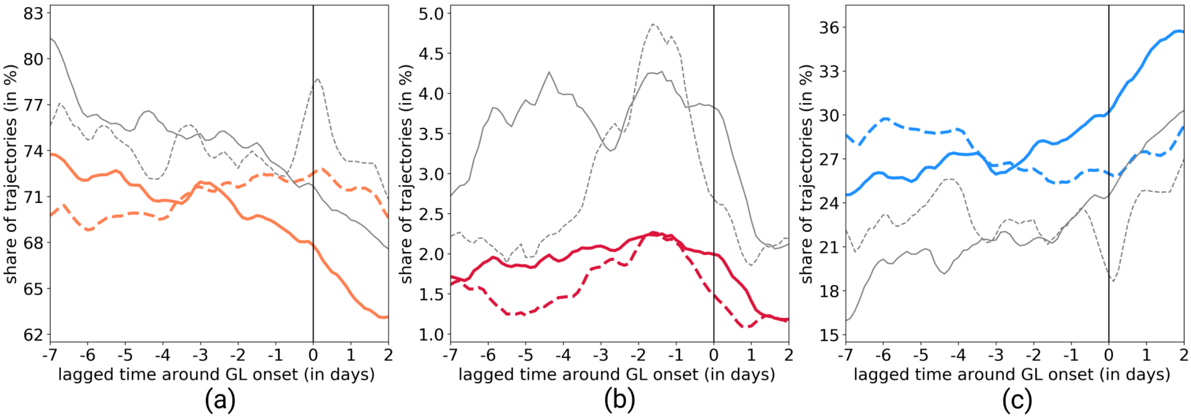

Figure 7.14: Mean share of two-day backward trajectories that end up in the onset PVAs$^-$ and that are associated with one of the three categories for the time period -7 to +2 days around GL onset: (a) ascending air parcels of less than 600 hPa, (b) rapidly ascending air parcels of at least 600 hPa, and (c) descending air parcels. The solid and dashed colored thick lines point to the year-round mean of the retrogression and upstream pathway, respectively. The thin gray lines (solid and dashed) represent the means for retrogression and upstream pathway exclusively for GL life cycles in extended winter. The vertical black line marks the time of GL onset. Curves are smoothed by the consideration of the two neighboring values.

eastern flank of the onset PVAs$^-$ (Fig. 7.13g,h).

For retrograding PVAs$^-$, the temporal evolution of the DIV$_{div}$ contribution exhibits different characteristics. The amplification of onset PVAs$^-$ occurs evenly over the entire week before GL onset, which results in a similar net contribution of DIV$_{div}$ for the period of -7 to -3.5 days compared to the period extending from -3.5 days to onset (Fig. 7.9c,d; Fig. 7.10b). Thereby, negative tendencies of DIV$_{div}$ are located more towards the western or northwestern flank, while positive tendencies of DIV$_{div}$ are located on the eastern or northeastern flank (Fig. 7.13a-c). However, the signals in the spatial composites of DIV$_{div}$ do not appear as clear as for the upstream PVAs$^-$. One reason is that PVAs$^-$, that retrograde towards Greenland, exhibit a large area (cf. Fig. 7.5a) and might be linked to a higher variability in size and shape, such that canceling effects in the composite of DIV$_{div}$ occurs. After GL onset, the contribution of DIV$_{div}$ slowly decreases to zero as upper-level convergence dominates within the onset PVAs$^-$ and mainly occurs in the center and the eastern half of the PVA$^-$ area (Fig. 7.13d). In summary, the contribution of DIV$_{div}$ is of leading importance for the amplification of PVAs$^-$, especially for the upstream pathway. Strikingly, for the retrogression pathway, it is in particular the contribution of UP and $\mathscr{B}$nd that leads to the observed highest amplification 4–5 days before GL onset, as the contribution of DIV$_{div}$ has been stable during this time period (Fig. 7.10b).

Following Steinfeld and Pfahl (2019), backward trajectories with LAGRANTO launched within the onset PVAs$^-$ are considered to provide a clearer link between DIV$_{div}$ and moist processes. Somewhat modified from their original method, the change in pressure ($\Delta p = p_{min} - p_{max}$) along the two-day backward trajectories is used to classify each trajectory into one of the following categories: (a) ascending air parcels, which experience a pressure change of less than 600 hPa ($0 < \Delta p < 600$ hPa if $t_{pmin} > t_{pmax}$); (b) rapidly ascending air parcels, associated with a pressure change of more than 600 hPa (600 hPa $\geq \Delta$ p if $t_{pmin} > t_{pmax}$); and (c) descending air parcels with a pressure difference of less than 0 hPa (Δ p < 0 hPa if $t_{pmin} < t_{pmax}$). Although the change in potential temperature is not studied here, a large pressure difference indicates the influence of latent heating for ascending air parcels or longwave radiative cooling for descending air parcels. Figure 7.14 shows the mean share of trajectories that fall into each of the three categories separately for the two pathways. Due to more baroclinicity in the winter months, the same analysis is shown for GL regime life cycles in extended winter.

The majority of trajectories ($\sim$75 %) that end up in the upper-tropospheric onset PVA$^-$ ascend, which points to their origin from lower levels (Fig. 7.14a,b). A small fraction of air parcels even shows a rapid ascent of 600 hPa within 48 hrs before they reach the onset PVA$^-$, which suggest the presence of latent heat release (Fig. 7.14a). The remaining trajectories ($\sim$25 %) are descending (Fig. 7.14c). These air parcels most likely experience longwave radiative cooling and are characterized by a descent in the upper troposphere.

The share of the three trajectory categories varies with time and exhibits clear differences between the two pathways. In particular, the share of ascending air parcels is linked to the contribution of DIV$_{div}$ in the amplitude evolution. For retrograding onset PVAs$^-$, the share of ascending air parcels is highest a week before GL onset and then decreases beyond the GL onset (Fig. 7.14a). The share of rapidly ascending air parcels is constant before the onset (Fig. 7.14b), and together with the fraction of ascending air parcels some similarity in the evolution is evident compared to the evolution of DIV$_{div}$ (cf. Fig. 7.10b). This points to the fact that phases with high contributions of DIV$_{div}$ to the amplification of the onset PVAs$^-$ co-occur with a large fraction of ascending air parcels that end up in the onset PVAs$^-$ and have likely experienced latent heating on their way. The share of ascending air parcels is lowest for the PVAs$^-$ that follow the upstream pathway around one week before the GL onset (Fig. 7.14a). Towards the onset, an increasing fraction of air parcels ascends and even rapidly ascends (Fig. 7.14a,b), suggesting an increased contribution of moist processes, which is reflected in the strengthening contribution of DIV$_{div}$ before the onset (cf. Fig. 7.10a). The highest fraction of rapidly ascending air parcels is found one day before the onset, when the amplitude evolution of upstream PVAs$^-$ peaks (cf. Fig 7.10a).

If the shares are investigated exclusively for extended winter, the qualitative course does not change, but the shares of (rapidly) ascending air parcels that end up in the onset PVAs$^-$ are clearly increased for both pathways. In particular, the share of rapidly ascending air parcels is more than twice as high in extended winter (Fig. 7.14b). WCBs are often detected via two-day trajectories that fulfill the criterion of an ascent of at least 600 hPa, which is on average associated with 20 K of latent heat release Madonna et al. (2014). The increased share of rapidly ascending air parcels in winter compared to the year-round

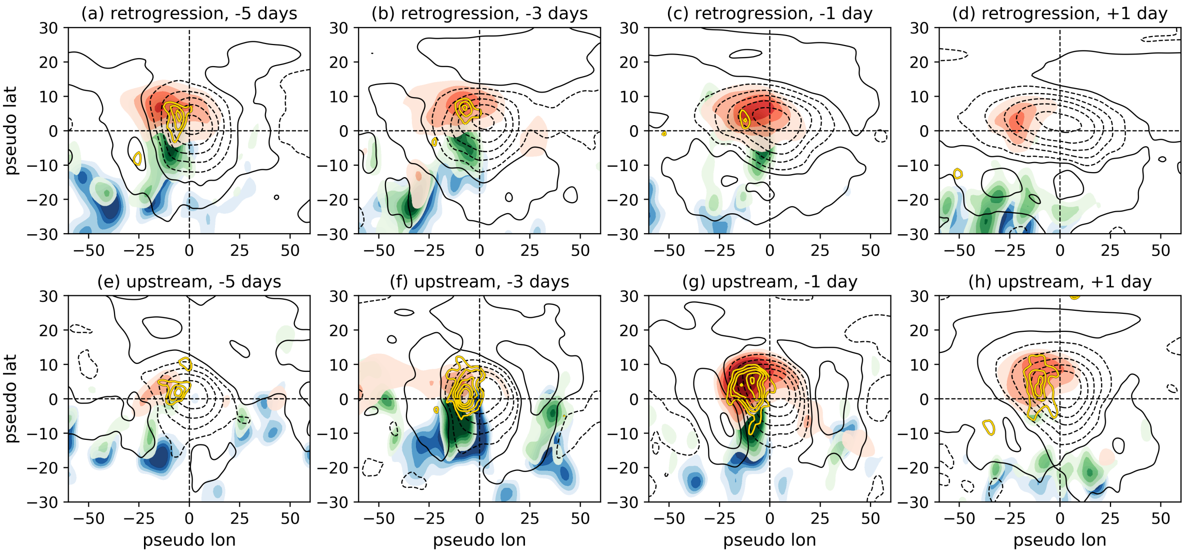

Figure 7.15: Composites centered on the position (center of mass) of onset PVAs$^-$ for selected times relative to GL onset (columns) and for the two pathways separately (rows) showing the occurrence of different WCB stages (shading) and VAPV' (black contours). Colored shading indicates the frequency of WCB inflow in the lower troposphere (blue, from 0.02 to 0.04 in steps of 0.005), WCB ascent in the mid-troposphere (green, from 0.02 to 0.045 in steps of 0.005), and WCB outflow in the upper troposphere (red, 0.06 to 0.16 in steps of 0.02). Black contours in solid and dashed illustrate the positive and negative VAPV' (500–150 hPa), respectively. The contour levels displayed are [-1.3, -1.0, -0.7, -0.4, -0.1, 0.1, 0.4, and 0.7] PVU. PV tendencies of DIV$_{div}$ are shown in gold with contour levels of [-6, -8, -10, -12, -14] 10^6 PVU m^2 s^{-1}. All fields shown are smoothed by a Gaussian filter with $\sigma = 2$.

picture fits well to the more frequent occurrence of WCBs in the winter months (e.g., Madonna et al., 2014) and elucidates the presence and contribution of diabatic processes associated with WCBs.

A further analysis is conducted, which aims to investigate if the contributions of DIV$_{div}$ are related to moist processes linked to WCBs. The Eulerian identification method of Quinting and Grams (2022, cf. Sect. 4.5) is used for this analysis. Figure 7.15 shows the frequency of the three different WCB stages (inflow, ascent, outflow) and DIV$_{div}$ in a composite centered on the center of mass position of onset PVAs$^-$ for multiple times relative to GL onset. Split up into the different pathways, Figure 7.15 provides information about the presence of WCB activity and amplifying tendencies of DIV$_{div}$ for the retrograding PVAs$^-$ (upper row) and PVAs$^-$ from upstream (lower row) separately.

The occurrence of WCBs in the vicinity of the onset PVAs$^-$ agrees well with the evolution of DIV$_{div}$ for both pathways, shown in Figure 7.10. A clear structure of the different stages of a WCB is evident with WCB inflow in the lower troposphere to the southwest of the upper-level PVA$^-$, WCB ascent slightly shifted to the north of WCB inflow and in the southwestern corner of the PVA$^-$, and WCB outflow in the northwestern or even northern branch of the PVA$^-$ (Fig. 7.15). For the retrogression pathway, WCB outflow occurs consistently before and even after onset, whereas an increase in WCB outflow frequency towards the onset is found for PVAs$^-$ that reach Greenland from upstream. The spatial extent of the PVAs$^-$ measured by the extent of PV anomalies (dashed contours) indicates once again that retrograding PVAs$^-$ exhibit a larger and meridionally elongated area than the more compact upstream PVAs$^-$ (cf. Fig. 7.5a).

Around five days prior to GL onset, the retrograding PVAs$^-$ are on average more co-located with WCB activity than the upstream PVA$^-$, most likely linked to synoptic-scale cyclone activity upstream indicated by the positive upper-tropospheric PV anomalies in the southwest quadrant (Fig. 7.15a,e). Two days later, the retrograding PVAs$^-$ are still associated with WCB activity without major changes. In contrast, strong signals in WCB inflow and ascent are evident for the PVAs$^-$ from upstream but the signals in WCB outflow still remain weak (Fig. 7.15b,f). The assumption arises that the WCB has just formed and not yet influences the upper tropospheric structure. Alternatively, it could indicate that the exact location of WCB outflow varies spatially, such that WCB occurrences cancel out on average. Shortly before GL onset, PVAs$^-$ experience the highest occurrence of WCB outflow independent of the pathway on the northwestern area of the PVA$^-$ (Fig. 7.15c,g). The frequencies of WCB outflow, ascent and inflow exhibit higher values for the upstream PVAs$^-$ pointing to a more important role of WCB activity for upstream PVAs$^-$ shortly before GL onset. This is in agreement with the higher contribution of DIV$_{div}$ to the amplification of upstream PVAs$^-$ rather than retrograding PVAs$^-$. The signals in positive PV anomalies in the southwestern quadrant points to the presence of a trough that most likely initiated the WCB (Fig. 7.15g). One day after GL onset, the occurrence of WCBs has already decreased (Fig. 7.15d,h). This also matches closely with the temporal evolution of the DIV$_{div}$ contribution that decreases from the onset (cf. Fig. 7.10).

Overall, the agreement between WCB occurrence and the contribution of DIV$_{div}$ to the amplification of the PVA$^-$ amplitude agrees very well and therefore further strengthens the link between the DIV$_{div}$ tendency and moist processes that occur throughout for retrograding PVAs$^-$ before onset and mainly shortly before onset for PVAs$^-$ from upstream. Hence, the rapid intensification of upstream PVAs$^-$ resulting from high contributions of DIV$_{div}$ shortly before GL onset is linked to WCB activity and driven by diabatic processes.

Some of the retrograding PVAs$^-$ have contributed to another blocked regime in the North Atlantic-European region before, which suggests that PVAs$^-$ can have very different lifetimes at the time of the regime onset. Therefore, it is investigated to what extent diabatic processes in the sense of WCBs occur in already very long-lived PVAs$^-$ and whether there are fundamental differences compared to very short-lived PVAs$^-$. With the novel quasi-Lagrangian tracking algorithm, the onset PVAs$^-$ are traced back to their origin, i.e. to the time when they are first detected. Two sub categories are created based on the 20. and 80. percentile of the temporal differences between the time of the first detection of the onset

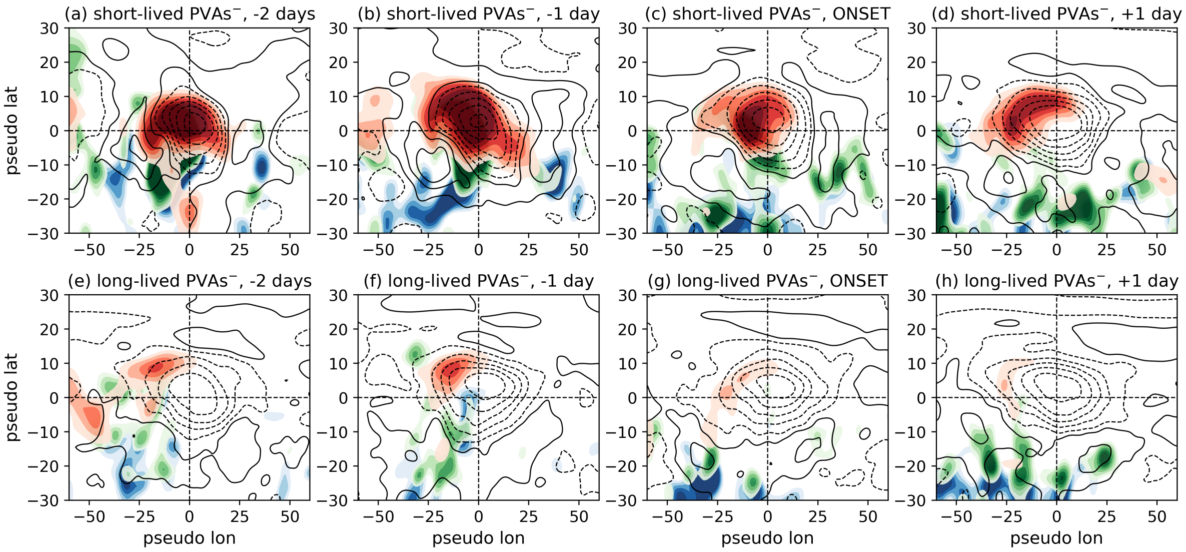

Figure 7.16: Composites centered on the position (center of mass) of onset PVAs^{-} for selected times relative to GL onset showing the occurrence of different WCB stages (shading) and VAPV' (black contours) for two different categories: (1) short-lived onset PVAs^{-} that exhibit a lifetime duration before GL onset of less than 6.3 days (upper row), and (2) long-lived PVAs^{-} that already live for more than 29.5 days at the time of the GL onset (lower row). Colored shading indicates the frequency of WCB inflow in the lower troposphere (blue, from 0.02 to 0.04 in steps of 0.005), WCB ascent in the mid-troposphere (green, from 0.02 to 0.045 in steps of 0.005), and WCB outflow in the upper troposphere (red, 0.06 to 0.16 in steps of 0.02). Black contours in solid and dashed illustrate the positive and negative VAPV' (500–150 hPa), respectively. The contour levels displayed are [-1.3, -1.0, -0.7, -0.4, -0.1, 0.1, 0.4, and 0.7] PVU. The WCB fields and VAPV' fields are smoothed by a Gaussian filter and the choice of $\sigma = 2$.

PVA^{-} and the GL onset independent of the pathway. The first category includes the PVAs^{-} that exhibit a lifetime prior to GL onset of less than 6.3 days. They are referred to as 'short-lived PVA^{-}' in the following. Around 39 % of the regime life cycles that fall into this category are linked to the upstream pathway and 61 %, and therefore the majority of regime life cycles, are linked to the retrogression pathway. The second category comprises all PVAs^{-} with a lifetime before GL onset of at least 29.5 days and refers to as 'long-lived PVA^{-}'. Two thirds of the regime life cycles that exhibit a long-lived onset PVA^{-} belong to the retrogression pathway.

Figure 7.16 shows the WCB frequency for the two categories for the time period -2 days to +1 day around GL onset, and reveals that more WCB activity co-occurs with short-lived PVAs^{-} than with long-lived PVAs^{-}. This points to the importance of diabatic processes not only for the initial development of PVAs^{-} but also for the rapid intensification of in-situ emerging PVAs^{-} that initiate a blocked flow over Greenland. For both categories, the highest WCB frequencies occur on the day before GL onset (Fig. 7.16b,f). However, the WCB frequencies are much more pronounced for the short-lived than for the long-lived PVAs^{-}. This might be the result of stronger positive PV anomalies southwest of the PVA^{-} center for short-lived PVAs^{-}, indicating that the conditions necessary for WCBs to develop are absent for the long-lived PVAs^{-}. Furthermore, the more meridionally elongated extent of negative PV anomalies

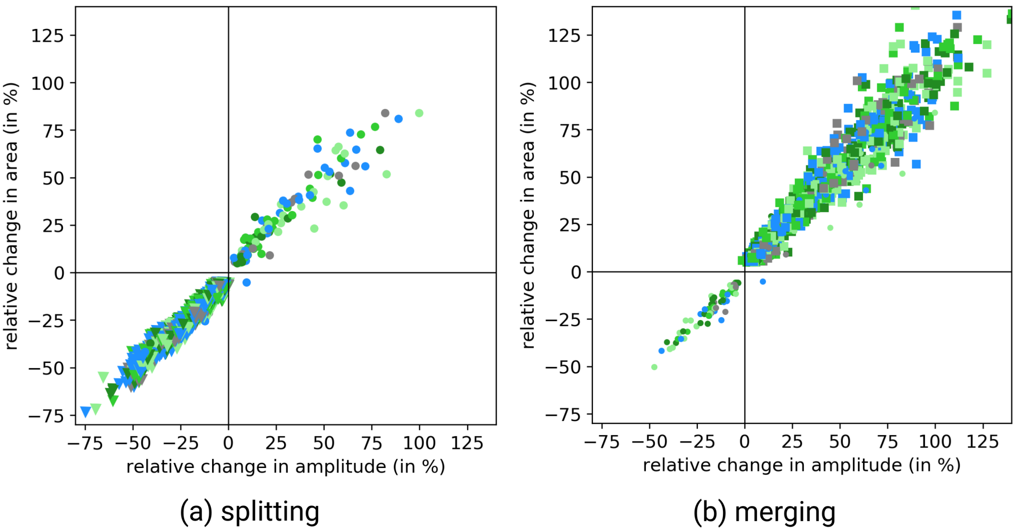

(a) splitting

(b) merging

Figure 7.17: Effect of detected (a) splitting and (b) merging events along the traced onset PVA$^-$ track in the time period -7 to +2 days around GL onset as relative change (in %) of the area and the amplitude. The triangle markers in (a) and the square markers in (b) indicate splitting and merging events, respectively. The dot markers point to the simultaneous occurrence of splitting and merging in both subfigures. The color of the markers indicates the timing relative to GL onset: -7 to -5 days (dark green), -5 to -3 days (medium green), -3 to -1 days (light green), -1 day to onset (grey), and onset to +2 days (blue). Only events are shown that exhibit a change in area of at least 5 %.

(dashed contours) for long-lived PVAs$^-$ compared to short-lived PVAs$^-$ shows the dominant proportion of retrograde migrating PVAs$^-$. As mentioned earlier, canceling effects can occur that may arise due to the higher variability in PVAs$^-$ size and shape.

This additional analysis emphasizes that diabatic processes exhibit a larger contribution to the intensification of PVAs$^-$ before GL onset for short-lived PVAs$^-$ rather than for long-lived PVAs$^-$.

7.5 Role of synoptic-scale anticyclonic eddies

After elaborating on the role that moist processes play in the amplification of onset PVAs$^-$, the focus in this section is on the role of synoptic-scale anticyclonic eddies that merge into the onset PVA$^-$ or split up from the onset PVA$^-$. Extraordinary values in $\mathscr{B}$nd result from large changes in the onset PVA$^-$ area and indicate a merging or splitting event of the anomaly. The feedback of synoptic-scale eddies on the block has already been studies for the maintenance of a block (e.g., Shutts, 1983; Yamazaki and Itoh, 2013). With the novel quasi-Lagrangian tracking algorithm that additionally identifies splitting and merging events along PVA$^-$ tracks, it is for the first time possible to quantify if observed area changes are the result of splitting and merging, or if a rapid growth and decay takes place that is linked to other processes. Compared to previous studies that focus on blocking maintenance (e.g., Yamazaki and Itoh, 2013), the effect of splitting and merging is examined here before onset. This allows to investigate whether these events influence the evolution of onset PVAs$^-$ already before a blocked flow has established, which is a

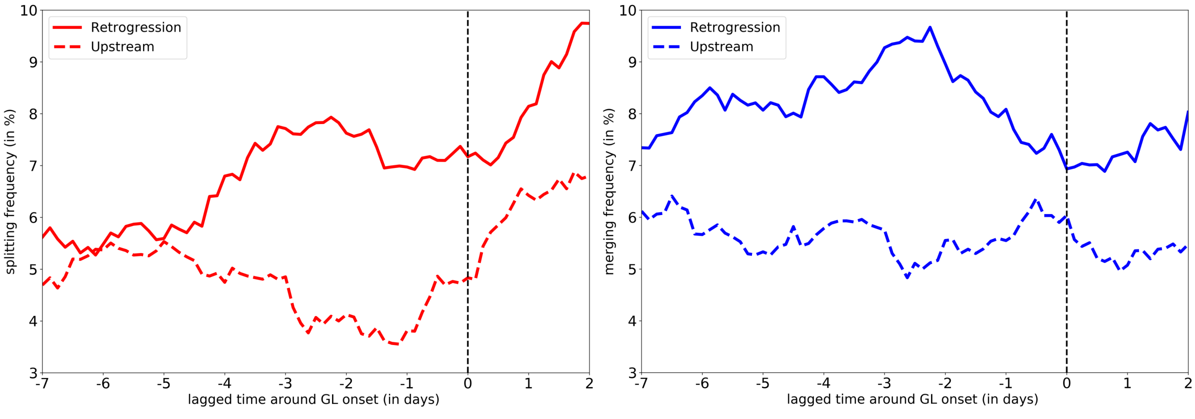

(a) splitting

(b) merging

Figure 7.18: Frequency of (a) splitting and (b) merging events relative to GL onset for the two pathways of onset PVAs$^-$ separately. For smoothing, the values of +/- one day around each time step are used. The vertical dashed line points to the GL onset.

topic that has not been covered by previous literature yet.

Figure 7.17 gives a first insight into the effect of splitting and merging events along the onset PVA$^-$ track of GL. The large number of events can be attributed to the fact that no minimum area criterion (in m^2) is applied to filter out small merging and splitting PVAs$^-$. For a clearer overview, events that trigger a relative area change in the onset PVA$^-$ of less than 5 % were excluded from the analysis in Figure 7.17. The frequency of splitting and merging events along the onset PVA$^-$ track is shown for the retrogression and upstream pathways separately in Figure 7.18. Most of the PVAs$^-$ that split up from the onset PVA$^-$ lead to a decrease in area and amplitude of the onset PVA$^-$ (Fig. 7.17a). Vice versa, if a smaller-scale PVA$^-$ merges into the onset PVA$^-$ it causes an increase in the area and amplitude in the onset PVA$^-$. Overall, the effects of splitting and merging on the PVA$^-$ area and amplitude are linear (Fig. 7.17). This means that, for example, a splitting event associated with a large relative change in onset PVA$^-$ area exhibits also large relatives changes in the onset PVA$^-$ amplitude. However, not all identified splitting and merging events are associated with expected changes in the area or amplitude of onset PVAs$^-$, which is the result of simultaneous splitting and merging (dots in Fig. 7.17). For splitting and merging, only events associated with both are predominantly located in the first and third quadrant, respectively. In the end, the net change in onset PVA$^-$ area and amplitude is determined by the event type that has the largest effect on the PVA$^-$.

The mean frequency of splitting and merging events along the onset PVA$^-$ track differs depending on the pathway, with more events along the tracks of retrograding PVAs$^-$ (Fig. 7.18). In particular, for splitting, retrograding onset PVAs$^-$ experience twice as often splitting before GL onset compared to the onset PVAs$^-$ following the upstream pathway (Fig. 7.18a). One reason for this could be that the large retrograding onset PVAs$^-$ are associated with RWB, causing portions of the low-PV air to split off that

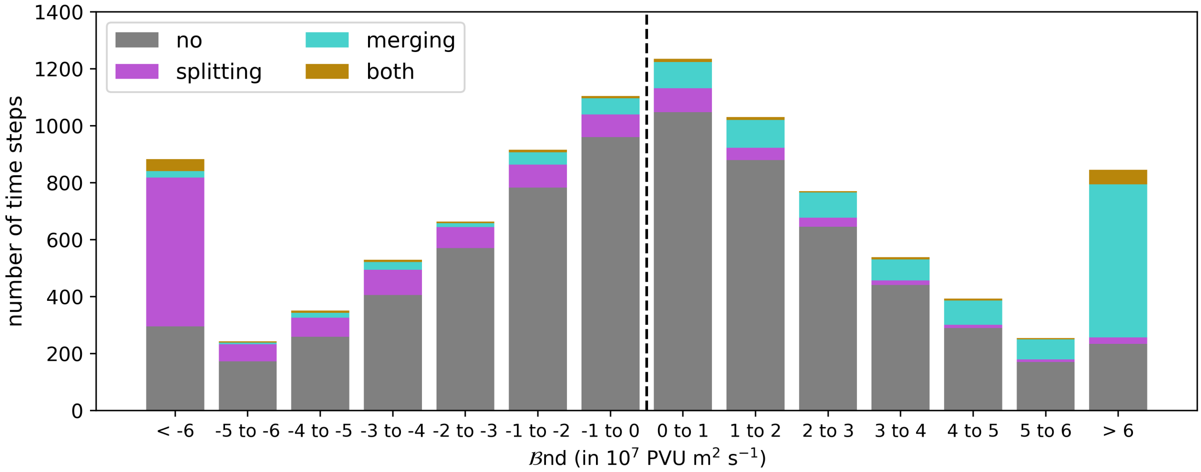

Figure 7.19: Link between the occurrence of splitting and merging identified with the quasi-Lagrangian tracking algorithm and $\mathscr{B}$nd from the PV tendency framework. The bars each represent a particular range of values of $\mathscr{B}$nd, and the colors show what absolute proportion of that range of values occurs simultaneously with splitting (violet), merging (turquoise), both simultaneously (ocher), or neither (gray). All $\mathscr{B}$nd values along the onset PVA$^-$ tracks for the time period -7 days to +2 days around GL onset are calculated according to Equation 5.6.

re-enters the area of climatologically low PV to the south. For the frequency of merging, retrograding PVAs$^-$ experience more merging than upstream PVAs$^-$ (Fig. 7.18b). Fewer mechanisms were identified to restrengthen retrograding PVAs$^-$ before onset, such that the merging of other PVAs$^-$ into the onset PVA$^-$ might be an important contribution to the maintenance or even re-strengthening of the PVAs$^-$ before onset. The frequent occurrence of splitting and merging along the track raises the question of the net effect on the amplitude and area over a certain time. The majority of onset PVAs$^-$ exhibit a net gain in area and amplitude in the period -7 days to +2 days around GL onset, independent of the pathway (Fig. B.2). In other words, the PVAs$^-$ lose less amplitude and area by splitting than they gain in amplitude and area by merging. Consistent with the finding that merging plays a larger role for retrograding PVAs$^-$, the mean net effect is higher than for upstream PVAs$^-$ (Fig. B.2).

Finally, the occurrence of splitting and merging is associated with the $\mathscr{B}$nd term of the PV tendency framework. Teubler and Riemer (2021) have argued that the occurrence of splitting and merging leads to exceptional values in $\mathscr{B}$nd. However, it was never quantified and only discussed qualitatively. One of the two terms contained in $\mathscr{B}$nd is proportional to the area change. The area change is determined for each time step in the period from -7 to +2 days around the GL onset, and it is additionally checked if splitting or merging occurs. This allows for checking whether changes in area are linked to splitting or merging, or if they are the result of a more natural increase or decay. Figure B.3 depicts the proportion of area change values associated with splitting, merging, both simultaneously, or neither. As expected, the proportion of splitting and merging increases with increasing negative and positive relative area changes, respectively. Small relative changes in area are more related to natural growth or decline of the PVA$^-$. However, not all high relative changes in area are linked to splitting or merging. For example, high growth rates

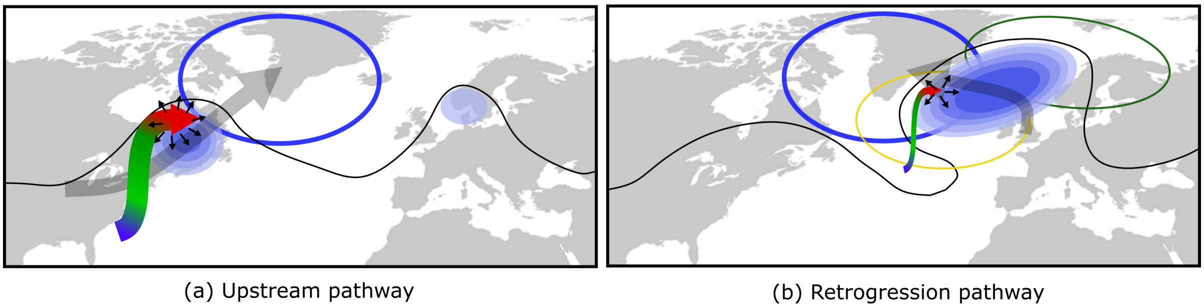

(a) Upstream pathway

(b) Retrogression pathway

Figure 7.20: Schematic summary of the main results on GL onset dynamics obtained from the quasi-Lagrangian framework, split up into the two pathways of onset PVAs$^-$: (a) upstream pathway, and (b) retrogression pathway. Gray arrows indicate the pathways. Onset PVAs$^-$ are shown shortly before the onset in different shades of blue, pointing to the amplitude strength. The blue contour line centered on the southern tip of Greenland is the regime mask of GL. The dark green and yellow contours point to the regime masks of ScBL and AR. The black line indicates the flow shortly before the GL onset. The colored arrow represents a WCB with WCB inflow (blue), WCB ascent (green), and WCB outflow (red). The thickness of the arrow is a measure of WCB activity. Black arrows show the location of divergent outflow in the upper troposphere.

occur when a PVA$^-$ initially develops and is identified for the first time. However, the complete $\mathscr{B}$nd term is not only proportional to the area change but also contains a term that describes the divergence of the PV anomaly flux (cf. Eq. 5.6). The relationship between the value ranges of the complete $\mathscr{B}$nd term and the occurrence of splitting and merging is finally shown in Figure 7.19. Exceptional high positive values of $\mathscr{B}$nd, which contribute to a sudden increase in the PVA$^-$ amplitude, predominantly occur simultaneously with merging. Vice versa, a high share of exceptional large negative $\mathscr{B}$nd values, contributing to an erratic PVA$^-$ amplitude weakening, is linked to splitting events. The occurrence of splitting and merging rarely happens in case of small changes in the $\mathscr{B}$nd term, and gets more frequent with increasing values of $\mathscr{B}$nd.
Overall, this is the first time that the relationship between high values of the $\mathscr{B}$nd term and the occurrence of splitting and merging along an anomaly is quantitatively determined.

7.6 Summary

This chapter shed light onto the dynamics of the onset of GL from the novel quasi-Lagrangian perspective. For all 177 regime life cycles in the period 1979–2021, the PVAs$^-$ that triggered the onset of the regime life cycles were identified and further investigated.

The key finding in this chapter is the elaboration of two pathways (Fig. 7.20). By tracing the onset PVAs$^-$ backwards in time, two pathways of PVAs$^-$ were found on which PVAs$^-$ propagate to Greenland in the days before GL onset. One pathway describes the northeastward propagation of PVAs$^-$ from North America upstream of Greenland (referred to as 'upstream pathway') and resembles the dominant pathway of PVAs$^-$ from March to November (Fig. 7.20a, gray arrow). The second pathway, further referred to as 'retrogression pathway', describes the northwestward displacement of PVAs$^-$ from the eastern

North Atlantic and Europe and strongly dominates in winter (Fig. 7.20b, gray arrow). However, the increased frequency of PVAs$^-$ west of Scandinavia when the upstream pathway is active indicates that both pathways can occur simultaneously (Fig. 7.20a, blue shading). Retrograding PVAs$^-$ often exhibit a connection to the active regime before when it is associated with a large-scale anticyclonic circulation anomaly, here in particular to AR and ScBL (Fig. 7.20b, dark green and yellow contour). This suggests that PVAs$^-$ following the retrogression pathway have contributed to another (blocked) regime before, whereas less than 10 % of the upstream PVAs$^-$ show an active contribution to a blocked regime before.

The pathways not only share different links to regime transitions, but also indicate a very different evolution of characteristics, and physical and dynamical processes. PVAs$^-$ that reach Greenland from upstream are relatively small and weak in the days before GL onset, but intensify and grow rapidly just before onset. In contrast, retrograding PVAs$^-$ are already considerably larger than the upstream PVAs$^-$ in the days before onset, more meridionally elongated and only experience slow but steady amplification before the onset (Fig. 7.20, blue shading). With the help of the PV tendency framework, the share of dry and moist contributions to the amplitude evolution of onset PVAs$^-$ has been quantified and unveiled that the dynamical differences between pathways are much larger than the seasonal variability. The largest differences in the contributions to the amplitude evolution emerged from the quasi-barotropic PV tendency term (UP) that counteracts the rapid amplification of the upstream PVAs$^-$, but, in contrast, has an amplifying contribution for retrograding PVAs$^-$. It has been further found that moist processes play a crucial role in the amplification of onset PVAs$^-$ in the days before onset (Fig. 7.20, colored arrow). Various proxies for moist contributions (DIV_{div}, WCB activity, air mass analyses) indicated uniformly a consistently moderate role of latent heating by the presence of WCBs for the amplification of retrograding PVAs$^-$. For upstream PVAs$^-$, the peak activity of moist processes revealed that in particular the rapid increase in amplitude and area shortly before GL onset is diabatically driven. A breakdown by the lifetime of PVAs$^-$ at the time of onset further demonstrated that long-lived PVAs$^-$, mostly associated with the retrogression pathway, are less diabatically driven than short-lived PVAs$^-$ linked to high WCB activity in the few days before onset.

Lastly, the novel quasi-Lagrangian tracking tool shed light onto the occurrence of splitting and merging along the onset PVA$^-$ tracks. It was found that splitting and merging occur more frequently for retrograding PVAs$^-$, but the net effect of both event types is positive before onset, i.e., it has a net increasing effect on amplitude and area evolution. For the first time, it was possible to quantify the occurrence of splitting and merging in the PV tendency budget originally developed by Teubler and Riemer (2016), and to objectively and clearly assign jumps in the observed amplitude change to these events.

Previous studies on the dynamics of GL or the negative NAO are very limited in number and tend to examine the dynamics from a Eulerian perspective (e.g., Feldstein, 2003) or more related to predictability and representation in climate models (e.g., Parker et al., 2018; Michel et al., 2021). Sometimes indications of the existence of the pathways are given in figures of these studies. For example, ensemble sensitivities have been detected upstream and downstream of Greenland, associated with positive Z500 anomalies over the US East Coast and over the East Atlantic (Parker et al., 2018). However, no previous study has identified these two pathways, which are also distinct due to their dynamics. This result therefore represents a novelty that could only be elaborated through the quasi-Lagrangian perspective.

8 Synopsis of blocked regime life cycles in the North Atlantic-European region

The previous chapter has shed light onto the dynamics associated with GL. From the quasi-Lagrangian perspective, novel insights were obtained into the pathways of onset PVAs^{-} and the importance and timing of moist contributions in the amplification of onset PVAs^{-} relative to GL onset.

As blocking exhibits natural variability (e.g., Woollings et al., 2018), it is of interest how the results obtained for GL in the previous chapter compare to blocking in other regions within the North Atlantic-European region, such as blocking over Europe (EuBL), blocking over Scandinavia (ScBL), and blocking over the central Atlantic (AR). In order to study the similarity and variability of blocked regimes, the chapter at hand provides a comprehensive synopsis of the dynamics of all four blocked regimes in the period 1979–2021. Teubler et al. (2023) investigated the onset dynamics of the four blocked regimes from a Eulerian perspective and revealed that linear Rossby wave dynamics and nonlinear eddy fluxes of PV are the dominant contributions to the formation of blocked regimes. In contrast, the contributions of baroclinic coupling and divergent amplification are minor. However, based on previous studies, one could expect a major and even dominant contribution of moist processes, in particular for EuBL (e.g., Grams et al., 2018; Steinfeld and Pfahl, 2019; Wandel, 2022). One limitation of the Eulerian framework has already been discussed in Section 6.5, which addresses the problem of capturing (important) signals of moist-baroclinic growth at some distance from the regime pattern. The quasi-Lagrangian view is applied here to assess if the anticipated moist dynamical signal would be quantified for the blocked regimes and how the development of PVAs^{-} differs between regimes. The chapter at hand provides insights into the PV dynamics of the full regime life cycle, namely the onset, maximum, and decay stage of all four blocked regimes. This will result, for the first time, in a complete and comprehensive synopsis of the PV dynamics of year-round blocked regime life cycles from the novel quasi-Lagrangian PV perspective.

Chapter 8 contains three sections, each comprises the analyses relative to a regime life cycle stage: onset (Sect. 8.1), maximum (Sect. 8.2), and decay (Sect. 8.3). For simplification of the complexity that multiple PVAs^{-} can contribute to the same regime life cycle, only the PVA^{-} that covers the largest share of the anticyclonic regime mask area (cf. Fig. 5.6) at the time of onset (onset PVA^{-}), maximum (maximum PVA^{-}), or decay (decay PVA^{-}) with some margin of +/- one day is considered per life cycle at each of the three life cycle stages.

8.1 Onset dynamics

This section focuses on the PV dynamics around the regime onset for all four blocked regimes. With a focus on the onset PVAs$^-$, the following aspects are addressed in this section: (i) Origin of onset PVAs$^-$ depending on blocked regime type (Sect. 8.1.1), (ii) link of onset PVA$^-$ origin to preceding regime (Sect. 8.1.1), (iii) development of onset PVA$^-$ amplitude before regime onset and the relative importance of dry and moist dynamics (Sect. 8.1.2), and (iv) role of WCB activity associated with moist processes (Sect. 8.1.2).

8.1.1 Pathways of PVAs$^-$ and link to regime transitions

Origin of onset PVAs$^-$

Equivalent to the investigation of GL pathways, it is here of interest where onset PVAs$^-$ come from and if the two pathway types of onset PVAs$^-$ for GL also exist for the three remaining blocked regimes. Figure 8.1 shows the frequency of onset PVAs$^-$ (black contours) and the relative deviation of the PVA$^-$ frequency from the 30-day running-mean climatology of PVAs$^-$ (1979–2021) for selected time steps before the regime onset. The latter provides an additional consideration of PVA$^-$ behavior independent of the onset PVAs$^-$.

The highest onset PVAs$^-$ frequency is located southwest of the anticyclonic regime part around five days before the regime onset, revealing that PVAs$^-$ contributing to regime onset originate from upstream (Fig. 8.1a,d,g,j). This suggests that most onset PVAs$^-$ are not built up locally within the regime mask and is in good agreement with the studies of Croci-Maspoli et al. (2007) and Steinfeld and Pfahl (2019), who mark the western North Atlantic as a genesis region for atmospheric blocks. Towards the regime onset, the onset PVAs$^-$ appear to propagate northeastwards (Fig. 8.1b,e,h,k). Around one day prior to regime onset, the onset PVA$^-$ frequency maximum is situated within the regime mask, indicating that onset PVAs$^-$ make up the anticyclonic part of the regime pattern during regime onset (Fig. 8.1c,f,i,l). GL exhibits two distinct PVA$^-$ frequency maxima upstream and downstream of the antecedent blocked region (Fig. 8.1j). In contrast, there is no distinct indication of multiple frequency maxima for the other three blocked regimes. Thus, the pronounced frequency maxima of onset PVAs$^-$ upstream and downstream of GL are a clear characteristic of GL and highlight two source regions of equal importance.

Despite the dominant location of onset PVAs$^-$ upstream of the blocked regime region, the same categorization as for GL in Section 7.2 is performed to assign regime life cycles and their associated onset PVAs$^-$ to an upstream and a retrogression pathway. Tracks of the onset PVAs$^-$ in the three days before regime onset are considered based on the center of mass position, which is determined by the use of the VAPV' field (cf. Sect. 5.1). A three-day track is placed in the upstream or retrogression category depending on whether the majority of positions are located west or east of the regime mask, respectively.

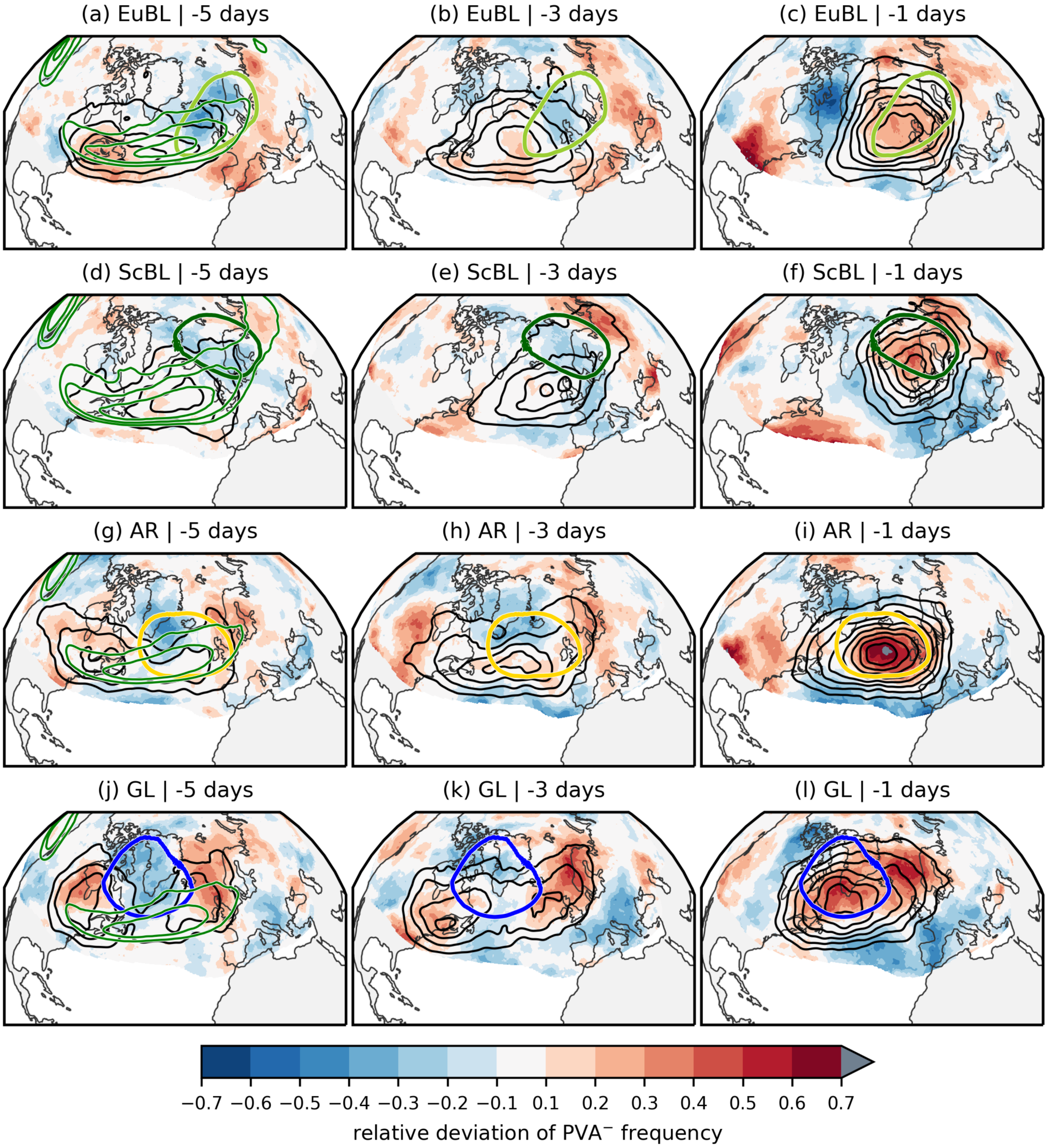

Figure 8.1: Deviation of PVA$^-$ frequency for the four blocked regimes (rows) and for selected time steps (columns) around the onset life cycle stage (shading). Black contours show the absolute frequency of the onset PVA$^-$ for the regime life cycles (in steps of 0.2, 0.25, 0.3, 0.35, 0.4, 0.45), which has been slightly smoothed with a Gaussian filter ($\sigma = 1$). The colored thick contours are the regime masks for each regime (cf. Fig. 5.6). Green contour lines in the first column show the climatological PVA$^-$ frequency in steps of 0.55, 0.6, 0.65. Note that for each time lag, the time steps +/- 6 hours around are used to obtain a clearer picture. Deviations of PVA$^-$ frequency exhibit high values in regions where the climatological frequency is exceptionally low, particularly in the subtropics, such that values are masked when the climatological frequency falls below 0.2.

Table 8.1: Division of regime life cycles into the two subcategories, depending on which pathway the defined onset PVA$^-$ follows.

	EuBL	ScBL	AR	GL
center of mass longitude	0.5 °E	13.0 °E	24.0 °W	51.5 °W
all	183	192	177	177
retrogression pathway	43 (23.5 %)	66 (34.4 %)	76 (42.9 %)	102 (57.6 %)
upstream pathway	140 (76.5 %)	126 (65.6 %)	101 (57.1 %)	75 (42.4 %)

The center of mass longitude of the regime masks used for the categorization, as well as the number of regime life cycles that fall into each of these two categories, are given in Table 8.1. Figure 8.2 displays the mean tracks of the two pathways for each of the four blocked regimes.

As previously suspected, the upstream pathway is the year-round dominant pathway of onset PVAs$^-$ for EuBL, ScBL, and AR with occurrence frequencies of 76.5 %, 65.6 % and 57.1 %, respectively (Tab. 8.1). The associated eastward propagation of PVAs$^-$ that form the anticyclonic anomaly of the regime around onset is well-known (e.g., Croci-Maspoli et al., 2007), and as such the dominant upstream pathway has been expected as the primary source of PVAs$^-$ (Fig. 8.2). Onset PVAs$^-$ from upstream are still located outside the target region (regime mask) a few days before onset and only migrate into the regime mask over time. This propagation suggests that in particular the onset of EuBL could be linked to a Rossby wave train from the subtropical western Atlantic, which is in line with Michel and Rivière (2011) and Drouard and Woollings (2018).

However, some blocked regime life cycles are assigned to the retrogression pathway of onset PVAs$^-$ with occurrence frequencies of 23.5 %, 34.4 % and 42.9 % for EuBL, ScBL and AR, respectively (Tab. 8.1). Anomalous high frequencies of PVAs$^-$ (shading in Fig. 8.1) are located east of the regime masks for all time steps before the onset and are indicative of the retrogression pathway, despite the lack of a secondary maximum in absolute onset PVAs$^-$ frequency. For some time steps, the signals downstream of the regime mask in the deviations from the climatological PVA$^-$ frequency are even more pronounced than upstream, even though the retrogression pathway is less frequent (e.g., Fig. 8.1b,e). One reason is that retrograding PVAs$^-$ are often located east of the North Atlantic, where the climatological PVA$^-$ frequency is low, such that the relative deviations can reach high values. In addition, and despite the dominant upstream pathway, it could suggest that secondary PVAs$^-$ contributing to the blocked regime are located downstream, pointing to a simultaneous occurrence of both pathways. Retrograding onset PVAs$^-$ are already near the regime mask in the days before (Fig. 8.1 right column, Fig 7.10). Interestingly, the mean pathway of retrograding onset PVAs$^-$ shows partly eastward propagation a few days before the onset, which is mostly evident for AR (Fig. 8.2c). This indicates that retrograding PVAs$^-$ eventually develop in the storm track, but experience a retrogression just before the regime onset. Based on the spatial track length, retrograding PVAs$^-$ appear to move slower than upstream PVAs$^-$, which

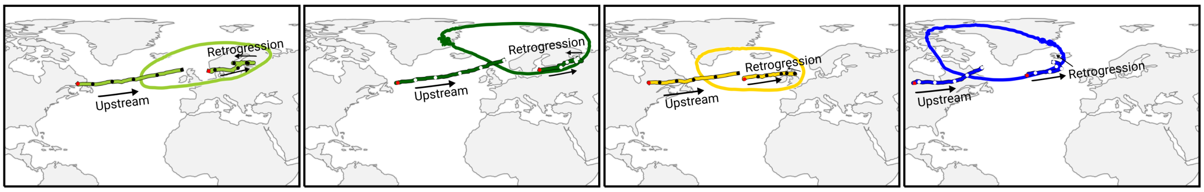

(a) EuBL (b) ScBL (c) AR (d) GL

Figure 8.2: Mean tracks of the upstream and retrogression pathways of onset PVAs$^-$ for the four blocked regimes: (a) EuBL, (b) ScBL, (c) AR, and (d) GL. Tracks are shown for the five days before onset in the respective regime color. Black and white points are set for every day, and red points correspond to the location of onset PVAs$^-$ at exactly five days before onset. The closed contour marks the position of the regime mask. For clearness, black arrows give the direction of traveling decay PVAs$^-$.

could be linked to the fact that retrograding PVAs$^-$ are more long-lived than the PVAs$^-$ from upstream before the onset (Fig. C.1). Additionally, retrograding PVAs$^-$ exhibit a certain size which allows retrograde migration at all. The slower propagation velocity also suggests that retrograding PVAs$^-$ have previously contributed to another regime in the North Atlantic-European region and consequently exhibit a more quasi-stationary behavior.

Link of onset PVA$^-$ pathways to regime transitions

The pathways of onset PVAs$^-$ sometimes cross or touch regions to earlier time lags where the block resides during other blocked regimes. Vautard (1990) investigated regime transitions in the North Atlantic-European region and found that a blocking high migrates either northward, moves eastward or decays during a regime transition. This brings up the question of whether the pathways of onset PVAs$^-$ are linked to preferred regime transitions from the angle of the seven year-round regimes. Figure 8.3 illustrates the frequencies of regime transitions into blocked regimes, split up into the two onset pathways of PVAs$^-$. Equivalent to the analysis for GL in Section 7.2, the hatching in the bars of Figure 8.3 shows the relative number of transitions in which the onset PVA$^-$ contributed to the previous regime. As a reminder, a contribution is calculated only for the regimes that exhibit a moderate anticyclonic regime anomaly (EuBL, ScBL, AR, GL, ScTr) and is defined when the onset PVA$^-$ overlaps the regime mask of the previous regime.

Generally, the preferred transition to EuBL is from ZO or ScBL (cf. Fig. 4.2b). Both regimes, ZO and ScBL, exhibit positive Z500 anomalies to the south and northeast of the EuBL regime mask, suggesting a propagation or expansion of existing PVAs$^-$, particularly for the blocked regime ScBL. Indeed, the most preferred transition to EuBL is ScBL for the retrograding pathway, and all onset PVAs$^-$ have contributed to the ScBL regime before (Fig. 8.3a). A close look at the mean retrogression pathway of onset PVAs$^-$ of EuBL reveals its location within the regime mask of ScBL that indicates a possible connection to retrograding PVAs$^-$ that make up the anticyclonic PVA$^-$ during ScBL onset. The transition to EuBL of

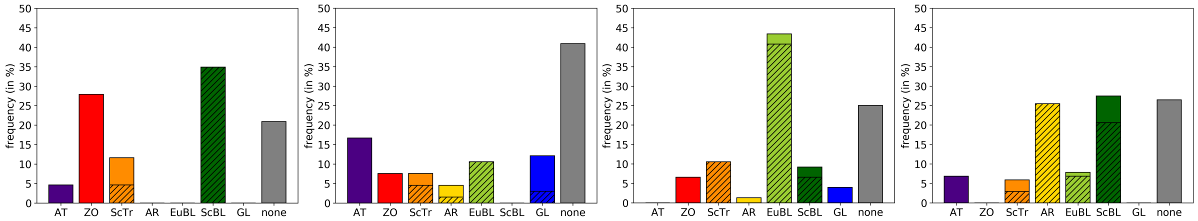

(a) EuBL, Retrogression (b) ScBL, Retrogression (c) AR, Retrogression (d) GL, Retrogression

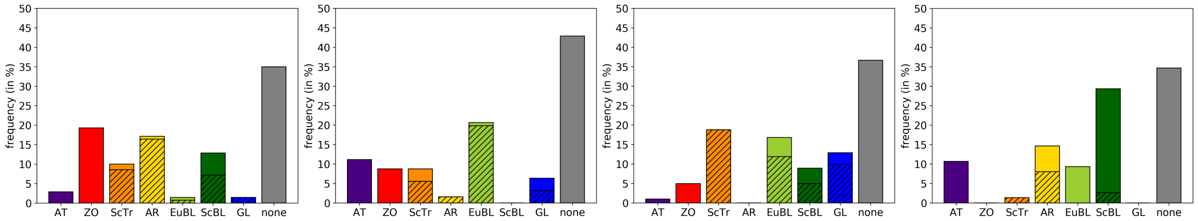

(e) EuBL, Upstream (f) ScBL, Upstream (g) AR, Upstream (h) GL, Upstream

Figure 8.3: Frequencies (in %) of regime transitions to the four blocked regimes, depending on the dominant pathway of onset PVAs$^-$: retrogression pathway (upper row) and upstream pathway (lower row). Frequencies are relative to the number of life cycles within the pathway subset. The share of regime life cycles whose onset PVA$^-$ contributes to the regime before (exhibits a spatial overlap with the regime mask of the regime before) is displayed in hatching. The contribution calculation is only performed for EuBL, ScBL, AR, GL, and ScTr, because of their moderate anticyclonic regime anomaly.

secondary importance is from ZO, which occurs in around 27 % of all transitions linked to the retrogression pathway. If onset PVAs$^-$ follow the upstream pathway, every third regime life cycle develops out of no active regime life cycle before (Fig. 8.3e). The share in the frequency of anticyclonic and cyclonic regime life cycles is equal. Still, the most frequent transition to EuBL from an active regime life cycle occurs from the cyclonic ZO regime. The preferred transition from ZO, which corresponds to the positive phase of the NAO in a good approximation, to EuBL (in the literature referred to as the blocking regime) has been recognized by many studies (e.g., Ferranti et al., 2018; Büeler et al., 2021). Interestingly, the transition from ZO to EuBL is often underestimated in sub-seasonal predictions (e.g., Büeler et al., 2021). Vautard (1990), who studied the successors of ZO, found that the most common transition from ZO occurs to blocking over Europe and is very fast and often associated with a general westward propagation of circulation anomalies. However, the present analysis shows that the transition from ZO to EuBL occurs with almost similar frequency in both pathways (Fig. 8.3a,e), such that the occurrence of the transition from ZO does not depend on the pathway. One assumption is that the extended Azores High during ZO may turn into the surface high linked to the block over Europe during EuBL. The second most frequent regime transition following the upstream pathway emerges from AR to EuBL. It suggests that PVAs$^-$ associated with AR move eastwards, which is in line with the upstream pathway that crosses the regime mask of AR before the EuBL onset (Fig. 8.2a). And indeed, nearly all onset PVAs$^-$ have contributed to AR before (hatching in Fig. 8.3e).

More than 40 % of the ScBL regime life cycles develop without a preceding regime (Fig. 4.2b, Fig. 8.3b,f). Apart from transitions out of none of the regimes, the most common transition to ScBL is from EuBL.

For the retrogression pathway, the most frequent transition occurs from the cyclonic AT regime that is characterized by a weak positive Z500 anomaly over Eurasia and suggests a westward displacement of the associated PVAs$^-$ (cf. Fig. 4.1a). This retrograding of existing PVAs$^-$ linked to blocking is quite common in transition seasons over the Eurasian Ural region (e.g., Croci-Maspoli et al., 2007). The most frequent transition when onset PVAs$^-$ follow the upstream pathway is from EuBL to ScBL (Fig. 8.3f). Almost all onset PVA$^-$ in the transition from EuBL have contributed to EuBL before and then likely moved downstream and northwards towards Scandinavia (Fig. 8.2b, Fig. 8.3f). However, in most cases, no particular regime is active beforehand (Fig. 8.3f).

For AR, the retrogression cluster strongly prefers transitions from blocked regimes in around 58 % of the cases (Fig. 8.3c). The most common transition is from EuBL (45 %), which is also the overall preferred transition independent of the PVA$^-$ pathway (cf. Fig. 4.2b). Büeler et al. (2021) indicates that this could be related to the upstream propagation of the anticyclone associated with EuBL, which is also evident in the mean track in Figure 8.2c. Almost all onset PVAs$^-$ contributed to EuBL before in the regime transition from EuBL to AR and further affirms the hypothesis of Büeler et al. (2021). For the upstream pathway, the signal for preferred transitions is less clear for AR (Fig. 8.3g). The transition from EuBL to AR is still likely, but the dominant active regime before AR is ScTr, which exhibits a climatologically weak anticyclonic circulation anomaly in proximity to the AR regime mask (Fig. 5.6, Fig. A.1). For this transition (ScTr to AR), all onset PVA$^-$ linked to the upstream pathway have previously contributed to the ScTr regime life cycle. A further preferred active regime before is GL, indicating a possible downstream propagation of the PVA$^-$ over Greenland that builds up the block over the eastern North Atlantic.

The analysis of the contributions of onset PVA$^-$ to the previous active regime has been discussed in Section 7.2 and is here linked to the actual regime transitions. In general, the most common transition to GL is from AR and ScBL (cf. Fig. 4.2b), which are also the two preferred regime transitions for both pathways (Fig. 8.3d,h). For the retrogression pathway, the transitions of AR and ScBL are the most important ones that match the results of previous studies (e.g., Croci-Maspoli et al., 2007; Michel and Rivière, 2011; Ferranti et al., 2018). The dominant regime transition for the upstream pathway of PVAs$^-$ is from ScBL to GL (Fig. 8.3h). This indicates that the transition from ScBL to GL does not necessarily have to be related to a retrograde migration of the PVA$^-$ linked to ScBL. A further signal points to transitions from AT to GL for the retrogression pathway. The mean pattern of AT shows the presence of positive Z500 anomalies west of Greenland at higher latitudes, suggesting a downstream migration of PVA$^-$ towards Greenland that could trigger a regime transition (cf. Fig. 4.1).

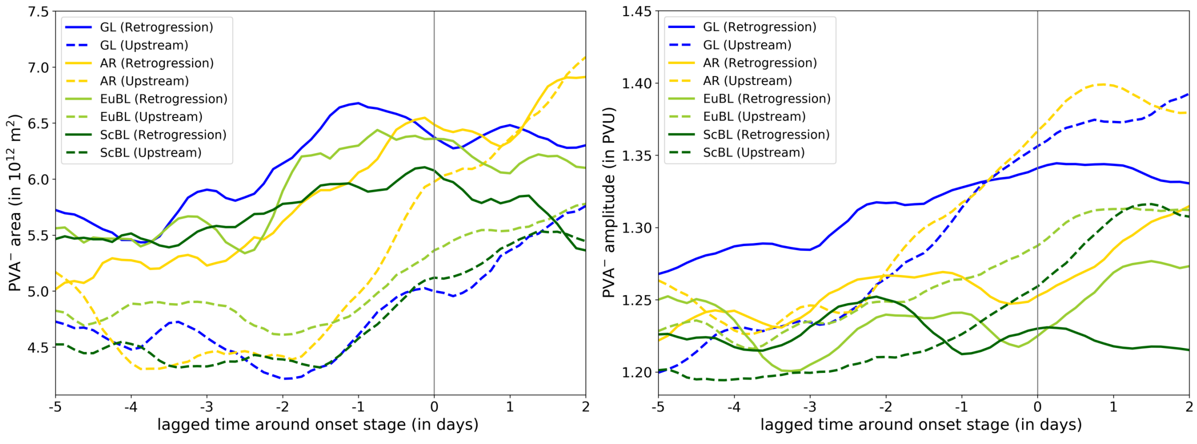

(a) (b)

Figure 8.4: Temporal evolution of (a) the onset PVA$^-$ area, and (b) the onset PVA$^-$ amplitude for onset PVAs$^-$ that follow the retrogression pathway (RG, solid) or the upstream pathway (US, dashed). The amplitude is the weighted mean based on the VAPV' field (150–500 hPa, cf. Sect. 5). The vertical line marks the time of the regime onset. The temporal evolution is slightly smoothed, considering the values +/- 6 hours around a point in time.

Summary

The tracks of PVAs$^-$ linked to blocked regime onsets in the North Atlantic-European region reveal that onset PVAs$^-$ develop remotely and propagate along different pathways to the blocking area. The two pathways found for GL in the previous chapter are also identified for the remaining three blocked regime types, with a dominant occurrence of the upstream pathway compared to the retrogression pathway. The partitioning of regime life cycles into the two different pathways of onset PVAs$^-$ gives indications to preferred transitions and the contribution of onset PVAs$^-$ to previous active regimes. Preferred regime transitions from another blocked regime often suggest a spatial shift of an existing anomaly. This is, in particular, the case for blocked regimes centered on the North Atlantic-European region, such as AR or EuBL. For the regimes with anticyclonic anomalies near the edges of the domain (GL, ScBL), the contribution of onset PVAs$^-$ is more one-handed, with contributions of upstream PVAs$^-$ for ScBL and contributions of retrograding PVAs$^-$ for GL. However, no clear differences in preferred regime transitions emerge between the pathways. Therefore, distinct constellations of regime transitions cannot be used alone as a proxy for the two pathways, which shows, for example, that not every retrograde migrating anomaly is responsible and decisive for a blocked regime onset.

8.1.2 Insights into the dynamics of the two onset PVA$^-$ pathways

This section investigates whether there are differences in the development of onset PVAs$^-$ based on the two different pathways. First, the course of the area and amplitude evolution is discussed. This if followed by investigating the contributing processes to the amplitude evolution of onset PVAs$^-$. A short insight is given into the occurrence of WCBs in the close vicinity of onset PVAs$^-$.

Temporal evolution of the onset PVA$^-$ area and amplitude

Figure 8.4 shows the temporal evolution of the area and amplitude of onset PVAs$^-$ split up by the pathway for the four different blocked regimes around the regime onset. Independent of regime and pathway, onset PVAs$^-$ grow most rapidly in the three days before regime onset (Fig. 8.4a). This agrees with the results of Steinfeld and Pfahl (2019), who found that blocks increase in size prior to blocking onset. Nevertheless, the two pathways exhibit distinct differences, with a generally larger area of the retrograding onset PVAs$^-$. This is somehow expected, given that retrograde behavior occurs primarily when the wave number is low, i.e., when long waves (and thus large-scale circulation anomalies) dominate the extratropical flow pattern. Given that onset PVAs$^-$ from upstream exhibit a shorter lifetime before regime onset than the retrograding ones (cf. Fig. C.1) supports the hypothesis that retrograding onset PVAs$^-$ are more advanced in their life cycle and might have already been part of a RWP before. Onset PVAs$^-$ from upstream exhibit a smaller area than retrograding PVAs$^-$ but experience a much stronger area growth shortly before onset. Even after regime onset, upstream PVAs$^-$ further grow in size after regime onset, while retrograding PVAs$^-$ (apart from AR) stop to grow and even shrink in size. Onset PVAs$^-$ associated with AR are characterized by a continuous growth in area that strongly continues after onset, a behavior not observed as intensively for the other regimes.

The amplitude evolution of onset PVAs$^-$ reveals an amplitude growth of the onset PVAs$^-$ for almost all regimes and pathways before the regime onset (Fig. 8.4b). Onset PVAs$^-$ associated with the upstream pathway experience a continuous and strong amplification in the days before the regime onset that continues into the active life cycle. Again, this aligns with Steinfeld and Pfahl (2019), who show that blocks generally amplify around onset. The amplification of onset PVAs$^-$ is maximum for GL and AR, and weaker for EuBL and ScBL. One possible reason arises from the definition of PV anomalies due to the presence of the stationary ridge over Europe in the climatological background field (cf. Fig. 2.1), which leads to weaker anomalies in this area. Retrograding onset PVAs$^-$ exhibit a less pronounced and not continuous amplification compared to the onset PVAs$^-$ associated with the upstream pathway. Given that retrograding PVAs$^-$ do not change much in area, either suggests that processes for strengthening and weakening of the amplitude and area are in balance. GL exhibits the largest amplitude for retrograding onset PVAs$^-$ and reveals an almost continuous but weak amplification compared to the other regimes. One reason for the striking development of the amplitude is the westward propagation of PVAs$^-$ from Scandinavia during ScBL to GL transitions (cf. Sect. 8.1.1). These PVAs$^-$ reside in a high latitude region, which is climatologically associated with high values of PV, such that PVAs$^-$ thus exhibits stronger anomalies than PVAs$^-$ in more southern latitudes with similar strength in measures of absolute PV (cf. Fig. C.2a).

Contributions to amplitude evolution of onset PVAs^{-}

The differences in the temporal evolution of the onset PVA^{-} amplitude depending on pathway and regime type raise the hypothesis that the processes contributing to the amplitude evolution differ between the regimes, particularly between the pathways. For a compact overview, Figure 8.5 shows the net effects of individual PV tendency terms - integrated over the onset PVA^{-} areas - for two defined periods of equal length before onset for the four blocked regimes and the two pathways separately. The first period (P_{early}) spans the period -7 days to -3.5 days before onset, and the second period ranges from -3.5 days before onset to the time of onset (P_{late}). For this investigation, time steps with large jumps in the area (relative change in area > 20 %) that mainly arise due to splitting and merging are excluded, as this would lead to very high values and sudden jumps in $\mathscr{B}$nd. Figure C.3 provides a more detailed view on this analysis by showing the timeline of mean integrated PV tendencies. Centered composites on the center of mass position of onset PVA^{-} for the three days before onset are shown in Figure 8.6 and illustrate the exact location of PV tendencies linked to different processes. The contributions of RES and DIV_{adv} are small, such that the net effects are negligible. Therefore, these terms are not further discussed but are still displayed in the figures for completeness.

Independent of pathway and regime, the mean composite of the diagnosed amplitude change of onset PVAs^{-} highlights a net strengthening of the amplitude in the two periods (P_{early}, P_{late}) before regime onset (Fig. 8.5). The diagnosed PVA^{-} evolution for the pathways and the four blocked regimes reveals that onset PVAs^{-} from upstream exhibit a higher net amplification during P_{late} than during P_{early}. This is in contrast to retrograding PVAs^{-}, which mostly amplify stronger during P_{early}, and shows that the timing of maximum amplification differs depending on the pathway. The comparison between the diagnosed amplitude change (black line) of the onset PVAs^{-} with the observed amplitude change (gray line) points to a good agreement in particular for the upstream PVAs^{-}, which means that the diagnosed PV tendencies capture and describe the true course of the amplitude change (Fig. C.3). For some time steps, an offset is recognizable, mostly associated with an overestimation of the true amplitude evolution by the diagnostic PV tendencies. A variety of reasons for this offset were discussed earlier (cf. Sect. 5.5, Sect. 7.3). Most importantly, the lack of the NON-CONS PV tendency term in the systematic analysis and the problems of the diagnostic to deal with deformations during highly nonlinear evolution are likely the two main reasons for the offset.

The almost continuous dominant contribution to the strengthening of the onset PVAs^{-} amplitude independent of the pathway is DIV_{div} (dark red, Fig. 8.5). This points to the importance of upper-level divergence and associated moist processes for the amplification of onset PVAs^{-} before the blocked regime onset. Negative PV tendencies of DIV_{div}, leading to an overall amplification of the PVA^{-} amplitude, are predominantly located in the northwestern corner of the PVA^{-}, whereas positive tendencies of DIV_{div}

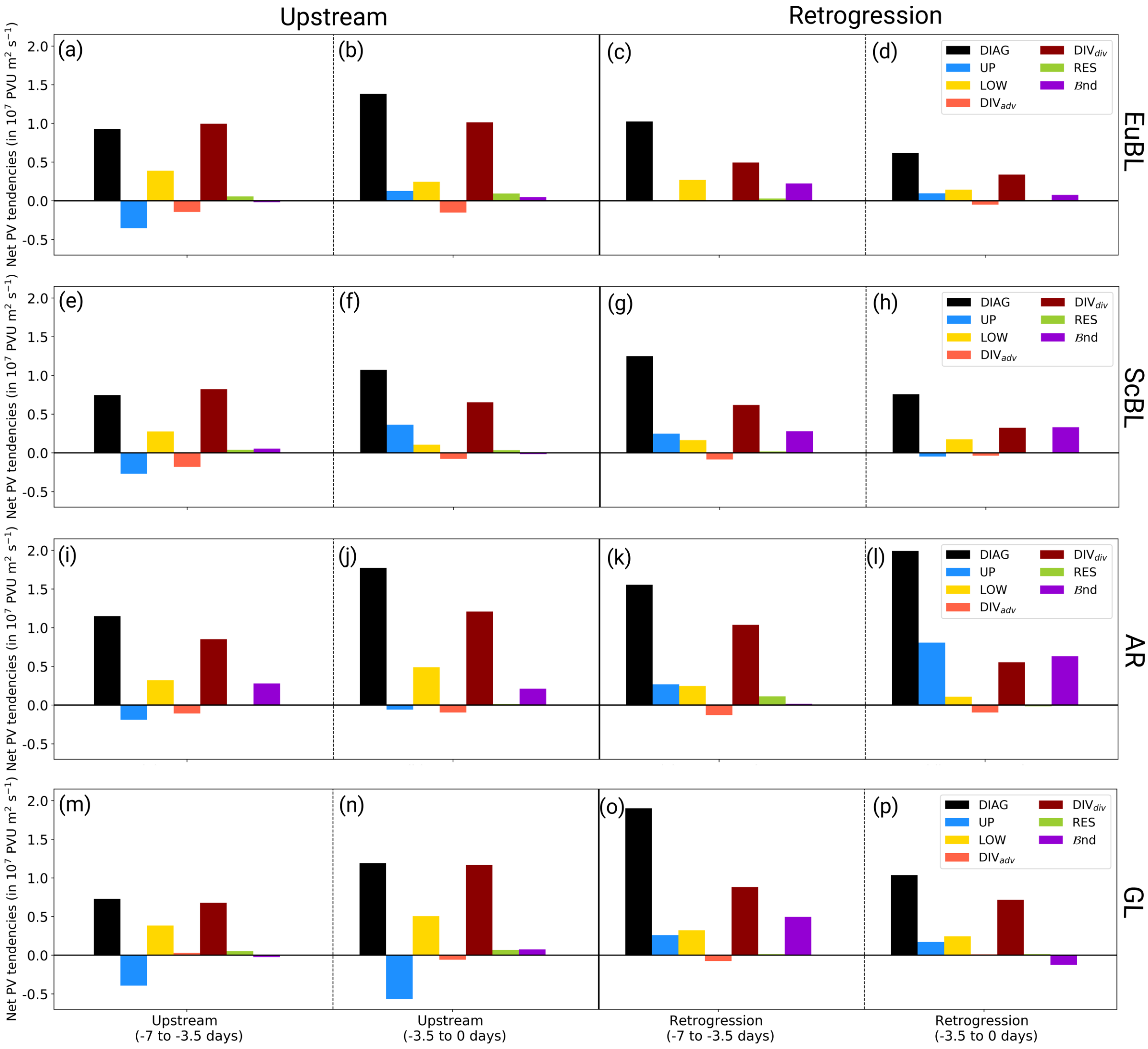

Figure 8.5: Net effect of each PV tendency to the onset PVA$^-$ amplitude evolution for the four regimes (rows) and the two pathways (double columns). The net effect is shown for two periods separately: (1) from -7 days to -3.5 days before regime onset (first and third column), and (2) from -3.5 days before regime onset to the onset (second and fourth column). The following PV tendency terms are displayed: UP ($-\mathbf{v}'_{up} \cdot \nabla q_0$), LOW ($-\mathbf{v}'_{low} \cdot \nabla q_0$), DIV$_{adv}$ ($-\mathbf{v}'_{div} \cdot \nabla q_0$), DIV$_{div}$ ($q'(\nabla \cdot \mathbf{v}'_{div})$), RES ($-\mathbf{v}'_{res} \cdot \nabla q_0$), $\mathscr{B}$nd (cf. Eq. 5.6), DIAG (= UP + LOW + DIV$_{adv}$ + DIV$_{div}$ + RES + $\mathscr{B}$nd), and OBS as the observed amplitude change (cf. Sect. 5). The composite includes only the time steps with a relative change in PVA$^-$ area change to the next time step of less than 20 %.

are located more in the eastern part of the anomaly (Fig. 8.6). The highest net contribution of DIV$_{div}$ occurs for upstream PVAs^{-} shortly before the onset during P$_{late}$ (Fig. 8.5). In contrast, the contribution of DIV$_{div}$ for retrograding PVAs^{-} is lowest during P$_{late}$, which points to a more important role of moist processes for upstream than for retrograding PVAs^{-} in the three days before regime onset. However, the higher contribution of DIV$_{div}$ during P$_{early}$ than during P$_{late}$ suggests that the retrograding PVAs^{-} might experience a really early amplification by DIV$_{div}$. Even in the two days after regime onset, DIV$_{div}$ further contributes to a strengthening of the PVA^{-} amplitude, suggesting a moist dynamic contribution that goes even beyond the regime onset (Fig. C.3). A more detailed discussion of DIV$_{div}$ focusing on the different regime types in comparison follows later.

The effect of UP ($-\mathbf{v}'_{up} \cdot \nabla q_0$) on the onset PVA^{-} amplitude evolution is often smaller than DIV$_{div}$, but still provides an important contribution (blue, Fig. 8.5). The largest difference in the contribution is evident between the pathways, with an almost continuous weakening contribution of UP for onset PVAs^{-} from upstream and a strengthening contribution for retrograding PVAs^{-}. The weakening effect of UP on upstream PVAs^{-} is most pronounced for GL (Fig. C.3g), but weakest for ScBL with an even positive net effect during P$_{late}$ (Fig. C.3c, Fig. 8.5f,n). From a climatological perspective, the frequency of RWP initiation and RWP decay shows peaks in longitudes near Greenland and near Scandinavia, respectively (Quinting and Vitart, 2019). As a result, upstream propagating PVAs^{-} of ScBL are located in a region where RWPs end such that usually the trough located upstream exhibits a larger amplitude, which leads to a quasi-barotropic strengthening of the onset PVAs^{-} on their western edge (Fig. 8.6f). In contrast, onset PVAs^{-} of GL from upstream propagate through a region where RWPs are typically initiated and represent the trailing edge of a RWP. The net weakening of the onset PVAs^{-} of GL by UP is indicated by the stronger downstream trough (Fig. 8.6h). However, closer to the onset, UP decreases in strength and even turns positive, indicating that the onset PVAs^{-} has become a more central part of the RWP (Fig. C.3g). For retrograding PVAs^{-}, UP exhibits a strengthening contribution that is in particular strongest for AR shortly before the onset during P$_{late}$ (Fig. 8.5l). The high positive contribution refers to the presence of a stronger trough upstream than downstream of the onset PVAs^{-}, which can trigger synoptic activity and, in turn, potentially reinforce the existing, retrograde-migrating onset PVAs^{-} (e.g., Mullen, 1987).

The contribution of LOW ($-\mathbf{v}'_{low} \cdot \nabla q_0$) consistently strengthens the amplitude of onset PVAs^{-} pointing to baroclinic growth (Fig. 8.5). Generally, the net effect of LOW is higher for upstream PVAs^{-} compared to retrograding PVAs^{-}, most likely because of the location of upstream PVAs^{-} over the North Atlantic where high baroclinicity prevails. For upstream PVAs^{-}, the contribution of LOW is highest for AR and GL (Fig. 8.5i,j,m,n), indicating baroclinic growth by the coupling between the upper-level wave and the temperature wave on the surface. This baroclinic growth is visible by negative tendencies of LOW (dashed yellow) within the area of the PVAs^{-} (Fig. 8.6g,h). In contrast, the rather small contribution of LOW for onset PVAs^{-} of ScBL likely arises due to the lack of a favorable phase shift, which causes

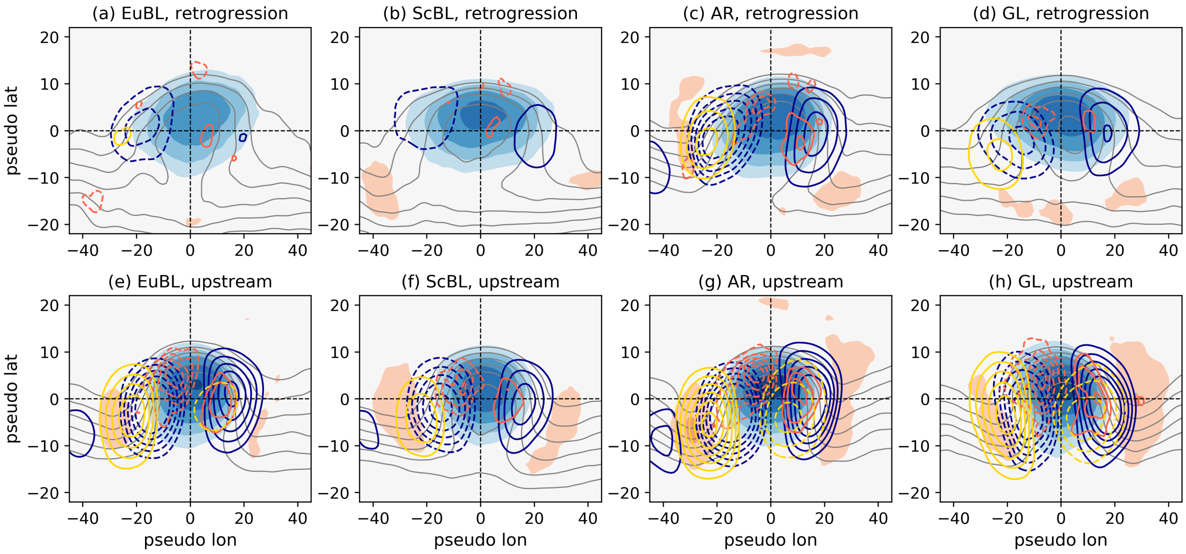

Figure 8.6: Centered composites of PV tendency terms on the center of mass position of onset PVAs$^-$ for the four different blocked regimes (columns) and the two pathways (rows) for the period -3 days before onset to onset. Red and blue shading shows positive and negative VAPV' (500–150 hPa, cf. Sect. 5.1) for the levels +/- 0.5, 1, 1.5, 2, 2.5, 3 PVU, respectively. Absolute PV (2.5, 3, 3.5, 4, 4.5, 5 PVU) is displayed in gray contour lines for selected isentropic levels (cf. Sect. 5). The main contributing three PV tendency terms are shown in colored contour lines: (i) UP (blue, $-\mathbf{v}'_{up} \cdot \nabla q_0$) in steps of +/- 1, 1.4, 1.8, 2.2, 2.6 $\cdot$ 10^7 PVU m^2 s^{-1}, (ii) LOW (gold, $-\mathbf{v}'_{low} \cdot \nabla q_0$) in steps of +/- 1.2, 1.6, 2, 2.4, 2.8, 3.2 $\cdot$ 10^6 PVU m^2 s^{-1}, and (iii) DIV$_{div}$ (red, $q'(\nabla \cdot \mathbf{v}'_{div})$) in steps of +/- 3, 5, 7, 11, 13, 15 $\cdot$ 10^7 PVU m^2 s^{-1}. Solid and dashed contours mark positive and negative PV tendencies, respectively. The tendencies of DIV$_{div}$ and the absolute PV field were smoothed with a Gaussian filter (σ = 1).

baroclinic growth. For retrograding onset PVAs$^-$, the contribution of LOW decreases from P$_{early}$ to P$_{late}$ and is small, in particular for the low-latitude blocked regimes EuBL and AR (Fig. 8.5c-d, k-l). In addition, no spatial overlap with negative tendencies of LOW with the onset PVA$^-$ area is found that could point to baroclinic coupling (Fig. 8.6c,d). The previously observed amplification of onset PVAs$^-$ after the onset is dominated by LOW, most likely because of a favorable phase shift that leads to baroclinic interaction (Fig. C.3e,f).

The contributions of $\mathscr{B}$nd are of magnitude smaller than the other PV tendency terms mentioned above (Fig. 8.5). In most cases, the net effect of $\mathscr{B}$nd is positive, which indicates a net growth of the area and agrees with the findings in Figure 7.5a. A comparison between the pathways demonstrates that $\mathscr{B}$nd exhibits a larger net effect on the amplitude for retrograding PVAs$^-$, likely due to the larger area of retrograding PVAs$^-$ compared to upstream PVAs$^-$ (Fig. 7.5a, Fig. 8.5).

Role of WCB activity before the regime onset

The analysis of PV tendencies revealed an important dominant contribution of the PV tendency related to the divergent wind field on the PVA$^-$ amplification. As divergent outflow is linked to latent heat release below, it is of interest to analyze the spatial occurrence of WCB activity and DIV$_{div}$. Figure 8.7 shows

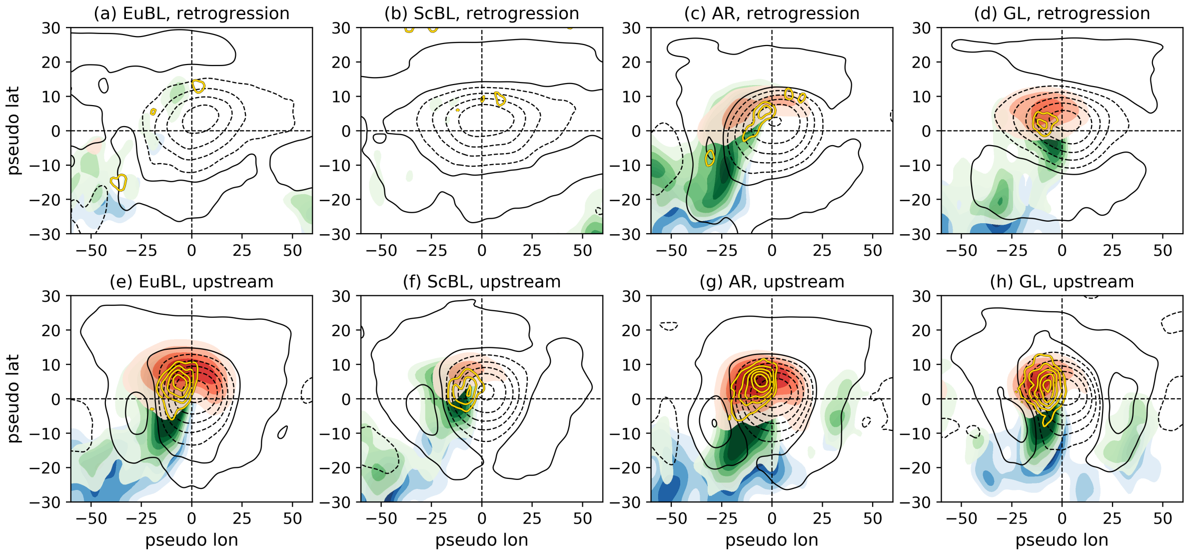

Figure 8.7: Centered composite of WCB frequency (in shading) and PV tendencies of DIV$_{div}$ on the center of mass position of onset PVAs$^-$ for the four blocked regimes (columns) and the two pathways (rows). Solid and dashed black lines indicate positive and negative VAPV' (500–150 hPa) in steps of -1.3, -1.0, -0.7, -0.4, -0.1, 0.1, 0.4, 0.7 PVU. Negative PV tendencies of DIV$_{div}$ are shown in yellow contours in steps of -3, -5, -7, -9, -11, -13, -15 $\cdot 10^6$ PVU m^2 s^{-1}. The WCB frequency is shown for the different stages of the WCB separately: (1) WCB inflow (blue shading) in contours of 1.5, 2, 2.5, 3, 3.5 %; (2) WCB ascent (green shading) in contours of 1.5, 2, 2.5, 3, 3.5, 4 %; and (3) WCB outflow (red shading) in contours of 6, 8, 10, 12, 14, 16 %. Note that the WCB frequencies and the PV anomalies are smoothed with a Gaussian filter and the choice of $\sigma = 2$ and the PV tendencies of DIV$_{div}$ with the choice of $\sigma = 1$.

composites of WCB frequency (split up in WCB inflow, ascent, and outflow) and DIV$_{div}$ on the center of mass position of onset PVAs$^-$ for the different blocked regimes (columns) and the two pathways (rows). The composites are centered on the center of mass positions of onset PVAs$^-$ and shown for the three days before onset, equivalent to Figure 8.6. The onset PVA$^-$ frequency is included in Figure 8.7 and serves as an orientation for the average share and extent of the onset PVAs$^-$. Note that the maximum frequency of onset PVAs$^-$ is not automatically associated with the center of the composite. This is because the investigated onset PVAs$^-$ are not perfectly round and compact, and can even feature very strongly deformed shapes. In terms of onset PVA$^-$ shape, the PVAs$^-$ following the retrogression pathway are significantly more extended in longitude than the PVAs$^-$ from upstream. This supports the hypothesis from above that PVAs$^-$ require a large extent for a retrogression within the mean flow.

Figure 8.7 reveals the presence of WCB activity in the close vicinity of onset PVAs$^-$ in the three days before regime onset. In line with the general picture of WCBs and their link to upper-level ridges, WCB ascent occurs predominantly west of the PVAs$^-$ center, WCB inflow southwest and the WCB outflow predominantly in the northwestern part of the PVAs$^-$. Positive PV anomalies (black lines in Fig. 8.7) in the southwestern corner of the composite are strong during high WCB activity and indicate a pronounced trough upstream. This trough suggests the presence of extratropical cyclones on the eastern flank of the upstream trough, which initiate a WCB. Negative tendencies of DIV_{div} coincide with the maximum frequencies of WCB activity, especially for ascent and outflow, which emphasizes the strong connection between divergent outflow, WCB activity and the link to moist processes (cf. Teubler and Riemer, 2021; Steinfeld and Pfahl, 2019).

Clear differences are evident in the frequency of WCBs for the different pathways, with higher WCB frequencies for the upstream PVAs^{-} (lower row) than for the retrograding PVAs^{-} (upper row). Likewise, tendencies of DIV_{div} are stronger for the upstream PVAs^{-} and lead to an overall higher contribution to the amplification of the upstream PVAs^{-} in the three days before regime onset (cf. Fig. 8.5). Therefore, the degree of WCB activity matches the strength of negative DIV_{div} tendencies, such that the relative contribution of DIV_{div} to the amplitude evolution is a good measure for the occurrence of WCBs.

Differences in WCB activity between the blocked regimes and pathways can be linked to the climatological frequency of WCBs, which peaks in the storm track region over the North Atlantic (e.g., Madonna et al., 2014). Consequently, onset PVAs^{-} following a pathway that crosses the North Atlantic region experience more WCB activity than pathways that cross only continental regions (Fig. 8.7). This is in line with Steinfeld and Pfahl (2019), who noted that contributions of moist processes to blocking are higher over oceans than over land. With the upstream pathway located in the close vicinity of the storm track (cf. Fig. 8.2), onset PVAs^{-} of AR exhibit the strongest signals in WCB activity before the onset (Fig. 8.7g), which matches the overall highest contribution of DIV_{div} to the amplification. The same applies for the upstream PVA^{-} pathway of EuBL (Fig. 8.7e). Although the upstream pathway of GL has a more continental origin, WCB activity is still high and comparable to the pathways that cross the ocean basin (Fig. 8.7h). The upstream PVA^{-} of GL propagate over the Labrador Sea shortly before GL onset, which has been identified as a moisture source for enhanced moisture transport (e.g., Papritz et al., 2022). This suggests that cyclones passing along the US East Coast and the western North Atlantic can trigger an intense activity in WCBs that amplify the onset PVAs^{-}. For upstream PVAs^{-}, WCB activity is lowest for ScBL, most likely because the track of PVAs^{-} touches the storm track regions rather early and in particular not in the three days before onset (Fig. 8.7f). Moderate WCB activity is found for retrograding PVAs^{-} linked to AR and GL, likely due to the propagation over the region of climatologically high WCB frequency from the eastern to the central North Atlantic and from the central to the western North Atlantic, respectively (Fig. 8.7c,d). Thereby, the occurrence of WCB outflow in the northwestern part of the retrograding PVAs^{-} could not only cause a re-strengthening of the PVAs^{-} but also cause the retrograde displacement of the PVAs^{-}. Lastly, less WCB activity is found for retrograding PVAs^{-} that are associated with EuBL and ScBL, which arises most likely because the pathways are located over the continent where WCBs do not occur regularly (Fig. 8.7a,b).

Summary

Onset PVAs$^-$ exhibit differences in the temporal evolution of characteristics depending on the pathway. Therefore, upstream PVAs$^-$ are smaller and weaker than retrograding PVAs$^-$ on the days before the onset. However, shortly before the onset, the upstream PVAs$^-$ rapidly grow and strengthen in amplitude, revealing a different timing of the amplification between the two pathways before the onset. A division into the individual contributions showed that the rapid amplitude amplification before the onset of the upstream PVAs$^-$ occurs predominantly through PV tendencies of DIV_{div}, which are linked to a high occurrence frequency of WCB activity and the associated presence of moist processes. For retrograding PVAs$^-$, the contribution of moist processes is of less importance in the days before regime onset but still provides a mechanism for the re-intensification and the westward displacement of the PVAs$^-$.

8.2 Maximum stage dynamics

This section focuses on the dynamics of the maximum stage of blocked regimes from a quasi-Lagrangian PV perspective. Blocking anticyclones are expected to remain stationary over a certain area during a blocking episode. However, the definition of weather regimes via the I_{WR} and low-pass filtered Z500 anomalies allows for a replacement of the PVA^- by another one. To investigate the dynamics around the maximum stage, only the maximum $PVAs^-$ are considered. The shares of regime life cycles where the maximum PVA^- is the same PVA^- as the onset PVA^- are 44.8 % for EuBL, 45.3 % for ScBL, 56.5 % for AR, and 58.2 % for GL, which justifies the decision to define maximum PVA^- for the analysis of the maximum stage.

First, the propagation of maximum $PVAs^-$ is investigated around the maximum stage (Sect. 8.2.1). Analogously to the onset $PVAs^-$, insights into the temporal evolution of maximum PVA^- characteristics are presented, with a focus on the amplitude evolution and contributions from PV tendency terms (Sect. 8.2.2). A full picture of the dynamics of regime life cycles from onset to decay based on the maximum $PVAs^-$ is given in Section 8.2.3. Motivated by a recent study of Drouard et al. (2021), a short excursion handles very short and very long regime life cycles separately and analyses, whether differences in the contributions to the amplitude evolution of maximum $PVAs^-$ determine the regime life cycle length.

8.2.1 Propagation of maximum $PVAs^-$

During the maximum stage of blocked flow patterns, the blocking anticyclone has reached its maximum manifestation and is stationary. Such a behavior is also expected from a regime perspective, as the maximum stage is defined as a local maxima in the I_{WR} within a regime life cycle. High values in the I_{WR} result not only from the correct positions of Z500 anomalies, but also from the strength. Consequently, the further strengthening of the I_{WR} before the I_{WR} maximum can be associated with either a strengthening of a quasi-stationary PVA^- within the regime mask (cf. Fig. 5.6) or the migration of a PVA^- into the regime mask. Analogously, the decrease in I_{WR} after the maximum stage could be associated with a local weakening of a quasi-stationary PVA^- or the migration away from the regime mask.

Figure 8.8 shows the anomalous frequency of $PVAs^-$ normalized with the PVA^- climatology and the frequency of the maximum $PVAs^-$ around the maximum stage. For all four blocked regimes, the maximum $PVAs^-$ are precisely centered over the regime mask at the maximum stage (black contours in the middle column of Fig. 8.8). It corroborates the idea of the weather regime life cycle thinking that a weather regime is well pronounced and roughly corresponds to its mean pattern at the maximum stage. An anomalous low frequency of $PVAs^-$ prevails almost completely around the regime mask. This reflects the location of the jet or cyclonic weather systems, which are blocked or redirected. Even three

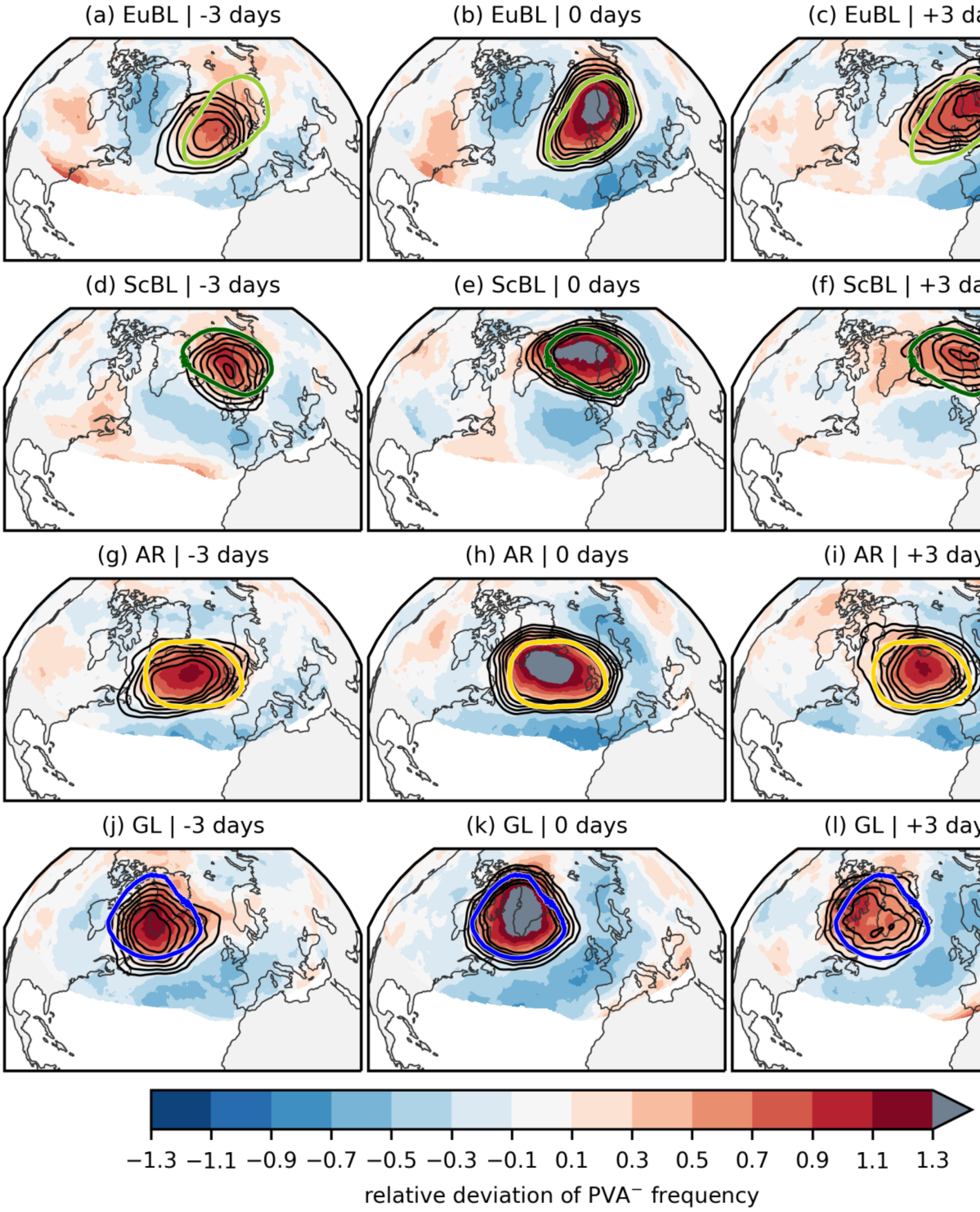

Figure 8.8: Relative deviation of PVA$^-$ frequency for the four blocked regimes (rows) and for selected time steps (columns) around the maximum life cycle stage (shading). Black contours show the frequency of the maximum PVAs$^-$ in steps of 0.2, 0.25, 0.3, 0.35, 0.4, 0.45. Colored contours represent the regime masks for each regime (cf. Fig. 5.6). Note that for each time lag the time steps +/- 6 hours around are used in addition for a clearer picture. The relative deviations in the subtropics exhibit high values in the relative deviation and are masked when the climatological frequency falls below a frequency of 20 %.

days before and after the maximum stage, the maximum PVAs$^-$ are still close to the regime mask's center, revealing a quasi-stationary behavior of the PVAs$^-$ around the maximum stage. This behavior is consistent with the observations and studies of atmospheric blocking (e.g., Steinfeld and Pfahl, 2019). It emphasizes that similar characteristics can be found when blocking is investigated from a weather regime perspective.

However, the northeastward motion of the strongest relative positive deviation of the PVA$^-$ frequency around EuBL maximum points to a more transient behavior of maximum PVAs$^-$ (Fig. 8.8a-c). Three days before the EuBL maximum, an increased frequency of PVAs$^-$ over Scandinavia suggests that the block associated with the maximum PVA$^-$ extends to higher latitudes (Fig. 8.8a). At the same time, the anomalous high frequency of PVAs$^-$ over the eastern United States could point to feeding anticyclonic eddies or to an evolving RWP with another ridge located at the US East Coast (Fig. 8.8b). An equivalent signal develops for ScBL before the maximum stage (Fig. 8.8d). The anomalous high frequency of PVAs$^-$ after ScBL maximum northwest of the regime mask (Fig. 8.8f) points to a retrograding behavior of PVAs$^-$ after the maximum stage, consistent with ScBL being a frequent precursor to GL (cf. Sect. 8.1.1). For AR, a north-south stretching of the signal in the maximum PVA$^-$ location is visible just before the maximum stage, and a slight tendency for maximum PVA$^-$ to retrograde northwestward after the maximum (Fig. 8.8g,f). The north-south stretching could be linked to the pathways of onset PVAs$^-$, with a displacement of a PVA$^-$ from Europe to the central North Atlantic via the preferred transition from EuBL to AR, and an eastward propagation of a PVA$^-$ over the western North Atlantic linked to the ScTr to AR transition (cf. Sect. 8.1.1). Although the majority of maximum PVAs$^-$ are centered over Greenland before the maximum stage, the anomalous high frequency of PVAs$^-$ over Scandinavia (Fig. 8.8j) suggests retrograding feeding anticyclonic eddies from the east or even westward migrating maximum PVA$^-$ towards Greenland, which can occur during the frequent ScBL to GL transitions (cf. Sect. 8.1.1).

8.2.2 Characteristics of maximum PVAs$^-$

The findings above raise a follow-up question on how properties, such as the area and amplitude, change with time around the maximum stage. Due to the stationarity of the maximum PVAs$^-$, insights into the different PV tendency contributions to the amplitude evolution before and after the maximum stage will shed light on the processes linked to the maximum manifestation of blocked regimes.

Handling of the different lengths of regime life cycles

One major challenge in the systematic evaluation of blocked regime dynamics around the maximum stage is the highly variable regime life cycle length. The mean length from onset to maximum stage and from maximum stage to decay is five days, but can generally range from two to 29 days (Fig. C.4a).

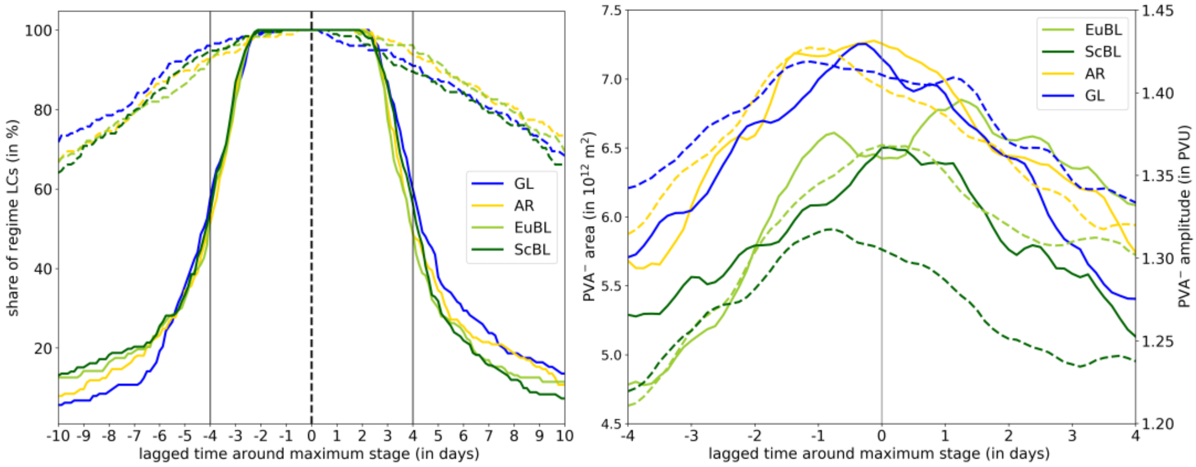

(a) (b)

Figure 8.9: (a) Relative number of regime life cycles that are active (solid, in %) and percentage of regime life cycles with an existing maximum PVA^{-} (dashed, in %) relative to the maximum stage of the regime life cycles. The two vertical solid lines at -4 days and +4 days point to the dates where approximately 50 % of the life cycles are active. (b) Temporal evolution of the area (solid, left y-axis) and the amplitude (dashed, right y-axis) of maximum PVAs^{-} relative to the maximum stage. The amplitude is measured as mean in the VAPV' field within the maximum PVA^{-} (cf. Sect. 5.1). Note the changes in the x-axis extent between the two subfigures.

Consequently, the analysis time around the maximum stage needs to be limited, as the focus is set on the evolution of maximum PVAs^{-} *within* the active regime life cycle. This also prevents a mixing of signals from different life cycle stages, which would occur beyond a certain time lag caused by very short regime life cycles. Figure 8.9a displays the number of active regime life cycles and the number of existing maximum PVA^{-} relative to the maximum stage for all four blocked regimes. The plateau in the share of regime life cycles (solid lines) visible at +/- 2.5 days around the maximum stage is an artifact due to the specified life cycle length of at least five days (cf. Grams et al., 2017). With temporal distance from the regime maximum, an increasing number of regime life cycles approach their onset or decay, which leads to a decaying number of active regime life cycles. In addition, some maximum PVAs^{-} form earlier than others and decay later than others, such that the sample size of life cycles that can be investigated shrinks with increasing temporal distance to the maximum stage (dashed lines). As around 50 % of the regime life cycles are still active four days before and after the maximum stage, the following analyses are limited to this period.

In almost half of all regime life cycle, the maximum PVA^{-} is the same PVA^{-} as the onset PVA^{-}. This raises the question of whether there is a link to the regime life cycle length. Figure C.4b shows the distribution of regime life cycle lengths based on the two categories: (a) the maximum PVA^{-} corresponds to the onset PVA^{-}, or (b) the maximum PVA^{-} has no connection to the onset PVA^{-}. In fact, if the maximum PVA^{-} is still the same as around the onset, there is a tendency for a shorter life cycle length. Vice versa, life cycles are longer when the main contributing PVA^{-} changes between the onset and the maximum stage. This suggests that for longer regime life cycles, the replacement of the onset PVA$^-$ by another PVA$^-$ is essential for maintaining the regime pattern.

Temporal evolution of maximum PVA$^-$ area and amplitude

The evolution of maximum PVA$^-$ area (solid lines) and amplitude (dashed lines) is illustrated in Figure 8.9b. Note that the evolution of PVA$^-$ amplitude measured in VAPV instead of VAPV' is shown in Figure C.2. For all blocked regimes, the maximum PVA$^-$ strengthens and increases in size before the regime life cycle maximum is reached and weakens afterward while losing in area. However, some differences in the evolution of area and amplitude exist between the regimes. First, the maximum PVAs$^-$ of AR and GL are stronger and larger than the maximum PVAs$^-$ of EuBL and ScBL. And second, differences occur in the timing of the maximum area and amplitude relative to the maximum stage. All blocked regimes except for EuBL are characterized by a nearly symmetric buildup and breakdown of the maximum PVA$^-$ area relative to the maximum stage. The amplitude of PVA$^-$ peaks already before the life cycle maximum for all blocked regimes except for EuBL. This suggests that the growth in area is not necessarily associated with an amplification. As a result, the temporal evolution of maximum PVAs$^-$ around the EuBL maximum life cycle stage stands out. Maximum PVAs$^-$ associated with EuBL indicate the most rapid and strongest growth in both area and amplitude before the maximum stage. This differs from the results of Steinfeld and Pfahl (2019), who argue that the area and amplitude of blocks remain stable and constant during the blocking mature stage. Miller and Wang (2022), who investigated the onset mechanisms for blocks, point to the fact that blocks over Europe rapidly develop as they are associated with high-frequency synoptic processes, which agrees well with the findings presented here. Even after the regime maximum, the maximum PVAs$^-$ of EuBL seems to increase further in area, with a peak around two days after the maximum.

Contributions to the amplitude evolution of maximum PVAs$^-$

Although the temporal evolution of maximum PVAs$^-$ generally agrees very well between the four blocked regimes, the small differences discussed above suggest some distinct variability in the underlying dynamics between the regimes. Integrated PV tendencies over the maximum PVAs$^-$ are displayed in Figure 8.10 for all four blocked regimes. Note that, consistent with the previous analyses of PV tendencies, only the time steps are considered that are associated with a relative change in PVA$^-$ area of less than 20 %.

All maximum PVAs$^-$ experience a strengthening of the amplitude before the maximum stage and a weakening of the amplitude after the maximum stage, independent of blocked regime type (Fig 8.10). UP ($-\mathbf{v}'_{up} \cdot \nabla q_0$) contributes to the amplification before the maximum stage and is the leading contribution to the amplitude weakening after the maximum stage. This behavior of UP is in good agreement

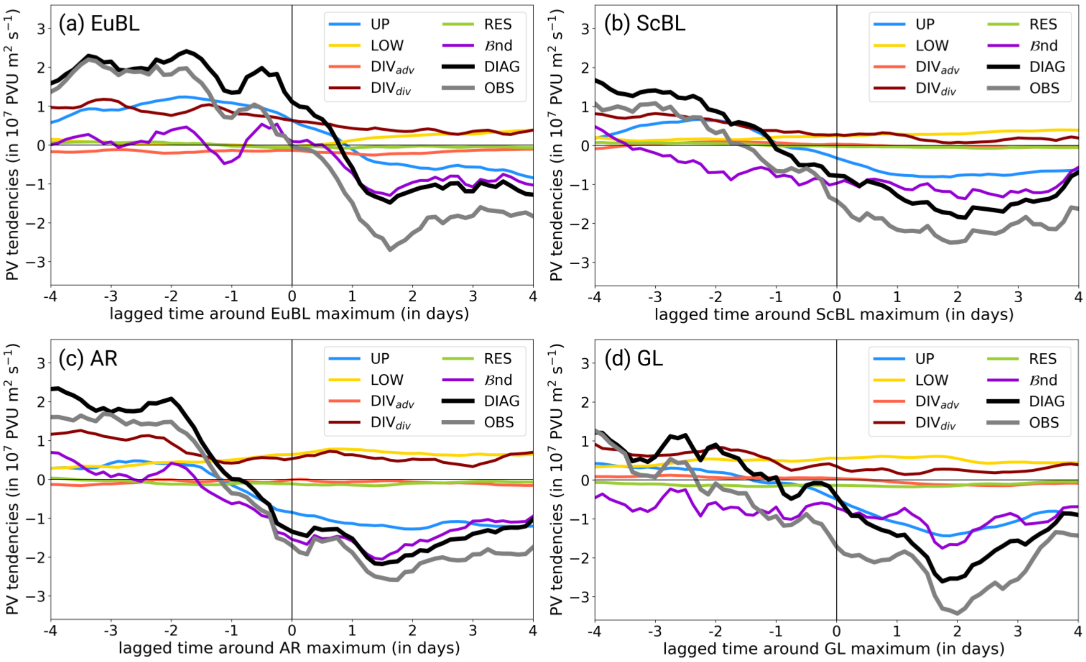

Figure 8.10: Year-round perspective of integrated PV tendencies of the maximum PVA$^-$ areas for the period -4 to +4 days around regime life cycle maximum for the four blocked regimes: (a) EuBL, (b) ScBL, (c) AR, and (d) GL. Positive and negative PV tendency terms point to the mean strengthening and weakening of the maximum PVAs$^-$, respectively. DIAG represents the sum of all processes, such that DIAG = UP + LOW + DIV$_{adv}$ + DIV$_{div}$ + RES + $\mathscr{B}$nd. OBS denotes the observed change in amplitude, defined as the forward difference in the integrated PVA over the maximum PVA$^-$ area. As $\mathscr{B}$nd can exhibit very large values in case of extraordinary changes in the area (e.g., by significant splitting and merging events), PV tendencies from single time steps are excluded from the analysis when the relative change in area from to another time step exceeds +/- 20 %. For each time step displayed, a mean +/- 6 hours around the time step is selected for a smoother illustration of the temporal evolution.

with Teubler and Riemer (2021), who found that their quasi-barotropic PV tendency term dominates the decay of PVA amplitude associated with ridges within a RWP. The contribution of LOW ($-\mathbf{v}'_{low} \cdot \nabla q_0$) is always to strengthen the amplitude, thus indicating baroclinic growth of the maximum PVAs$^-$. LOW exhibits larger contributions after the maximum stage than before, which constitutes a behavior that has also been noted by Teubler and Riemer (2021). Moreover, the fact that LOW growths in strength after UP reached its maximum contribution to the amplification suggests downstream baroclinic development as described by Teubler and Riemer (2021): Ridges are first amplified by upper-level wave dynamics and then grow further due to the presence of baroclinicity. In most cases, DIV$_{div}$ (q'($\nabla\cdot$ $\mathbf{v}'_{div}$)) is the leading term in the amplification of maximum PVAs$^-$ before the maximum stage. This suggests that the maximum in PVA$^-$ amplitude is strongly related to the amplification by upper-level divergent outflow, consistent with the findings of Teubler and Riemer (2021). After the maximum stage, the contribution of DIV$_{div}$ is still positive but weaker. The contribution of $\mathscr{B}$nd is strongly negative after the maximum stage and is a leading contribution in the weakening of the maximum PVAs$^-$, most likely as the PVA$^-$ decreases in size.

However, differences are evident between the four regime types and discussed in the following. First, a major difference between the regimes is the dominant contribution of UP to the strengthening of maximum PVAs$^-$ before the EuBL maximum stage (Fig 8.10a). This suggests an asymmetry of the troughs upstream and downstream of the maximum PVAs$^-$ that leads to a net strengthening on the western flank of the PVAs$^-$ due to a strong trough upstream. The positive contribution of UP remains even beyond the maximum stage when UP turned already negative for the other regimes. Second, downstream baroclinic development as indicated by Teubler and Riemer (2021) is most evident for EuBL and ScBL, but occurs earlier for ScBL than for EuBL (Fig 8.10a,b). Third, differences occur in the contribution of $\mathscr{B}$nd. Before the maximum stage, $\mathscr{B}$nd contributes to a strengthening of the PVAs$^-$ for EuBL and AR, which resemble the more southern blocking configurations (Fig 8.10a,c). Despite the criterion that only time steps are considered when the relative change of the area does not exceed 20 %, merging of smaller anticyclonic PVAs$^-$ could potentially play a role in addition to the steady growth in the PVA$^-$ area (Fig. 8.9b). In contrast, for the high-latitude blocks GL and ScBL, $\mathscr{B}$nd is already negative before the maximum stage and contributes to a weakening of the maximum PVAs$^-$ (Fig 8.10b,d).

8.2.3 Active regime life cycle dynamics

As mentioned before, the regime life cycles exhibit different lengths, which makes a systematic evaluation of the importance of various processes for the full regime life cycles difficult (cf. Fig. C.4a). Calculating the net effect of PV tendency terms for a specific period (cf. Fig. 7.9) is one way to capture the dynamics of the full regime life cycle, independent of the regime life cycle length. Here, the net effect of PV tendency terms on the amplitude integrated over the area of maximum PVAs$^-$ is shown for two periods: (1) from onset to the maximum stage and (2) from maximum stage to decay. In order to account for the differences in period lengths between the regime life cycles, the summed up PV tendencies are normalized by the number of time steps within the respective period. Again, only time steps are included with a relative area change of less than 20 % to the following time step.

Analysis for all regime life cycles

Figure 8.11 shows the net effects on the maximum PVAs$^-$ for the four blocked regimes for the two different periods before and after the maximum stage. Independent of the regime type, maximum PVAs$^-$ experience a net increase in amplitude from onset to maximum stage and a net decrease in amplitude from maximum stage to decay (black bars). This agrees well with the analysis of maximum PVAs$^-$ around the maximum stage in Figure 8.9. In the following, the focus is set on novel insights and differences to the analysis above in order to avoid redundancy.

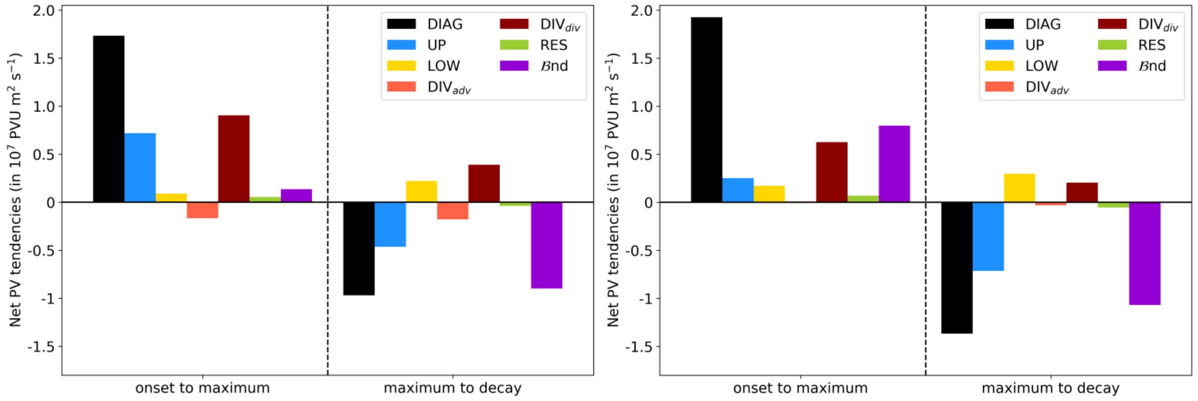

(a) EuBL (b) ScBL

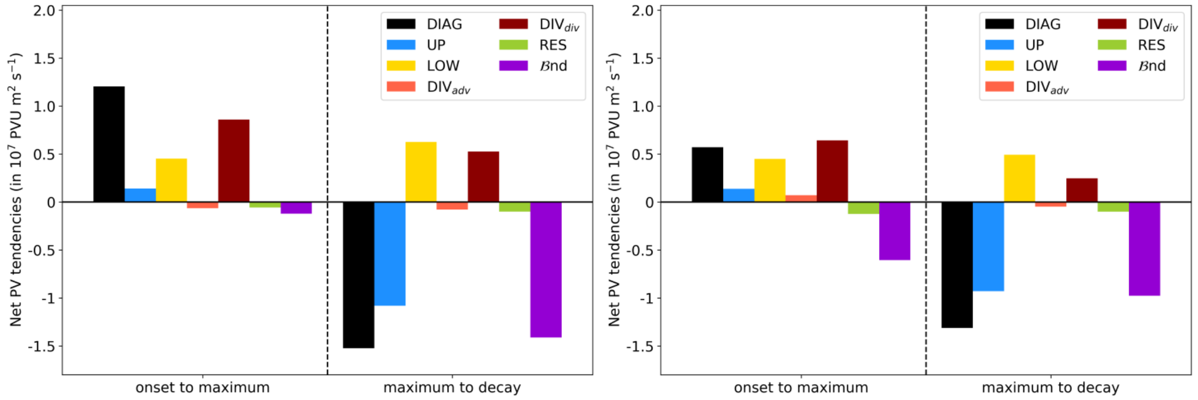

(c) AR (d) GL

Figure 8.11: Net effect of different PV tendency terms for the two periods of each life cycle integrated over the maximum $PVAs^-$: (a) active regime life cycle from onset to maximum, and (b) active regime life cycle from maximum to decay. The net PV tendency for each PV tendency term and the two periods is calculated as the mean of all time steps that fall into the category. A negative or positive net PV tendency points to a net weakening or strengthening contribution to the amplitude evolution of the maximum $PVAs^-$, respectively. As $\mathscr{B}$nd can exhibit very large values in case of extraordinary changes in the area (e.g., by large splitting and merging events), PV tendencies from single time steps are excluded from the analysis when the relative change in area from to another time step exceeds +/- 20 %.

Most importantly, the insight into the full regime life cycle from onset to decay agrees with the results obtained from the maximum PVA^- in the +/- four days around the maximum stage. This indicates that an analysis around the maximum regime life cycle is sufficient to describe the full active regime life cycle dynamics, as around half of the regime life cycles exhibit such a length that the full life cycle is covered within the analysis period +/- four days around the maximum stage. In agreement with Figure 8.10, the contribution of UP before the maximum is highest for EuBL (Fig. 8.11a) and further supports the finding that quasi-barotropic upper-tropospheric wave dynamics make an important contribution, as already recognized in Figure 8.10a. The contribution of DIV_{div} dominates the net amplification of the maximum PVA^- prior to maximum stage for all blocked regimes (Fig. 8.11). The highest contributions are found for EuBL and AR, which are the low-latitude blocked regimes that exhibit their anticyclonic circulation anomaly in the proximity of the storm track regions where an interaction between the maximum PVA$^-$ and synoptic-scale systems and associated features like WCBs can make moist-dynamical contributions to the amplification. Compared to the period between the onset and the maximum stage, the net contribution of DIV$_{div}$ is weaker after the maximum stage. This suggests that moist processes linked to DIV$_{div}$ are an important maintenance and reinforcement contribution for the PVAs$^-$.

A major difference between the analysis here and the insights around the maximum stage provided in Figure 8.10 is the net contribution of $\mathscr{B}$nd for ScBL before the maximum stage (Fig. 8.11b). The period between the onset and the maximum stage is the longest for ScBL compared to the three other blocked regimes (cf. Fig. C.4a), such that differences to Figure 8.10 are most anticipated for ScBL. A net contribution of $\mathscr{B}$nd is negative for the four days before the maximum stage (Fig. 8.10b), but strongly positive between the onset and maximum stage (Fig. 8.11b). This indicates that the maximum PVAs$^-$ undergo some net growth of the area earlier in the regime life cycle. This is not captured in the analysis limited to a few days around the maximum stage. Consequently, the analysis of the full regime life cycle is important to capture the overall development within the regime life cycle.

Comparison of dynamics for long and short regime life cycles

The blocked regime life cycles vary heavily in length, such that the question arises whether there are distinct discrepancies in the net contributions of PV tendencies for very short and very long life cycles. Such an analysis could reveal if short regime life cycles lack certain processes important for the maintenance of maximum PVA$^-$ that depicts the anticyclonic part of the regime pattern. For this purpose, the 20 % longest and the 20 % shortest regime life cycles are selected, and the same analysis as in Figure 8.11 is performed for each regime type. Figure 8.12 shows the net contributions to the amplitude change of the maximum PVAs$^-$ split into very short (left) and very long (right) regime life cycles. Short life cycles exhibit maximum lengths of less than seven days, and long life cycles comprises life cycles with more than 14 days.

No uniform statement can be made on the net amplitude change of maximum PVAs$^-$ between long and short regime life cycles (Fig. 8.11). For AR and GL, the net change in amplitude is similar for short and long regime life cycles before the maximum stage. However, for EuBL, a higher net amplitude growth is identified for shorter regime life cycles, which indicates a rapid amplification of the maximum PVAs$^-$ in the few days between onset and maximum stage (Fig. 8.11a,b). In contrast, the net effect of the amplitude growth is substantially larger for longer life cycles of ScBL before the maximum (Fig. 8.11c,d). It suggests that the maximum PVA$^-$ of ScBL is further and consistently amplified, leading to the longevity of the maximum PVA$^-$ and the regime life cycle.

Differences in the contributions to the amplitude evolution provide indications on mechanisms for long and short regime life cycles from the perspective of maximum PVA$^-$. Most importantly, DIV$_{div}$ exhibits

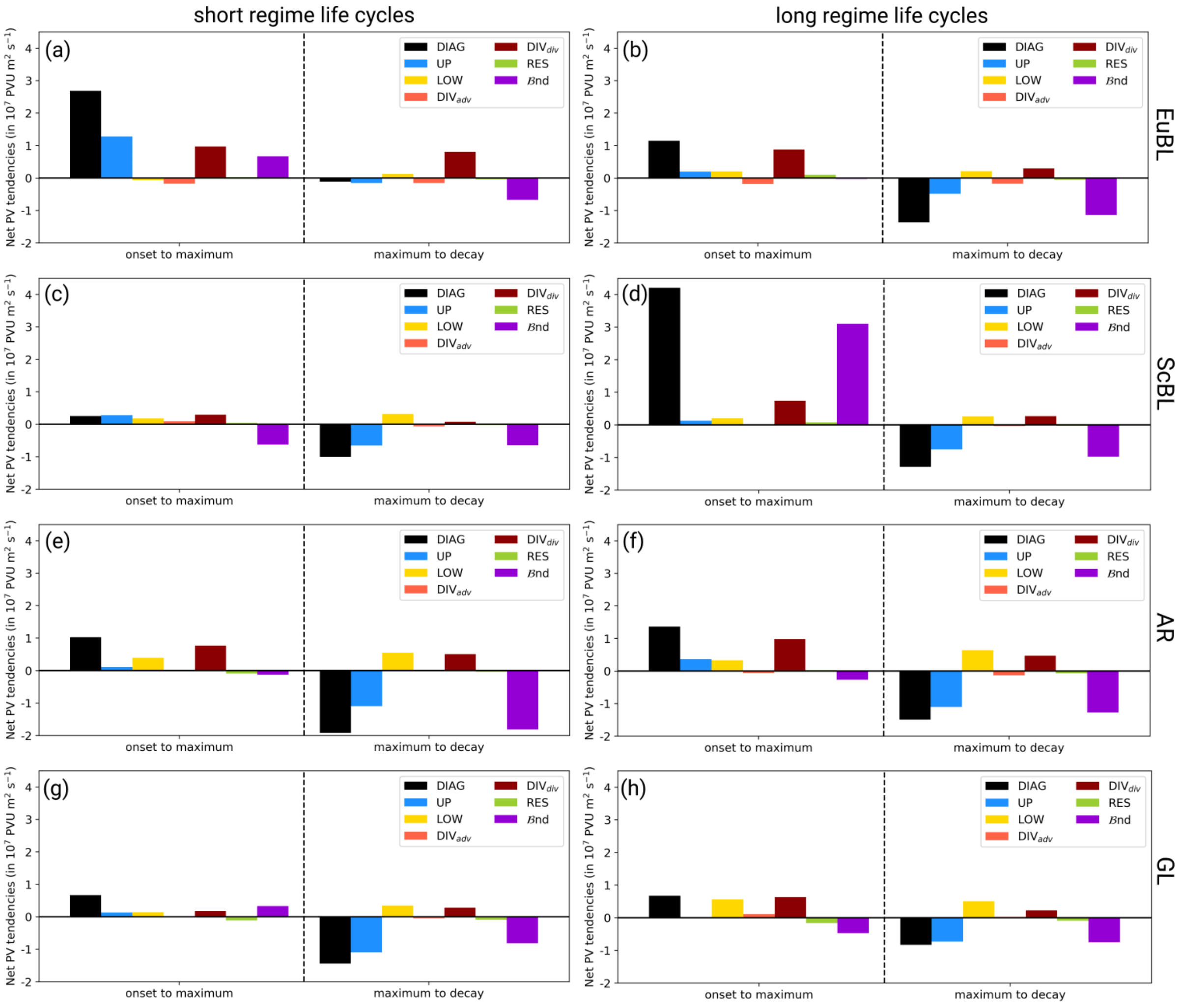

Figure 8.12: Net effect of different PV tendency terms for the two periods of each life cycle integrated over the maximum PVAs^{-}, separated into short blocks (left column) and long blocks (right column). A negative or positive net PV tendency value points to a net weakening or strengthening contribution to the amplitude evolution of the maximum PVAs^{-}, respectively.

larger contributions for longer than for shorter life cycles before the maximum stage (Fig. 8.11). This points to the importance of moist processes for the maintenance of the long regime life cycle, such that the decay or lack of moist processes could be one factor that limits the life cycle length. Furthermore, UP shows a large net contribution before the maximum stage for very short life cycle, which contrasts with the nearly negligible net effect for very long life cycles (Fig. 8.12a,b). This suggests a strong asymmetry in the trough-ridge couplets in the upper troposphere, with a likely stronger trough upstream of the maximum PVA$^-$. It creates optimal conditions for synoptic-scale activity upstream, which influences the maximum PVA$^-$ evolution for the rapidly evolving short regime life cycles. The contribution of LOW is consistently positive. Another difference in the processes between short and long life cycles is evident for LOW, which has a stronger positive contribution for the very long life cycles (Fig. 8.12). It points to the importance of LOW to decelerate the decay of maximum PVA$^-$, which could favor longer life cycles. This is in particular the case for AR (Fig. 8.12f). Last, $\mathscr{B}$nd exhibits a large positive net effect before the maximum stage for long regime life cycles of ScBL in contrast to the negative effect for short regime life cycles, which leads to an overall highly positive net effect on the amplitude change (Fig. 8.12b,d). Together with a net effect of DIV$_{div}$ twice as large as for short regime life cycles, it suggests that the maximum PVAs$^-$ experience a stronger growth in area, likely linked to the presence of moist processes, which leads to the maintenance of the regime pattern. Apart from ScBL, $\mathscr{B}$nd is linked to a small or even negative net effect for long regime life cycles before the maximum stage.

Summary

The investigation of the dynamics around the regime life cycle maximum stage from the quasi-Lagrangian PV perspective reveals that the maximum PVAs$^-$ are mainly stationary, which coincides with the definition of blocking. Consequently, the maximum PVAs$^-$ describe the evolution of the anticyclonic part of all four blocked regime patterns around the maximum stage. The amplitude of maximum PVA$^-$ increases before the maximum stage, mainly dominated by DIV$_{div}$ and UP, which suggests that synoptic moist-dynamic activity upstream of the maximum PVA$^-$ is important for the amplification. After the maximum stage, UP and $\mathscr{B}$nd dominate the amplitude weakening. However, LOW and DIV$_{div}$ counteract the decay of the maximum PVA$^-$ pointing to moist-baroclinic downstream development.

The investigation of the active regime life cycles from onset to decay revealed novel insights into the dynamics beyond the analysis of the four days around the maximum stage. Independent of the blocked regime type, the maximum PVAs$^-$ show a mean net amplification from onset to maximum stage and a mean net weakening from maximum to decay, indicating that the life cycle of the maximum PVAs$^-$ follows the life cycle of the regime. DIV$_{div}$ makes a major and often dominant contribution to the strengthening of the maximum PVA$^-$ before the maximum stage, while UP leads together with $\mathscr{B}$nd the weakening of the maximum PVA$^-$ after the maximum stage. Two major differences in the contributions between the regimes are evident. First, UP has an important positive contribution to the amplification of the maximum PVAs$^-$ of EuBL before the maximum stage, which is often linked to very short regime life cycles that build up and decay again rapidly. Second, $\mathscr{B}$nd shows a large positive net effect on the maximum PVA$^-$ amplitude for ScBL in particular during long life cycles, which suggests a continuous growth of the anomaly over the long period between the onset and the maximum stage.

8.3 Decay dynamics

After the insights into the dynamics around the onset and the maximum stage of regime life cycles, the section on hand investigates the dynamics around regime decay. Thereby, the question arises as to why a regime pattern weakens and, thus, the regime life cycle ends. From a quasi-Lagrangian PV perspective, it raises the question of whether the degradation of the regime is a result of the weakening of the anomaly or whether it reflects the migration of the anomaly out of the region. Equivalent to the onset and maximum stage, the PVA$^-$ that represents the largest spatial overlap in the regime mask at the time of decay (decay PVA$^-$) is investigated here. The share of regime life cycles where the decay PVA$^-$ is the same PVA$^-$ as the maximum PVA$^-$ is nearly equal to the shares between the onset and maximum PVAs$^-$ with 48.1 % for EuBL, 44.3 % for ScBL, 59.9 % for AR, and 57.6 % for GL. Again, it justifies the decision to define decay PVAs$^-$ for the focus on the decay.

The section is structured as follows. First, the propagation of decay PVAs$^-$ and the link to regime transitions after the blocked regime life cycles are investigated (Sect. 8.3.1). Insights into the temporal evolution of decay PVA$^-$ characteristics are the content of Section 8.3.2 with a focus on the amplitude evolution and contributions from PV tendency terms (Sect. 8.2.2).

8.3.1 Pathways of decay PVAs$^-$ and link to regime transitions

Propagation of decay PVAs$^-$

Figure 8.13 shows the anomalous frequency of PVAs$^-$ normalized with the climatological frequency of PVAs$^-$ for selected time steps around regime decay. In addition, contours of decay PVA$^-$ frequency indicate the position of the decay PVAs$^-$. The area of the regime mask is associated with an anomalous high frequency of PVAs$^-$ at the time of the regime decay, pointing to the still established regime pattern in the large-scale flow (Fig. 8.13a,d,g,j). There is very good agreement with the frequency of decay PVAs$^-$, which shows that decay PVAs$^-$ still make up the dominant anticyclonic part of the full regime pattern. Two days after decay, positive relative deviations in PVA$^-$ frequency prevail no longer within the regime mask, indicating that the decay PVAs$^-$ either degraded or moved away (Fig. 8.13b,e,h,k). The overall frequency of decay PVAs$^-$ reveals that some PVAs$^-$ are displaced to the west and some are displaced to the east. It appears that more decay PVAs$^-$ in ScBL and AR migrate downstream, while in EuBL, the tendency is for decay PVAs$^-$ to remain stationary or migrate slightly retrograde. For GL, the frequency of decay PVAs$^-$ shows a nearly symmetric maximum upstream and downstream of the regime mask and indicates that there is no preferred propagation of the decay PVAs$^-$ after regime decay (Fig. 8.13k). Four days after regime decay, the negative relative deviations within the regime masks of the blocked regimes show the striking change in the large-scale pattern that is even associated with a depressed occurrence of PVA$^-$ in the blocked region (Fig. 8.13c,f,i,l). A tendency for a retrograde migration of decay PVAs$^-$ is visible for EuBL and GL. In particular for EuBL, an area of anomalous high frequency of PVAs$^-$

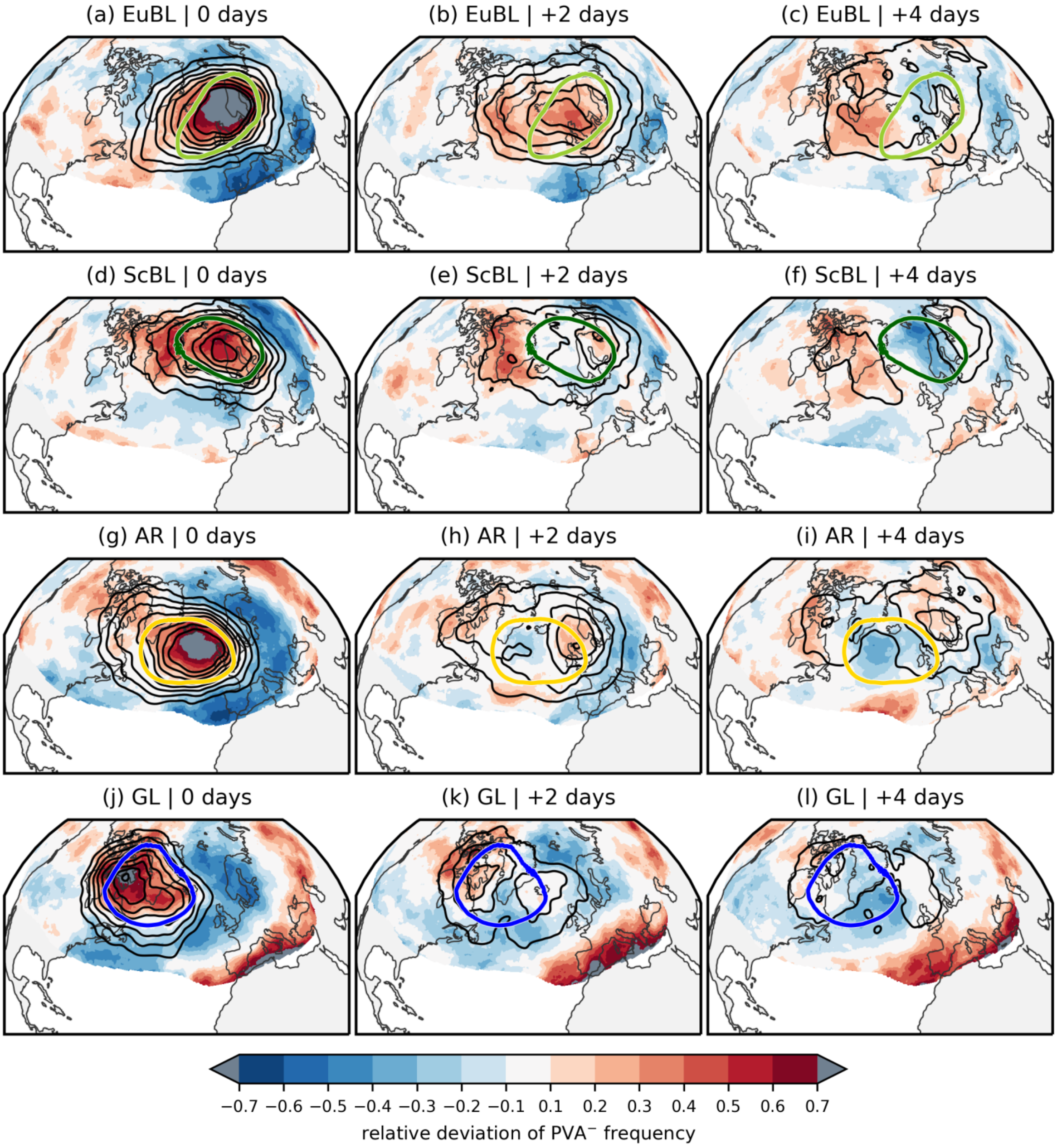

Figure 8.13: Relative deviation of PVA$^-$ frequency for the four blocked regimes (rows) and for selected time steps (columns) around the decay life cycle stage (shading, in %). Black contours show the slightly smoothed frequency of the onset PVA$^-$ for the regime life cycles (in steps of 0.2, 0.25, 0.3, 0.35, 0.4, 0.45). The colored contours are the regime masks for each regime. Note that for each time lag, the time steps +/- 6 hours around are used in addition for a clearer picture. The relative deviations in the subtropics exhibit high values in the relative deviation and are masked here when the climatological frequency falls below a frequency of 20 %.

Table 8.2: Division of regime life cycles into the two subcategories depending on which pathway the defined decay PVA^{-} follows after regime decay.

	EuBL	ScBL	AR	GL
center of mass longitude	0.5 °E	13.0 °E	24.0 °W	51.5 °W
all	183	192	177	177
retrogression pathway	80 (43.7 %)	92 (47.9 %)	65 (36.7 %)	83 (46.9 %)
downstream pathway	103 (56.3 %)	100 (52.1 %)	112 (63.3 %)	94 (53.1 %)

is located upstream near the southern tip of Greenland (Fig. 8.13c,l). In contrast, higher frequencies of decay PVAs^{-} are found downstream for ScBL and AR (Fig. 8.13f,i), indicating a preferred migration towards the east after regime decay. Interestingly, the decay PVA^{-} frequency is lower upstream of the regime mask of ScBL, but at the same time, the relative deviation points to a stronger anomalous increase in PVA^{-} frequency upstream than downstream (Fig. 8.13e,f). This brings up the assumption that although most of the decay PVAs^{-} migrate downstream, other PVAs^{-} make their way into the North Atlantic-European region. Knowing that the regime transition from ScBL to GL is well-known and has often been associated with a retrograding block from Scandinavia to Greenland (e.g., Vautard, 1990), the quasi-Lagrangian perspective sheds light on the fact that the transition is not necessarily associated with a retrograding block. It may also happen that the PVA^{-} associated with the block over Scandinavia migrates downstream and a new PVA^{-} is built up over Greenland.

The overall frequency of decay PVAs^{-} in the days after the decay reveals a displacement of some PVAs^{-} to the west and the east (Fig. 8.13, middle and right column). This motivates a breakdown of decay PVAs^{-} into two pathways, analogously to the regime onset (cf. Sect. 8.1.1). The three-day tracks of decay PVAs^{-} after the decay are used for the division. PVAs^{-} that migrate downstream are associated with the 'downstream pathway', and the PVAs^{-} that propagate towards the west fall into the 'retrogression pathway'. Table 8.2 shows the occurrence frequency of the pathways for the four blocked regime types. Figure 8.14 illustrates the mean course of the pathways for each blocked regime type. For all regimes, the majority of decay PVAs^{-} migrate downstream after regime decay and are located over northeastern Europe around ten days after decay (Fig. 8.14). The downstream pathway emerges most clearly for AR, where 63.3 % of decay PVAs^{-} (and hence life cycles) propagate eastward. In turn, for ScBL it is almost equally likely that the decay PVA^{-} migrates downstream or retrogrades toward the eastern North Atlantic. The retrogression pathway describes the westward propagation of decay PVAs^{-} after regime decay, and occurs less often than the downstream pathway. Interestingly, the retrogression pathway does not show a continuous westward propagation of decay PVAs^{-} (Fig. 8.14). In agreement with the retrogression pathway during the onset, the westward propagation of the PVAs^{-} is short-lived and lasts for a few days, such that the decay PVAs^{-} also propagate downstream after some time.

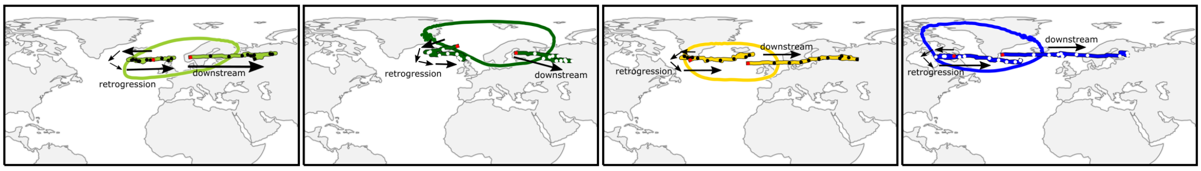

(a) EuBL (b) ScBL (c) AR (d) GL

Figure 8.14: Mean tracks of the retrogression and downstream pathways of decay PVAs$^-$ for the four blocked regimes: (a) EuBL, (b) ScBL, (c) AR, and (d) GL. Tracks are shown for the period from decay to 10 days after decay. Black or white dots are set for every day between the decay and the ten days afterward. Red points correspond to the time of the regime decay. The closed contour marks the position of the regime mask. Black arrows point to the direction of traveling decay PVAs$^-$.

Link of decay PVA$^-$ pathways to regime transitions

The two pathways of decay PVAs$^-$ raise the question of whether there is a link between the pathways and preferred regime transitions after blocked regimes. Figure 8.15 shows the transition frequencies, split up into blocked regime type and pathway. In addition, the hatching of bars in Figure 8.15 indicates the number of cases where the decay PVAs$^-$ contributed to the successive regime life cycle. Large difference are evident in the preferred transitions between the two pathways within the same blocked regime.

There is clear preferred transition from EuBL to AR in around 40 % of the cases, when the decay PVA$^-$ follows the retrogression pathway (Fig. 8.15a). As the decay PVA$^-$ exhibits a spatial overlap with the regime mask of AR (hatching in Fig. 8.15a), this indicates that the retrograding decay PVA$^-$, which contributed before to EuBL, causes the transition to AR. In contrast, when the decay PVA$^-$ of EuBL propagates downstream, none of the transitions is dominating (Fig. 8.15e). However, a transition into ScBL occurs most frequently, which suggests a northeastward shift of the decay PVA$^-$ toward Scandinavia.

With around 40 %, the transition from ScBL to GL is the most frequent transition within the retrogression cluster of decay PVAs$^-$ (Fig. 8.15b). As previously hypothesized, the decay PVA$^-$ of ScBL exhibits a certain overlap with the regime mask of GL, suggesting that the decay PVA$^-$ contributes to both regimes and is displaced to the west during the regime transition. In contrast, when decay PVAs$^-$ follow the downstream pathway after ScBL decay, 35 % of the regime life cycles decay into none of the seven regimes (Fig. 8.15f). PVAs$^-$ migrate out of the regime region toward Eurasia and thus cannot contribute to any blocked regime over the region. Nevertheless, transitions occur with a probability of around 30 % and slightly more than 15 % to EuBL and GL, respectively. This clearly shows that a transition from a blocked regime to a (different) blocked regime over Europe does not have to be associated with the same PVA$^-$, but also newly formed anomalies from upstream can constitute the anticyclonic anomaly of a blocked regime pattern. However, some decay PVAs$^-$ of ScBL that propagate downstream show a

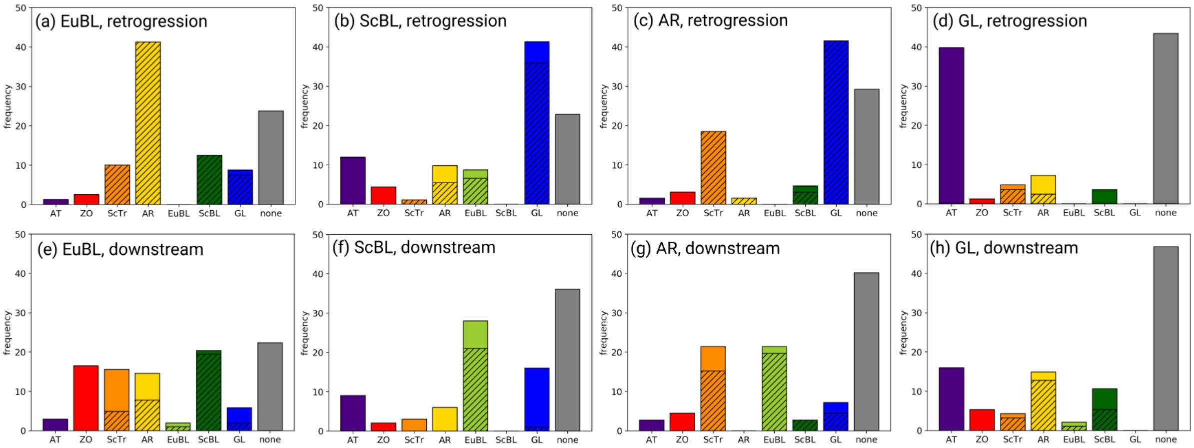

Figure 8.15: Frequencies (in %) of regime transitions from the four blocked regimes depending on the pathway of decay PVAs$^-$: retrogression pathway (upper row) and downstream pathway (lower row). Frequencies are relative to the number of regime life cycles within the pathway subset. The hatching points to the share of regime life cycles (in %) where the decay PVA$^-$ contributed to the successive regime life cycle, analogue to Figure 8.3.

certain overlap with the EuBL regime mask, which could be linked to an elongated shape of the decay PVAs$^-$.

The transition from AR to GL is the most preferred transition when decay PVAs$^-$ follow the retrogression pathway after AR decay (Fig. 8.15c). Same as for ScBL, decay PVAs$^-$ of AR that retrograde towards the west are linked to the successive GL regime life cycles. The second most likely transition is from AR to ScTr, which occurs in 20 % of the cases. For the downstream propagating decay PVAs$^-$ of AR, 40 % of the life cycle transitions into none of the seven regimes (Fig. 8.15g). Still, in around 20 % of the cases, a transition into ScTr or EuBL takes place. Especially for EuBL, this transition points to the downstream propagation of the decay PVA$^-$ towards Europe.

A preferred transition from GL into AT is observed, with a probability of around 40 % for the retrograding decay PVAs$^-$ (Fig. 8.15d). This indicates that retrograding decay PVAs$^-$ towards the Arctic latitudes helps to build up the AT regime pattern, which is associated with negative PV anomalies near Baffin Bay (cf. Fig. A.1). More than 40 % of the GL regime life cycles that fall into the retrogression pathway show no transition into one of the seven regimes, presumably because, among other things, the anticyclonic circulation anomaly cannot contribute to any regime as it moves out of the North Atlantic-European region. When decay PVAs$^-$ follow the downstream pathway during GL decay, the PVAs$^-$ prevail in the regime region, which is also displayed in the transitions (Fig. 8.15h). Although the probability of a transition into none of the regimes is highest, the transition into a blocked regime is more preferred in comparison to the transition probabilities in the retrogression pathway, pointing to the propagation of the PVAs$^-$ towards the eastern North Atlantic and Europe where they contribute to a successive regime life cycle.

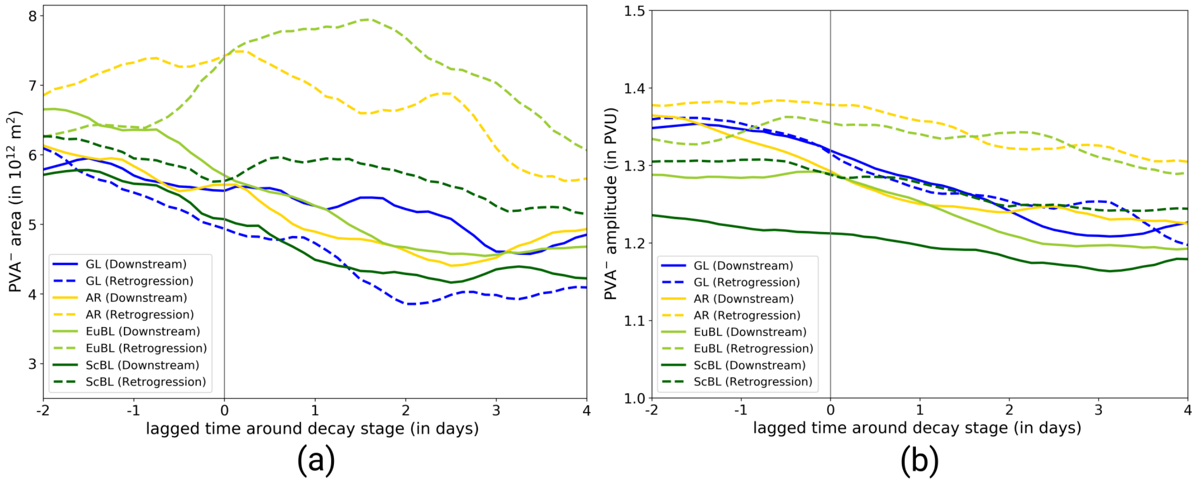

Figure 8.16: Temporal evolution of (a) the decay PVA$^-$ area, and (b) the decay PVA$^-$ amplitude for onset PVAs$^-$. The solid lines represent the course for the retrogression pathways, and the dashed lines represent the downstream pathways. The amplitude is the weighted mean based on the VAPV' field (150–500 hPa, cf. Sect. 5). The vertical line marks the time of the regime decay. The temporal evolution is slightly smoothed, considering the values +/- 6 hours around a point in time.

8.3.2 Evolution of decay PVA$^-$ characteristics

Temporal evolution of decay PVA$^-$ area and amplitude

The previous subsection revealed two pathways of decay PVAs$^-$ after regime decay. It is now of interest to investigate the decay PVA$^-$ characteristics around the regime decay. Figure 8.16 shows the temporal evolution of the area and the amplitude of decay PVAs$^-$. Again, the amplitude evolution based on VAPV instead of VAPV' is displayed in Figure C.2c. Using integrated PV tendencies, the contributions of different processes on the amplitude evolution are quantified for all blocked regimes and pathways separately (Fig. 8.17).

Decay PVAs$^-$ following the downstream pathway experience in the mean an area decline shortly before until days after regime decay (Fig. 8.16a). This is accompanied by a decrease in amplitude, which already starts before the regime decay (Fig. 8.16b). This links the decaying process of a regime to the decay in the PVAs$^-$ life cycle. It stands out that the decay PVAs$^-$ of ScBL show by far the smallest mean area relative to the other regimes, and the amplitude is the weakest as well. PVAs$^-$ of ScBL and GL that are linked to the retrogression pathway exhibit similar characteristics as the downstream propagating PVAs$^-$ with a general decrease in both, area and amplitude. In contrast, PVAs$^-$ that migrate westward after EuBL and AR decay are associated with an increase in area around regime decay, and a nearly constant amplitude throughout the time considered. EuBL stands out as decay PVAs$^-$ show a maximum in area around two days after regime decay with a constantly high amplitude (Fig. 8.16b). The differences in the evolution of area and amplitude between the two pathways are evident apart from GL, where the decay PVAs$^-$ experience the same amplitude evolution independently of the pathway. In contrast to the other three blocked regimes, downstream retrograding PVAs$^-$ exhibit a larger area than retrograding PVAs$^-$ (Fig. 8.16a).

Contributions to the amplitude evolution of decay PVAs$^-$

A partition of the amplitude evolution of decay PVAs$^-$ on selected isentropic surfaces allows quantifying which processes cause the short-term amplification just before the decay for some pathways and regimes and, more extensively, the weakening of the PVA$^-$ amplitude. Figure 8.17 shows the integrated PV tendency terms for the retrogression pathway (left column) and the downstream pathway (right column) of decay PVAs$^-$ separately. Independently of the blocked regime type and pathway, the weakening of decay PVAs$^-$ after regime decay is dominated by UP and $\mathscr{B}$nd, although DIV_{div} and LOW try to act against the weakening of the amplitude. However, some differences are evident between the pathways and also between the regime types, which are highlighted below.

First, the amplification of decay PVAs$^-$ before the decay occurs only for EuBL and is dominated by DIV_{div} (Fig. 8.17a,b). Following the retrogression pathway of EuBL, decay PVAs$^-$ are additionally amplified by a strong contribution of UP, which suggests the presence of a strong trough upstream of the PVA$^-$ (Fig. 8.17a). If the divergent outflow linked to DIV_{div} is located northwest of the PVA$^-$, as for the onset (Fig. 8.7), this may be an important contributor to the retrograde migration of the PVA$^-$ through the amplification of growth of the PVA$^-$ at the western edge. If decay PVAs$^-$ linked to EuBL follow the downstream pathway, they are in addition to DIV_{div} amplified by $\mathscr{B}$nd (Fig. 8.17b). The large positive contribution of $\mathscr{B}$nd indicates a growth of the decay PVA$^-$ shortly before the regime decay.

Second, apart from EuBL, the decay PVAs$^-$ of the other blocked regimes do not experience an amplification around regime decay (Fig. 8.17). Although LOW has larger effects on the amplification of decay PVAs$^-$ for the other blocked regimes and would point to an amplification via baroclinic growth, UP and $\mathscr{B}$nd contribute strongly to the dominant weakening of the PVA$^-$ amplitude. This means that the decay PVAs$^-$ sit on the trailing edge of a RWP, such that a strong trough upstream is missing, which, ideally coupled with synoptic activity, would lead to re-intensification. Consequently, the maintenance process is absent, and the PVA$^-$ decreases in area (shown by negative, strong contribution of $\mathscr{B}$nd), which in turn affects the amplitude.

Third, the increase in the retrograding decay PVA$^-$ areas before and during the decay for EuBL and AR (cf. Fig. 8.16a), which should be reflected in $\mathscr{B}$nd, is missing (Fig. 8.17a,e). Normally, this effect would be represented in $\mathscr{B}$nd but also indirectly in DIV_{div}, which describes the divergence of the divergent wind in the upper troposphere and is often associated with an increase in the PVA$^-$ area. DIV_{div} exhibits high values for EuBL and AR, but $\mathscr{B}$nd contributes negatively (Fig. 8.17a,e). The reason for the missing positive contribution of $\mathscr{B}$nd might be linked to the filtering since only time points are taken into ac-

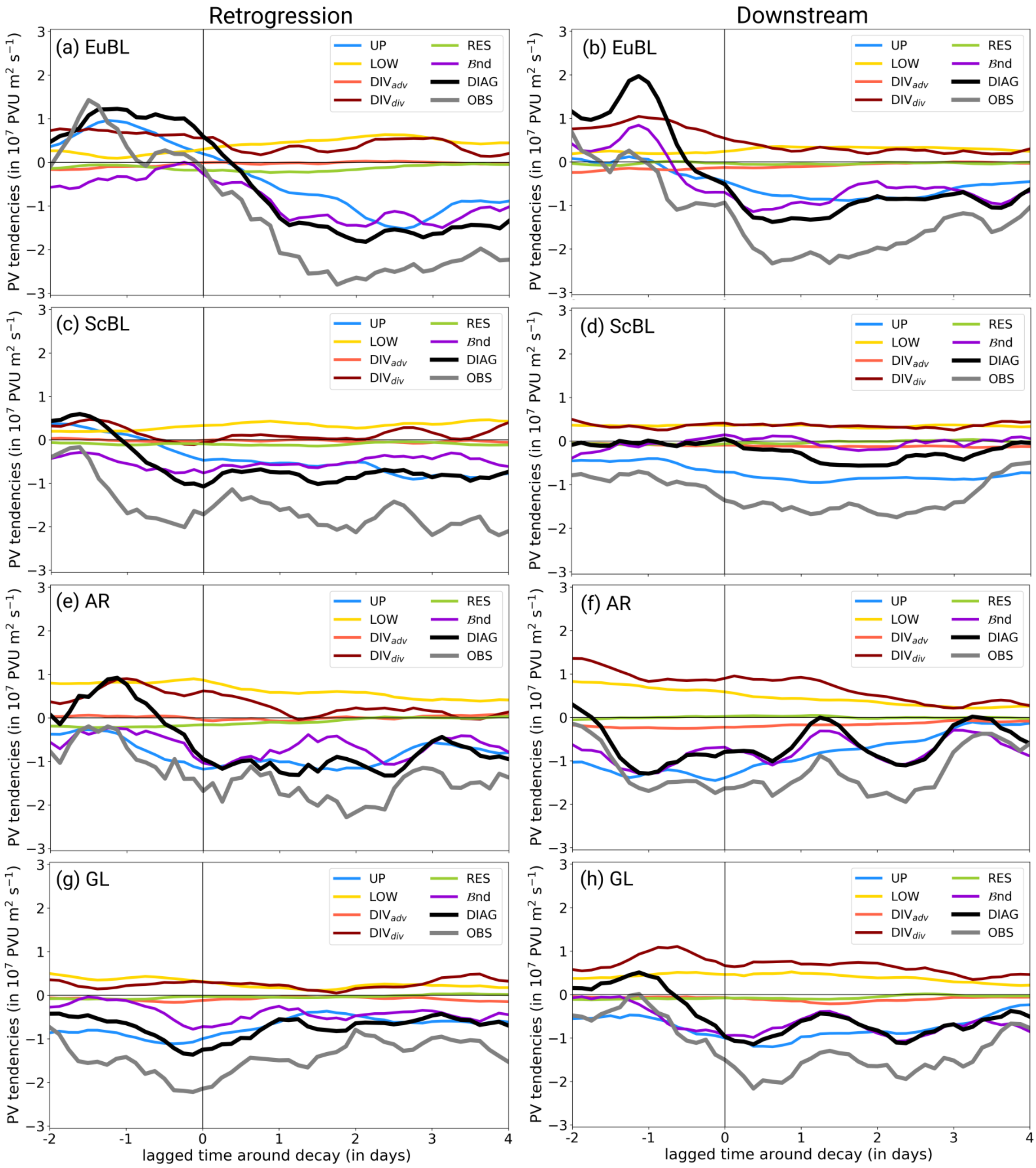

Figure 8.17: Integrated mean PV tendency terms over decay PVAs$^-$ around regime decay for the ones following the retrogression pathway (left column) or the downstream pathway (right column) for EuBL (a,b), ScBL (c,d), AR (e,f), and GL (g,h). The vertical black line marks the regime decay. Note that only time steps fall within this composite when the relative area change is less than 20 %, as otherwise $\mathcal{B}$nd exhibits very large values when splitting or merging events occur. The temporal evolution for the single PV tendency terms is smoothed by considering the time steps +/- 6 hours around.

count, with a relative area change of the decay PVAs$^-$ of less than 20 % within three hours compared to the previous area. Thus, splitting and merging events with a large impact are discarded for the analysis in Figure 8.17.

Summary

The quasi-Lagrangian PV framework revealed a link between the decay of the regime life cycles and the migration of decay PVAs$^-$ out of the region. The tracking of the decay PVAs$^-$ identified two pathways of decay PVAs$^-$ after the regime decay. The pathway, which describes the eastward propagation of decay PVAs$^-$ after regime decay, dominates for all four blocked regimes. Preferred transitions into the successive regime depend on the pathway, in particular for retrograding decay PVAs$^-$ with preferred transitions from EuBL to AR, ScBL to GL, and AR to GL.

Insights into the temporal evolution of decay PVA$^-$ characteristics showed that retrograding decay PVAs$^-$ mainly exhibit a larger area and amplitude after decay in comparison to downstream migrating decay PVAs$^-$. However, all decay PVAs$^-$ experience an amplitude weakening after the decay, which is dominated by UP and $\mathscr{B}$nd.

8.4 Summary

This chapter investigated the PV dynamics of the four blocked weather regime life cycle types (EuBL, ScBL, AR, and GL) in the period 1979–2021 from a quasi-Lagrangian perspective and shed light on the dynamics of the three life cycle stages, namely onset, maximum, and decay. The key findings are schematically summarized in Figure 8.18.

It has been found that PVAs$^-$ that trigger the onset of blocked regimes (onset PVAs$^-$) originate from different regions before they end up as the anticyclonic regime part of the blocked regime pattern. For each regime, two pathways (arrows pointing towards the regime mask) were identified that describe the propagation of onset PVAs$^-$ from the west (upstream pathway) and from the east (retrogression pathway). Except for GL, the upstream pathway dominates for blocked regimes. Preferred regime transitions are linked to the pathway of onset PVAs$^-$ such as the transition from ScBL to EuBL, or from EuBL to AR, which demonstrate that the onset PVAs$^-$s have contributed to the precursor regime before their westward displacement. Various characteristics were traced along the track of the onset PVAs$^-$ and revealed distinct differences that are larger between the two pathways than between the four blocked regimes. In particular, retrograding PVAs$^-$ exhibit a larger area in general and a larger amplitude several days before the onset compared to upstream PVAs$^-$. Shortly before the regime onset, the upstream PVAs$^-$ rapidly grow in size and gain in amplitude. This strong amplification before the onset has been linked to WCB activity upstream associated with enhanced divergent outflow in the upper troposphere (DIV_{div}), which points to an important contribution of moist processes in the formation of a blocked regime pattern.

The PVAs$^-$ linked to the maximum stage of the blocked regime life cycles exhibit a quasi-stationary behavior in the days around the regime maximum. In general, maximum PVAs$^-$ grow in size and amplitude before the maximum stage and decrease afterward for all blocked regimes. The investigation of the processes associated with the growth before the maximum stage indicates a leading contribution of DIV_{div} for all blocked regimes and a further important contribution of quasi-barotropic wave dynamics (UP) for EuBL. The decrease in amplitude after the maximum stage is dominated for all four blocked regimes by UP and a general decrease in area, although moist-baroclinic processes (LOW and DIV_{div}) still counteract the decrease in amplitude strength. With a focus on the full regime life cycles from onset to decay, it has been found that DIV_{div} plays an important role in the strengthening of the maximum PVAs$^-$ until the maximum stage, which points to the importance of moist processes in the maintenance of blocked regimes. In particular, for very long regime life cycles, an increased contribution of the divergent PV tendency is important to maintain the strength of the maximum PVAs$^-$.

Lastly, the decay regime life cycle stage and associated PV dynamics from a quasi-Lagrangian perspective were analyzed. Similar to the onset, two pathways of PVAs$^-$ were identified that describe the

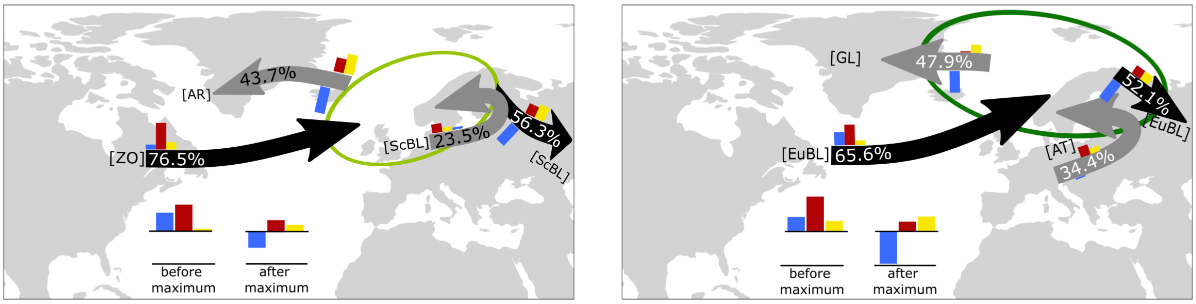

(a) EuBL (b) ScBL

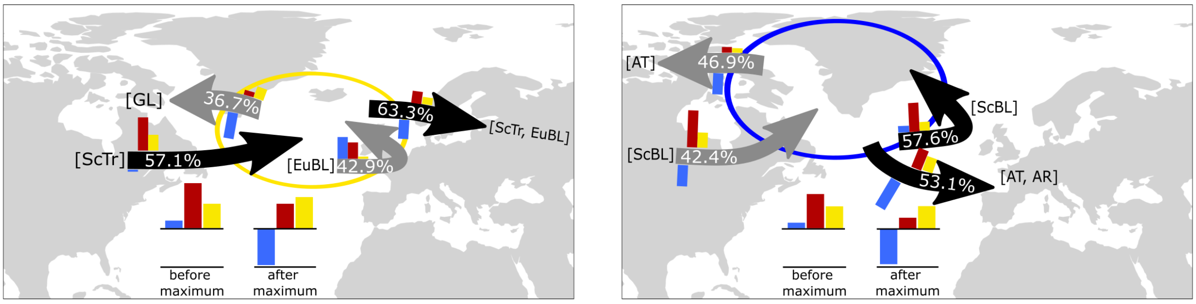

(c) AR (d) GL

Figure 8.18: Schematic summary of the main findings in Chapter 8 for the four blocked regimes: (a) EuBL, (b) ScBL, (c) AR, and (d) GL. The regime masks are highlighted in colored contours. Arrows mark the two pathways of onset PVAs$^-$ around the onset (upstream and retrogression pathways, arrows pointing towards the regime mask), and the two pathways of decay PVAs$^-$ after the decay (retrogression and downstream pathways, arrows pointing out of the regime mask). Black shading of the arrows indicates the dominant pathway. The percentages on the arrows indicate the frequency of the pathways. The regimes indicated in square brackets are the most frequent regime transitions linked to the respective pathways. The colored bars indicate the contributions of different processes to the amplitude evolution of onset PVAs$^-$, maximum PVAs$^-$, and decay PVAs$^-$s: UP (blue), LOW (yellow), and DIV$_{div}$ (dark red). Is the bar of a process placed above the arrow, it then points to a positive contribution to the PVAs$^-$ amplitude evolution. Vice versa, a bar below the arrow points to a contribution to the weakening of the PVA$^-$ amplitude. The net contributions before the maximum stage (onset–maximum stage) and after the maximum stage (maximum stage–decay) are displayed in the lower center of the subfigures.

downstream propagation and the retrograding of PVAs$^-$ after the regime decay (arrows pointing out of the regime mask). For all blocked regimes, the downstream pathway is the dominating pathway. Some preferred transitions occur depending on the pathway. For example, the transition from EuBL to AR, ScBL to GL, or AR to GL for downstream migrating PVAs$^-$, which contribute to the successive blocked regime. A comparison between the characteristics of decay PVAs$^-$ revealed a general weakening of the area and amplitude of decay PVAs$^-$ with a leading contribution of UP in particular after the regime decay.

9 Conclusions and Outlook

This thesis set out to shed light onto the dynamics of blocked weather regime life cycles in the North Atlantic-European region, with a specific focus on the relative importance of moist-dynamical and dry-dynamical processes. Therefore, a novel quasi-Lagrangian framework based on potential vorticity (PV) thinking was introduced. Complemented by a year-round regime life cycle definition, insights were gained into the processes that govern blocking onset, maximum, and decay. This chapter summarizes and discusses the main findings of the thesis in a broader context by addressing the research questions posed in Chapter 3. The chapter closes with an outlook for future work.

Conclusions

Regional weather patterns and the occurrence of extreme weather events are often linked to large-scale, long-lived circulation patterns that exhibit a dominant high-pressure system. These patterns are referred to as atmospheric blocking. Understanding and predicting atmospheric blocking is crucial for effective weather forecasting, climate modeling, and developing strategies to mitigate the associated societal and economic impacts. Despite advancements in numerical weather prediction models and improved observations, accurately forecasting the formation and duration of blocking events remains challenging. One of the primary difficulties in predicting atmospheric blocking arises from the limited understanding of the underlying mechanisms that initiate and maintain these events. Especially in the last decade, new studies on blocking dynamics have enhanced the understanding of blocking. However, these studies often highlight a single aspect of the dynamics and are limited to a case study or a specific stage in the blocking life cycle. Some studies even produce contradictory results, in particular regarding the relative contributions of dry and moist processes. As blocking is approached from different perspectives, these discrepancies stem from the lack of a holistic framework to unify the perspectives.

A novel quasi-Lagrangian PV framework has been developed in this thesis, which reconciles the previously separate perspectives on blocking dynamics. By tracking PV anomalies in the upper troposphere linked to blocking, the quasi-Lagrangian PV framework enables a new perspective on blocking dynamics and bridges the gap between established Eulerian and Lagrangian approaches. The framework was applied to blocking in the North Atlantic-European region in the period 1979–2021 and led, for the first time, to a systematic evaluation of blocking dynamics from a different perspective. Using a year-round weather regime definition, four different blocked regime patterns were distinguished over the North

Atlantic-European region: European Blocking (EuBL), Scandinavian Blocking (ScBL), Atlantic Ridge (AR), and Greenland Blocking (GL). The objective determination of blocked regime life cycles allowed the investigation of the dynamics of full blocking life cycles from onset, over the maximum stage, to the decay. The nine research questions (RQ1–RQ9) introduced in Chapter 3 were addressed in chapters 5–8, and the main findings are summarized and discussed in the following.

RQ-1 How can the PV-θ-framework of Teubler and Riemer (2016) be used for the investigation of blocked weather regime dynamics?

In order to use the PV-θ-framework to disentangle the role of dry and moist dynamics for blocking, negative PV anomalies (PVAs$^-$) linked to the four blocked regimes were identified and tracked in the upper-troposphere. The tracking is not limited to stationary PVAs$^-$ during blocking, such that transient PVAs$^-$ can be tracked over the full lifetime from their origin until the degradation. The PV-θ-framework was refined and adapted for transient and highly variable PVAs$^-$, which enables quantifying the contributions of dry and moist processes to the PVA$^-$ amplitude evolution, and accounting for changes in the area of the PVA$^-$ object. Overall, the combination of the methods by Schwierz et al. (2004) and Grams et al. (2017), and the adaption of the PV-θ-framework of Teubler and Riemer (2016) resulted in a novel PV framework from a quasi-Lagrangian perspective, which unifies different theories on blocking, and forms a basis for the investigation of regime life cycle dynamics from a new angle.

RQ-2 How does the novel quasi-Lagrangian PV framework compare to previous Eulerian and Lagrangian approaches?

Eulerian and Lagrangian perspectives have contributed to an advanced understanding of blocking in the last decades, but reveal a contradictory importance of moist dynamics, such that these perspectives could not be unified yet. By following the PVAs$^-$ linked to blocking and investigating the contributions to their amplitude evolution, the novel PV framework in this thesis resolves this contradictory importance of moist dynamics by a quasi-Lagrangian perspective. The PVA$^-$ linked to a European Blocking (EuBL) regime life cycle in March 2016 developed far away from Europe with dominant moist contributions during its formation. The Eulerian approach, which indicated a minor role of moist processes for the same event, missed this important remote development due to the focus on Europe. This highlights the use of the quasi-Lagrangian PV framework as a novel tool to combine Eulerian (e.g., Benedict et al., 2004; Michel and Rivière, 2011) and Lagrangian (e.g., Pfahl et al., 2015; Steinfeld and Pfahl, 2019) aspects of the dynamics.

RQ-3 What is the relative role of moist dynamics and WCB activity during the onset of the EuBL regime life cycle in March 2016? Can the hypothesized dominance of moist dynamics by Grams et al. (2017) be confirmed?

The quasi-Lagrangian PV framework revealed that the PVA^- linked to the block originated far away from Europe over the East Coast of the United States during the days before the onset. The PVA^- propagated towards Europe, where it strongly amplified over the North Atlantic. The framework unveils a dominant contribution of moist processes linked to divergent PV tendencies, strongly connected to warm conveyor belt (WCB) activity over the North Atlantic. A contribution of moist processes and in particular WCBs to the formation of the poorly predicted block over Northern Europe has been suspected by Magnusson (2017) and Grams et al. (2018), and could finally be confirmed from the novel quasi-Lagrangian perspective.

RQ-4 What are the dominant processes governing the amplitude evolution of relevant PV anomalies, and where and when do they occur relative to the blocking onset?

Applied to a multitude of blocked regime life cycles, the quasi-Lagrangian PV framework revealed a systematic remote development of the PVA^-. Two pathways of PVAs^- were identified during the three days before the regime onset: (1) Retrogression pathway (PVAs^- are located east of the regime region and retrograde to the west before regime onset), and (2) upstream pathway (PVAs^- are located west of the regime region and propagate to the east). Despite their retrogression before the regime onset, the back-tracking unveiled the eventual development of retrograding PVAs^- in the storm track. Upstream PVAs^- experience a rapid strengthening of their amplitude before the regime onset, whereas retrograding PVAs^- exhibit a more steady and slower amplification. The dominant contribution to the amplification of PVAs^- before the onset arises from the divergent PV tendencies, followed by baroclinic PV tendencies. Larger differences between the pathways occur for the quasi-barotropic PV tendency term, which contributes to a strengthening of retrograding PVAs^-, but to a weakening of upstream PVAs^-. Overall, the pathways and associated dynamics to blocking onset are novel findings of this thesis obtained by the quasi-Lagrangian perspective.

RQ-5 How important are moist processes in the development of the blocked regimes, and where do they occur?

Moist processes, quantified by divergent PV tendencies and WCB activity, are the leading-order processes for the amplification of PVAs^- linked to blocking. In the three days before regime onset, moist processes exhibit a stronger contribution to the rapid amplification of upstream PVAs^- than for retrograding PVAs^-. However, they also play an important role in the retrogression of

PVAs$^-$, as moist processes often occur in the northwestern part of the PVAs$^-$, such that the retrogression occurs not purely by phase velocity but also by a diabatically-driven re-intensification on the western flank of the PVA$^-$. Moist processes are often the leading-order process for the maintenance of blocking, and in particular for the long-lived blocks. During the decay of the blocking, the contribution of moist processes decline. These insights agree well with previous findings on the important contribution of moist dynamics in around the onset and maximum stage of blocking (e.g., Pfahl et al., 2015; Steinfeld and Pfahl, 2019; Teubler and Riemer, 2021), and with earlier hypotheses that the lack of moist processes leads to the decay of a block (e.g., Woollings et al., 2018). Overall, the analyses in this thesis represent for the first time a complete systematic investigation on the relative importance of moist processes for complete blocked regime life cycles.

RQ-6 How do interactions of PV anomalies linked to a block with other small-scale anticyclonic eddies influence its evolution?

The detection of the occurrence of splitting and merging along the PVA$^-$ tracks is one of the many advantages the quasi-Lagrangian perspective offers. The tracking tool revealed that splitting and merging can lead to high changes in the evolution of PVA$^-$ amplitude and area. However, with the introduction of a boundary term $\mathscr{B}$nd that quantifies the change in the area along the PVA$^-$ in the integrated PV framework, it is possible to determine if changes in PVA$^-$ area are related to growth or to the occurrence of splitting or merging. For the onset PVAs$^-$ of GL, merging occurs more frequently than splitting, which suggests that feeding eddies reinforce the PVAs$^-$ before onset. Retrograding PVAs$^-$ experience more frequently splitting and merging compared to upstream PVA$^-$ before the onset, suggesting that large PVAs$^-$ are more often subject to splitting and merging. For the first time, the importance of eddy interaction can be examined regarding the selective absorption mechanism of Yamazaki and Itoh (2009) in a consistent framework, together with the amplitude evolution of PVAs$^-$. The results obtained from the quasi-Lagrangian PV framework point to merging as one of the maintenance mechanisms for blocking (e.g., Mullen, 1987; Yamazaki and Itoh, 2013; Luo et al., 2014).

RQ-7 Does the PV anomaly life cycles have a connection with the regime life cycles at the time of the regime maximum stage? And which processes cause a regime life cycle not to be further maintained?

The quasi-Lagrangian PV framework revealed that the stationary PVAs$^-$ linked to blocking around the maximum stage reach their maximum amplitude simultaneously with the maximum regime stage. For most regimes, moist processes in the presence of baroclinic interaction dominate the amplification of PVAs^- before reaching the maximum stage. After that, the contribution of moist processes weakens, and a quasi-barotropic degradation of the PVAs^-, coupled with a decrease in the PVA^- area, leads to the weakening of the PVAs^-. The absence of the moist processes not only initiates the degradation of the PVA^-, but is also decisive for the length and persistence of the blocked regime life cycle. The leading contribution of quasi-barotropic dynamics to the weakening of the PVA^- amplitudes agrees well with the findings of Teubler and Riemer (2021), who point to a non-linear evolution during the decay of ridges.

RQ-8 Is the end of a blocked regime life cycle evoked by the weakening of the PV anomalies, and how does it relate to regime transitions?

The PVAs^- linked to the blocked regime decay do not dissipate in the blocking region, but show two pathways out of the regime region after decay. One pathway describes the eastward propagation of PVAs^- after the decay (downstream pathway), and the second pathway describes the westward propagation of PVAs^- (retrogression pathway). Independent of pathway and blocked regime type, the PVAs^- experience a weakening of the amplitude around and after the decay, dominated by quasi-barotropic wave dynamics. This highlights that both evoke the decay of a blocked regime, the propagation of PVAs^- out of the region and a simultaneous decrease in strength. Preferred regime transitions occur depending on the pathway and blocked regime type. Transitions into another blocked regimes are often linked to a displacement of PVAs^- after the decay, such as the transitions from AR to GL and from ScBL to AR (retrograding pathway) or the transition from AR to EuBL (downstream pathway). That existing blocking anticyclones propagate and form a new blocking configuration somewhere else was suspected early on (e.g., Vautard, 1990), but was never systematically investigated. The quasi-Lagrangian PV framework reveals for the first time that PVAs^- contribute to multiple regime life cycles, or even trigger the transition to another (blocked) regime by the displacement of an existing PVA^-.

RQ-9 What are the most important differences in dynamics between the various blocked regime types

The quasi-Lagrangian PV framework reveals that the characteristics of the PVAs^- are more different within than between the regimes, dominated by the pathways of the PVAs^-. Figure 8.18 in Chapter 8 gives a schematic summary of the key findings. First, differences arise in the occurrence frequency of pathways before regime onset. The upstream pathway of PVAs^- is the dominant pathway for EuBL, ScBL, and AR, whereas the retrogression pathway dominates for

GL. Second, moist processes show a larger relative contribution for the amplitude development of onset PVAs$^-$, when PVAs$^-$ travel within the storm track region over the North Atlantic, such as the upstream pathways of all blocked regimes and the retrogression pathway of GL. And third, the relative importance of processes in blocking maintenance differs between the regimes. The role of quasi-barotropic dynamics is of equal importance as moist processes in the maintenance of EuBL and ScBL, and points to downstream development. In contrast, for AR and GL, baroclinic and divergent PV tendencies indicate a more moist-dynamical strengthening of the PVA$^-$ amplitude before the maximum stage, mostly resulting from their location over the North Atlantic.

Overall, this thesis contributes to important progress toward a comprehensive understanding of blocking from the perspective of weather regimes. The quasi-Lagrangian PV framework, developed in this thesis, provides a novel method to obtain a holistic view on blocking dynamics by combining Eulerian and Lagrangian methods. The different pathways of PVAs$^-$ are a key result in this thesis and indicate that PVAs$^-$ do not form and dissipate locally but rather upstream and downstream of the blocked regime region. Moist processes contribute predominantly to the amplification of PVAs$^-$ around the onset and before the regime maximum stage. Dry dynamics make prominent contributions as well, pointing to a complex interaction.

Outlook

This thesis, for the first time, shed light onto the life cycle dynamics of blocking from a regime life cycle definition. Some dynamical aspects of blocking known from previous studies could be corroborated, but further analyses are needed to explore some hypotheses that could not be tested more intensively. As the dynamics of blocking are rather complex, as processes on different spatial and temporal scales act simultaneously, it is important to investigate how the results from the quasi-Lagrangian perspective relate to processes that have not been considered in this thesis. One limitation of the quasi-Lagrangian PV framework is the focus on only the anticyclonic part of the blocked regime. Further development of the framework and adjustments to positive PV anomalies are important to investigate the full regime pattern from the quasi-Lagrangian perspective, which would provide a full picture of the regime pattern dynamics.

The occurrence frequency of individual blocked weather regimes and their characteristics vary between the seasons (e.g., Cassou et al., 2005), such that future work should investigate seasonal differences in the pathways, their occurrence, and the dynamical processes. As WCBs occur less frequently in summer compared to winter (e.g., Madonna et al., 2014), less latent heating and thus contributions from moist processes mainly over the storm tracks region would be expected for the PVA$^-$ amplitude evolution in summer. Teubler et al. (2023), who analyzed the onset dynamics of the same blocked regimes but from a

Eulerian perspective, highlight that the differences in the dynamics are larger between the two pathways of PVA^- than between different seasons. Further analysis is needed to check whether this is the case from a quasi-Lagrangian perspective.

Previous studies focus on the link of low-frequency modes – such as ENSO and MJO – and the occurrence of weather regimes in the North Atlantic-European region. Cassou (2008) found that the occurrence of ScBL is significantly increased ten days after MJO phase 2 when the convective maximum is located over the central Indian Ocean. In contrast, an increased frequency of GL is observed 10 days after MJO phase 6, when the convection linked to the MJO is over the western North Atlantic, leading to more predictive skill for GL (Ferranti et al., 2018). In winter, the state of the SPV can trigger certain regime transitions in combination with active low-frequency modes over Europe (e.g., Garfinkel et al., 2012; Lee et al., 2019a). The question here arises if low-frequency modes like the MJO, ENSO, or SPV influence the pathways of PVA^-.

Further analyses are needed on the role of synoptic-scale processes in the investigation of weather systems and, more in detail, the tracks of extratropical cyclones. It would be interesting to consider the occurrence and propagation of cyclones depending on the pathway, and whether an increased occurrence of cyclones upstream contributes to a strengthening of a block (e.g., Nakamura and Wallace, 1993). A further hypothesis to test is whether the weakening of the block is related to an anomalously low frequency of cyclones upstream and the associated lack of synoptic activity.

Last, this thesis has not investigated the link between the results presented here and predictability. An ongoing study investigates how the set of PV tendencies differ in ERA5 reforecasts compared to ERA5 reanalysis for the blocked weather regimes used in this thesis. This analysis will shed light on the problems that numerical weather prediction models face and aims to obtain a comprehensive understanding of the dynamics of error growth up to the regime scale. Investigating if certain blocked regimes are associated with a higher predictive skill depending on the pathways of PVAs^- is of further interest. For example, the relatively high skill of GL in winter (Büeler et al., 2021) and the dominance of the retrogression pathway for GL would suggest that numerical weather prediction models can better predict the occurrence of GL when the PVA^- reaches Greenland via the retrogression pathway. And lastly, the results in this thesis need to be considered, particularly in the climate modeling community. The previous underestimation of blocking frequency in climate models could be attributed to difficulties in the representation of moisture processes, which are of enormous importance, especially in a warmer climate with more available moisture (cf. Steinfeld et al., 2022).

A Appendix for Chapter 5

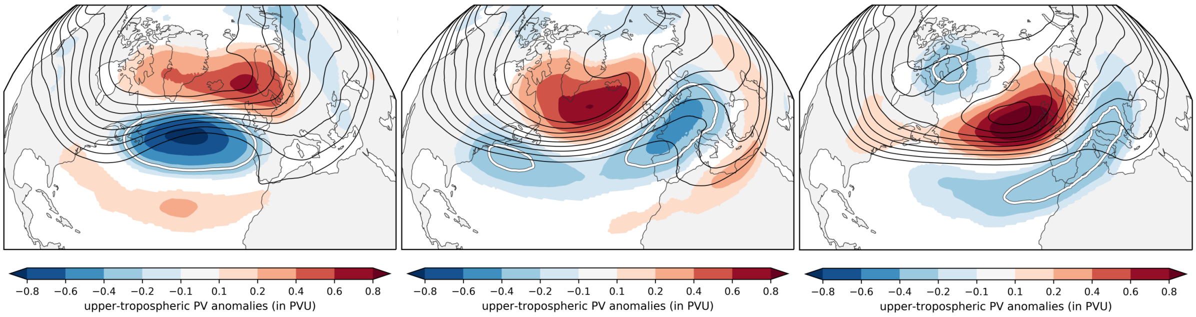

(a) ScTr (b) ZO (c) AT

Figure A.1: Vertically averaged PV anomalies between 500 and 150 hPa (shading, in PVU) for all days within an active blocked regime life cycle: (a) ScTr, (b) ZO, and (c) AT. Solid black lines indicate contour lines of vertically averaged PV (from 1.5 to 3.5 PVU in steps of 0.25). Colored contour lines indicate the regime masks as defined by the -0.3 PVU contour in the vertically averaged PV anomaly composite for each regime.

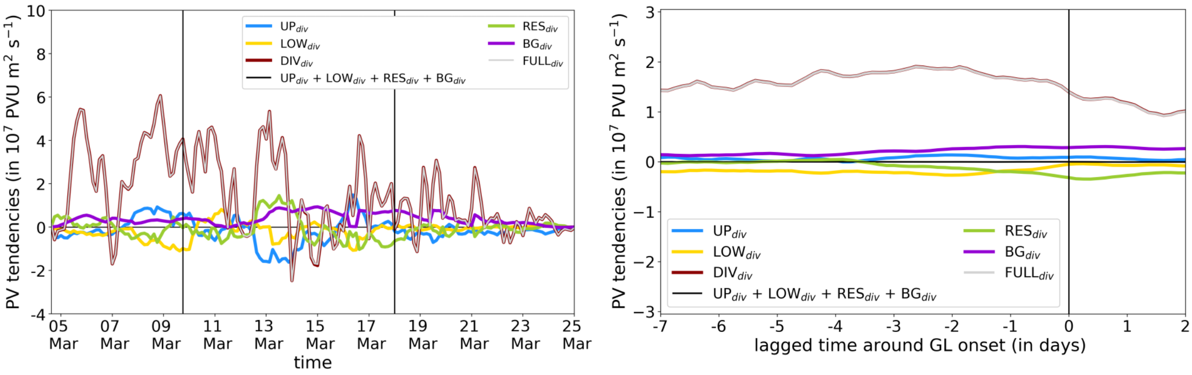

(a) (b)

Figure A.2: Division of the divergence term in Equation 5.3 (last row, term II) into the different contributions resulting from the partitioning of the full wind field (Eq. 4.5): UP$_{div}$ (q'($\nabla \cdot \mathbf{v}'_{up}$)), LOW$_{div}$ (q'($\nabla \cdot \mathbf{v}'_{low}$)), RES$_{div}$ (q'($\nabla \cdot \mathbf{v}'_{res}$)), UP$_{BG}$ (q'($\nabla \cdot \mathbf{v}_0$)), and FULL$_{BG}$ (q'($\nabla \cdot \mathbf{v}$)). (a) Evolution of PV tendencies linked to the divergence term for the EuBL regime life cycle in March 2016, which is the content of Chapter 6. (b) Composite of PV tendencies linked to the divergence term for the systematic evaluation of GL regime life cycles around onset (Chapt. 7). Lines in (b) are smoothed by a rolling mean of +/- 6 hours.

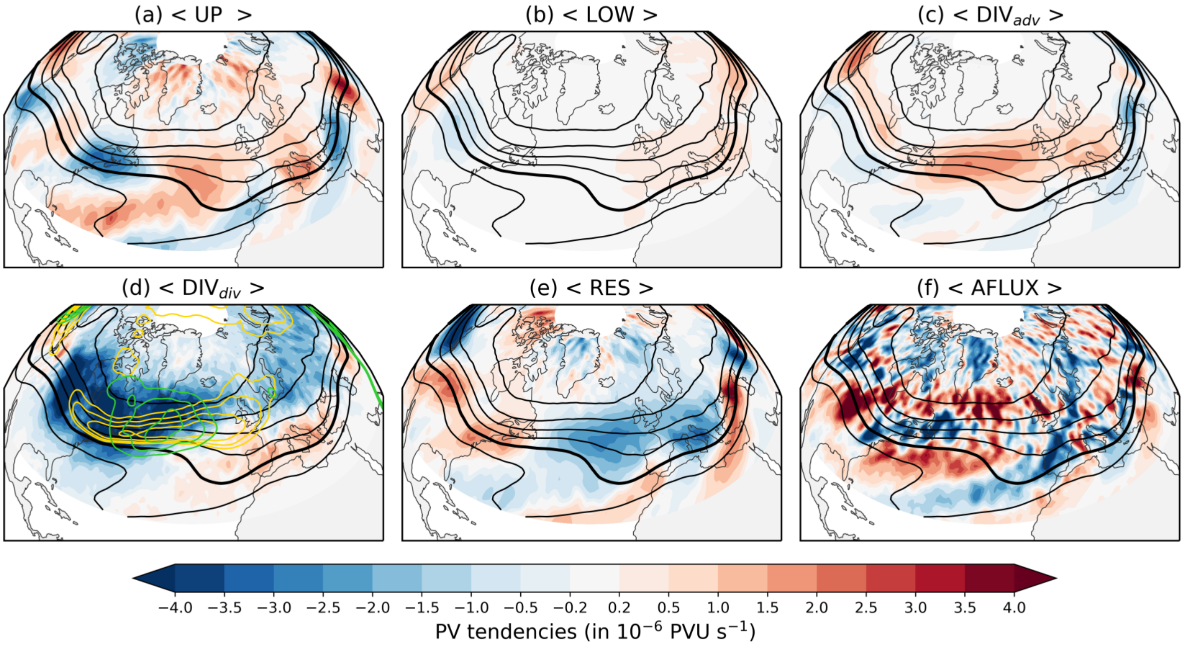

Figure A.3: Climatological footprints of PV tendency terms (shading, in 10^{-6} PVU s^{-1}) centered on July 15, 00 UTC: (a) advection of PV background with upper-tropospheric wind field ($-\mathbf{v}'_{up} \cdot \nabla q_0$; UP), (b) advection of PV background with lower-tropospheric wind field ($-\mathbf{v}'_{low} \cdot \nabla q_0$; LOW), (c) advection of PV background with divergent wind field ($-\mathbf{v}'_{div} \cdot \nabla q_0$; DIV$_{adv}$), (d) divergence term of divergent wind field ($q'(\nabla \cdot \mathbf{v}'_{div})$; DIV$_{div}$), (e) advection of background PV with residual wind field ($-\mathbf{v}'_{res} \cdot \nabla q_0$; RES), and (f) the divergence of the PV anomaly flux as part of the boundary term $\mathscr{B}$nd ($-\nabla \cdot (\mathbf{v}q')$). PV tendency terms are shown as isentropic mean between 315 and 325 K in steps of 5 K. Black contours show PV contours at 320 K (from 1–5 PVU in steps of 1 PVU). The 2-PVU-contour that points to the location of the dynamical tropopause is displayed in bold. The green and yellow contour lines in (d) show the climatological frequency of WCB outflow (with Eulerian metric, cf. Sect. 4.5), and the frequency of negative upper-tropospheric PV anomalies (cf. Sect. 5.2), respectively. Contour intervals for the WCB outflow frequency are displayed for 2, 2.5, and 3 %, and the frequencies of negative PV anomalies is displayed for 30, 32, 34, 36, and 38 %. Note that both climatology fields are smoothed here slightly.

B Appendix for Chapter 7

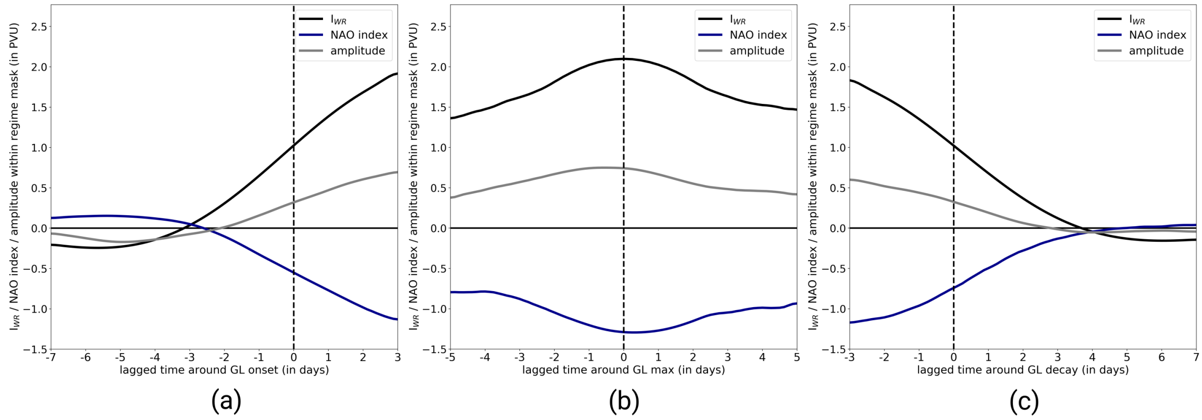

Figure B.1: Temporal evolution of the I_{WR} of GL (black), the NAO index (in blue, NOAA Climate Prediction Center, 2023) and the amplitude evolution within the GL regime mask (in gray, cf. Sect. 5.6) measured as mean PVA strength based on vertically averaged PV anomalies between 500 and 150 hPa (in PVU) for the three regime life cycle stages: (a) onset, (b) maximum, (c) decay. The dashed vertical line indicates the time of the onset, maximum and decay, respectively. All lines have been smoothed by taking into account the time steps +/- 6 hours around. The Pearson correlation coefficient between the I_{WR} and the NAO index is -0.8.

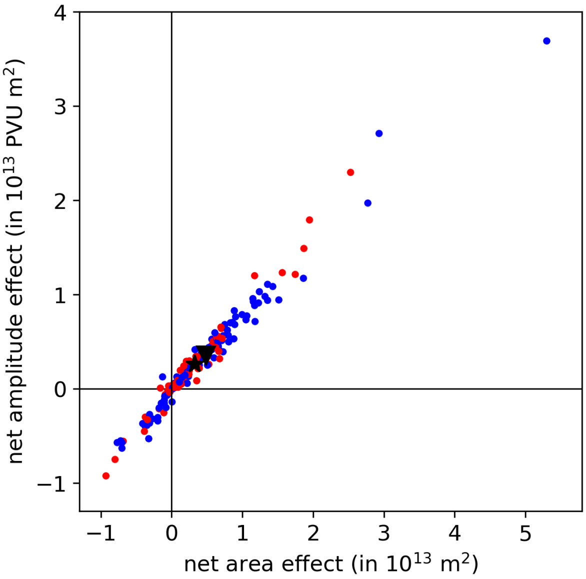

Figure B.2: Net effect of splitting and merging events on the amplitude and area of onset PVAs$^-$ that follow the retrogression (blue) and upstream (red) pathway. Each dot represents the net change in area and amplitude of the onset PVA$^-$ for the period -7 days to +2 days around GL onset that arises due to splitting and merging. The black triangle and the black star indicate the mean net effect for the retrogression and upstream pathway, respectively.

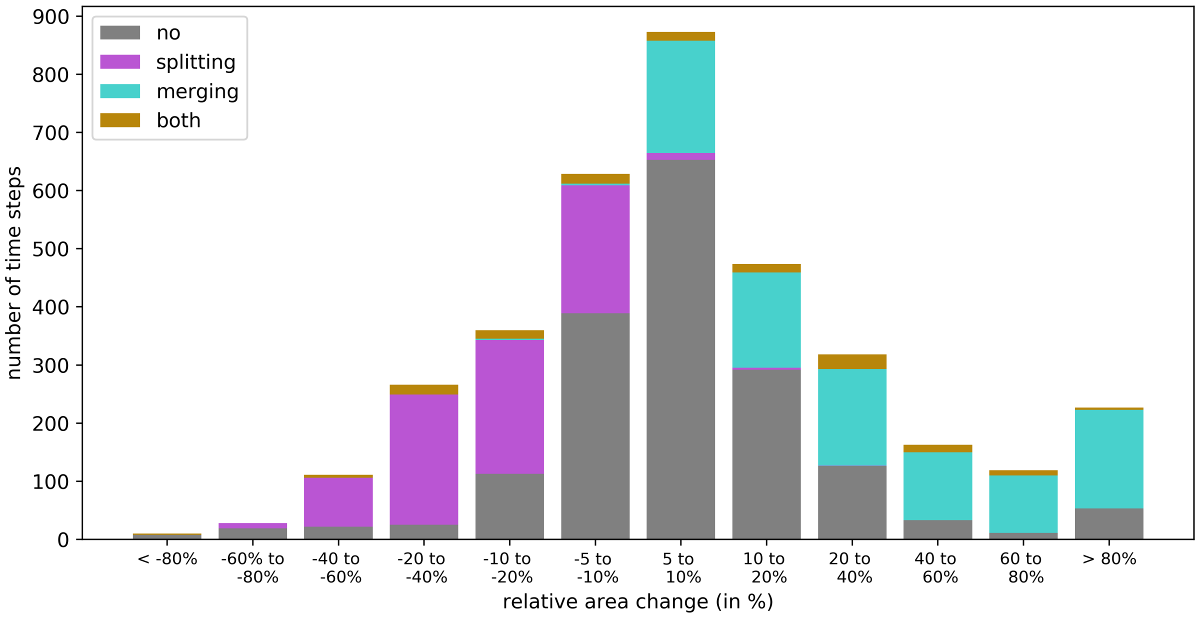

Figure B.3: Contribution of splitting and merging on the relative area changes along the onset PVA$^-$ tracks for the time period -7 days to +2 days around GL onset. Each bar represents the number of time steps that fall into a specific relative area change range. The colors indicate how many time steps are associated with a splitting event (violet), a merging event (turquoise), both types simultaneously (ocher), or with none of these types that lead to the observed relative changes in area.

C Appendix for Chapter 8

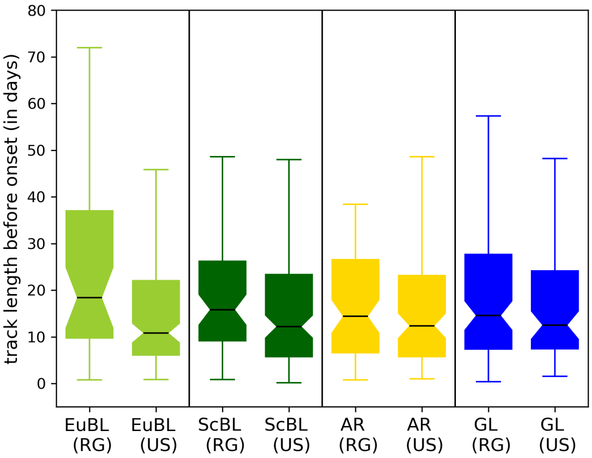

Figure C.1: Track length of onset PVAs$^-$ (in days) before the regime onset, depending on the pathway (RG for retrogression, US for upstream) and blocked regime type. The black line within the box plot marks the median.

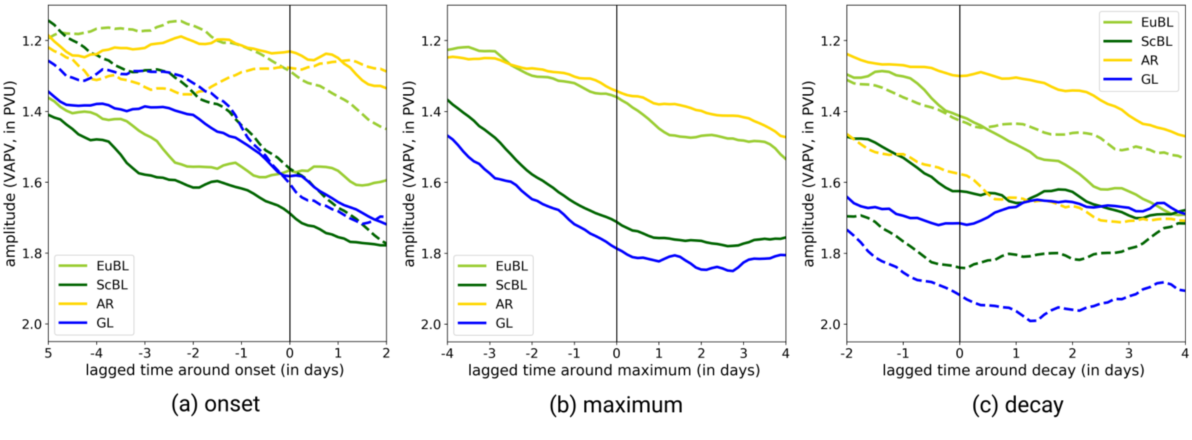

(a) onset

(b) maximum

(c) decay

Figure C.2: Mean amplitude of PVAs$^-$ measured in area-integrated VAPV (500–150 hPa, in PVU) around the three regime life cycles: (a) onset, (b) maximum stage, (c) decay. Around the onset (a), solid lines represent the retrograding onset PVAs$^-$ and dashed lines represent the onset PVAs$^-$ from upstream. Around the decay, downstream propagating decay PVAs$^-$ are displayed in solid lines and retrograding decay PVAs$^-$ are shown in dashed lines.

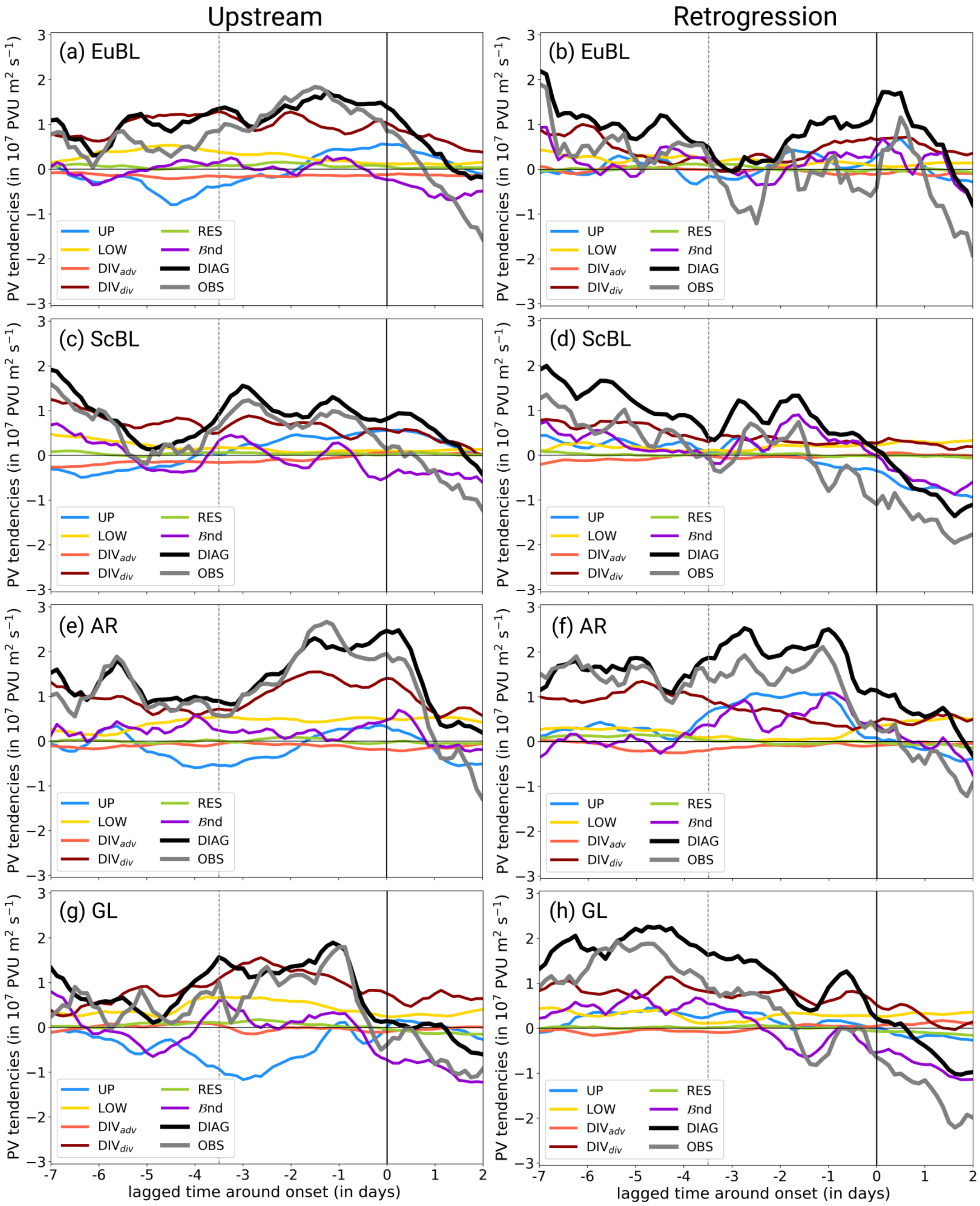

Figure C.3: Integrated mean PV tendency terms over onset PVAs$^-$ around regime onset for the ones following the upstream pathway (left column) or the retrogression pathway (right column) for EuBL (a,b), ScBL (c,d), AR (e,f), and GL (g,h). A description of the terms shown is given in the caption of Figure 8.5. The vertical black line marks the regime onset. Note that only time steps fall within this composite when the relative area change is less than 20 %, as otherwise $\mathscr{B}$nd exhibits very large values when splitting or merging events occur. The temporal evolution for the single PV tendency terms is smoothed by taking into account the time steps +/- 6 hours around.

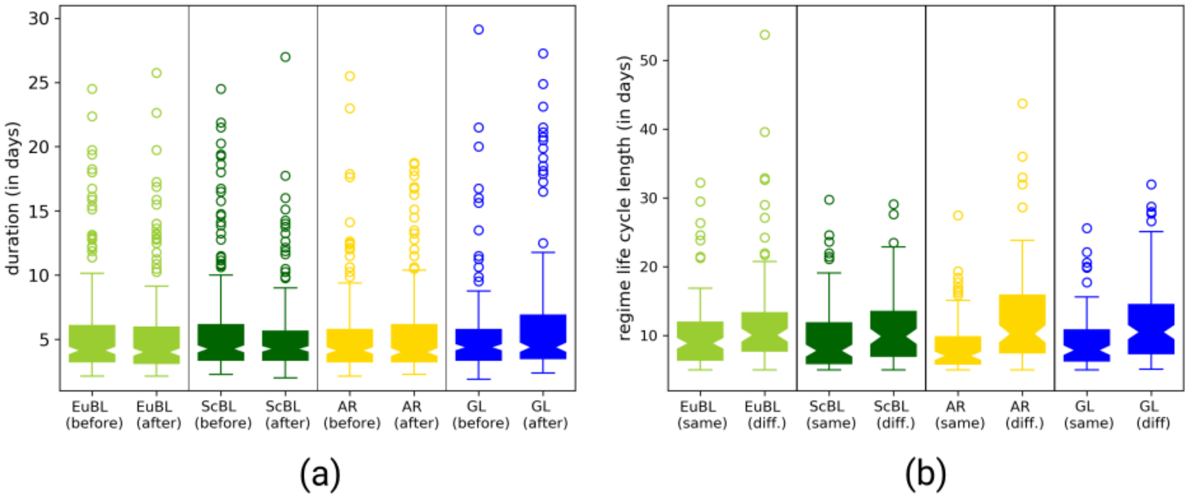

Figure C.4: (a) Distribution of period length between the onset and maximum stages (short: before) and the period length between maximum and decay regime life cycle stages (short: after) for all blocked regime life cycles (in days). (b) Distributions of the full regime life cycle length (onset–decay, in days) for the regime life cycle where the onset PVA$^-$ is also the maximum PVA$^-$ (same) and where it is not the case (diff.).

D Bibliography

Altenhoff, A. M., O. Martius, M. Croci-Maspoli, C. Schwierz, and H. C. Davies, 2008: Linkage of atmospheric blocks and synoptic-scale Rossby waves: A climatological analysis. *Tellus A: Dynamic Meteorology and Oceanography*, **60 (5)**, 1053–1063.

Alvarez-Castro, M. C., D. Faranda, and P. Yiou, 2018: Atmospheric dynamics leading to West European summer hot temperatures since 1851. *Complexity*, **2018**.

Austin, J. F., 1980: The blocking of middle latitude westerly winds by planetary waves. *Quarterly Journal of the Royal Meteorological Society*, **106 (448)**, 327–350.

Barnes, E. A., E. Dunn-Sigouin, G. Masato, and T. Woollings, 2014: Exploring recent trends in Northern Hemisphere blocking. *Geophysical Research Letters*, **41 (2)**, 638–644.

Baur, F., P. Hess, and H. Nagel, 1944: *Kalender der Grosswetterlagen Europas vom 1. I 1881 bis 31. XII 1943*. Bad Homburg v.d.H.

Beerli, R. and C. M. Grams, 2019: Stratospheric modulation of the large-scale circulation in the Atlantic–European region and its implications for surface weather events. *Quarterly Journal of the Royal Meteorological Society*, **145 (725)**, 3732–3750.

Benedict, J. J., S. Lee, and S. B. Feldstein, 2004: Synoptic view of the North Atlantic Oscillation. *Journal of the Atmospheric Sciences*, **61 (2)**, 121–144.

Berggren, R., B. Bolin, and C.-G. Rossby, 1949: An aerological study of zonal motion, its perturbations and break-down. *Tellus*, **1 (2)**, 14–37.

Bluestein, H., 1993: *Synoptic-Dynamic Meteorology in Midlatitudes: Vol II Observations and Theory of Weather Systems*. Oxford University Press, New York, 594 pp.

Breeden, M. L., B. T. Hoover, M. Newman, and D. J. Vimont, 2020: Optimal North Pacific blocking precursors and their deterministic subseasonal evolution during boreal winter. *Monthly Weather Review*, **148 (2)**, 739 – 761.

Brunner, L., N. Schaller, J. Anstey, J. Sillmann, and A. K. Steiner, 2018: Dependence of present and future European temperature extremes on the location of atmospheric blocking. *Geophysical Research Letters*, **45 (12)**, 6311–6320.

Büeler, D., R. Beerli, H. Wernli, and C. M. Grams, 2020: Stratospheric influence on ECMWF sub-seasonal forecast skill for energy-industry-relevant surface weather in European countries. *Quarterly Journal of the Royal Meteorological Society*, **146 (733)**, 3675–3694.

Büeler, D., L. Ferranti, L. Magnusson, J. F. Quinting, and C. M. Grams, 2021: Year-round sub-seasonal forecast skill for Atlantic–European weather regimes. *Quarterly Journal of the Royal Meteorological Society*, **147 (741)**, 4283–4309.

Burkhardt, J. P. and A. R. Lupo, 2005: The planetary- and synoptic-scale interactions in a southeast Pacific blocking episode using PV diagnostics. *Journal of the Atmospheric Sciences*, **62**, 1901–1916.

Cassou, C., 2008: Intraseasonal interaction between the Madden-Julian Oscillation and the North Atlantic Oscillation. *Nature*, **455**, 523–527.

Cassou, C., L. Terray, J. W. Hurrell, and C. Deser, 2004: North Atlantic winter climate regimes: Spatial asymmetry, stationarity with time, and oceanic forcing. *Journal of Climate*, **17 (5)**, 1055 – 1068.

Cassou, C., L. Terray, and A. S. Phillips, 2005: Tropical Atlantic influence on European heat waves. *Journal of Climate*, **18 (15)**, 2805 – 2811.

Chagnon, J. M., S. L. Gray, and J. Methven, 2013: Diabatic processes modifying potential vorticity in a North Atlantic cyclone. *Quarterly Journal of the Royal Meteorological Society*, **139 (674)**, 1270–1282.

Chang, E. K. M., 1993: Downstream development of baroclinic waves as inferred from regression analysis. *Journal of Atmospheric Sciences*, **50 (13)**, 2038 – 2053.

Charlton-Perez, A. J., R. W. Aldridge, C. M. Grams, and R. Lee, 2019: Winter pressures on the UK health system dominated by the Greenland blocking weather regime. *Weather and Climate Extremes*, **25**, 100 218.

Charney, J., 1955: The use of the primitive equations of motion in numerical prediction. *Tellus*, **7 (1)**, 22–26.

Charney, J. G. and J. G. DeVore, 1979: Multiple flow equilibria in the atmosphere and blocking. *Journal of Atmospheric Sciences*, **36 (7)**, 1205 – 1216.

Colucci, S. J., 1985: Explosive cyclogenesis and large-scale circulation changes: Implications for atmospheric blocking. *Journal of Atmospheric Sciences*, **42 (24)**, 2701 – 2717.

Colucci, S. J. and D. P. Baumhefner, 1998: Numerical prediction of the onset of blocking: A case study with forecast ensembles. *Monthly Weather Review*, **126 (3)**, 773–784.

Croci-Maspoli, M., C. Schwierz, and H. C. Davies, 2007: A multifaceted climatology of atmospheric blocking and its recent linear trend. *Journal of Climate*, **20 (4)**, 633 – 649.

Davini, P., C. Cagnazzo, S. Gualdi, and A. Navarra, 2012: Bidimensional diagnostics, variability, and trends of Northern Hemisphere blocking. *Journal of Climate*, **25 (19)**, 6496 – 6509.

Davini, P. and F. D'Andrea, 2016: Northern Hemisphere atmospheric blocking representation in global climate models: Twenty years of improvements? *Journal of Climate*, **29 (24)**, 8823 – 8840.

Davini, P., A. Weisheimer, M. Balmaseda, S. J. Johnson, F. Molteni, C. D. Roberts, R. Senan, and T. N. Stockdale, 2021: The representation of winter Northern Hemisphere atmospheric blocking in ECMWF seasonal prediction systems. *Quarterly Journal of the Royal Meteorological Society*, **147 (735)**, 1344–1363.

Davis, C. A., 1992: Piecewise potential vorticity inversion. *Journal of the Atmospheric Sciences*, **49 (16)**, 1397–1411.

Davis, C. A. and K. A. Emanuel, 1991: Potential vorticity diagnostics of cyclogenesis. *Monthly Weather Review*, **119 (8)**, 1929–1953.

Davis, C. A., E. D. Grell, and M. A. Shapiro, 1996: The balanced dynamical nature of a rapidly intensifying oceanic cyclone. *Mon. Wea. Rev.*, **124 (1)**, 3–26.

Davis, C. A., M. T. Stoelinga, and Y.-H. Kuo, 1993: The integrated effect of condensation in numerical simulations of extratropical cyclogenesis. *Mon. Wea. Rev.*, **121 (8)**, 2309–2330.

Dee, D. P., S. M. Uppala, A. J. Simmons, P. Berrisford, P. Poli, S. Kobayashi, U. Andrae, M. A. Balmaseda, G. Balsamo, P. Bauer, P. Bechtold, A. C. M. Beljaars, L. van de Berg, J. Bidlot, N. Bormann, C. Delsol, R. Dragani, M. Fuentes, A. J. Geer, L. Haimberger, S. B. Healy, H. Hersbach, E. V. Hólm, L. Isaksen, P. Kållberg, M. Köhler, M. Matricardi, A. P. McNally, B. M. Monge-Sanz, J.-J. Morcrette, B.-K. Park, C. Peubey, P. de Rosnay, C. Tavolato, J.-N. Thépaut, and F. Vitart, 2011: The ERA-Interim reanalysis: Configuration and performance of the data assimilation system. *Quarterly Journal of the Royal Meteorological Society*, **137 (656)**, 553–597.

Drouard, M. and T. Woollings, 2018: Contrasting mechanisms of summer blocking over Western Eurasia. *Geophysical Research Letters*, **45 (21)**, 12,040–12,048.

Drouard, M., T. Woollings, D. M. H. Sexton, and C. F. McSweeney, 2021: Dynamical differences between short and long blocks in the Northern Hemisphere. *Journal of Geophysical Research: Atmospheres*, **126 (10)**, e2020JD034 082.

Duchon, C. E., 1979: Lanczos filtering in one and two dimensions. *Journal of Applied Meteorology and Climatology*, **18 (8)**, 1016 – 1022.

Duncan, S., 2021: New all-time Canadian heat record. [Created by Scott Duncan on 30 June 2021 on Twitter, last access of URL on 16 June 2023], URL `https://twitter.com/ScottDuncanWX/status/1410097020912742404`.

Eady, E. T., 1949: Long waves and cyclone waves. *Tellus*, **1 (3)**, 33–52.

Ertel, H., 1942: Ein neuer hydrodynamischer Erhaltungssatz. *Die Naturwissenschaften*, **30 (36)**, 543–544.

Faranda, D., G. Masato, N. Moloney, Y. Sato, F. Daviaud, B. Dubrulle, and P. Yiou, 2016: The switching between zonal and blocked mid-latitude atmospheric circulation: A dynamical system perspective. *Climate Dynamics*, **47 (5-6)**, 1587–1599.

Feldstein, S. B., 2003: The dynamics of NAO teleconnection pattern growth and decay. *Quarterly Journal of the Royal Meteorological Society*, **129 (589)**, 901–924.

Ferranti, L., S. Corti, and M. Janousek, 2015: Flow-dependent verification of the ECMWF ensemble over the Euro-Atlantic sector. *Quarterly Journal of the Royal Meteorological Society*, **141 (688)**, 916–924.

Ferranti, L., L. Magnusson, F. Vitart, and D. S. Richardson, 2018: How far in advance can we predict changes in large-scale flow leading to severe cold conditions over Europe? *Quarterly Journal of the Royal Meteorological Society*, **144 (715)**, 1788–1802.

Fischer, E. M., S. Sippel, and R. Knutti, 2021: Increasing probability of record-shattering climate extremes. *Nature Climate Change 2021 11:8*, **11 (8)**, 689–695.

Garfinkel, C. I., S. B. Feldstein, D. W. Waugh, C. Yoo, and S. Lee, 2012: Observed connection between stratospheric sudden warmings and the Madden-Julian Oscillation. *Geophysical Research Letters*, **39 (18)**.

Grams, C. M. and H. M. Archambault, 2016: The key role of diabatic outflow in amplifying the midlatitude flow: A representative case study of weather systems surrounding western North Pacific extratropical transition. *Monthly Weather Review*, **144 (10)**, 3847 – 3869.

Grams, C. M., R. Beerli, S. Pfenninger, I. Staffell, and H. Wernli, 2017: Balancing Europe's wind power output through spatial deployment informed by weather regimes. *Nature Clim Change*, **7**, 557–562.

Grams, C. M., S. C. Jones, C. A. Davis, P. A. Harr, and M. Weissmann, 2013: The impact of Typhoon Jangmi (2008) on the midlatitude flow. Part I: Upper-level ridgebuilding and modification of the jet. *Quarterly Journal of the Royal Meteorological Society*, **139 (677)**, 2148–2164.

Grams, C. M., L. Magnusson, and E. Madonna, 2018: An atmospheric dynamics perspective on the amplification and propagation of forecast error in numerical weather prediction models: A case study. *Quarterly Journal of the Royal Meteorological Society*, **144 (717)**, 2577–2591.

Grams, C. M., H. Wernli, M. Böttcher, J. Čampa, U. Corsmeier, S. C. Jones, J. H. Keller, C.-J. Lenz, and L. Wiegand, 2011: The key role of diabatic processes in modifying the upper-tropospheric wave guide: A North Atlantic case-study. *Quarterly Journal of the Royal Meteorological Society*, **137 (661)**, 2174–2193.

Grose, W. L. and B. J. Hoskins, 1979: On the influence of orography on large-scale atmospheric flow. *Journal of Atmospheric Sciences*, **36 (2)**, 223 – 234.

Hanna, E., J. Cappelen, X. Fettweis, S. H. Mernild, T. L. Mote, R. Mottram, K. Steffen, T. J. Ballinger, and R. J. Hall, 2021: Greenland surface air temperature changes from 1981 to 2019 and implications for ice-sheet melt and mass-balance change. *International Journal of Climatology*, **41 (S1)**, E1336–E1352.

Hannachi, A., D. M. Straus, C. L. Franzke, S. Corti, and T. Woollings, 2017: Low-frequency nonlinearity and regime behavior in the Northern Hemisphere extratropical atmosphere. *Reviews of Geophysics*, **55 (1)**, 199–234.

Hauser, S., S. Mueller, X. Chen, T.-C. Chen, J. G. Pinto, and C. M. Grams, 2023a: The linkage of serial cyclone clustering in Western Europe and weather regimes in the North Atlantic-European region in boreal winter. *Geophysical Research Letters*, **50 (2)**, e2022GL101 900.

Hauser, S., F. Teubler, M. Riemer, P. Knippertz, and C. M. Grams, 2023b: Towards a holistic understanding of blocked regime dynamics through a combination of complementary diagnostic perspectives. *Weather and Climate Dynamics*, **4 (2)**, 399–425.

Heifetz, E., C. H. Bishop, B. J. Hoskins, and J. Methven, 2004: The counter-propagating Rossby-wave perspective on baroclinic instability. I: Mathematical basis. *Quarterly Journal of the Royal Meteorological Society*, **130 (596)**, 211–231.

Held, I. M., 1975: Momentum transport by quasi-geostrophic eddies. *Journal of Atmospheric Sciences*, **32 (7)**, 1494 – 1497.

Held, I. M. and A. Y. Hou, 1980: Nonlinear axially symmetric circulations in a nearly inviscid atmosphere. *Journal of Atmospheric Sciences*, **37 (3)**, 515 – 533.

Henderson, S. A., E. D. Maloney, and E. A. Barnes, 2016: The influence of the Madden-Julian Oscillation on Northern Hemisphere winter blocking. *Journal of Climate*, **29 (12)**, 4597–4616.

Hermann, M., L. Papritz, and H. Wernli, 2020: A Lagrangian analysis of the dynamical and thermodynamic drivers of large-scale Greenland melt events during 1979-2017. *Weather and Climate Dynamics*, **1 (2)**, 497–518.

Hersbach, H., B. Bell, P. Berrisford, S. Hirahara, A. Horányi, J. Muñoz-Sabater, J. Nicolas, C. Peubey, R. Radu, D. Schepers, A. Simmons, C. Soci, S. Abdalla, X. Abellan, G. Balsamo, P. Bechtold, G. Biavati, J. Bidlot, M. Bonavita, G. De Chiara, P. Dahlgren, D. Dee, M. Diamantakis, R. Dragani, J. Flemming, R. Forbes, M. Fuentes, A. Geer, L. Haimberger, S. Healy, R. J. Hogan, E. Hólm, M. Janisková,

S. Keeley, P. Laloyaux, P. Lopez, C. Lupu, G. Radnoti, P. de Rosnay, I. Rozum, F. Vamborg, S. Villaume, and J.-N. Thépaut, 2020: The ERA5 global reanalysis. *Quarterly Journal of the Royal Meteorological Society*, **146 (730)**, 1999–2049.

Hochman, A., G. Messori, J. F. Quinting, J. G. Pinto, and C. M. Grams, 2021: Do Atlantic-European weather regimes physically exist? *Geophysical Research Letters*, **48 (20)**, e2021GL095 574.

Holton, J. R. and G. J. Hakim, 2012: *An introduction to dynamic meteorology: Fifth edition*, Vol. 9780123848. Elsevier, 1–532 pp.

Hoskins, B., 1997: A potential vorticity view of synoptic development. *Meteorological Applications*, **4 (4)**, 325–334.

Hoskins, B. J., M. E. McIntyre, and a. W. Robertson, 1985: On the use and significance of isentropic potential vorticity maps. *Quarterly Journal of the Royal Meteorological Society*, **111 (6)**, 877–946.

Hoskins, B. J. and P. J. Valdes, 1990: On the existence of storm-tracks. *Journal of Atmospheric Sciences*, **47 (15)**, 1854 – 1864.

Houze, R. A., K. L. Rasmussen, S. Medina, S. R. Brodzik, and U. Romatschke, 2011: Anomalous atmospheric events leading to the summer 2010 floods in Pakistan. *Bulletin of the American Meteorological Society*, **92 (3)**, 291 – 298.

Kautz, L.-A., O. Martius, S. Pfahl, J. G. Pinto, A. M. Ramos, P. M. Sousa, and T. Woollings, 2022: Atmospheric blocking and weather extremes over the Euro-Atlantic sector – a review. *Weather and Climate Dynamics*, **3 (1)**, 305–336.

Kidston, J., D. M. W. Frierson, J. A. Renwick, and G. K. Vallis, 2010: Observations, simulations, and dynamics of jet stream variability and annular modes. *Journal of Climate*, **23**, 6186–6199.

Lackmann, G., 2012: *Midlatitude synoptic meteorology: Dynamics, analysis, and forecasting*. American Meteorological Society, Boston, 360 pp.

Lee, R. W., S. J. Woolnough, A. J. Charlton-Perez, and F. Vitart, 2019a: ENSO modulation of MJO teleconnections to the North Atlantic and Europe. *Geophysical Research Letters*, **46 (22)**, 13 535–13 545.

Lee, S. H., J. C. Furtado, and A. J. Charlton-Perez, 2019b: Wintertime North American weather regimes and the Arctic stratospheric polar Vortex. *Geophysical Research Letters*, **46 (24)**, 14 892–14 900.

Legras, B., T. Desponts, and B. Piguet, 1987: Cluster analysis and weather regimes. *ECMWF seminar proceedings: The nature and prediction of extratropical cyclones*, Reading, UK, Vol. 2, 123–149.

Lenggenhager, S., M. Croci-Maspoli, S. Brönnimann, and O. Martius, 2019: On the dynamical coupling between atmospheric blocks and heavy precipitation events: A discussion of the southern Alpine flood in October 2000. *Quarterly Journal of the Royal Meteorological Society*, **145 (719)**, 530–545.

Liu, C. and E. A. Barnes, 2015: Extreme moisture transport into the Arctic linked to Rossby wave breaking. *Journal of Geophysical Research: Atmospheres*, **120 (9)**, 3774–3788.

Liu, P., Y. Zhu, Q. Zhang, J. Gottschalck, M. Zhang, C. Melhauser, W. Li, H. Guan, X. Zhou, D. Hou, M. Peña, G. Wu, Y. Liu, L. Zhou, B. He, W. Hu, and R. Sukhdeo, 2018: Climatology of tracked persistent maxima of 500-hPa geopotential height. *Climate Dynamics*, **51 (1-2)**, 701–717.

Luo, D., J. Cha, L. Zhong, and A. Dai, 2014: A nonlinear multiscale interaction model for atmospheric blocking: The eddy-blocking matching mechanism. *Quarterly Journal of the Royal Meteorological Society*, **140 (683)**, 1785–1808.

Luo, D., Y. Xiao, Y. Yao, A. Dai, I. Simmonds, and C. L. Franzke, 2016: Impact of Ural blocking on winter warm Arctic-cold Eurasian anomalies. Part I: Blocking-induced amplification. *Journal of Climate*, **29 (11)**, 3925–3947.

Lupo, A. R., 1997: A diagnosis of two blocking events that occurred simultaneously in the midlatitude Northern Hemisphere. *Monthly Weather Review*, **125 (8)**, 1801 – 1823.

———, 2021: Atmospheric blocking events: A review. *Annals of the New York Academy of Sciences*, **1504 (1)**, 5–24.

Lupo, A. R. and L. F. Bosart, 1999: An analysis of a relatively rare case of continental blocking. *Quarterly Journal of the Royal Meteorological Society*, **125 (553)**, 107–138.

Lynch, P., 1989: Partitioning the wind in a limited domain. *Monthly Weather Review*, **117 (7)**, 1492 – 1500.

Madonna, E., H. Wernli, H. Joos, and O. Martius, 2014: Warm conveyor belts in the ERA-Interim dataset (1979–2010). Part I: Climatology and potential vorticity evolution. *Journal of Climate*, **27 (1)**, 3 – 26.

Magnusson, L., 2017: Diagnostic methods for understanding the origin of forecast errors. *Quarterly Journal of the Royal Meteorological Society*, **143 (706)**, 2129–2142.

Martin, J. E., 2006: *Mid-Latitude atmospheric dynamics: A first course*. Wiley, 336 pp.

Martineau, P., H. Nakamura, A. Yamamoto, and Y. Kosaka, 2022: Baroclinic blocking. *Geophysical Research Letters*, **49 (15)**, e2022GL097 791.

Martius, O., C. Schwierz, and H. C. Davies, 2010: Tropopause-level waveguides. *Journal of the Atmospheric Sciences*, **67 (3)**, 866 – 879.

Masato, G., B. J. Hoskins, and T. Woollings, 2013: Winter and summer Northern Hemisphere blocking in CMIP5 models. *Journal of Climate*, **26 (18)**, 7044 – 7059.

Masato, G., B. J. Hoskins, and T. J. Woollings, 2012: Wave-breaking characteristics of midlatitude blocking. *Quarterly Journal of the Royal Meteorological Society*, **138 (666)**, 1285–1296.

Matsueda, M., 2009: Blocking predictability in operational medium-range ensemble forecasts. *SOLA*, **5**, 113–116.

Matsueda, M. and M. Kyouda, 2016: Wintertime East Asian flow patterns and their predictability on medium-range timescales. *SOLA*, **12**, 121–126.

Matsueda, M. and T. N. Palmer, 2018: Estimates of flow-dependent predictability of wintertime Euro-Atlantic weather regimes in medium-range forecasts. *Quarterly Journal of the Royal Meteorological Society*, **144 (713)**, 1012–1027.

McLeod, J. T. and T. L. Mote, 2015: Assessing the role of precursor cyclones on the formation of extreme Greenland blocking episodes and their impact on summer melting across the Greenland ice sheet. *Journal of Geophysical Research: Atmospheres*, **120 (24)**, 12 357–12 377.

Michel, C., E. Madonna, C. Spensberger, C. Li, and S. Outten, 2021: Dynamical drivers of Greenland blocking in climate models. *Weather and Climate Dynamics*, **2 (4)**, 1131–1148.

Michel, C. and G. Rivière, 2011: The link between Rossby wave breakings and weather regime transitions. *Journal of the Atmospheric Sciences*, **68 (8)**, 1730–1748.

Michelangeli, P.-A., R. Vautard, and B. Legras, 1995: Weather regimes: Recurrence and quasi stationarity. *Journal of Atmospheric Sciences*, **52 (8)**, 1237 – 1256.

Miller, D. E. and Z. Wang, 2022: Northern Hemisphere winter blocking: Differing onset mechanisms across regions. *Journal of the Atmospheric Sciences*, **79 (5)**, 1291 – 1309.

Mitchell, D., C. Heaviside, S. Vardoulakis, C. Huntingford, G. Masato, B. P Guillod, P. Frumhoff, A. Bowery, D. Wallom, and M. Allen, 2016: Attributing human mortality during extreme heat waves to anthropogenic climate change. *Environmental Research Letters*, **11 (7)**, 074 006.

Mohr, S., U. Ehret, M. Kunz, P. Ludwig, A. Caldas-Alvarez, J. E. Daniell, F. Ehmele, H. Feldmann, M. J. Franca, C. Gattke, M. Hundhausen, P. Knippertz, K. Küpfer, B. Mühr, J. G. Pinto, J. Quinting, A. M. Schäfer, M. Scheibel, F. Seidel, and C. Wisotzky, 2023: A multi-disciplinary analysis of the exceptional flood event of July 2021 in central Europe – Part 1: Event description and analysis. *Natural Hazards and Earth System Sciences*, **23 (2)**, 525–551.

Mullen, S. L., 1987: Transient eddy forcing of blocking flows. *Journal of Atmospheric Sciences*, **44 (1)**, 3–22.

Nakamura, H., M. Nakamura, and J. L. Anderson, 1997: The role of high- and low-frequency dynamics in blocking formation. *Monthly Weather Review*, **125 (9)**, 2074–2093.

Nakamura, H. and J. M. Wallace, 1990: Observed changes in baroclinic wave activity during the life cycles of low-frequency circulation anomalies. *Journal of Atmospheric Sciences*, **47 (9)**, 1100 – 1116.

———, 1993: Synoptic behavior of baroclinic eddies during the blocking onset. *Monthly Weather Review*, **121 (7)**, 1892 – 1903.

Nakamura, N. and C. S. Y. Huang, 2018: Atmospheric blocking as a traffic jam in the jet stream. *Science*, **361 (6397)**, 42–47.

Narinesingh, V., J. F. Booth, S. K. Clark, and Y. Ming, 2020: Atmospheric blocking in an aquaplanet and the impact of orography. *Weather and Climate Dynamics*, **1 (2)**, 293–311.

Newton, C. W. and A. V. Persson, 1962: Structural characteristics of the subtropical jet stream and certain lower-stratospheric wind systems. *Tellus*, **14 (2)**, 221–241.

NOAA Climate Prediction Center, 2023: Daily NAO index since January 1950. URL `https://www.cpc.ncep.noaa.gov/products/precip/CWlink/pna/nao.shtml`.

Oertel, A., M. Pickl, J. F. Quinting, S. Hauser, J. Wandel, L. Magnusson, M. Balmaseda, F. Vitart, and C. M. Grams, 2023: Everything hits at once: How remote rainfall matters for the prediction of the 2021 North American heat wave. *Geophysical Research Letters*, **50 (3)**, e2022GL100 958.

Osserman, R., 1978: The isoperimetric inequality. *Bulletin of the American Mathematical Society*, **84**, 1182–1238.

Otero, N., O. Martius, S. Allen, H. Bloomfield, and B. Schaefli, 2022: Characterizing renewable energy compound events across Europe using a logistic regression-based approach. *Meteorological Applications*, **29 (5)**, e2089.

O'Reilly, C. H., S. Minobe, and A. Kuwano-Yoshida, 2016: The influence of the Gulf Stream on wintertime European blocking. *Climate Dynamics*, **47 (5-6)**, 1545–1567.

Papritz, L., D. Hauswirth, and K. Hartmuth, 2022: Moisture origin, transport pathways, and driving processes of intense wintertime moisture transport into the Arctic. *Weather and Climate Dynamics*, **3 (1)**, 1–20.

Parker, T., T. Woollings, and A. Weisheimer, 2018: Ensemble sensitivity analysis of Greenland blocking in medium-range forecasts. *Quarterly Journal of the Royal Meteorological Society*, **144 (716)**, 2358–2379.

Parker, W. S., 2016: Reanalyses and observations: What's the difference? *Bulletin of the American Meteorological Society*, **97 (9)**, 1565 – 1572.

Pelly, J. L. and B. J. Hoskins, 2003: A new perspective on blocking. *Journal of the Atmospheric Sciences*, **60 (5)**, 743 – 755.

Petoukhov, V., S. Rahmstorf, S. Petri, and H. J. Schellnhuber, 2013: Quasiresonant amplification of planetary waves and recent Northern Hemisphere weather extremes. *Proceedings of the National Academy of Sciences*, **110 (14)**, 5336–5341.

Pettersen, C., S. A. Henderson, K. S. Mattingly, R. Bennartz, and M. L. Breeden, 2022: The critical role of Euro-Atlantic blocking in promoting snowfall in Central Greenland. *Journal of Geophysical Research: Atmospheres*, **127 (6)**, e2021JD035 776.

Pfahl, S., E. Madonna, M. Boettcher, H. Joos, and H. Wernli, 2014: Warm conveyor belts in the ERA-Interim dataset (1979–2010). Part II: Moisture origin and relevance for precipitation. *Journal of Climate*, **27 (1)**, 27 – 40.

Pfahl, S., C. Schwierz, M. Croci-Maspoli, C. M. Grams, and H. Wernli, 2015: Importance of latent heat release in ascending air streams for atmospheric blocking. *Nature Geoscience*, **8 (8)**, 610–614.

Pfahl, S. and H. Wernli, 2012: Quantifying the relevance of atmospheric blocking for co-located temperature extremes in the Northern Hemisphere on (sub-)daily time scales. *Geophysical Research Letters*, **39 (12)**.

Pinheiro, M. C., P. A. Ullrich, and R. Grotjahn, 2019: Atmospheric blocking and intercomparison of objective detection methods: Flow field characteristics. *Climate Dynamics*, **53 (7-8)**, 4189–4216.

Preece, J. R., L. J. Wachowicz, T. L. Mote, M. Tedesco, and X. Fettweis, 2022: Summer Greenland blocking diversity and its impact on the surface mass balance of the Greenland ice sheet. *Journal of Geophysical Research: Atmospheres*, **127 (4)**, e2021JD035 489.

Quinting, J. F. and C. M. Grams, 2021: Toward a systematic evaluation of warm conveyor belts in numerical weather prediction and climate models. Part I: Predictor selection and logistic regression model. *Journal of the Atmospheric Sciences*, **78 (5)**, 1465 – 1485.

———, 2022: Eulerian identification of ascending airstreams (ELIAS 2.0) in numerical weather prediction and climate models – Part 1: Development of deep learning model. *Geoscientific Model Development*, **15 (2)**, 715–730.

Quinting, J. F. and F. Vitart, 2019: Representation of synoptic-scale Rossby wave packets and blocking in the S2S prediction project database. *Geophysical Research Letters*, **46 (2)**, 1070–1078.

Rex, D. F., 1950: Blocking action in the middle troposphere and its effect upon regional climate. *Tellus*, **2 (3)**, 196–211.

———, 1951: The effect of Atlantic blocking action upon European climate. *Tellus*, **2 (3)**, 100–112.

Riemer, M. and S. C. Jones, 2010: The downstream impact of tropical cyclones on a developing baroclinic wave in idealized scenarios of extratropical transition. *Quarterly Journal of the Royal Meteorological Society*, **136 (648)**.

———, 2014: Interaction of a tropical cyclone with a high-amplitude, midlatitude wave pattern: Waviness analysis, trough deformation and track bifurcation. *Quarterly Journal of the Royal Meteorological Society*, **140 (681)**, 1362–1376.

Riemer, M., S. C. Jones, and C. A. Davis, 2008: The impact of extratropical transition on the downstream flow: An idealized modelling study with a straight jet. *Quarterly Journal of the Royal Meteorological Society*, **134 (630)**, 69–91.

Robertson, A. W., N. Vigaud, J. Yuan, and M. K. Tippett, 2020: Toward identifying subseasonal forecasts of opportunity using North American weather regimes. *Monthly Weather Review*, **148 (5)**, 1861 – 1875.

Rodwell, M. J., L. Magnusson, P. Bauer, P. Bechtold, M. Bonavita, C. Cardinali, M. Diamantakis, P. Earnshaw, A. Garcia-Mendez, L. Isaksen, E. Källén, D. Klocke, P. Lopez, T. McNally, A. Persson, F. Prates, and N. Wedi, 2013: Characteristics of occasional poor medium-range weather forecasts for Europe. *Bulletin of the American Meteorological Society*, **94 (9)**, 1393–1405.

Rossby, C.-G., 1940: Planetary flow patterns in the atmosphere. *Quarterly Journal of the Royal Meteorological Society*, **66**, 68–87.

Röthlisberger, M., O. Martius, and H. Wernli, 2018: Northern Hemisphere Rossby wave initiation events on the extratropical jet — A climatological analysis. *Journal of Climate*, **31 (2)**, 743 – 760.

Schäfler, A., M. Boettcher, C. M. Grams, M. Rautenhaus, H. Sodemann, and H. Wernli, 2014: Planning aircraft measurements within a warm conveyor belt. *Weather*, **69 (6)**, 161–166.

Schäfler, A., G. Craig, H. Wernli, P. Arbogast, J. D. Doyle, R. McTaggart-Cowan, J. Methven, G. Rivière, F. Ament, M. Boettcher, M. Bramberger, Q. Cazenave, R. Cotton, S. Crewell, J. Delanoë, A. Dörnbrack, A. Ehrlich, F. Ewald, A. Fix, C. M. Grams, S. L. Gray, H. Grob, S. Groß, M. Hagen, B. Harvey, L. Hirsch, M. Jacob, T. Kölling, H. Konow, C. Lemmerz, O. Lux, L. Magnusson, B. Mayer, M. Mech, R. Moore, J. Pelon, J. Quinting, S. Rahm, M. Rapp, M. Rautenhaus, O. Reitebuch, C. A. Reynolds, H. Sodemann, T. Spengler, G. Vaughan, M. Wendisch, M. Wirth, B. Witschas, K. Wolf, and T. Zinner, 2018: The North Atlantic waveguide and downstream impact experiment. *Bulletin of the American Meteorological Society*, **99 (8)**, 1607 – 1637.

Schneider, T., 2006: The general circulation of the atmosphere. *Annual Review of Earth and Planetary Sciences*, **34**, 655–688.

Schneidereit, A., S. Schubert, P. Vargin, F. Lunkeit, X. Zhu, D. H. W. Peters, and K. Fraedrich, 2012: Large-scale flow and the long-lasting blocking high over Russia: Summer 2010. *Monthly Weather Review*, **140 (9)**, 2967 – 2981.

Schwierz, C., M. Croci-Maspoli, and H. Davies, 2004: Perspicacious indicators of atmospheric blocking. *Geophys. Res. Lett.*, **31**, L06 125.

Shi, N. and H. Nakamura, 2021: A new detection scheme of wave-breaking events with blocking flow configurations. *Journal of Climate*, **34 (4)**, 1467–1483.

Shutts, G. J., 1983: The propagation of eddies in diffluent jetstreams: Eddy vorticity forcing of 'blocking' flow fields. *Quarterly Journal of the Royal Meteorological Society*, **109 (462)**, 737–761.

Sillmann, J., M. Croci-Maspoli, M. Kallache, and R. W. Katz, 2011: Extreme cold winter temperatures in Europe under the influence of North Atlantic atmospheric blocking. *Journal of Climate*, **24 (22)**, 5899 – 5913.

Simonson, J. M., S. D. Birkel, K. A. Maasch, P. A. Mayewski, B. Lyon, and A. M. Carleton, 2022: Association between recent U.S. northeast precipitation trends and Greenland blocking. *International Journal of Climatology*, **42 (11)**, 5682–5693.

Sousa, P. M., D. Barriopedro, R. García-Herrera, T. Woollings, and R. M. Trigo, 2021: A new combined detection algorithm for blocking and subtropical ridges. *Journal of Climate*, **34 (18)**, 7735 – 7758.

Spensberger, C., E. Madonna, M. Boettcher, C. M. Grams, L. Papritz, J. F. Quinting, M. Röthlisberger, M. Sprenger, and P. Zschenderlein, 2020: Dynamics of concurrent and sequential Central European and Scandinavian heatwaves. *Quarterly Journal of the Royal Meteorological Society*, **146 (732)**, 2998–3013.

Spreitzer, E., R. Attinger, M. Boettcher, R. Forbes, H. Wernli, and H. Joos, 2019: Modification of potential vorticity near the tropopause by nonconservative processes in the ECMWF model. *Journal of the Atmospheric Sciences*, **76 (6)**, 1709 – 1726.

Sprenger, M. and H. Wernli, 2015: The LAGRANTO Lagrangian analysis tool - Version 2.0. *Geoscientific Model Development*, **8 (8)**, 2569–2586.

Stan, C. and D. M. Straus, 2007: Is blocking a circulation regime? *Monthly Weather Review*, **135 (6)**, 2406–2413.

Steinfeld, D., 2019: The role of latent heating in atmospheric blocking: climatology and numerical experiments. *Doctoral Thesis ETH Zurich.*

Steinfeld, D., M. Boettcher, R. Forbes, and S. Pfahl, 2020: The sensitivity of atmospheric blocking to upstream latent heating – numerical experiments. *Weather and Climate Dynamics*, **1 (2)**, 405–426.

Steinfeld, D. and S. Pfahl, 2019: The role of latent heating in atmospheric blocking dynamics: A global climatology. *Climate Dynamics*, **53 (9-10)**, 6159–6180.

Steinfeld, D., M. Sprenger, U. Beyerle, and S. Pfahl, 2022: Response of moist and dry processes in atmospheric blocking to climate change. *Environ. Res. Lett*, **17**, 84 020.

Suitters, C. C., O. Martínez-Alvarado, K. I. Hodges, R. K. H. Schiemann, and D. Ackerley, 2023: Transient anticyclonic eddies and their relationship to atmospheric block persistence. *Weather and Climate Dynamics*, **4 (3)**, 683–700.

Teubler, F., 2018: Dynamik von Rossbywellenpaketen aus einer quantitativen PV-Perspektive. Dissertation, Johannes Gutenberg-Universität Mainz.

Teubler, F. and M. Riemer, 2016: Dynamics of Rossby wave packets in a quantitative potential vorticity-potential temperature framework. *Journal of the Atmospheric Sciences*, **73 (3)**, 1063–1081.

———, 2021: Potential-vorticity dynamics of troughs and ridges within Rossby wave packets during a 40-year reanalysis period. *Weather and Climate Dynamics*, **2 (3)**, 535–559.

Teubler, F., M. Riemer, C. Polster, C. M. Grams, S. Hauser, and V. Wirth, 2023: Similarity and variability of blocked weather-regime dynamics in the Atlantic-European region. *Weather and Climate Dynamics*, **4 (2)**, 265–285.

Tibaldi, S. and F. Molteni, 1990: On the operational predictability of blocking. *Tellus, Series A*, **42 A (3)**, 343–365.

Tsou, C.-H. and P. J. Smith, 1990: The role of synoptic/planetary–scale interactions during the development of a blocking anticyclone. *Tellus A*, **42 (1)**, 174–193.

Tyrlis, E. and B. J. Hoskins, 2008: Aspects of a Northern Hemisphere atmospheric blocking climatology. *Journal of the Atmospheric Sciences*, **65 (5)**, 1638 – 1652.

Vautard, R., 1990: Multiple weather regimes over the North Atlantic: Analysis of precursors and successors. *Monthly Weather Review*, **118 (10)**, 2056 – 2081.

Vautard, R. and B. Legras, 1988: On the source of midlatitude low-frequency variability. Part II: Nonlinear equilibration of weather regimes. *Journal of Atmospheric Sciences*, **45 (20)**, 2845 – 2867.

Vigaud, N., A. Robertson, and M. K. Tippett, 2018: Predictability of recurrent weather regimes over North America during winter from submonthly reforecasts. *Monthly Weather Review*, **146 (8)**, 2559 – 2577.

Wallace, J. M., G.-H. Lim, and M. L. Blackmon, 1988: Relationship between cyclone tracks, anticyclone tracks and baroclinic waveguides. *Journal of Atmospheric Sciences*, **45 (3)**, 439 – 462.

Wandel, J. L., 2022: Representation of warm conveyor belts in sub-seasonal forecast models and the link to Atlantic-European weather regimes. Ph.D. thesis, Karlsruher Institut für Technologie (KIT).

Wernli, H., 1997: A Lagrangian-based analysis of extratropical cyclones. II: A detailed case-study. *Quarterly Journal of the Royal Meteorological Society*, **123 (542)**, 1677–1706.

Wernli, H. and H. C. Davies, 1997: A Lagrangian-based analysis of extratropical cyclones. I: The method and some applications. *Quarterly Journal of the Royal Meteorological Society*, **123 (538)**, 467–489.

Wernli, H. and C. Schwierz, 2006: Surface Cyclones in the ERA-40 dataset (1958–2001). Part I: Novel identification method and global climatology. *Journal of the Atmospheric Sciences*, **63 (10)**, 2486–2507.

Wiel, K. V. D., H. C. Bloomfield, R. W. Lee, L. P. Stoop, R. Blackport, J. A. Screen, and F. M. Selten, 2019: The influence of weather regimes on European renewable energy production and demand. *Environmental Research Letters*, **14**.

Wills, R. C., R. H. White, and X. J. Levine, 2019: Northern Hemisphere stationary waves in a changing climate. *Current Climate Change Reports*, **5 (4)**, 372–389.

Winters, A. C., D. Keyser, L. F. Bosart, and J. E. Martin, 2020: Composite synoptic-scale environments conducive to North American polar–subtropical jet superposition events. *Monthly Weather Review*, **148 (5)**, 1987 – 2008.

Wirth, V., M. Riemer, E. K. Chang, and O. Martius, 2018: Rossby wave packets on the midlatitude waveguide - A review. *Monthly Weather Review*, **146 (7)**, 1965–2001.

Woollings, T., D. Barriopedro, J. Methven, S. W. Son, O. Martius, B. Harvey, J. Sillmann, A. R. Lupo, and S. Seneviratne, 2018: Blocking and its response to climate change. *Current Climate Change Reports*, **4 (3)**, 287–300.

Woollings, T., A. Hannachi, and B. Hoskins, 2010: Variability of the North Atlantic eddy-driven jet stream. *Quarterly Journal of the Royal Meteorological Society*, **136 (649)**, 856–868.

Woollings, T., B. Hoskins, M. Blackburn, and P. Berrisford, 2008: A new Rossby wave–breaking interpretation of the North Atlantic Oscillation. *Journal of the Atmospheric Sciences*, **65 (2)**, 609 – 626.

Yamazaki, A. and H. Itoh, 2009: Selective absorption mechanism for the maintenance of blocking. *Geophysical Research Letters*, **36 (5)**.

———, 2013: Vortex-vortex interactions for the maintenance of blocking. Part I: The selective absorption mechanism and a case study. *Journal of Atmospheric Sciences*, **70**, 725–742.

Yao, Y., W. Zhang, D. Luo, L. Zhong, and L. Pei, 2022: Seasonal cumulative effect of Ural blocking episodes on the frequent cold events in China during the early winter of 2020/21. *Advances in Atmospheric Sciences*, **39 (4)**, 609–624.

Yiou, P. and M. Nogaj, 2004: Extreme climatic events and weather regimes over the North Atlantic: When and where? *Geophysical Research Letters*, **31 (7)**.

Zierl, B. and V. Wirth, 1997: The Influence of radiation on tropopause behavior and stratosphere-troposphere exchange in an upper tropospheric anticyclone. *Journal of Geophysical Research: Atmospheres*, **102 (D20)**, 23 883–23 894.

Ziv, B. and P. Alpert, 1994: Isobaric to isentropic interpolation errors and implication to potential vorticity analysis. *Journal of Applied Meteorology and Climatology*, **33 (6)**, 694 – 703.

Acknowledgments

The last four years have definitely been a challenging time with ups and downs, and I would like to take this opportunity to thank all those who have actively supported me on this journey.

I would like to start by thanking my first reviewer and main supervisor Christian Grams for the opportunity to work on the topic of blocked weather regime dynamics and to write my dissertation in his research group. My journey started already in spring 2018 with my master thesis during a time when the young investigator research group was newly formed. Being in a young team motivated and convinced me to do a PhD under his supervision. Thank you, Christian, for all the scientific discussions, advice, and the motivation boosts whenever I felt a bit puzzled. I am so grateful for your help to build a scientific network and to the freedom to bring in own research ideas.

Many thanks go to Peter Knippertz, my second reviewer, who gave some important guidance during the PhD. Peter, thank you for the fruitful discussions and your feedback that always brought different perspectives and new ideas for my work. Further gratitude is given to Michael Riemer from the Johannes-Gutenberg University (JGU) in Mainz, who volunteered to be my external supervisor within the Waves To Weather (W2W) project. Thank you for many scientific discussions, your help in shaping the project, and the time you took whenever I visited JGU for an intensive scientific exchange. I would also like to thank my close project partner Franziska Teubler from JGU, who actively supported me by providing the piecewise PV tendencies in ERA5, for many discussions on the PV-θ-framework, and the countless off-topic discussions.

Furthermore, I would like to thank all members in the A8 project within W2W. I really enjoyed the numerous project meetings as well as the associated visits to JGU, which often ended up in diverse non-scientific activities after work. Thank you for your feedback and input on my work in the last four years. In this sense, I would also like to thank W2W. I really enjoyed it being a part of Phase 2 and to be surrounded by so many inspiring scientists. Especially the research area meetings, the annual project meetings and early career scientists meetings were absolutely enjoyable. Collaborations within W2W have also been fruitful, most recently leading to two joint papers with the subprojects B8 and C8. I am also very grateful to W2W for the financial support during this time, because I had the chance to participate in numerous conferences and workshops, as far as also to do a research stay in Madison, Wisconsin. Thank you for supporting the organization of the Atmospheric Blocking Workshop in the fall of 2021 -

a highlight during my PhD that helped among other things to build up my scientific network.

I am very grateful to have been part of the 'Large-scale dynamics and predictability' group of Christian Grams during my PhD. Already during my master thesis in the group, I felt the strong team spirit and the common joy in scientific work and highly enjoyed the time together. I couldn't have imagined a better group and atmosphere - together we managed the pandemic with countless virtual coffee breaks in home office very well. I want to thank you all for valuable scientific discussions within the weekly team meeting, honest and encouraging feedback on my work, and the mental support when it was needed (especially in the last months prior to submission!). I really enjoyed the conference trips as a group, and our group retreats in Klingenmünster. In addition, the countless free-time activities like bowling, group hikes, BBQs, and skiing trips have demonstrated even more how strong the bond is and how much we enjoy the company of each other within the group.

I would like to briefly mention a few people individually, who have supported me, particularly during my doctoral studies. Thank you to everybody at the IMK-TRO institute for enjoyable coffee breaks between TRO-seminar talks or in the coffee room on the 3rd floor. Thank you, Roswitha Marioth, Rosalba Gräbner, Alexandra Beideck, Sarah Schneitz, and Gabi Klinck for administrative and IT support during my PhD time. Thank you, Jonathan Martin and Stephanie Henderson, for being my hosts during the research stay in Madison in May/June 2022 and giving me scientific input on my research. It was lovely to meet you again at the AMS conference in Denver and showed, that even short research stays can trigger future collaboration. Thank you, Julian Quinting (aka Juqu), for your tireless technical support and valuable scientific input and further ideas for the project. I want to thank my PhD fellow Jan Wandel (aka Blumen-Jan) for sharing mostly the 316a office, complaining about the downs of the PhD, for taking care of all our office plants when I was on vacation, and for the off-topic discussions on German TV shows and pop singers. I would especially like to thank Moritz Deinhard (aka Mopi) for his immense support and day-to-day motivation. During the PhD, you need that one person in the office who always brings you back down to earth and de-emotionalizes the facts, that at first seem very (!) dramatic. Thank you for singing with me in the office and playing tennis across our desks (Gabi, I promise we made sure to keep distance to the computers!). I also want to thank my meteorology fellow students, most of them I have known for ten years now. Thank you, Franziska Vogel, Sascha Bierbauer, Lisa Muth, Konstantin Krüger, Nils König, Jonas Straub, Julia Kaufmann, Johannes Speidel, Sven Werchner, and Philipp Diez for the enjoyable off-topic discussions and free-time activities after lectures/work and on the weekends.

Last but not least, I want to thank my closest friends and my family. Thank you, Laura Zistler, Katrin Hartmann, Katharina Küpfer, and Maria Madsen for the endless support and motivation. My greatest gratitude goes to my parents, and my brother for the continuous support and love. I could not have done it without you.